EVOLUTION OF THE EARLY MIOCENE CARBONATE:

BATURAJA FORMATION IN NORTHWEST JAVA BASIN, INDONESIA

A Dissertation

by

ROBET WAHYU WIDODO

Submitted to the Office of Graduate and Professional Studies of
Texas A&M University
in partial fulfillment of the requirements for the degree of

DOCTOR OF PHILOSOPHY

Chair of Committee,	Juan Carlos Laya
Committee Members,	Michael C. Pope
	Robert S. Reece
	Carlos A. Alvarez Zarikian
Head of Department,	Michael C. Pope

August 2018

Major Subject: Geology

ABSTRACT

The Oligocene-Miocene carbonate successions around the world are fundamental targets for hydrocarbon exploration and production. New findings indicate the importance of the red algae and large benthic foraminifera (LBF) association for this geological time, proposed as the main carbonate producers worldwide, accompanied by the scattered and small coral colonies. This skeletal domination also occurs in the Baturaja Formation, one of the prolific reservoirs in the Northwest (NW) Java Basin, Indonesia. This Early Miocene unit was deposited on a ramp setting governed by a north-south fault system. Previously, a classic barrier-reef to lagoon model, was applied to this formation, with corals as major carbonate factory which is a common setting for modern environments.

The Early Miocene is characterized by global conditions of warm temperature and higher carbon productivity and higher CO_2. The abundace of the red algae and LBF association might be related to their ability to adapt to these specific conditions. Contrastingly, corals tend to have difficulties in the euphotic zone and to build rigid and wave-resistant reefs to sea level in this setting. A regional paleogeography and depositional model are proposed for the Baturaja Formation using this skeletal association scheme. The ramp configuration also was controlled by the pre-existing topography and might be responsible for the facies variety across the ramp, facies distribution, stratigraphic architecture, and geometry of its carbonate mounds.

The Baturaja Formation reservoir porosity have been known to be influenced by meteoric diagenetic processes, especially in its carbonate mound settings. Evidences of this meteoric dissolution events occur as dissolution voids and ^{13}C-depleted intervals. Subaerial exposure episodes are indicated by the negative-shifts of δ^{13}C. Acidic meteoric water flushing and soil-derived CO_2 are responsible for the dissolution of mainly ellipsoidal red algae and perforated LBF, that produced extensive moldic porosity with a fabric selective dissolution texture. This dissolution was then followed by precipitation of calcite cement while retaining its moderate strontium content. Meanwhile, pore spaces resulted by a possible burial dissolution are inferred by higher CO_2 contaminants in the reservoir intervals at the well located at the deeper inter-mound depositional setting; an area unaffected by meteoric dissolution events. Mantle degassing- and magmatic-derived CO_2 are likely the sources for this gas. The upward pathways for this corrosive CO_2 are facilitated by deep-seated faults to the basement and intrusion-related faults formed in the area. Non-fabric selective dissolution texture is resulted by burial dissolution processes and it cuts across all the carbonate components. The burial dissolution porosity generation suggests to the shifting of the hydrocarbon exploration play from the well-known carbonate mound to the deeper inter-mound depositional target. Red algal-LBF packstone-grainstone facies with good moldic and vuggy porosity are expected.

Meanwhile, fieldwork in the Mason County, central Texas, on the Early Cretaceous Fort Terrett Formation shows that the subtidal to peritidal succession consists of mud-dominated facies with minor intervals of grainy bioclastic facies. Dolomite beds are observed throughout this formation, in addition to the matrix-replaced dolomite layers in the Hensel Formation. Dolomite formations in these units resulted from the progressive development and recrystallization of the dolomite type. Interconnected fenestral porosity is proposed to have had a significant impact on initial permeability within the muddy succession of Fort Terrett Formation and provided the pathways and conduits for Mg-rich dolomitizing brines. A density head driven-mechanism, generated by dense hypersaline fluids from an evaporating lagoon, was responsible for the downward movement of the dolomitizing fluids.

ACKNOWLEDGEMENTS

I would like to thank my advisor, Dr. Juan Carlos Laya, to give me challenging experiences through this one-in-a-lifetime chance to get the doctoral degree. I would also express my gratitude to my committee members, Dr. Mike Pope, Dr. Bobby Reece, and Dr. Carlos Zarikian for their guidance, constructive review, and support of this research.

I want to thank all the PT PERTAMINA colleagues, managements and board of directors especially Bapak Syamsu Alam, Ibu Rusalida Raguwati, Bapak Herutama Trikoranto, Bapak Nanang Abdul Manaf, Bapak Indra Prasetya, Bapak Asep Samsyu Arifin, Suprayitno Adhi Nugroho, Yosa Al Mizani, Muchamad Oktasena, Alexis Badai Samudra, Kang Dadan Kriswandi, and Cecep Ajid Ambali for their help to get the data permission and collection.

For the fieldwork in Mason, I also thank for the help of Riza El Putranto, J Campbell Craig and MMWMA management, especially Mark Mitchell, for letting us undertake the research in the area. Sample preparations for the thin sections were helped by Benjamin Hill and Dara Pajouhafsar, while stable isotope and trace element analysis were helped by Taryn Taylor, Andrea Flores, Rodrigo Mendoza and Shukuru Makanyaga.

Credit also is due to Luz Romero, a technical laboratory coordinator for the R. Ken Williams '45 Radiogenic Isotope Geosciences Laboratory and Chris Maupin, a facility manager for the Stable Isotope Geosciences Facility at Texas A&M University for their help and instruction for the sample preparation and its analysis.

I also would like to thank all my colleagues (Jonathan Sulaica, Roy Conte, Philipp Tesch, Kieron Prince, James Teoh, Made Suardana, Devri Agustianto, Adewale Amosu, Young Lim,

Hamdi Mahmood, Tanner Mills, “P” Pondthai, Tom Somchat and Pin Shuai), faculty and staff (Trisha Fike, Elizabeth Collins, Suzanne Rosser, and Dawn Spencer) members of the Department of Geology and Geophysics at Texas A&M University for their willing to help and discussions in all aspects.

Finally, I would like to thank my wife Yanni A. Sutomo and my children Deltabara A. Robbani, Marinara O. Robbani and Texaterra A. Robbani for their support, motivation, and encouragement throughout my study where joys, laughs, and tears accompany our journey!

CONTRIBUTORS AND FUNDING SOURCES

This research was supported by a crash program scholarship of the PT PERTAMINA, Indonesia. Subsurface data was provided by PT PERTAMINA EP. Dr. Juan Carlos Laya funded the thin section preparation, stable isotope and trace element analysis used in this research.

This work was supervised by a dissertation committee consisting of Dr. Juan Carlos Laya (advisor), Dr. Mike Pope, and Dr. Bobby Reece of the Department of Geology and Geophysiscs and Dr. Carlos Alvarez Zarikian Professor of the IODP. All work for the dissertation was completed independently by the student.

TABLE OF CONTENTS

Page

LIST OF FIGURES

LIST OF TABLES

Page

CHAPTER 1

INTRODUCTION

1.1 General introduction

Carbonate reservoirs, worldwide, typically are heterogeneous in their depositional textures and reservoir properties including porosity and permeability. This type of reservoirs usually is characterized by highly variable hydrocarbon production because it has some complex porosity formed and controlled by diagenetic processes. Therefore, determining the controls that characterize these reservoirs for successful hydrocarbon exploration, reservoir development and hydrocarbon production are challenging and problematic.

The most prolific Oligocene-Miocene carbonate reservoirs play a significant role in hydrocarbon exploration and exploitation globally. In the case of SE Asia basins, these rocks have significant economic impact in the region, contain reserves of possible tens of billions barrels of oil-equivalent hydrocarbons, that make them very attractive for this business. However, many of the successions in SE Asian basins are poorly documented and geologically barely understood. This is also the case of the Early Miocene Baturaja Formation; previously referred to Middle Cibulakan Formation.

The Baturaja Formation is a thick carbonate succession and one of the main reservoirs in the northwest (NW) Java Basin. Lithologically, the Baturaja formation can be divided into lower and upper members. The Baturaja Formation was deposited in a marine transgression on a shallow marine ramp above mainly siliciclastic synrift deposits of the Talang Akar Formation and locally paleotopographic basement. Baturaja Formation consists of a wide range of carbonate textures from mudstone to rudstone. Even though various attempts have been made to describe and characterize these units for their sedimentology, facies and reservoir geometries (e.g. Burbury, 1977; IIAPCO, 1986; Wicaksono et al., 1995; Satyana, 2005; Clement and Hall, 2007), they mostly apply the classic coral barrier-reef to lagoon model. Based on this model, corals were the main carbonate factory; an interpretation that is not accurate in the case of the Baturaja Formation. During the Oligocene-Miocene, red algae and LBF were flourished globally (Pomar et al., 2017), hence these skeletal grains were the most significant rock volume of the successions deposited at this time.

In addition, the hydrocarbons produced from the Baturaja Formation are mainly from moldic and vuggy pores. This type of porosity was widely interpreted to result from dissolution of aragonitic skeletal grains and lime mud in a meteoric diagenetic setting (e.g. Larue, 1976; Ardila, 1982; IIAPCO, 1986; Tonkin et al., 1992; Park et al., 1995; Wicaksono, 1995). Contrastingly, subsurface data from the Melandong field shows that mostly meteoric dissolution processes leached red algae, and LBF resulting in more fabric-selective dissolution texture and more abundant moldic porosity in the carbonate mound area. The shallow ramp setting where the Baturaja Formation was deposited was susceptible to occasional meteoric exposure. Additionally, moldic and vuggy pores also occur in the inter-mound areas; deeper depositional settings in which subaerial exposure was very unlikely. Hence, burial dissolution process likely generated these pores through the dissolution of the limestone by aggressive fluids containing CO_2 from mantle degassing (i.e. Dai et al., 1996; Cooper et al., 1997; Noble et al., 1997) and possibly intrusive magma as the Baturaja reservoirs contain CO_2 ranging from 16 to 92% in the study area. Major faults, as a result of extensional tectonism during the early rifting system in the study area, formed favorable upward conduits for this corrosive gas as these faults connect the mantle CO_2 sources with the Baturaja reservoirs. The burial dissolution tends to produce non-fabric selective texture in which the CO_2 leached and cut across red algae, LBF, calcite cements, and carbonate mud. Overprinting of the pore volumes from previous meteoric events is very likely especially at the carbonate mound area.

This burial dissolution porosity generation implies to the new concept of hydrocarbon exploration for the Baturaja Formation, as the conventional carbonate mounds were discovered (Netherwood, 2000). A new play to a deeper structural area with reservoirs expected to have burial dissolutions is proposed. In addition, an area adjacent to the major deep-seated faults likely has a good chance to have CO_2 discharge from mantle and magmatic sources to dissolve the rock and create secondary porosity.

1.2. Objectives

This study attempts to integrate facies and diagenetic models of the Baturaja Formation with the Early Miocene global events in the onshore blocks of the NW Java Basin to provide a comprehensive reservoir characterization. The results will contribute to reduce uncertainty and enhance exploration and production activities on carbonate reservoirs, which are usually characterized by a highly variable hydrocarbon production, and propose an exploration play as the conventional model of carbonate mound reservoirs were discovered. The objectives of the study are:

- To define the facies types of the Baturaja Formation, its lateral distribution and reservoir geometries. All of these are affected by the combined global Early Miocene events controlling the paleogeography, facies architecture and depositional model of the Baturaja Formation in the region.

- To combine petrography with stable isotope and trace element values to construct a diagenetic model of the Baturaja Formation. The model will be a key to describe the diagenetic evolution controlling porosity generation.
- To analyze petrographic and geochemical methods to define facies and diagenetic processes, especially dolomite typing and the processes of dolomitization for the Early Cretaceous succession in central Texas.

To reach the overall objectives the project will be carried out using two different approaches: 1) a detailed study of the Baturaja Formation in a subsurface dataset from the Melandong area, onshore portion of the NW Java Basin; and 2) characterization of an outcrop in the central Texas, USA using similar methodology used for the Baturaja dataset.

1.3. Study area

The main study area is located in the Melandong area, onshore NW Java Basin. This section is one of the oil/gas fields operated by Pertamina EP (a subsidiary company of Pertamina: an Indonesian state-owned oil and natural gas corporation). It is situated in the Cipunegara sub-basin and bordered by the Pamanukan High to the west and the Kandanghaur-Gantar High to the east. This study will be complemented with the investigation of a surface fieldwork from the Fort Terrett Formation (Lower Edwards Group) in the central Texas. The outcrop is located within the Mason Mountain Wildlife Management Area (MMWMA), 17.7 km north of Mason, Texas. Outcrops occur on the western flank of the Llano Uplift and the eastern extension of the Edwards Plateau. Detailed descriptions of both areas are explained in Chapters 2 and 4.

1.4. Thesis outline

We address our study into three individual chapters written in the style of journal publications. Each chapter includes an abstract, introduction, methodology, results, discussion and conclusion sections. A common reference section is provided at the end.

Chapter 2. Carbonate components and facies distribution of the Early Miocene carbonate succession, northwest Java, Indonesia: The present is not the key to the past?

This chapter investigates the importance of red algae and LBF association as the main contributors to the carbonate factory of the Early Miocene carbonate succession. This new interpretation readdresses a common interpretation that coral reefs are the major reef builder in the Miocene carbonate mounds, as observed in modern environments.

Chapter 3. Origin of porosity and diagenetic evolution of the Early Miocene Baturaja Formation, northwest Java basin, Indonesia

This chapter defines the diagenetic events for the Baturaja Formation right after its deposition in marine conditions, during which multiple subaerial exposure events lead to most of meteoric vadose and phreatic zones, and burial processes. It discusses the generation of extensive moldic and vuggy pores in the reservoir intervals through meteoric and burial dissolution processes. In addition, implication of these processes on hydrocarbon exploration and production also is discussed.

Chapter 4. Controls on diagenesis and dolomitization of peritidal facies, Early Cretaceous Lower Edwards Group, central Texas, USA

This chapter presents an interpretation of interconnected fenestral porosity that could have had a significant impact on permeability within the muddy succession and provided the pathways and conduits for Mg-rich brines to dolomitize Lower Edwards Group strata. This chapter was published in the *Facies* journal (Widodo and Laya, 2017) and is presented in this thesis as a chapter with some editorial modifications.

Chapter 5. Conclusion

This chapter gives an overall summary, major findings and conclusion of the study. Additionally, an explanation for the future works is also presented.

Appendix

Appendix 1. Nomenclature

Appendix 2. Detailed core descriptions

Appendix 3. Petrographic analysis of the Melandong dataset using point counting to determine microfacies of the samples

Appendix 4. Porosity measurement of the Mason dataset

Appendix 5. Stable isotope and trace element analysis of the Melandong dataset

Appendix 6. Stable isotope and trace element analysis of the Mason dataset

Appendix 7. Published article on Facies Journal

CHAPTER 2

CARBONATE COMPONENTS AND FACIES DISTRIBUTION OF THE EARLY MIOCENE CARBONATE SUCCESSION, NORTHWEST JAVA, INDONESIA: THE PRESENT IS NOT THE KEY TO THE PAST?

2.1. Overview

The Oligocene-Miocene deposits in the Indo-Pacific province are significant targets for hydrocarbon exploration and production including carbonate successions such as the Baturaja Formation, a thick shallow marine carbonate succession formed in a post-rift setting. In spite of several studies on this unit the classic interpretation of the succession is problematic due to the major skeletal components building carbonate mounds and implications to the facies distributions.

The Early Miocene is characterized by globally warm temperatures, high sea levels, higher carbon productivity, and higher atmospheric CO_2. These conditions favor red algae and large benthic foraminifera (LBF) over other carbonate producing organisms. In contrast, corals were less able to develop significant buildups within the euphotic zone on top of the paleohighs.

This study focuses on the significance of the carbonate producers and their facies distribution in a highly hydrocarbon productive area. We propose a new regional paleogeography map that shows a carbonate ramp model in this area. The main bioclastic components are red algae and LBF which are the main constructors to the carbonate sediments for the Early Miocene deposits worldwide, accompanied by scattered and small coral colonies. This explanation differs from the common model presented for the region where the carbonate mounds are formed by coral reef frameworks. In addition, this interpretation might have global implication since the same model was repeated in different Neogene carbonate platform around the world.

2.2. Keywords

Northwest Java, Indonesia, Baturaja Formation, carbonate ramp, Early Miocene, red algae, large benthic foraminifera.

2.3. Introduction

Early Miocene carbonate successions are identified in many basins worldwide and they are very well documented especially in the hydrocarbon producing areas. Several examples of great importance can be highlighted in the literature including Nido Limestone of Malampaya (Fournier et al., 2004), Central Luconia carbonate (Epting, 1980), Zhujiang carbonate of Pearl River Mouth Basin (Turner and Zhong, 1996), Arun Limestone of North Sumatra (Wilson, 2002), and Kais Formation of Papua (Gibbson-Robinson & Soedirdja, 1986) from south east (SE) Asia among other localities such as Bombay Limestone of offshore India (Rao and Talukdar, 1980), Asmari limestone reservoir of Iran (van Buchem et al., 2010), Oligo-Miocene carbonate of Perla Field Venezuela (Pomar et al., 2015), and Nukhul carbonate of Gulf of Suez (Alsharhan, 2003). In Indonesia, large oil and gas fields represent more than 1-trillion-cubic-feet (TCF) gas and 80-million-barrel oil (MMBO). Within those reserves Oligocene-Miocene carbonate rocks provide remaining recoverable reserves of 1.5 MMBO and 64 TCFG (Wilson and Hall, 2010).

Many of these Early Miocene carbonate successions were described and interpreted by applying the classic barrier-reef to lagoon model (Pomar et al., 2015). However, many cases in the geological record show that "the present is not the key to the past" due to the different dominant carbonate components indicating biotic community replacements throughout different geological times. This is also the case for the Early Miocene deposits of the Baturaja Formation in Indonesia; previously referred to the Middle Cibulakan Formation. This thick carbonate succession is one of the main reservoirs in the northwest (NW) Java Basin and is the main focus for this study (Figure

2.1). The Baturaja Formation was deposited during a marine transgression on a shallow marine ramp that mostly onlaps the clastic synrift deposits of the Talang Akar Formation and locally basement highs. The Baturaja Formation consists of a wide range of carbonate textures from mudstone to rudstone.

Bioclastic to coral-rich packstone-grainstone and mudstone was described as major facies in the basin (Larue, 1976; Ardilla, 1982; Bishop, 2000; Satyana, 2005). However, their descriptions show that the red algal and LBF association dominates the succession. These skeletal grains form carbonate mounds, where topographic relief resulted from the colonization of the pre-existing topographic high above the sea floor. These mounds were interpreted to be reefal buildups constructed by corals, but, we demonstrate that these biostructures are mainly formed of red algal facies and LBF bioclastic components. Thus, the coral-rich facies, previously defined as the main reef builder (Djuanda, 1985; IIAPCO, 1986; Tonkin et al., 1992; Park et al., 1995; Wicaksono et al., 1995), is spatially limited and did not form framework structures to form a *sensu stricto* defined reef (Lowenstam, 1950; Riding, 2002).

Red algal and LBF facies, especially packstone, grainstone and floatstone comprise a significant rock volume of the carbonate mounds at the middle ramp. These facies contribute to improve reservoir quality by their extensive diagenetic porosity. Low-relief mound geometry is observed while relatively flat morphology is common for inter-mound deposits, parallel to the southward gently-dipping basin (Figure 2.2).

This study indicates the difficulty to interpreting all carbonate mound deposits using direct modern analogs as coral reef structures. We suggest that corals did not form reefs or buildups, instead the main carbonate producers of the Early Miocene mounts of this area are red algae and LBF. This is similar to many other Miocene successions worldwide (e.g. Jones and Hunter, 1994;

Corda and Palmiotto, 2015; Pomar et al., 2004; 2015; 2017). These skeletal grains form widely variable facies belts along the Baturaja Formation ramp. In addition, we suggest that global conditions of warmer temperature, higher CO_2 concentrations and moderate nutrients are the main controls for these carbonate components.

This study defines facies type, lateral distribution and reservoir geometries of the Baturaja Formation affected by the combined global Early Miocene events. We also present new paleogeography map, facies architecture and depositional model of the Lower Miocene deposits in the region.

2.4. Geological background

The NW Java Basin evolved in four distinct tectonic stages: a) Late Cretaceous to Early Paleogene, b) Oligocene to Early Miocene, c) Early to Late Miocene, and d) Plio-Pleistocene (Ben-Avraham and Emery, 1973; Netherwood, 2000). These stages are strongly linked with the tectonic evolution of SE Asia (Figure 2.3).

Initially during the Late Cretaceous to Early Paleogene, the older successions (Paleozoic and Mesozoic rocks) were metamorphosed and deformed into large structural blocks, which then were intruded by igneous rocks (Ben-Avraham and Emery, 1973). These igneous and metamorphic rock belts constitute the basement core of the Sundaland; the southeastern promontory of the Eurasian continental plate formed as a mosaic continental blocks or microplates rifted from Gondwana margins and constructed the continental part of the SE Asia (Netherwood, 2000; Hall, 2012; Zahirovic et al., 2014).

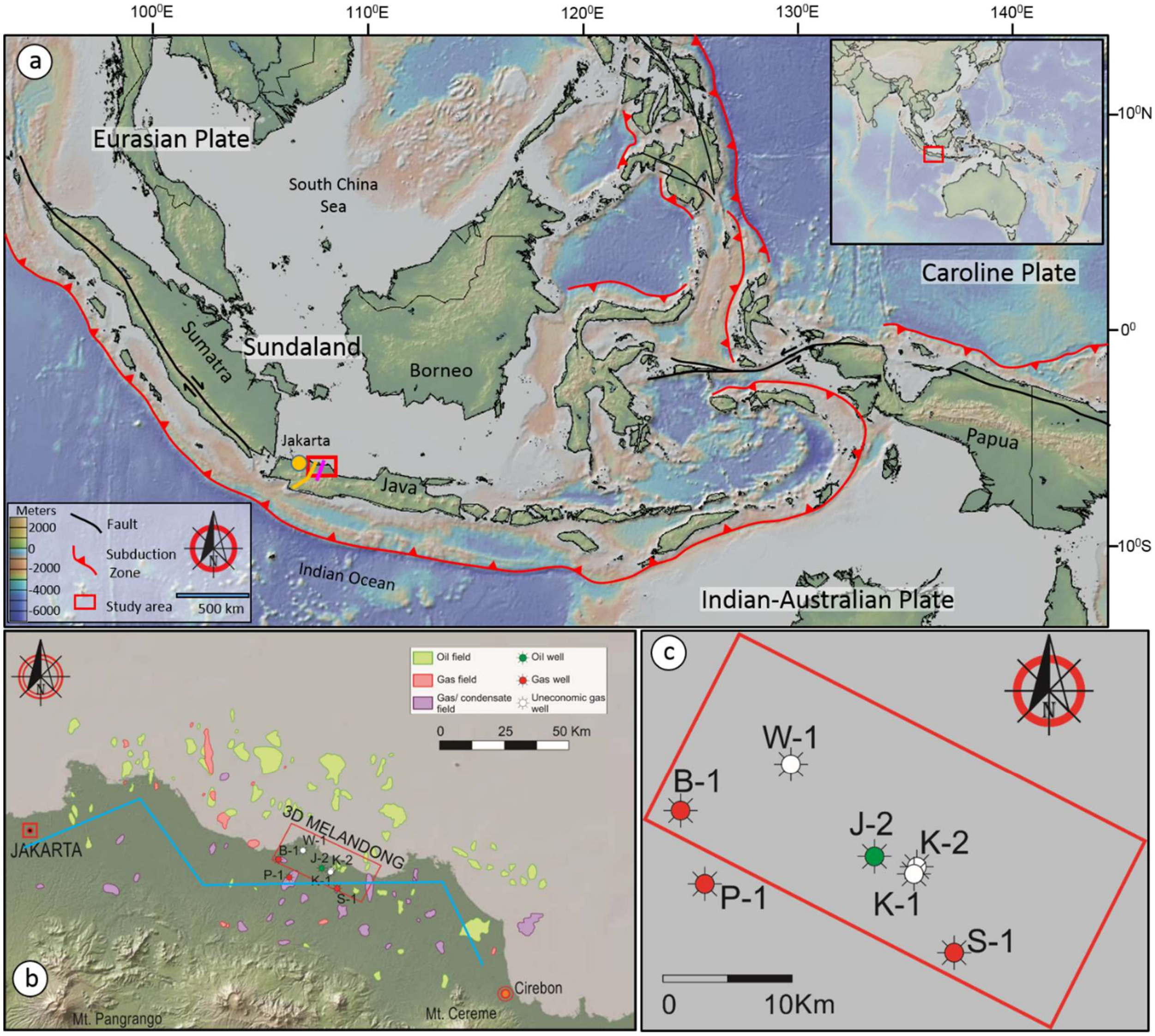

Figure 2.1. a. An Indonesian map showing structural features (subduction zones, strike-slip faults) and the Sundaland block as southeastern promontory of the Eurasian Plate. Shaded relief map, coastal line and country boundaries were taken from the GeoMapApp (http://www.geomapapp.org). Structural features were modified from Hall (2002). Note to the orange line used for a cross-section in Figure 2.2a and purple line for schematic diagram in Figure 2.9. b. The Melandong field is located at the NW Java area, a prolific hydrocarbon basin. Note to the blue line for regional west to east cross-section in Figure 2.2b. c. A basemap of 3D seismic (red rectangle) and wells data from the Melandong field.

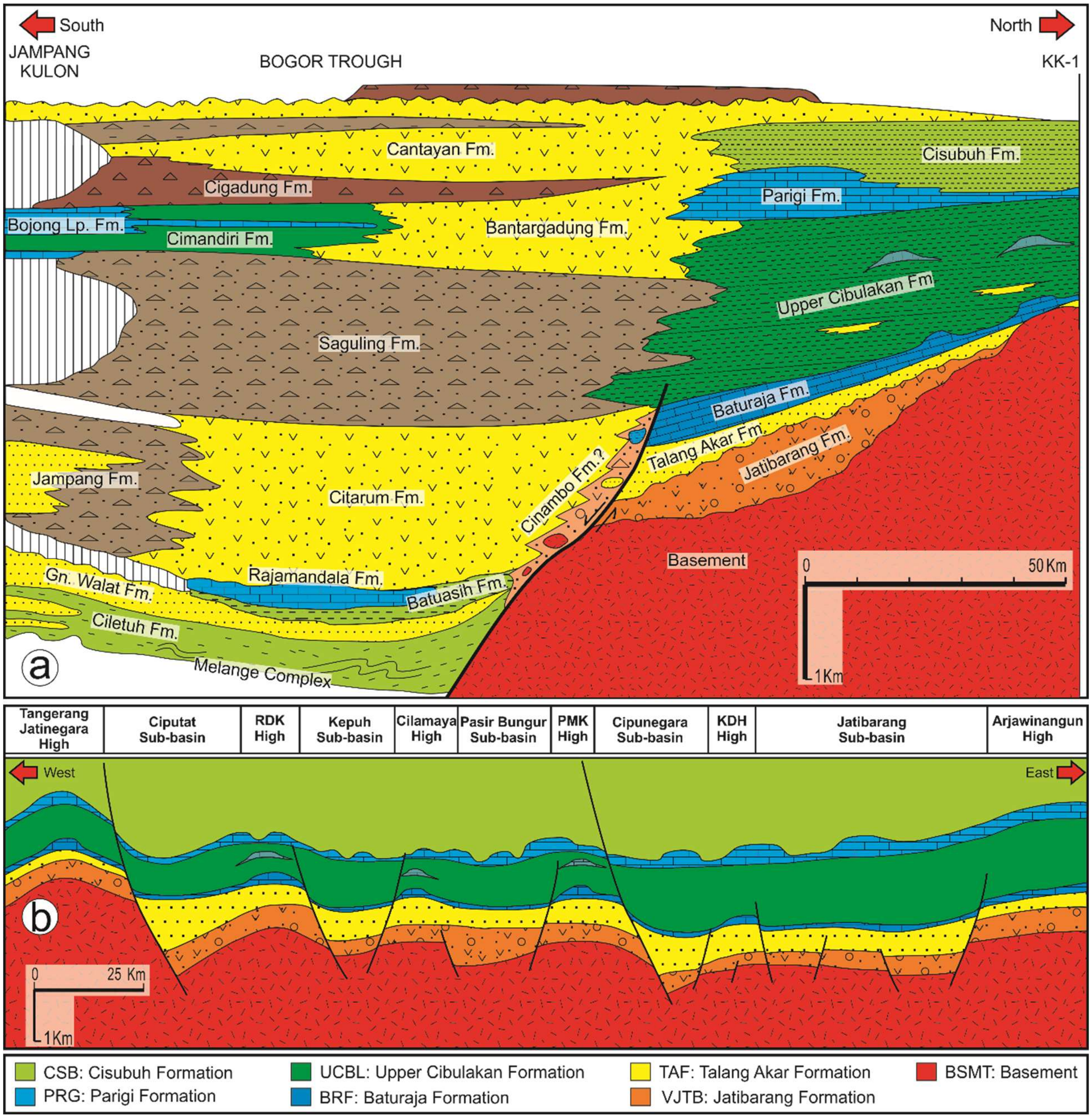

Figure 2.2. a. North to south cross-section of the NW Java Basin. Baturaja Formation was deposited on the mainly siliciclastic synrift deposits and is overlain by thick shale dominated deposits. Morphological differences between NW Java and Bogor Through to the south are interpreted as controlled by the Baribis Fault (modified from Martodjojo, 1984). b. West to east cross-section showing the Baturaja Formation mainly consisting of carbonate mounds developing on paleo-topographic highs and a relatively continuously carbonate beds on top of syn-rifting deposits, controlled mainly by N-S growth-faults. Study area is located at the Pamanukan High and Cipunegara sub-basin (Modified from Suyono et al., 2005).

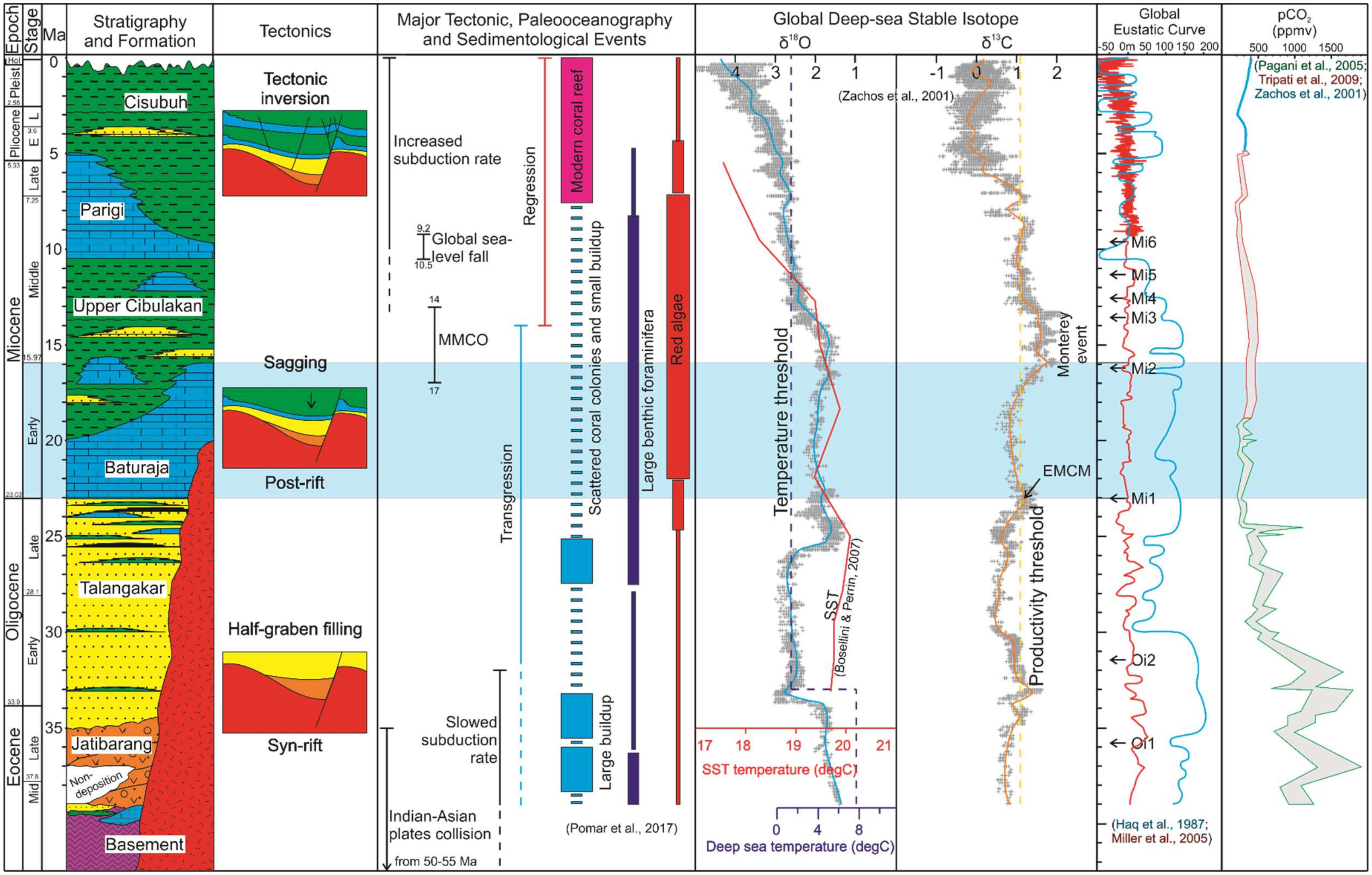

Figure 2.3. Column of regional stratigraphy and tectonic events for NW Java Basin. Global events, stable isotopes, eustatic curve, pCO_2 and seawater Mg/Ca are presented to correlate the stratigraphic succession on the global dimension. The Baturaja Formation is highlighted. MMCO: Mid-Miocene Climatic Optimum, SST: sea surface temperature. Adapted and modified from Soeria-atmadja et al. (1994), Netherwood (2000), Soeria-atmadja and Noeradi (2005), Suyono et al. (2005), and Wibowo (2013).

During the Early to Middle Eocene, the north-northeastward movement of the Australian plate slowed down from 18 to 3 cm/year (Hall, 2002) and resulted in a higher subduction angle and roll-back movement inducing back-arc rifting (Satyana and Purwaningsih, 2013). The NW Java Basin at this stage was southward dipping towards back-arc basin, with dominantly north-south (N-S) half-grabens (Netherwood, 2000). During the Early Miocene, the Sundaland experienced a gentle tilting and uplift to the north. Following this, an open marine environment was established to the south allowing deposition of shallow marine carbonates to deep marine deposits (Netherwood, 2000). It was during this transgression that Baturaja Formation was deposited (Wicaksono, 1995; Sukmono et al., 2006) on a gently dipping but faulted ramp.

Regionally, Baturaja Formation shows limestone units with shale breaks common in the lower portion of the formation. These mixed beds aggrade upwards into more massive limestone beds. Facies associations vary within the basin. Baturaja Formation in offshore areas is sub-divided into three informal members: lower, middle, and upper members (IIAPCO, 1986; Wicaksono et al, 1995). The lower member comprises of argillaceous carbonate mudstone-wackestone at the base, transitioning upward to branching coral dominated facies that are capped by thin coal seams that represents multiple rapid deepening-shallowing cycles (Wicaksono et al., 1995). Upwards, the middle member is formed of thin grey to brown marly shale to claystone (IIAPCO, 1986). Contrastingly, the upper member contains abundant branching coral debris and less clay content that represent a series of slower deepening processes characterizing highstand stage (Wicaksono et al., 1995). An exposured horizon is observed at the top of this upper member (Park et al., 1995; Wicaksono et al., 1995) indicating subaerial exposure events. Facies association of the Baturaja Formation at this offshore area includes coral-rich facies, skeletal-rich carbonate sands (packstone-grainstone) and mudstone-wackestone (Djuanda, 1985; IIAPCO, 1986; Doust and Noble, 2007).

Fossil assemblages are LBF, coral fragments, red algae (rhodoid), with lesser to minor amount of echinoids, molluscs, bryozoans, miliolids, sponges, gastropods, and planktonic foraminifera (Larue, 1976; Djuanda, 1985; IIAPCO, 1986; Park et al., 1995; Wicaksono et al., 1995). The Baturaja Formation is poorly developed and thins into the Asri sub-basin, an area very close to the Sundaland as a siliciclastic provenance region. At this location, interbedding of mud-rich carbonate and sandstone occurs (Young et al., 1991).

Three distinctive units (lower, middle, and upper members) also can be distinguished for the Baturaja Formation in the onshore portion of the NW Java Basin (Figure 2.4). Lower member is characterized by the intercalation of limestone and shale (0.5 to 8 m thick). Middle member consists of thin layers of shale and locally glauconitic sandstone. Upwards in the succession, upper member comprises of thick limestone beds (up to 200 m thick). It is also widely accepted, practically, that the Baturaja Formation has two distinctive facies: reefal-related and non reefal-related facies or “platform limestone” (Clements and Hall, 2007). Facies variations are similar to the offshore equivalent deposits: locally coral-rich floatstone-rudstone, skeletal packstone-grainstone, and mudstone-wackestone. Skeletal grains are composed of LBF, coral fragments, encrusted and fragmented red algae, echinoids, bryozoans, molluscs, and planktonic foraminifera (Setyowiyoto et al., 2007).

This study focuses on the Early Miocene carbonate succession located in the Melandong area, onshore NW Java Basin (Figure 2.1b). This section is one of the oil/gas fields operated by Pertamina EP. It is situated in the Cipunegara sub-basin and bounded by the Pamanukan High to the west and the Kandanghaur-Gantar High to the east.

The Melandong area is a part of a series of half-grabens bounded by normal faults. The Baturaja Formation displays slightly thinning in the inter-mounds depositional area (S-1 well) but shows thicker strata with topographic relief, characterizing a carbonate mound, on the Pamanukan High (Figure 2.4). The north-south (N-S) trend of normal and growth faults observed in the seismic section was a product of a tectonic inversion during the Late Miocene-Pliocene which form dextral strike-slip faults with distinctive flower structures. Basement's positive morphology with relatively chaotic reflectors and is bounded by strike-slip fault could be possibly magmatic intrusion or uplifted-lift block.

2.5. Age constraint

The age for the Baturaja Formation was determined mainly based on the biostratigraphic analysis of planktonic foraminifera and calcareous nannoplankton (e.g. Geoservices, 2013). Here, we use the 2016 version of International Chronostratigraphic Chart (Cohen et al., 2016) to define the time frame of the Early Miocene (23.03 Ma and 15.97 Ma).

The Baturaja Formation deposition varies in NW Java from the Late Oligocene to late Early Miocene. In the offshore area, it was deposited from the Chattian (Late Oligocene) to Langhian (early Late Miocene), i.e. 23 to 16 Ma (Djuanda, 1985; IIAPCO, 1986; Wight et al., 1986; Wicaksono et al., 1995; Noble et al 1997; Wight et al., 1997; Bishop 2000). Meanwhile, the onshore area shows the late Aquitanian to early Langhian (21-14 Ma) in the Early to Middle Miocene (Arpandi and Patmosukismo, 1975; Suyono et al., 2005). Interestingly, strontium isotopic dating in the offshore area provides an age of 27-21 Ma or the Chattian to Aquitanian in the Late Oligocene to Early Miocene (Miller and Kaldi, 1990).

All of these data show that the Baturaja Formation was deposited mainly in the Early Miocene range and its depositional age is diachronous throughout the basin. Hence, we prefer to define the depositional time of the Baturaja Formation from the beginning to the end of the Early Miocene (e.g. Djuanda, 1985; IIAPCO, 1986; Tonkin et al., 1992; Ageng et al., 2014). This depositional time range then is correlative to the global eustatic curve (Figures 2.3; Haq et al., 1987).

2.6. Methodology

To achieve our objectives a large dataset was used including 420 km^2 of 3D pre-stack time migration (PSTM) seismic data, well-logs, and samples from conventional and side-wall cores from seven wells. At the Baturaja Formation interval, the dominant frequency of the seismic data shows 40 to 43 Hertz and velocity ranges from 4.500 to 5.000 m/s (derived from sonic log) so that vertical resolution reaches 28 to 31 m. Horizontal resolution ranges from 840 m to 1185 m at the top and basal of Baturaja Formation, respectively. Conventional core descriptions were performed on three wells of B-1, C-1, and P-1 (Figure 2.1) with a total length of 27 m. Carbonate rock textures were described using Dunham's (1962) classification modified by Embry and Klovan (1971).

Standard petrography was completed for one hundred and eleven thin sections using an Olympus BX53MTRF petrographic microscope. Alizarin-red S was used to stain the thin-sections for mineralogical identification. Thin sections were scanned using a Nikon CoolScan 8000 and scanned images were used to complete digital point counts using the JMicroVision v1.2.7 software with a random grid applying a minimum of 300 points counted on each slide (Appendix 3). Scanning electron microscope (SEM), examined by Phenom XL device operating at accelerated voltage of 15 kV and low (60 Pa) vacuum, was used to define micro-texture and morphology of grains and lime mud. High-resolution elemental composition was determined using energy-dispersive X-ray (EDX) spectroscopy. Spot, line and mapping scans were conducted to characterize chemical component of the samples.

Facies analysis was constructed based on the lithological features, such as composition, grain size, bedding characteristics, sedimentary structures, and fossil content assembled on both core description and petrographic analysis. A depositional model was constructed using the facies scheme defined in this article (Figure 2.5 and Table 2.1) and correlated well-logs across the field for the Baturaja Formation.

Petrel 2016 was used to map top and base horizons of the Baturaja Formation and fault network in order to analyze the stratigraphic architecture and structural style controlling the development of the formation in the study area. The 3D seismic is used primarily in this study to define inter-well geometric distribution. Reflector terminations and internal characteristics are described to show ramp development and drowning-related geometries. Seismic attribute analysis of amplitude and variance was utilized to interpret several geologic features. Variance cube was generated to guide fault interpretation, to predict facies distribution and to define depositional setting. Such parameters i.e. 3x3 inline and cross-line range, vertical smoothing, dip correction, and dip guided smoothing are used.

A regional paleogeographic map was constructed by combining published data (Ardilla, 1982; IIAPCO, 1986, Hall, 2013) and the Melandong field interpretations. The literature review includes the Baturaja Formation isochron map of offshore NW Java Basin (Burbury, 1977), and regional well-to-well correlation from the offshore to onshore portion of the basin (PHE ONWJ-Pertamina EP, 2015). All the information was incorporated on a regional structural map from Noble et al. (1997). Facies distribution throughout the basin is extrapolated from the interpretation on the local scale and literature compilation.

2.7. Facies analysis

Six sedimentary facies are described for the Early Miocene Baturaja Formation (Figure 2.5 and Table 2.1). Facies were assigned based on lithological features such as bioclastic components, foraminiferal assemblages, grain size, and sedimentological features acquired during full-core descriptions (Figures 2.5, 2.6), cutting reports from mudlogs, and petrographic analyses (Appendix 2). Overall, the Baturaja Formation shows intercalation of carbonate facies and thin shale for the lower member, shale with locally glauconitic sandstone for the middle member and massive limestone with occasionally thin shale beds for the upper unit.

2.8. Baturaja depositional geometry and stratigraphic architecture

The Baturaja Formation has a thickness varies from 30 to 570 m across approximately 20,000 km^2 (IIAPCO, 1986; Adnan et al 1991; Woodling et al., 1991; Tonkin et al., 1992; Bishop 2000). Thickness is dependent on the position of the field or well in the basin, commonly thicker at the paleo-highs because of higher carbonate production and vertical aggradation at the mounds morphology and thinner in basinal areas. Mound extensions vary from less than 6 km^2 in the Sunda sub-basin to more than 300 km^2 at the Pamanukan area. Meanwhile, the Baturaja Formation in the Melandong area has a thickness of 300 m at the Pamanukan High, slightly thickening to the J-2, K-1, and K-2 area and thinning basinward to S-1 well area to ~120 m.

The top Baturaja horizon in the Melandong 3D seismic dataset is a relatively strong and continuous reflector whereas its basal horizon has low continuity; both can be traced throughout the 3D seismic data (Figure 2.6). Subtle changes in amplitude variation occurred laterally, especially in the inter-mound depositional settings. Divergent reflector patterns occur from the S-1 well area to the east, which terminates against the Kandanghaur Fault. Onlapping reflectors onto the basal Baturaja Formation horizon in the lower member record a retrogradational stacking pattern, while downlapping occurs basinward at the S-1 well area. Meanwhile, the upper member shows aggradational to slightly progradational stacking patterns. Talus deposits are identified at the fault margin of the Pamanukan High (Figure 2.7).

2.9. Discussion

2.9.1. Regional paleogeography

Several Early Miocene paleogeography maps of the NW Java Basin were constructed (Pertamina-BEICIP, 1985; Burbury, 1997; Clements and Hall, 2007). These previous authors suggested a widespread shallow marine setting for Early Miocene deposits that was initiated with coral reef buildups and muddy-platform interior carbonate rocks (Park et al., 1995; Clements and Hall, 2007). However, these earlier versions used local field to sub-basin scale data and modified a traditional coral-reef rimmed platform model (e.g. IIAPCO, 1986).

The paleogeography map that we propose shows inner, middle, and outer ramps depositional areas, carbonate mound structures, the emergent of Seribu Platform and several local basement topographies, in addition to the exposure of the Sundaland terrane (Figure 2.8). To the south, a deepened slope to the Bogor Trough developed.

The carbonate facies distribution on the paleogeography map is as follows: mudstone-wackestone of inner ramp, rhodoid and LBF-rich facies of rudstone-floatstone interbedded with rhodoid and LBF-rich grainstone to wackestone-packstone with locally mudstone-skeletal wackestone especially at the mounds of middle ramp, and possible mass-transport deposits of lithoclastic rudstone in outer ramp facies. The mound morphology is interpreted from the topographic relief and thickening carbonate succession. A N-S trend of growth faults controlled deposition, distribution, and geometry of these mounds as Burbury (1997) suggests.

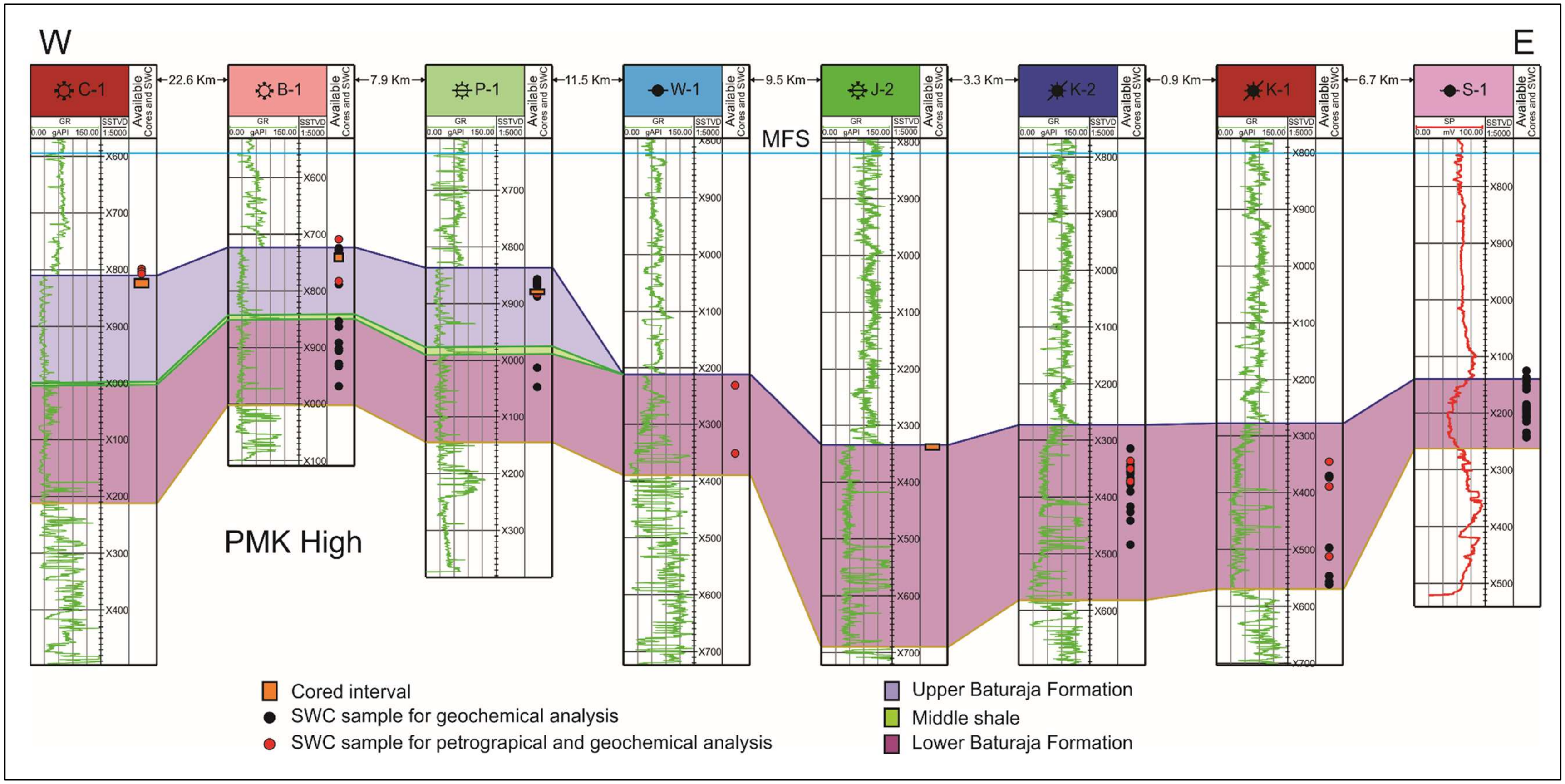

Figure 2.4. West to east well to well correlation, flattened on the MFS (Maximum Flooding Surface), in the Upper Cibulakan Formation. Gamma-ray and spontaneous potential logs are shown on the left tract as a lithology log. Four cored-intervals are shown in four wells along with side-wall core (SWC) data for petrography and geochemical analysis. PMK: Pamanukan.

Figure 2.5. Full core photography of J-2 well showing sedimentary facies from rhodoid/red algal-LBF packstone-grainstone (RPG), fine rhodoid-LBF floatstone-rudstone (RFR), and coarse rhodoid-LBF and coral floatsone-rudstone (CFR) (modified from Geoservices, 2013).

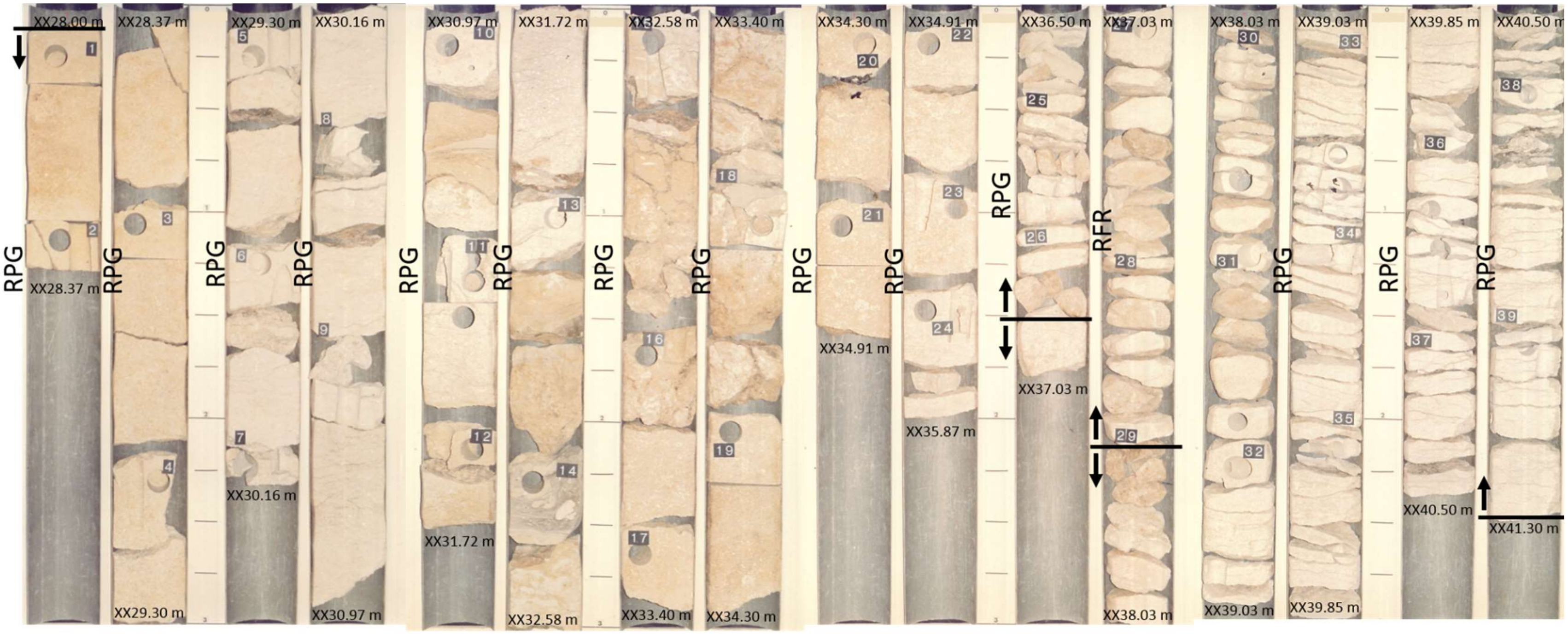

Figure 2.6. Full core photography of C-1 well showing sedimentary facies from rhodoid/red algal-LBF packstone-grainstone (RPG), fine rhodoid-LBF floatstone-rudstone (RFR) (modified from Lemigas, 1990).

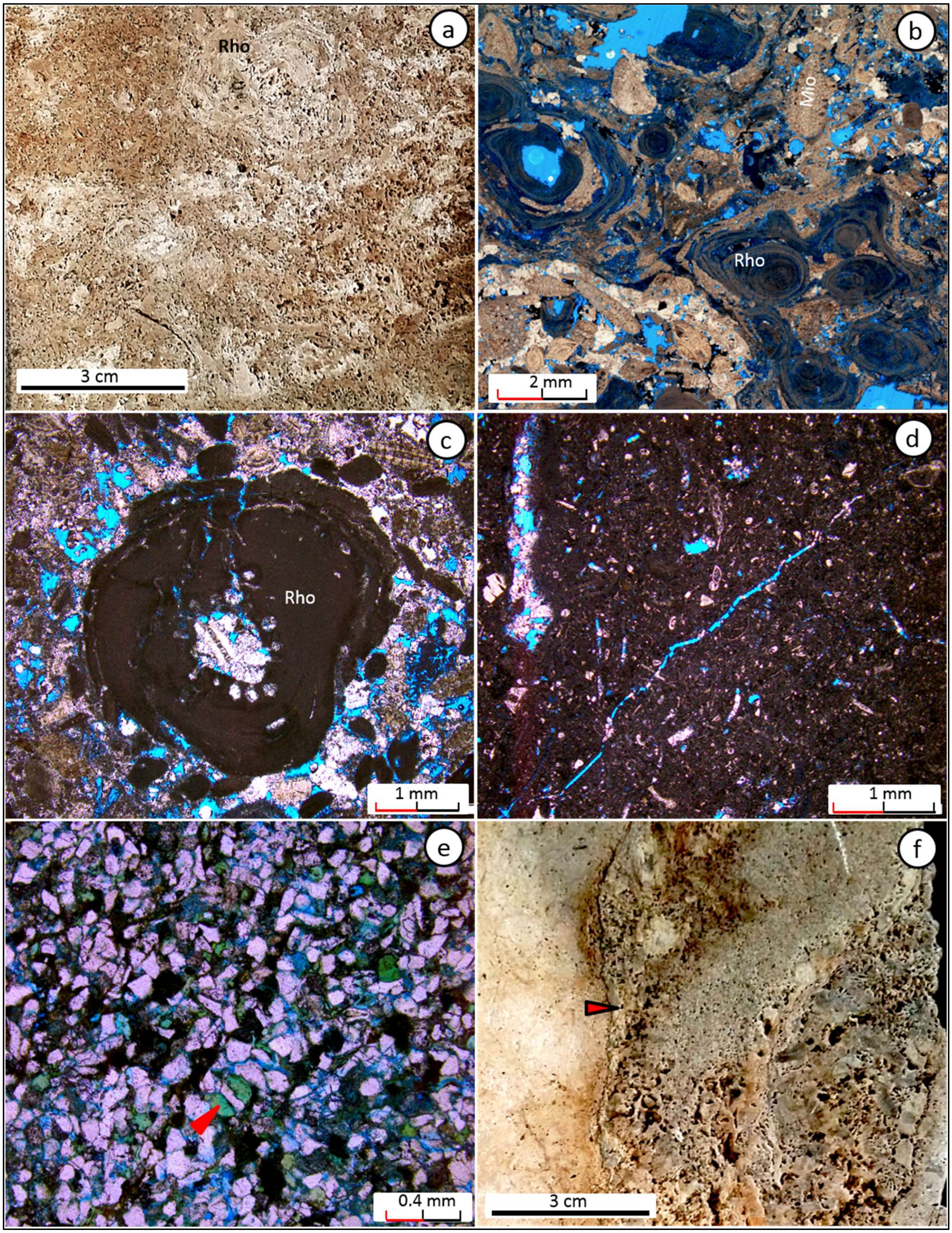
a
Rho
3 cm
b
Mio
Rho
2 mm
c
Rho
1 mm
d
1 mm
e
0.4 mm
f
3 cm

Figure 2.7. Sedimentary facies of the Baturaja Formation. a. Coarse rhodoid (rho) floatstone-rudstone (CFR) in red algal-large foram packstone-grainstone matrix and locally cemented by blocky calcite. Photo was taken from the upper part of B-1 well core. b. Rhodoid (rho)-LBF floatstone-rudstone (RFR) in red algal-large foram packstone-grainstone matrix. Rhodoids are mostly encrusted by *Acervulina* sp. Mio: *Miogypsina* sp. c. Rhodoid (rho)/red algal-LBF packstone-grainstone (RPG), a dominated facies in the samples. d. Red algal-LBF wackestone (RLW) facies, associated with plangtonic foraminifera. e. Very fine glauconitic quartz sandstone (GQS) showing poorly sorted, subrounded to subangular quartz grains, and grain supported with the lack of matrix. Glauconite pellet is indicated by red arrow. Bitumen (black) fills some pores. f. Coral fragment, possibly *Porites* sp., associated with CFR facies. Photo was taken from the upper part of B-1 well core.

Higher terrigenous material influx likely accumulated as deltaic deposits and they were identified in the subsurface data within the northern part of the basin at the offshore Asri sub-basin (IIAPCO, 1986). Hence, thin mixed siliciclastic-carbonate deposits occurred (Young et al., 1991) as this area was prone to possible decreased water transparency caused by terrigenous clay materials and algal blooms, which reduced photosynthetic efficiency.

2.9.2. Origin of carbonate ramp morphology

Two platform types were proposed for the Early Miocene deposits in NW Java Basin. 1) fault-block (Bosence, 2005) and 2) land-attached platform (Wilson, 2002; Satyana, 2005). Here, we suggest a fault-controlled distally-steepened ramp (Figure 2.9), based on several lines of evidence including seismic interpretation, published and non-published reports and studies by Burbury (1977), IIAPCO (1986), and PHE ONWJ-Pertamina EP (2015).

Table 2.1. A summary of the main facies of the Baturaja Formation from the Melandong data: sedimentologic features, skeletal components, and interpretation of light penetration zone and depositional environment.

No	Facies Name	Description	Components	Light Penetration Zone	Interpreted Depositional Environment
1	Coarse rhodoid-LBF and coral floatstone-rudstone (CFR)	Dark brown, poorly sorted, coarse rhodoid and LBF-rich floatstone to rudstone in red algal-large foram packstone-grainstone matrix and locally cemented by blocky calcite. Corals occur scattered. The common porosity types are vuggy, intra- and interparticle, fracture, and shelter. 2-13.5% porosity.	LBF: *Assilina* sp. (<12%), *Lepidocyclina* sp. (<14%), *Miogypsina* sp. (<6%), and rare *Miliolid* and *Operculina* . Red algae: *Neogoneolithon* sp. (14%), *Lithothamnion* sp. (12%), fragmented geniculate red algae (6%). Coral fragment (10%), few mollusc, echinoiderm, lithoclast, and stylolite.	Euphotic	Mound middle ramp
2	Fine Rhodoid-LBF floatstone-rudstone (RFR)	Tan in color with rhodoid, red algal and LBF-rich floatstone-rudstone in red algal-large foram packstone-grainstone matrix cemented by blocky, syntaxial-overgrowth, bladed to dogtooth cements. Porosity types are vuggy, intra-, and inter-particle porosities with vuggy and interparticle porosities occur very intensive in some of the floatstone facies. Bitumen occurs lining pore spaces in the intensive intra-porosity in some floatstone samples. 1.2-29.7% porosity.	Red algae: *Neogoneolithon* sp. (16%), *Lithothamnion* sp. (10%), fragmented geniculate red algae (5%), *Lithoporella* sp. (4%), *Sporolithon* sp. (2%). LBF: *Miogypsina* sp. (56%), *Lepidocyclina* sp. (30%), *Amphestigina* sp. (9%), *Assilina* sp. (8%), few *Operculina,* and rare *Miliolid* (56%).Coral fragments (5%), few mollusc, echinoderm, and rare planktonic foram.	Meso-oligophotic	Intermound middle ramp
3	Rhodoid/red algal-LBF packstone-grainstone (RPG)	Tan to dark brown with rhodoid, red algal and LBF-rich facies cemented by blocky, syntaxial-overgrowth, bladed to fibrous cements. Dissolution-made voids such as vuggy, intra- and inter-particle are dominant porosity types with rare fractures. Bitumen occurs lining in the dissolution pores. Stylolites are common and very intensive for packstone facies. 2.5-44.9% porosity.	LBF: *Miogypsina* sp. (65%), *Lepidocyclina* sp. (29%), *Discocyclina* sp. (27%), *Assilina* sp. (11%), *Operculina* sp. (10%), *Amphestigina* sp. (7%), *Miliolid* (6%). Red algae: Neogoneolithon sp. (10%), Lithothamnion sp. (8%), fragmented geniculate red algae (6%). Echinoderm (12%), coral fragment (4%), lithoclast (7%), and rare mollusc and planktonic foram.	Meso-oligophotic	
4	Red algal-LBF wackestone (RLW)	dark brown with red algal- and LBF-rich facies cemented by blocky, syntaxial-overgrowth, and bladed cements. Stylolite is common for the wackestone facies. Vuggy, intra-, inter-particle and fracture porosities are common. 0.9-23.6% porosity.	Red algae: *Neogoneolithon* sp. (12%), *Lithothamnion* sp. (10%), fragmented geniculate red algae (4%). Planktonic foram (28%). LBF: *Lepidocyclina* sp. (5%) and few *Assilina* sp. and *Discosyclina* sp. (4%). Few echinoderm, and rare mollusc.	Meso-oligophotic	
5	Very fine glauconitic quartz sandstone (GQS)	Light gray in color, poorly sorted, subrounded to subangular quartz grains, and grain supported with the lack of matrix content. Bitumen fills some pore spaces. 15.2% porosity.	The grains are very fine quartz (83%) and glauconite pellets (17%).		
6	Shale (SHL)	Dark gray to dark brown, calcareous, brittle and clay to silt grain size			

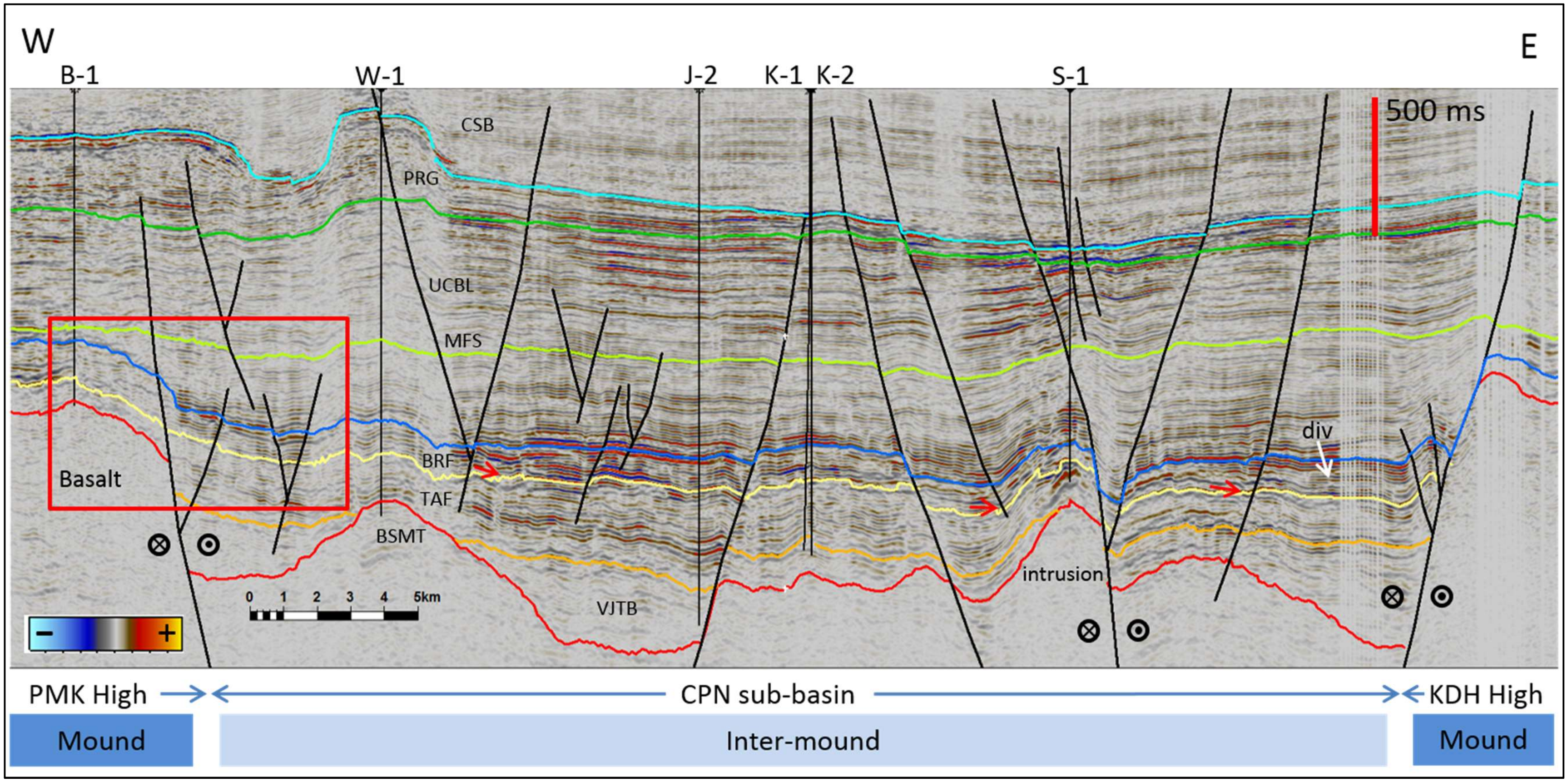

Figure 2.8. Traverse seismic section through the wells. Relatively N-S growth and normal faults are shown that evolved to strike-slip faults with distinctive flower structure. Possible magmatic intrusion or uplifted fault block is identified based on the positive intruded morphology beneath S-1 well. CPN sub-basin is located at the inter-mounds deeper depositional area. Zoom in cross-section in the red box is shown for the Figure 2.7. Red arrows point to downlapping reflectors. PMK: Pamanukan, CPN: Cipunegara, KDH: Kandanghaur, BSMT: basement, VJTB: Jatibarang Formation, TAF: Talang Akar Formation, BRF: Baturaja Formation, MFS: Maximum Flooding Surface, UCBL: Upper Cibulakan Formation, PRG: Parigi Formation, CSB: Cisubuh Formation, div: divergent reflectors.

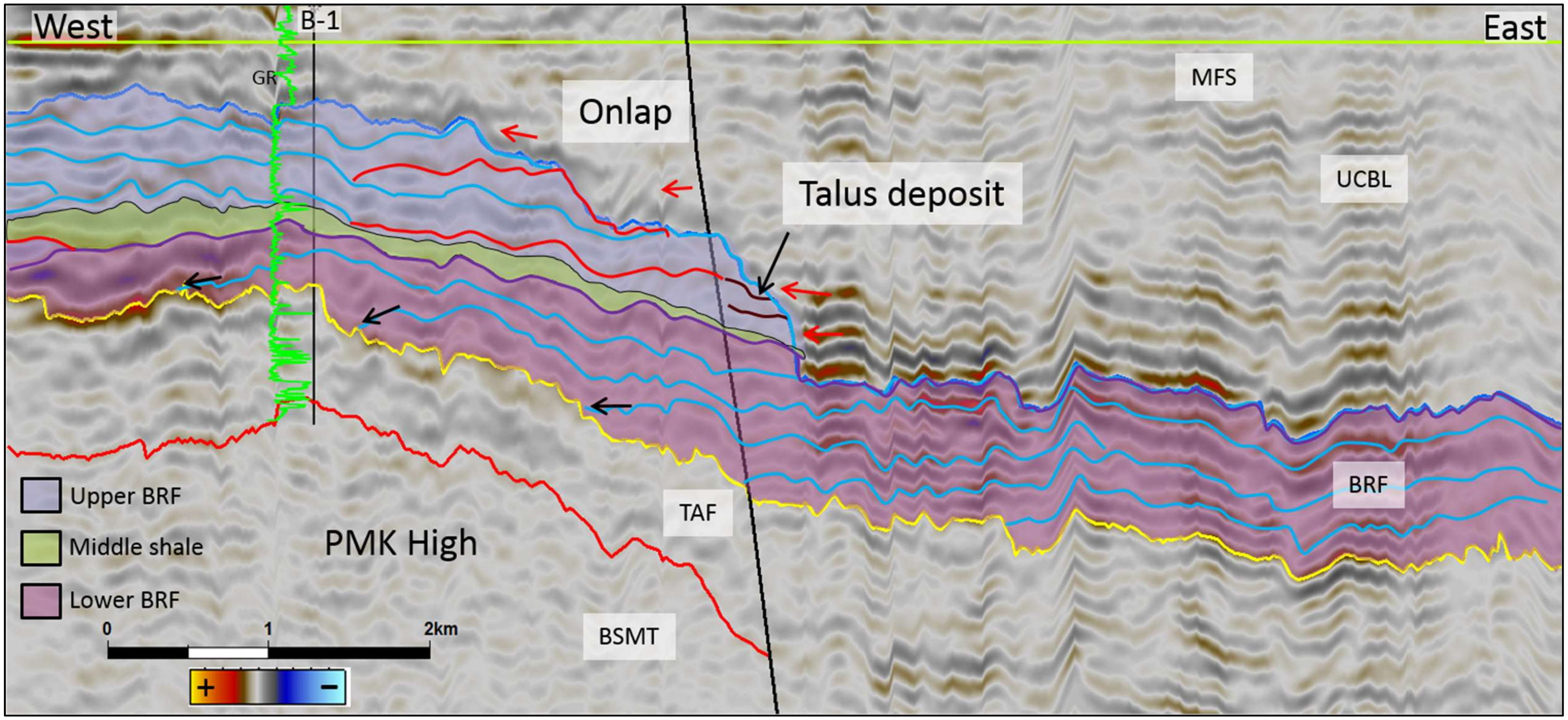

Figure 2.9. Detailed view of the seismic section from the red box of Figure 2.6 flatten on the MFS. The Baturaja Formation is characterized by semi parallel reflectors. Onlapping reflectors (black arrows) on to top Talang Akar Formation horizon (yellow) are identified as a product of rapid sea-level rise of transgressive system depositing the lower member. Purple horizon displays the highest transgressive stage of the Baturaja Formation depositing the middle shale member (green shade). Slower sea-level rise in highstand tract, intermittently interrupted by sea-level drops (red horizons), occurred depositing upper Baturaja Formation. A rapid sea-level rise flooded and drowned the ramp characterized by onlapping (red arrows) on to top Baturaja Formation (dark blue) which eventually, a thick shale succession of the Upper Cibulakan Formation covered the succession. Talus deposit is identified related to a sediment by-pass to the Pamanukan (PMK) Fault escarpment. BSMT: basement, TAF: Talang Akar Formation, BRF: Baturaja Formation, UCBL: Upper Cibulakan Formation, MFS: Maximum Flooding Surface.

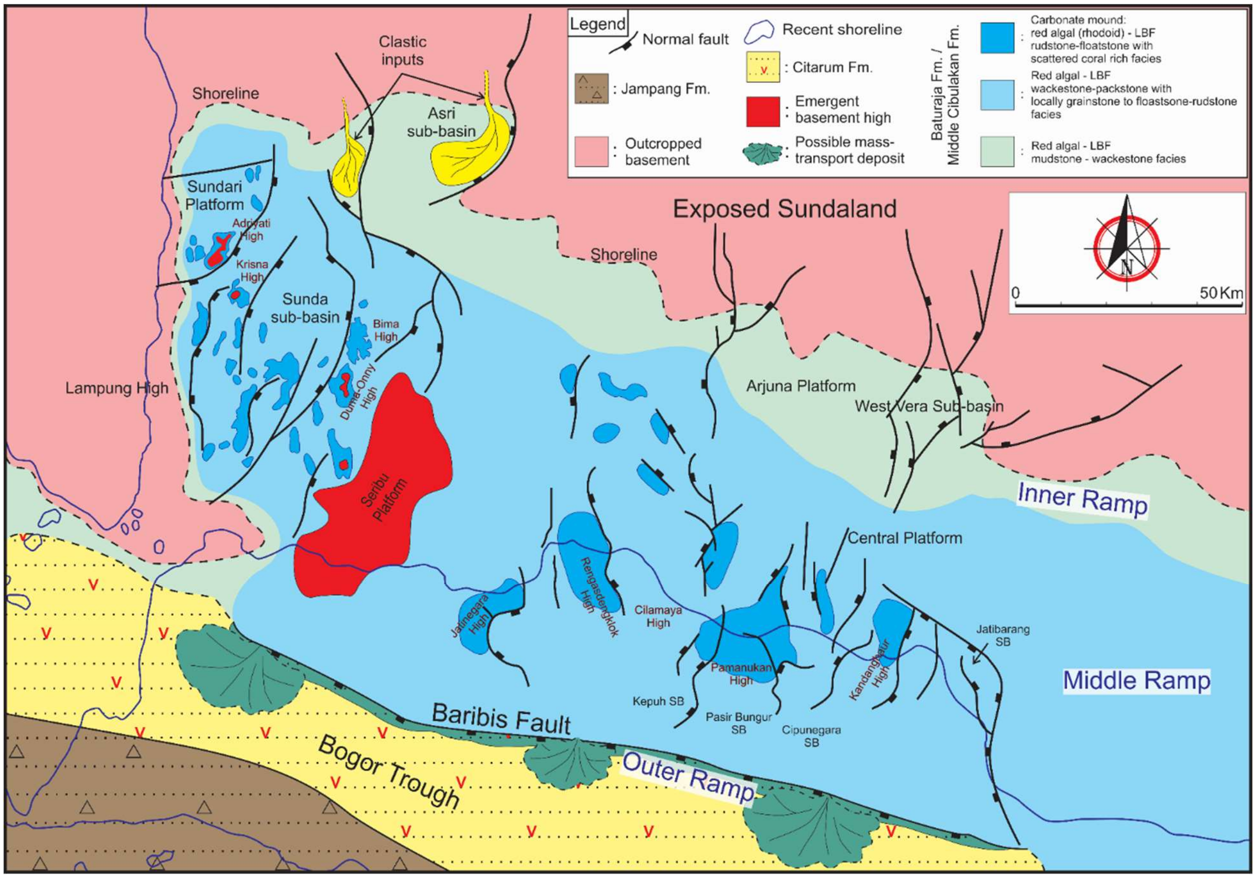

Figure 2.10. Paleogeography of the NW Java during the Early Miocene Baturaja Formation deposition. The area shows a southward gently tilting of the fault-controlled ramp that abruptly deepened to the Bogor Trough controlled by the Baribis Fault. North-south normal faults shown on the map possibly control the geometry and distribution of the Baturaja Formation mounds. Adapted and modified from Burbury (1977), Ardilla (1982), Martodjoyo (1984), IIAPCO (1986), and Noble et al (1997).

The Baturaja Formation is a carbonate succession deposited during a continuing transgression of the Early Miocene. Marine transgression started from the south of NW Java since the opening of the basin in the Late Eocene-Early Oligocene (Koesoemadinata and Pulunggono, 1974; Sudarmono et al., 1997; Bishop, 2000). The underlying topography of relatively flat areas with locally low hills and gently incised valleys, inherited from the Talang Akar Formation, provided a shallow marine setting for the transgressive carbonate facies (Park et al., 1995) in which red algae and LBF thrived.

During the Late Oligocene and Early Miocene, the volcanic arc, at the southern end of the modern Java island, became emergent and the shelf edge rapidly subsided. The Bogor Trough formed between this arc and shelf margin in response to loading by the conglomeratic volcanic-volcaniclastic deposits of the Jampang and Citarum formations (Figure 2.2) in the Late Eocene (Clements and Hall, 2007). This loading process likely triggered the W-E trend of the Baribis Fault (Satyana et al., 2002), which separates the NW Java Basin from the steeply southward dipping Bogor Trough (Ponto et al, 1988; Wu, 1991; Bishop 2000; Netherwood, 2000), thus forming a gently southward dipping distally-steepened carbonate ramp for the Baturaja Formation succession.

Southward of the NW Java Basin to the Bogor Trough margin, the east-west trend of Baribis normal fault formed a steep slope accommodating mass-transport deposit sedimentation with sediment material from the northern provenance (NW Java area) during the Oligocene to Pliocene (Satyana et al., 2002). The Baturaja Formation sediments were likely easily winnowed away by the currents and shed down-shelf to the slope area. On the other hand, conglomeratic volcanic-volcaniclastic deposits of the Jampang and Citarum Formations filled the Bogor Trough and the turbiditic sediment source was from the emergent volcanic arc to the south (Satyana et al., 2002; Clements and Hall, 2007). The intermixing of these sediment materials were then deposited along the fault escarpment as likely Cinambo Formation. The Baribis Fault was then inverted to become a back-arc thrust in the Pleistocene (Satyana et al., 2002; Clements et al., 2009).

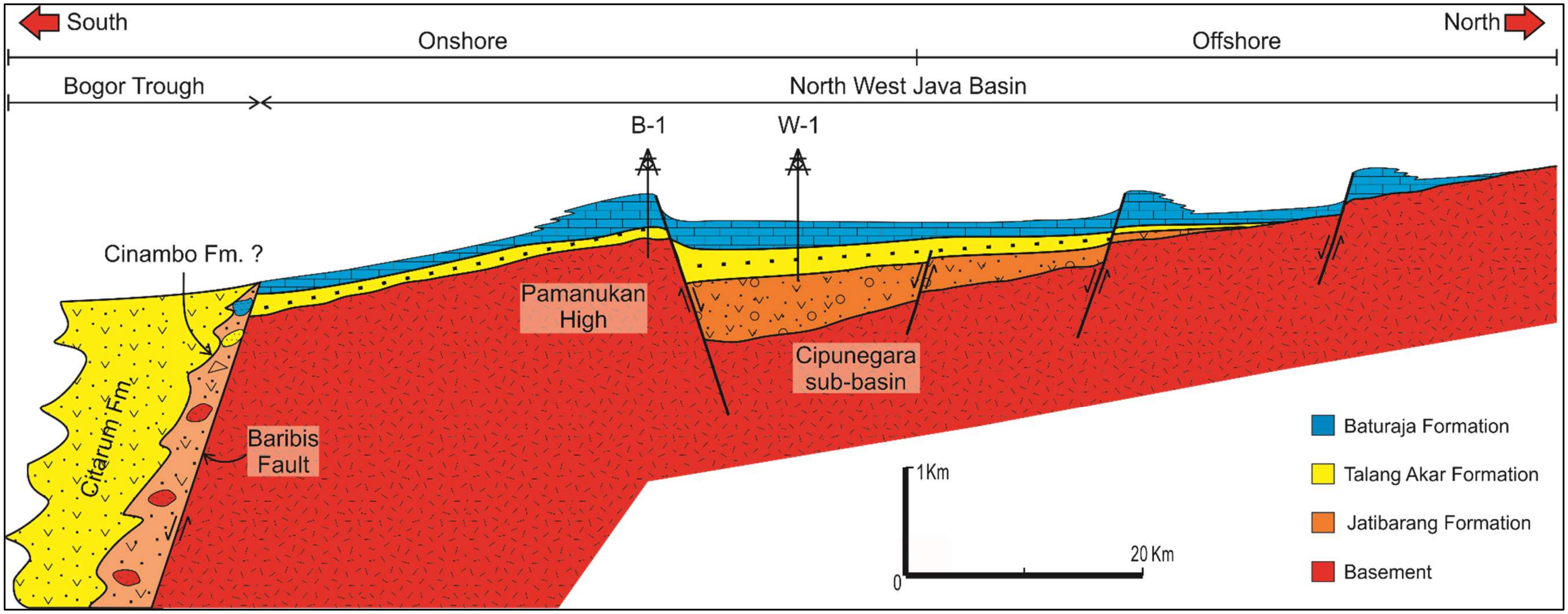

Figure 2.11. Schematic diagram of the Early Miocene Baturaja Formation ramp. The distally-steepened portion of the ramp was likely controlled by the Baribis Fault. Carbonate mounds were developed on the paleotopographic highs and uplifted fault blocks.

2.9.3. Local scale depositional model: Baturaja Formation development and its facies distribution

Development of the transgressive Baturaja succession, especially in the Melandong field, can be interpreted from the internal characteristic and reflector terminations of the seismic section (Figure 2.7). Semi-parallel reflectors and low-relief mounded characteristics are observed that is likely related to the sea-level fluctuations and a change in system tracts. Several onlapping reflectors onto the basal Baturaja Formation horizon are identified as a product of rapid sea-level rise reflecting a transgressive system tract. This process resulted in nearly flat lying strata of the lower member thinning on to the Pamanukan High. The middle shale member reflects a maximum marine flooding where a deposition of excessive fine-grained material occurred. This clay input is caused by continental weathering and runoff that was probably related to increasing precipitation in exposed Sundaland areas to the north. Slower sea level rise of highstand system tract was dominated when the upper member was deposited. Occasionally, slightly progradational geometries are observed in this member and formed by sea level falls.

It seems that during upper member deposition, an escarpment along the margin of the Pamanukan Fault influenced carbonate sediment-transfer in the area. In this post-rift setting, sediment loads could subside an area at the hanging-wall side of the fault. This event likely formed a deeper inter-mounds region and deceasing carbonate production at this area. Meanwhile, carbonate production at the footwall of the Pamanukan Fault was still active as the condition of optimum light at this higher structural area was maintained. Excess of the carbonate materials at the footwall area in addition to the elevation difference supported deposition of talus at the fault escarpment.

We propose a new depositional model to explain our facies distribution. Our field scale model is based on the morphology of the Baturaja Formation that corresponds to depositional environment shown in the structural map of the Melandong area (Figures 2.10b and 2.11) in combination with the facies map. This area is located at the middle ramp belt and is characterized by carbonate mounds at the Pamanukan High and inter-mounds depositional area at the slightly deeper meso-oligophotic zone. Morphologically, the topographically higher carbonate mounds were susceptible to the sea level fluctuation, therefore meteoric diagenesis was likely producing a good porosity-permeability system by dissolution processes. Hence, the mound morphology is a common hydrocarbon exploration target. Facies belts in this field are mainly controlled by their position relative to the light penetration zones. A southward gently-dipping middle ramp and deeper area is dominated by an association of finer rhodoid/ red algae and LBF. Increasing planktonic foraminifera percentage is observed with respect to an increasing depth to the south. Based on the small benthic foraminifera zonation, maximum depth at this area was 40 m (Geoservices, 2013).

In this model, carbonate mounds are dominated by coarse rhodoid/articulated red algal and LBF floatstone-rudstone facies (CFR). This facies consists mainly of red-algal and LBF floatstone-rudstone and packstone-grainstone and were probably located on the euphotic zone of the most upper part of the mounds. Red algae occur in the forms of rhodoid, articulated, encrusted and fragmental. Corals occur as fragments while *insitu* corals are absent. This suggests that small and scattered corals are common but were unable to build a structural barrier up to sea level (i.e. Pomar (2014).

The inter-mounds facies are rhodoid-LBF floatstone-rudstone (RFR), rhodoid/red algal-LBF packstone-grainstone (RPG) and red algal-LBF mudstone-wackestone (RLW); correspond to the increasing depth of the meso-oligophotic zone in a relatively low-energy environment. The latter facies shows an association with planktonic foraminifera as greater interaction with open seawater occurred.

Glauconitic quartz sandstone (GQS) occurs as thin submarine sandsheets. This GQS only occurs locally (only in J-2 well) and is very thin (less than 2 m). It is possible that the provenance of the very fine quartz is derived from the exposed Sundaland to the north. This facies likely formed by reworking and re-transportation of terrigenous deposits during high magnitude of the marine flooding.

2.9.4. The Early Miocene events controlling carbonate productions

Globally, the Early Miocene was characterized by an overall global warming trend (Figure 2.3) that was occasionally interrupted by minor glaciations (Mi1 to Mi6 events), up to the Mid-Miocene Climatic Optimum or MMCO (Miller et al, 1991; Zachos et al., 2001; Brandano et al., 2017). Positive shifts of the $\delta^{13}C$, occur at the Oligocene-Miocene boundary associated with the Mi-1 event, is known as the Early Miocene Carbon Maximum (EMCM). The second is a long-term positive $\delta^{13}C$ excursion known as the Monterey Carbon Isotope Excursion and correlated to the MMCO (Zachos et al., 2001; Brandano et al., 2017). These positive excursions reflect carbon cycle perturbations due to increased primary productivity of seawaters and higher rates of organic carbon storage (Flower, 1999; Brandano et al., 2017). These global events likely affected and controlled the evolution of the reef builders and carbonate producers, especially during Cenozoic (Pomar et al., 2017).

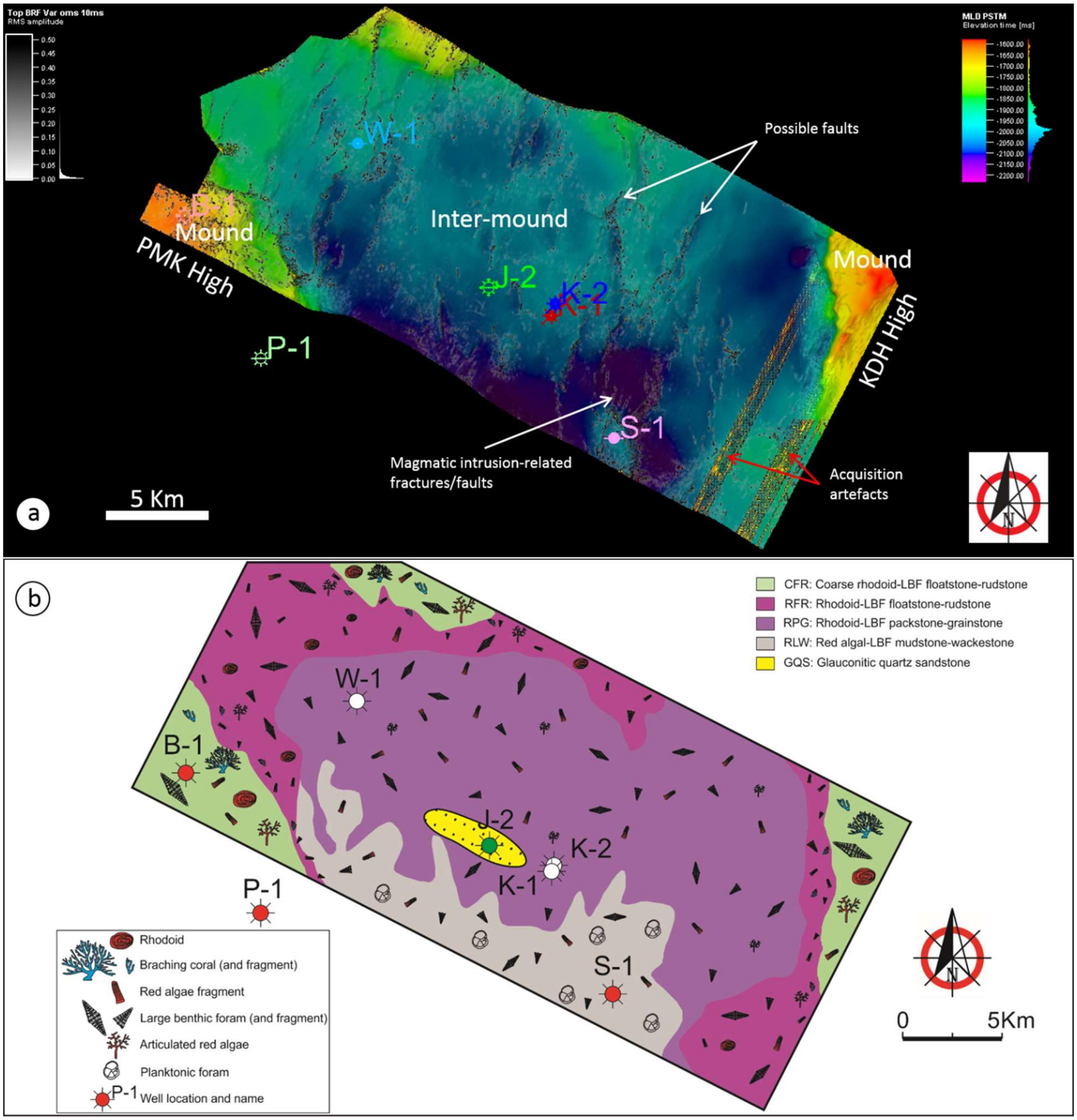

Figure 2.12. a. Overlay of the top Baturaja Formation time structure map on a variance slice through the top Baturaja Formation horizon. North to south alignments are interpreted as normal faults. Growth-faults separated lower structural area (inter-mound) and higher areas (mounds) of Pamanukan and Kandanghaur highs. Fractures and faults are clearly visible possible resulted from the magmatic intrusion beneath S-1 well. b. Interpreted facies map showing distribution of the facies belts in the Melandong area, dominated by association of red algae and LBF.

In addition, during the Early Miocene time, NW Java was positioned at the equator ~5 S latitude (Hall, 2002; 2013) within a warm, tropic, and humid climate (Wilson, 2008). Terrestrial runoff bringing nutrient input to the ocean was stable and expected to have abundant accumulation of nutrient (Wilson, 2008).

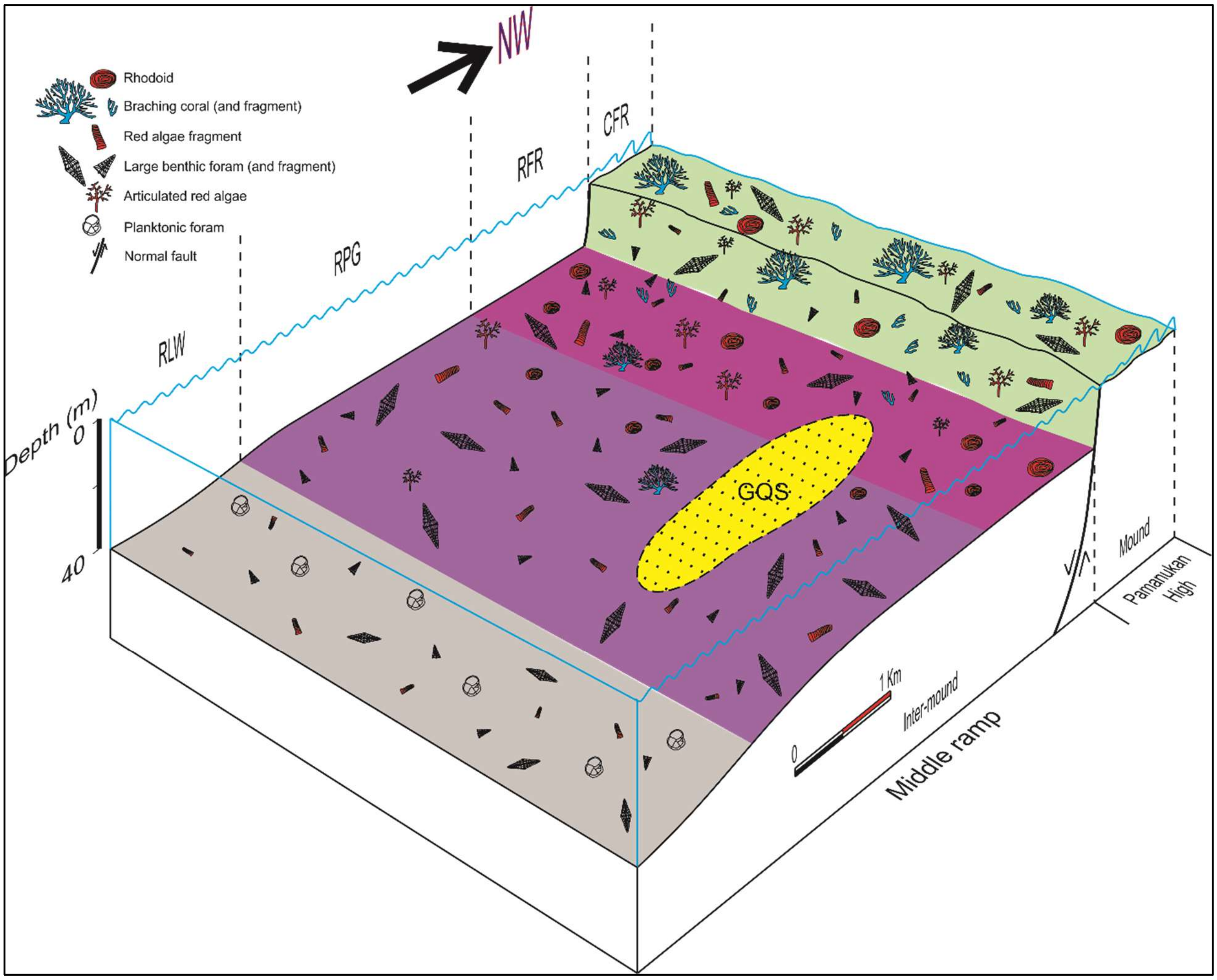

Figure 2.13. The Baturaja Formation depositional model for the Melandong Field. Facies belts are shown dominated by the red algae and LBF. Decreasing skeletal grain size coincidence with depth. Association of planktonic foraminifera occur in a deeper setting. CFR: coarse rhodoid-LBF floatstone-rudstone, RFR: fine rhodoid-LBF floatstone-rudstone, RPG: rhodoid/red algal-LBF packstone-grainstone, RLW: red algal-LBF mudstone-wackestone, and GQS very fine glauconitic quartz sandstone.

2.9.4.1. Temperature and carbon productivity

During the Early Miocene, red algae and LBF were dominant skeletal assemblages of carbonate successions (Figure 2.3). These assemblages possibly were controlled by global environmental settings during Cenozoic, including temperature, carbon cycle interpreted from deep-sea global oxygen and carbon isotopic records (Pomar et al., (2017), and pCO_2 (Zachos et al., 2001).

Based on the global deep sea stable isotopes data (Zachos et al., 2001), large coral buildups were likely to occur below temperature and productivity thresholds as explained by Pomar (2017). The temperature threshold is at 2^0 C for deep sea temperature that coincides with 19^0 C of sea surface temperature (SST). Meanwhile, the productivity threshold is at ~1‰ VPDB. Where coral reefs were small and scattered, the red algae and LBF association dominated instead.

Extensive distribution of LBF correlates with lower $\delta^{18}O$ values, which correspond to warmer temperatures. On the other hand, the red algae, as eurythermal organism able to tolerate a wide range of temperatures, dominated during this time corresponds to the positive excursion of the $\delta^{13}C$, above the value of the productivity threshold. Small, scattered coral colonies occur in the Early Miocene carbonate rocks. The corals become the main carbonate builder (Figure 2.3) developing large build-ups when the temperature and productivity declined below threshold valves (e.g. at the Late Eocene-Early Oligocene, Late Oligocene, and Late Miocene-Recent). The diagram also shows that the onset of the large buildups of modern coral reef started in the Tortonian as the temperature and carbon productivity declined at the same time (Pomar et al., 2017) meaning that carbonate successions dominated by coral reefs could not be applied to the Early Miocene setting.

2.9.4.2. Tectonics

During the early Paleogene time, major continental area in the western Indonesia was formed, extending to the southeast from Asia, as a consequence of microplates, blocks, and accreted terranes reorganization (Daly et al., 1991; Hall, 1996; Metcalfe, 2011). Faulted blocks and paleo-basement highs were then covered by carbonate rocks in the quiescence post-rift tectonic setting in the Early Miocene. Creation of accommodation space for this carbonate succession allowed relatively steady subsidence during high sea-level periods.

2.9.4.3. Sea-level

Third-order sea level cycles occurred during the deposition of the Baturaja Formation (Satyana, 2005). Rapid sea-level rise occurs in a transgression system depositing the lower member then reaching the maximum flooding during deposition of the middle shale unit and finally the upper member deposited during highstand system tract.

In addition, the Baturaja Formation depositional and early diagenetic events show a close correlation to the global-eustatic curve. Increasing sea level is correlated to the transgressive phase at 23.03 Ma whereas several sea level drops are observed at 22, 21 and 16.5 Ma. The latter event at 16.5 Ma, correlated to the onset of the Mi2 glaciation in Antarctica (Miller et al., 1991), is likely responsible for the development of the meteoric diagenesis which formed extensive vuggy and moldic porosity for the prolific hydrocarbon reservoirs in this unit.

2.9.4.4. Photic zones

The role of light-dependent symbiont, water transparency, and bathymetry were identified as an important influence on the skeletal grain association distribution dominated by the red algae and LBF (Pomar et al., 2004; Wilson and Vecsei, 2005). Carbonate producers need light either to photosynthesize for red algae or to maintain the metabolism of photosynthetic endosymbionts for

LBF and corals. There appears to be a close correlation between depth-related zonation of euphotic and oligophotic to the light-dependent symbiosis of dinoflagellate-housed corals and diatom-sheltered LBF (Pomar, 2004, Wilson and Vecsei, 2005). The coral-dinoflagellate symbionts absorb violet-blue and red wavelengths that are abundant in shallower depths of the euphotic zone. Meanwhile, LBF-diatom symbiosis allows photosynthesis under a broad light spectrum in any substantial depth range from euphotic to oligophotic zone (Wilson and Vecsei, 2005; Pomar et al., 2017). It is likely that the growth and development of coral-dinoflagellate symbionts are hindered at their shallower euphotic setting in the Early Miocene as the warmer temperature and higher solar irradiance can lead to photo-oxidative stress and bleaching (Pomar and Hallock, 2007). Hence, this situation favors the development of abundant red algae-LBF facies.

Heavier rainfalls triggering terrigenous material runoff might be a threshold factor limiting coral development while red algae and LBF are able to tolerate a slightly higher terrigenous influx (Wilson, 2000; Wilson and Lokier, 2002). A higher terrestrial influx corresponds to eutrophication near river mouths as deltaic deposits were identified within the offshore Asri sub-basin (IIAPCO, 1986). Consequently, water clarity decreases when more argillaceous materials are in the seawater, added by algal bloom phenomena influencing light penetration limiting development of red algae and LBF (Wilson and Vecsei, 2005) especially in the inner ramp setting.

2.9.4.5. Carbon dioxide (CO_2)

The Early Miocene (Figure 2.3) is characterized by higher pCO_2 values, in the range of 300-400 parts per million by volume/ ppmv (Pagani et al., 2005; Triparti et al., 2009). The higher atmospheric CO_2 is absorbed by the ocean to increase seawater pCO_2 causing changes in seawater chemistry, known as ocean acidification (Johnson and Carpenter, 2012). This process reduces seawater pH causing carbonate dissolution and declining species diversity while promoting photosynthesis and higher metabolism rate (Johnson and Carpenter, 2012; Noisette et al., 2013; Allen et al., 2017).

2.9.5. The Baturaja carbonate producers and reef builders: significant contribution and their paradox

The Baturaja Formation was previously described as a carbonate succession consisting of coral-reef and bioclastic facies (Doust and Noble, 2007). The reefal facies (related to the development of fringing reefs) was deposited in suspected higher energy environments around the submerged paleo-structural highs, such as Mela, Duma-Onny, Indriati, and Bima in the offshore Sunda sub-basin (IIAPCO, 1986). The facies vary from coral boundstone-bafflestone to coral fragment mudstone-grainstone and lesser amounts of red algae (Kovacs, 1982; Djuanda, 1985; Wicaksono et al., 1995). In contrast, many mounds developed on the paleohighs the coral-rich facies are mainly isolated, small and scattered. Massive corals in their living position are absent from the core descriptions, but coral fragments are common (Djuanda, 1985; Wicaksono et al., 1995). Interestingly, red algal and LBF rich wackestone-packstone facies dominate the cores taken on the palohighs with red algae and LBF as the main skeletal grains.

Therefore, we propose that the red algae and LBF skeletal association dominated the Early Miocene carbonate successions with minor and scattered corals rather than coral-rich facies that were traditionally described. The red algal-LBF skeletal association also was inferred at the Baturaja Formation type locality (Hadi and Simbolon, 1976). The facies formed by the red algae and LBF contribute to significant rock volume of the mound-like structures and inter-mound areas at the middle ramp, that consequently support to the potentially high-quality reservoirs in many other areas of the basin.

The non-framework builders and light dependent-biotas of red algae and LBF skeletal association were well-developed in non-tropical, cool-water depositional realms at 10-20^0 C (James and Jones, 2016). This grain association is classified as a "C" carbonate factory (Schlager, 2005) and is suggested to thrive in a zone with less light (oligophotic) from 20 to 100 m depth (Pomar 2001; 2004; James and Jones, 2016). The term rhodalgal was previously stated to describe mainly these red algae and LBF assemblages (Carannante et al. 1988; Halfar and Mutti, 2005; Wilson and Vecsei, 2005). A paradox occurs as this grain association is observed abundantly in the tropical, presumably warm waters of Oligocene-Miocene carbonate successions worldwide, such as in the Caribbean (Jones and Hunter, 1994; Pomar et al., 2015); western Mediteranean (Pomar et al., 2004; 2017), central Atlantic (Corda and Palmiotto, 2015) and, in this case, in our samples from equatorial Indonesia. Global temperature from isotopic signal of $\delta^{18}O$ (Zachos et al., 2001) and sea-surface temperature or SST (Bosellini and Perrin, 2007) indicate that warm water conditions occurred globally at the time of the deposition of these carbonate rocks, instead of cooler water temperatures. Hence, the red algae and LBF assemblages were well-developed and deposited in warm temperatures which prevented the optimum growth of corals (Wilson and Vecsei, 2005).

Furthermore, warm temperatures are likely not the only parameter controlling the abundances of red algae and LBF association globally. Increasing $\delta^{13}C$ significantly above productivity threshold (Figure 2.3) characterize the Early Miocene that might suggest global increased surface water productivity, organic carbon burial and higher nutrient conditions (Pomar et al., 2004; Halfar and Mutti, 2005). Possible evenly distributed mesotrophic conditions might have occurred where carbonate production is extensive, especially at the carbonate mounds; hence favorable for development of red algae (Halfar and Mufti, 2005). The intermediate-nutrient level occurs as the organisms reuse almost all the dissolved inorganic elements in the water column. This condition leads primary carbonate producers to have photosymbionts to provide additional energy and promote calcification (James and Jones, 2016), especially for the LBF and its diatom symbiont (Pomar et al., 2017). These symbioses are extremely sensitive to high nutrient levels as higher nutrients could promote the growth of symbionts and might overtake the holobionts or hosts (James and Jones, 2016). In addition, higher nutrients may promote other organism populations and diversity that in turn increasing competition to survive.

Carbonate mounds are inferred to have the highest carbonate production in the euphotic to oligophotic zones. This setting allows the highest calcification produced by autotrophic and mixotrophic organisms of red algae and LBF, respectively. Mesotrophic to slightly eutrophic conditions are expected in this setting (Halfar and Mutti, 2005). The carbonate production process represents a balance between food resources and water transparency. The mounds are located on the middle ramp quite a distance from siliciclastic resources of the exposed Sundaland; hence it has clear water for their photosynthesis. This condition was ideal for optimum growth of the red algae. In a consequence of clear water, nutrient resources at this location were decreased in which the LBF, known as sediment detritus feeder (Pomar et al., 2017), adapts to its light-dependent symbiont.

Red algae and LBF were favored in the most environments during the Early Miocene due to the global environmental conditions. Red algae are recognized as major carbonate producers in a wide range of environments mainly in shallow and warm tropical waters (Goreau, 1966; Adey and Macintyre, 1973; Steneck, 1986; Semesi et al 2009; Quaranta et al., 2012; Nash et al, 2015). These organisms are light-dependent and autotrophy/ producers (organisms able to produce complex organic compounds using mainly sunlights) that thrive under high- to low-nutrient conditions (Goreau, 1963; Adey and Macintyre, 1973; Halfar and Mutti, 2005). They play a major role in the ecology and expansion of benthic organisms throughout the world. In addition, their diversity peaked in the Early Miocene (Braga et al., 2017). Several survival strategies of red algae including space competition, biomineralization, and organic shielding were reported. Space competition involves an increase in growth (Adey and Macintyre, 1973; Steneck, 1986) to prevent other organisms occupying available spots. Dolomite-rich red algae were identified through their biomineralization and show lower dissolution rates under lower pH conditions by reducing skeleton wall porosity due to dolomite infilling (Nash et al., 2013). Meanwhile, the organic coating may protect the more soluble phases $CaCO_3$ of their HMC skeletal walls from being dissolved in the acidic seawater (Ries, 2011).

LBF, as mixotrophic organisms, adapted to these Early Miocene conditions by three different approaches (Pomar et al., 2017). One strategy is to involve symbiosis with diatoms that were capable of photosynthesizing in a broad light spectrum and thereby a large range of depths thus allowing them to provide energy in nutrient-deficient environments (Hallock, 1999; Pomar et al., 2017). The second adaptation is the shape of the tests as shown by rotalids that have flat and thin tests to adapt to low light intensities in low-energy environments (Mateu-Vicens et al., 2009; Pomar et al., 2017). The third approach is to produce organic sheaths, carbohydrate rich substrate, as an attachment mechanism to anchor tests in stronger hydrodynamic regimes. These sheaths are used as a source of energy for bacteria, fungi and algae; additional supplements in low-nutrient conditions (Hallock, 1999; Pomar et al., 2017).

The Early Miocene Indo-Pacific equatorial carbonate province, represented by this study, is dominated by light-dependent biota of red algae and LBF. These results are comparable to the studies by Wilson (2002; 2008) and Park et al. (1992; 1995) for their work on the Miocene carbonate successions in other Indonesian areas. This dominance of red algae and LBF is somewhat similar to the western Mediterranean carbonate province that the middle ramp, at meso-oligophotic zones, was the most prolific for carbonate production (Pomar et al., 2014; Pomar et al., 2017). The difference is the lack or non-existence of seagrass and green algae (*Halimeda*) in the inner ramp in the study area. This absence could be related to the lack of the well data from this area as it is thinner succession and does not have good hydrocarbon potential (Young et al., 1991). The other difference is that the Indo-Pacific province has a good development of carbonate mounds on the middle ramp with greater abundance of the red algae-LBF association.

Overall, the combination of all the global events in the Early Miocene favored preferential development of the red algae and LBF association. This association, as the main carbonate producers in the Indo-Pacific carbonate succession, thrived because they had the ability to tolerate and adapt to environmental conditions as opposed to aragonitic corals (Wilson and Lokier, 2002; Pomar et al., 2017).

2.10. Conclusions

1. This study provides arguments and evidence that the main carbonate builders for the Early Miocene carbonate successions in the Baturaja Formation, NW Java Basin, are dominated by assemblages of the red algae and LBF while small, scattered and possibly solitary coral colonies formed in this area instead of massive and rigid corals. The abundance of red algae and LBF could be associated with the lower capability of corals to thrive in the euphotic zone and to build three-dimensional wave-resistant reefs to sea level. The red algae and LBF-rich facies globally contribute to significant rock volumes and high-quality Early Miocene reservoirs.

2. The Early Miocene Baturaja Formation of the NW Java was deposited on a southward gently dipping ramp in which facies belts, dominated by red algal-LBF skeletal grains, vary across this ramp. High terrigenous influx possibly from the exposed Sundaland northward occurred in the inner ramp resulting in mixed siliciclastic-carbonate strata. Meanwhile higher carbonate production with good development of thick carbonate mounds, controlled by N-S trending basement-involved normal to growth faults, occurred in the middle ramp. Outer ramp is an area where mass-transport deposits formed along the steep slopes of the Baribis Fault.
3. The Early Miocene was a time of global warm temperature, concomitant with higher carbon productivity and pCO_2. The combination of these factors and the ability of the red algae and LBF skeletal association to adapt to these specific conditions favored its abundance and temporarily replaced rigid and framework corals. The key to the red algae and LBF association at this time is their ability to adapt and survive to changes in their environment.

CHAPTER 3

ORIGIN OF POROSITY AND DIAGENETIC EVOLUTION OF THE EARLY MIOCENE BATURAJA FORMATION, NORTHWEST JAVA BASIN, INDONESIA

3.1. Overview

The Early Miocene Baturaja Formation is one of the most prolific hydrocarbon reservoirs in the northwest (NW) Java Basin, Indonesia. This formation has complex porosity systems created by complex diagenetic events, dominated by moldic and vuggy porosity with minor intraskeletal, intercrystalline, and fractures porosity.

It was widely accepted that the porosity system in the Baturaja Formation pay zones was affected by meteoric-dissolution processes. Our core samples collected within the carbonate mounds that developed on pre-existing topographic highs were vulnerable to occasional subaerial exposure. Evidence for subaerial exposure events were interpreted from dissolution voids and ^{13}C-depleted intervals. Meanwhile, samples from deeper water on inter-mound localities have similar dominant moldic and vuggy pore types. For this location, burial dissolution is invoked as the driver of porosity creation as this region has deep-rooted faults which serve as vertical conduits for mantle- and magmatic-derived corrosive CO_2 gas; a dominant contaminant for gas production in the area. This interpretation is supported by the presence of cement-filled stylolite, and very negative values for carbon isotopes. Overprinting of the solution-enlarged voids and isotopic signals from previous freshwater leaching events is thought to occur as the carbonate mounds were buried and interacted with CO_2 via fault conduits, thus comingling the dissolution pores and isotopic compositions and leading to a similar end product from very different diagenetic regimes.

More intensive exploration to a deeper inter-mound area could be more encouraged by assumption that burial dissolution is responsible for porosity creation. Vertical conduits must be present to this dominant mud-rich facies area. The presence, geometry, and distribution of the burial pores could be accurately predicted by integrated study and complete subsurface datasets including gas analysis and fluid geochemistry.

3.2. Keywords

Baturaja Formation northwest Java Indonesia, diagenetic model, moldic, vuggy, burial dissolution, meteoric diagenesis

3.3. Introduction

Carbonate rocks are formed mainly from biochemical and biological process in primarily marine environments and they are prone to rapid diagenetic alteration that can change their mineralogy pore type and pore size. Porosity in carbonate rocks is mostly diagenetic in origin which adds complexity in classifying and quantifying porosity system (Choquette and Pray, 1970; Tucker and Wright 1990). Interpreting and understanding of the diagenetic processes are essential to describe and predict pore heterogeneity trends for hydrocarbon exploration and production (Longman, 1980). Pore type distribution, characterization and analysis allow for a more detailed reservoir models for optimum production and development phases of the mature oil field. This is the case for the Early Miocene Baturaja Formation, one of the main reservoirs in the NW Java Basin, Indonesia. This carbonate succession can be divided into lower, middle shale and upper members in the study area.

This study aims to distinguish different types of porosity within the Baturaja Formation, dominated by moldic and solution-enlarged vuggy pore spaces. These pore types in the formation were widely interpreted as meteoric-derived through the dissolution of aragonitic skeletal grains and lime muds (Larue, 1976; Ardila, 1982; IIAPCO, 1986; Tonkin et al., 1992; Park et al., 1995; Wicaksono, 1995). The dissolution reaction between carbonate minerals and meteoric waters (James and Jones, 2016) is simply expressed by the equation of:

$$CaCO_3 + CO_2 + H_2O \Leftrightarrow Ca^{2+} + 2HCO_3^- \qquad (1)$$

in which this reaction is reversible. The CO_2 influx into and out of the water determines this natural process. Addition of CO_2 will drive reaction to the right or dissolution while the opposite process results in carbonate precipitation (James and Choquette, 1984).

Occasional meteoric exposures of the lower and upper members of the Baturaja Formation from the onshore Melandong field is indicted by the extensive moldic pores forming fabric-selective dissolution texture and ^{13}C-depleted intervals within the mound area developed on paleotopographic high. In addition, burial dissolution processes could be applied to the moldic and vuggy pores i.e. by deeply originating aggressive fluids (e.g. Giles and Marshall, 1986; Choquette and James, 1987; Tucker and Wright, 1990; Mazzullo and Harris, 1992; Park et al., 1995; Moore, 1989; Machel, 2005; Shen et al., 20016). Such stylolite enlargement partly filled by calcite cements is an evidence for the burial dissolution processes by mantle- and magmatic-derived CO_2. Deep-seated faults in the Melandong area were the likely updip pathways for the delivery of this acidic gas.

We hypothesize that there are two possible scenarios of the origin of this dominant dissolution porosity in the Baturaja Formation: 1) meteoric dissolution or 2) burial dissolution based on CO_2 degassing originated in the mantle and moving upwards through deep-seated faults. The deeper inter-mound areas adjacent to major deep-seated faults is likely contain reservoirs with abundant burial dissolution-derived porosity. The dissolution processes leached the red algal-large benthic foraminiferal (LBF) rich facies of packstone-grainstone in the middle ramp setting. In addition, areas adjacent to major deep-seated faults are proposed to have more porosity created by mantle-derived acidic gases to dissolve the rock and create secondary porosity.

This paper describes the diagenesis of the Early Miocene Baturaja Formation in NW Java Basin. We used petrography combined with stable isotope geochemistry and trace element analysis to determine the diagenetic processes of this unit. In addition, we constructed a diagenetic model of the Baturaja Formation to identify the spatial and temporal influence of these processes that created this diagenetic history. These new ideas of the origin of the porosity in the Baturaja Formation may have implications on play concepts and prospect evaluation for hydrocarbon exploration in other Early Miocene carbonate sections.

3.4. Methodology

Core samples from the Melandong field used in this study were provided by PT. Pertamina EP. The fragmental samples were utilized for both petrography and geochemical analysis whereas powdered samples were for geochemical analysis only.

Conventional plane light petrography was used to describe 111 blue-impregnated thin sections using an Olympus BX53MTRF microscope. High-resolution photomicrographs were obtained to illustrate sedimentological and diagenetic features. Thin sections were scanned using a Nikon CoolScan 8000 and images were used to measure total thin-section porosity using ImageJ with the jPOR plug-in (Grove and Jerram 2011). In addition, we utilized this software to measure and calculate pore properties such as area and roundness to define micro-porosity (has pore area of less than 7.85 μm^2), moldic (more elongated and rounded) and irregular shape of vuggy pores. Alizarin-red S was used to partially stain the thin-sections to distinguish dolomite (unstained) from calcite (red-stained). Cathodoluminescence (CL) petrography was performed using a Technosyn Cold Cathode Luminescence Model 8200 MKII to determine dolomite compositional variations.

A scanning electron microscope (SEM) Phenom XL from Nanoscience technology was used to define micro-textures and morphology of grains and lime-mud in high magnifications from 300 to 1000X. Additionally, elemental compositions of specific particles were determined in thin-section samples using energy-dispersive X-ray (EDX) spectroscopy. Phenom XL SEM instrument was used operated at accelerated voltage of 15 kV and low (60 Pa) vacuum.

For stable isotope analysis, 173 powdered whole-rock samples were analyzed for carbon ($\delta^{13}C$) and oxygen ($\delta^{18}O$) isotopes in a Kiel IV carbonate device coupled to a Thermo-Scientific MAT 253 isotope ratio mass spectrometer in the Stable Isotope Geosciences Facility at Texas A&M University. The results are reported in VPDB standard with analytical precision of 0.04‰ for $\delta^{13}C$ and 0.08‰ for $\delta^{18}O$. Major and trace element analyses of 178 samples including magnesium (Mg), strontium (Sr), manganese (Mn) and iron (Fe), reported in parts per million (ppm) were determined by an Inductively-Coupled Plasma Mass Spectrometry (ICP-MS) in the Radiogenic Isotope Geosciences Laboratory of Texas A&M University. Precision of major and trace element analysis was 0.0015 ppm for Mg, 0.001 ppm for Sr, 0.003 ppm for Mn and 0.03 ppm for Fe.

Petrel 2014 was used to correlate logs from eight available wells. The cross-section was then flattened on the maximum flooding surface (MFS) to show the development of the Baturaja Formation shortly after its deposition. A neural network method was utilized, using the same software, to predict depositional facies of the formation. This method was used to address limited core data as we have sparse cored intervals. Defined depositional facies from core description and petrography were used as supervised input that each facies correlates to the specific gamma-ray (GR), resistivity, density and neutron log values as training data. The training processes, including 1000 iterations, 40% error limit, 60% cross validation and 0.2 probability threshold, allows the application recognizes the pattern between the input and the training data that then predict lithofacies in the un-cored intervals throughout the succession.

3.5. Facies analysis and dolomite

We described six facies (Table 2.1) in the Baturaja Formation: coral floatstone-rudstone (CFR); rhodoid-LBF floatstone-rudstone (RFR); rhodoid/red algal-LBF packstone-grainstone (RPG); red algal-LBF mudstone-wackestone (RLW); very fine glauconitic quartz sandstone (GQS); and shale (SHL). Lithological features, such as bioclastic components, foraminiferal assemblages, grain size, and sedimentological structures, were recorded from full-core descriptions, cutting reports from mudlogs, and petrographic analyses.

Dolomite occurs as a minor portion (observed in less than 2%) of the succession, occurring primarily in partially dolomitized samples of mudstone-wackestone of RLW facies (Figures 3.1a, b). Dolomite crystal size ranges from 6-55 μm with a mean of 21 μm (very fine to fine crystals), clear to cloudy, non-planar anhedral to planar euhedral, and mimetic fabric preservation. CL petrography (Figures 3.1c, d) shows that dolomite crystals have non- to red ambience luminescence. Brighter red luminescence of thin and slightly discontinuous rim also occurs.

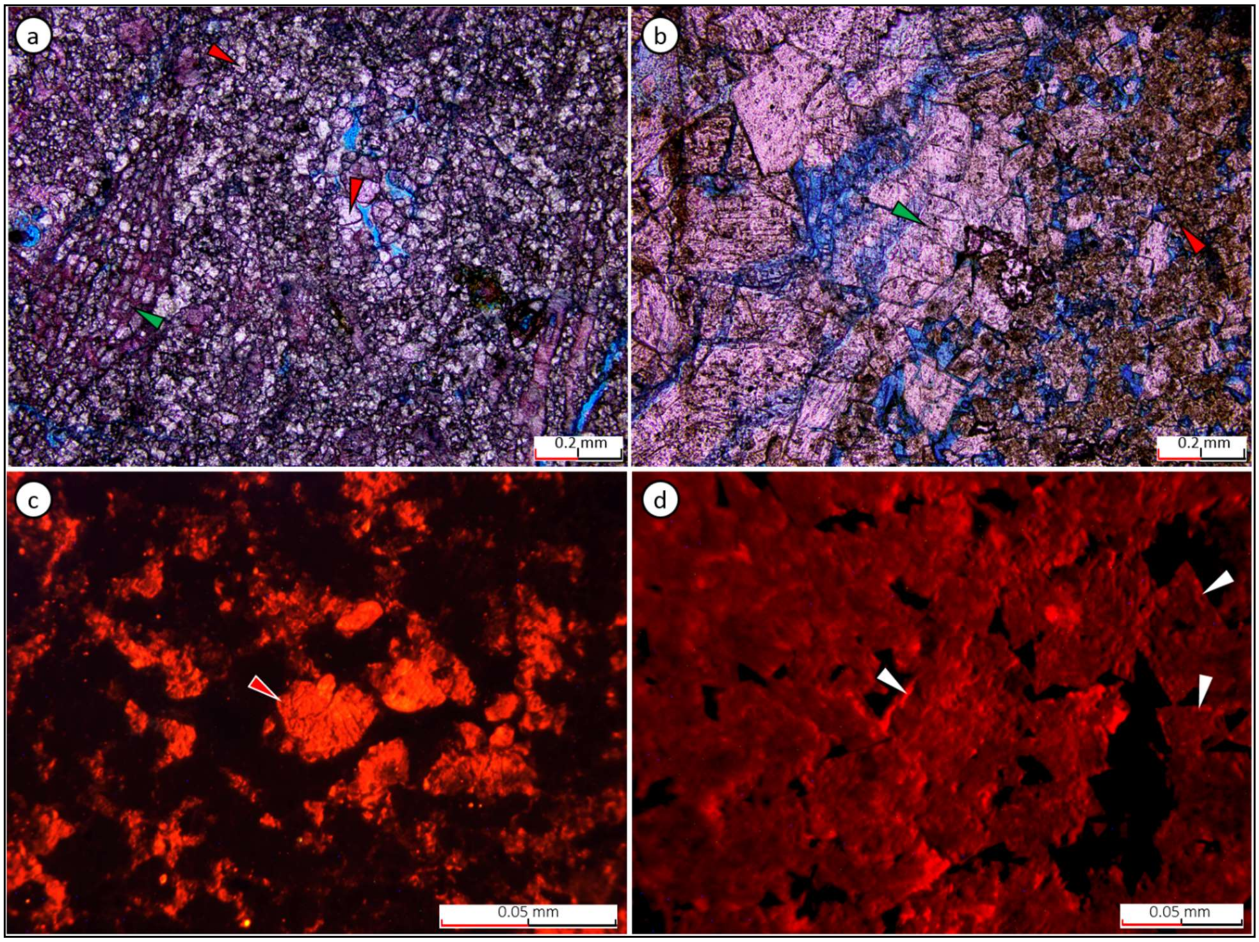

Figure 3.1. a. Partially dolomitized LBF wackestone showing dolomites with very fine to fine crystal size and non-planar anhedral crystal boundaries (red arrows). Green arrow shows partially dolomitized *Discocyclina sp.* b. Coarser dolomite with fine crystal size, cloudy, and planar euhedral to subhedral. c. Finer dolomite under CL shows non-luminescence for calcite crystal and moderate to bright orange luminescence for the dolomite (red arrow). d. Coarser dolomite has a red luminescence for the dolomite crystals and planar euhedral rhombs are visible. Moderate red luminescence is framed by brighter red outer thin and slightly discontinuous rim (white arrows).

3.6. Geochemistry

3.6.1. Stable Isotope Geochemistry

Isotopic composition of the Baturaja Formation (Figure 3.2) varies laterally with the $\delta^{18}O$ values ranging from -10.5 to -0.2‰ and $\delta^{13}C$ from -9.8 to +1.2‰. Grouped by the unit, the lower member has more negative in $\delta^{18}O$ (-10.5 to -0.2‰) and more enriched in ^{13}C (-4.7 to 1.2‰) than the upper section (-7.5 to -4.5‰ for $\delta^{18}O$ and -9.8 to -0.1‰ for $\delta^{13}C$).

Isotopic data show clustering values which can be assigned to three groups. Group 1 is depleted in ^{18}O (-7.0‰ to -0.2‰), slightly enriched in ^{13}C (0.0‰ to +1.2‰), and consists of all samples from J-2, most samples from K-1 and K-2, and a small fraction of samples from the B-1 well. Group 2 is comprised of more scattered negative values in $\delta^{18}O$ (-10.5‰ to -3.1‰) and more disperse in $\delta^{13}C$ (-4.7‰ to -0.1‰). It involves all samples from S-1, C-1, and P-1, most samples from B-1, along with the majority samples from K-1 and K-2 wells.

Vertical plot of these stable isotopes shows variations of $\delta^{18}O$ and $\delta^{13}C$ with depth on B-1, J-2 and K-1 wells (Figure 3.3). $\delta^{18}O$ values are almost all negative while $\delta^{13}C$ values are mostly negative for sample from the mound area (C-1 and B-1 wells) and a more scattered distribution from negative to positive values for inter-mound areas (P-1, J-2, K-1, K-2 and S-1 data). J-2 well displays entirely positive values for $\delta^{18}O$ while S-1 well has completely negative values for both $\delta^{18}O$ and $\delta^{13}C$.

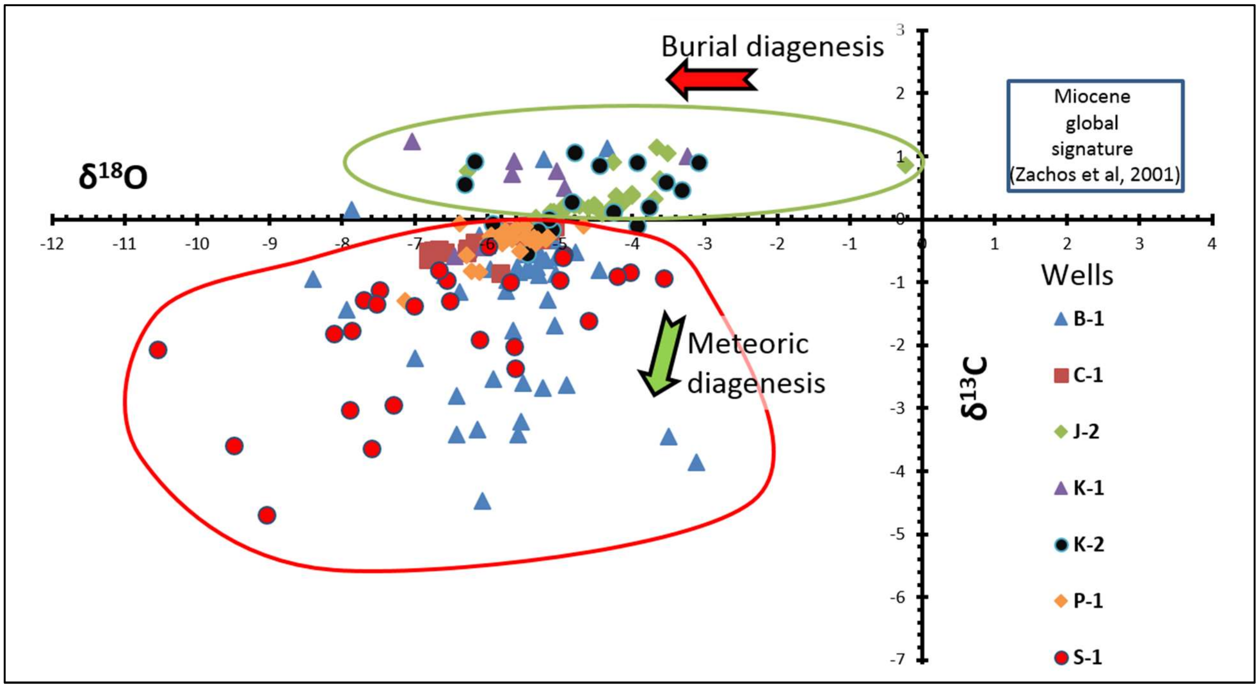

Figure 3.2. Whole rock stable isotope distribution plot from the Baturaja Formation dataset. Clustering of the data is shown by polygons. Group 1 in green polygon shows depleted in ^{18}O and slightly enriched in ^{13}C. Group 2 in red polygon displays more scattered negative values in δ^{18}O and δ^{13}C. Red arrow illustrates burial diagenetic effect for negative δ^{18}O whereas green arrow displays meteoric diagenetic influence for the samples with negative δ^{13}C.

3.6.2. Major and Trace Elements Data

The Baturaja Formation has a wide range of Fe and Mn concentrations from 1 ppm to 34,750 ppm of Fe and 2 ppm to 1,100 ppm of Mn (Figure 3.4). The concentrations generally show increasing values toward the lower member. There is more than double the Fe concentrations in the lower member (11 to 34,750 ppm with an average of 1,404 ppm) as compared to the upper member (0.5 to 4,470 ppm with an average of 625 ppm. Mn concentrations of the lower member (5 to 1,100 ppm with average of 157 ppm) are three and a half times larger than the upper member (1.4 to 378 ppm with average of 43 ppm).

The differences are also significant for Mg and Sr. Mg concentrations observed for the lower member (5 to 1,100 ppm with average of 157 ppm) are an order of magnitude lower than the upper member (2096 to 35,973 ppm with average of 8,812 ppm). For Sr, the difference of the lower (20 to 1,831 ppm with average of 370 ppm) is marginal than the upper members (265 to 1,429 ppm with average of 583 ppm). Sr concentrations are in the range of 20 to 855 ppm (for the CFR, RFR, RLW, RPG, and SHL facies) with an average value of 473 ppm, with outliers up to 1429 ppm present. Plotting Sr against Fe+Mn concentrations suggests an enrichment of Sr concentration for the RPG and RFR facies starting at 951 ppm to 1429 ppm (Figure 3.5).

Variations of these trace element data with depth shows that higher Mg contents (above 80 Kppm) are observed in several horizons of lower member for B-1 and K-1 wells. An increasing trend in Fe with depth occurs in the B-1 well and mostly coincides with increased values of Mn. Sr enrichment above 700 ppm occurs at multiple depths for both upper and lower members for C-1 and B-1 wells.

3.7. Porosity types and distributions

The predominant porosity types for the succession are moldic (or biomoldic) and vuggy porosity in 74% of samples (Figures 3.6a, b). Intraskeletal, interparticle, intercrystalline, microporosity, fracture and enlarged stylolite porosities are minor to rare. Total porosity of the Baturaja Formation from the imageJ analysis shows 0.2 to 44.8% with an average of 12.5%. Extensive moldic and vuggy porosity occurs in CFR, RFR, RPG, and RLW facies from the B-1, P-1, C-1, J-2, and K-1 wells.

Moldic porosity is indicated by selective dissolution of LBF, red algae, and minor corals, resulting in mainly ellipsoidal shape of dissolved skeletal walls. The moldic pores are up to 2 cm in diameter. Conversely, vuggy porosity forms irregular openings by the dissolution of skeletal grains, carbonate mud, early cements and likely the result of expansion of earlier moldic pores. The vuggy pore spaces range to 5 cm in diameter.

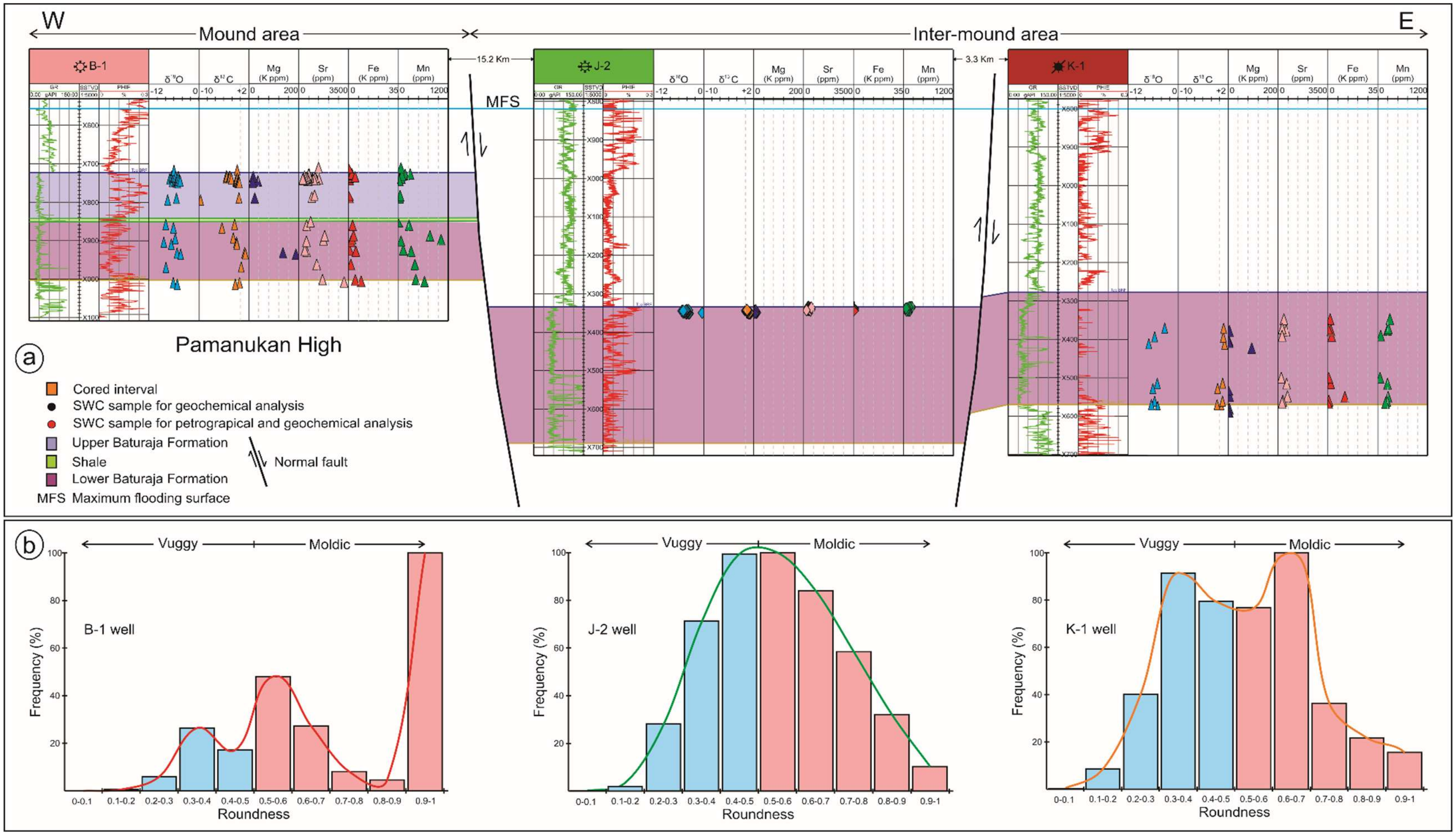

Figure 3.3. a. Well-to-well correlation of B-1, J-2, and K-1 to show physical (GR and effective porosity/PHIE) and geochemical (stable isotopes and trace elements) properties within two different morphologies: carbonate mound and inter-mound areas. Normal faults are shown to indicate structural control to the rock properties. B. Vuggy and moldic distribution for the three wells based on the roundness of the pore geometry. The B-1 well shows domination of moldic pore type while J-2 and K-1 wells have slightly similar distribution of moldic and vuggy porosity.

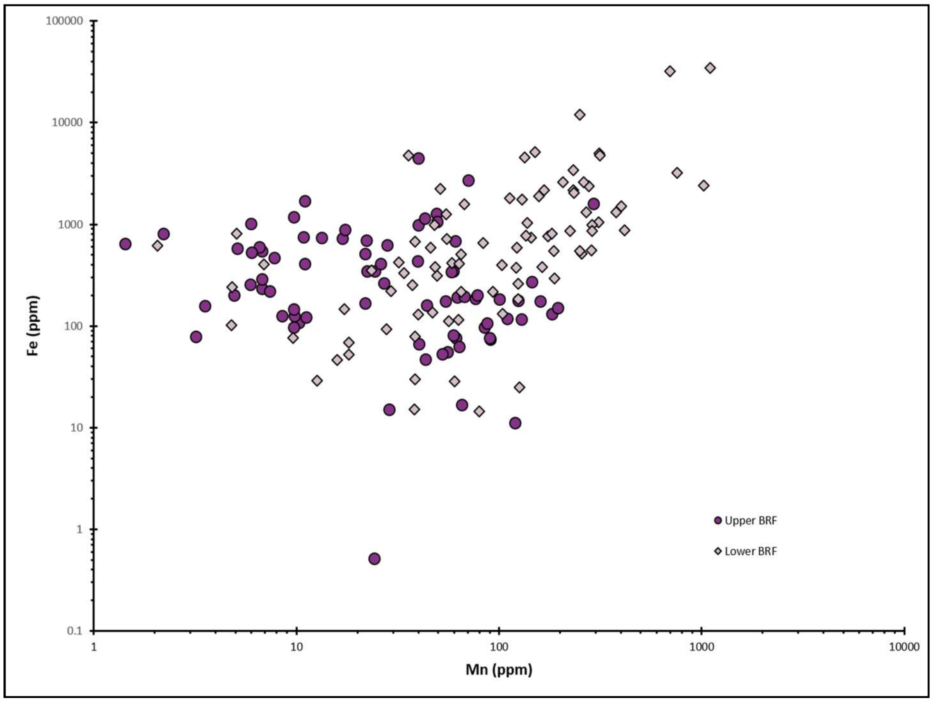

Figure 3.4. Crossplot of Fe and Mn showing increasing value toward the lower member of the Baturaja Formation.

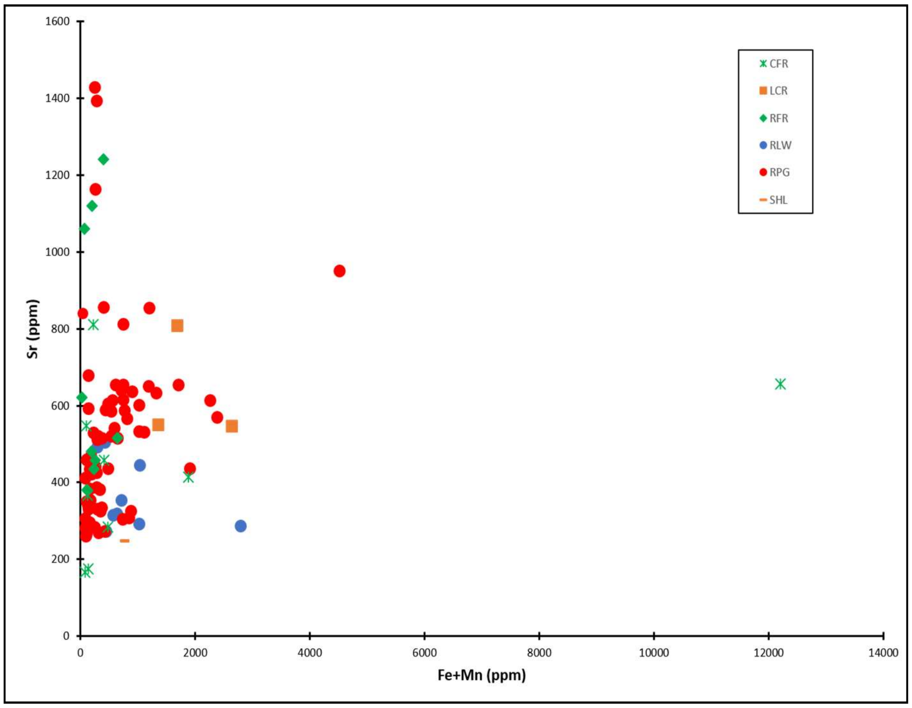

Figure 3.5. Plot of Sr against Fe+Mn concentrations. An enrichment of Sr concentration occurs in the portion of RPG and RFR facies, up to 1429 ppm.

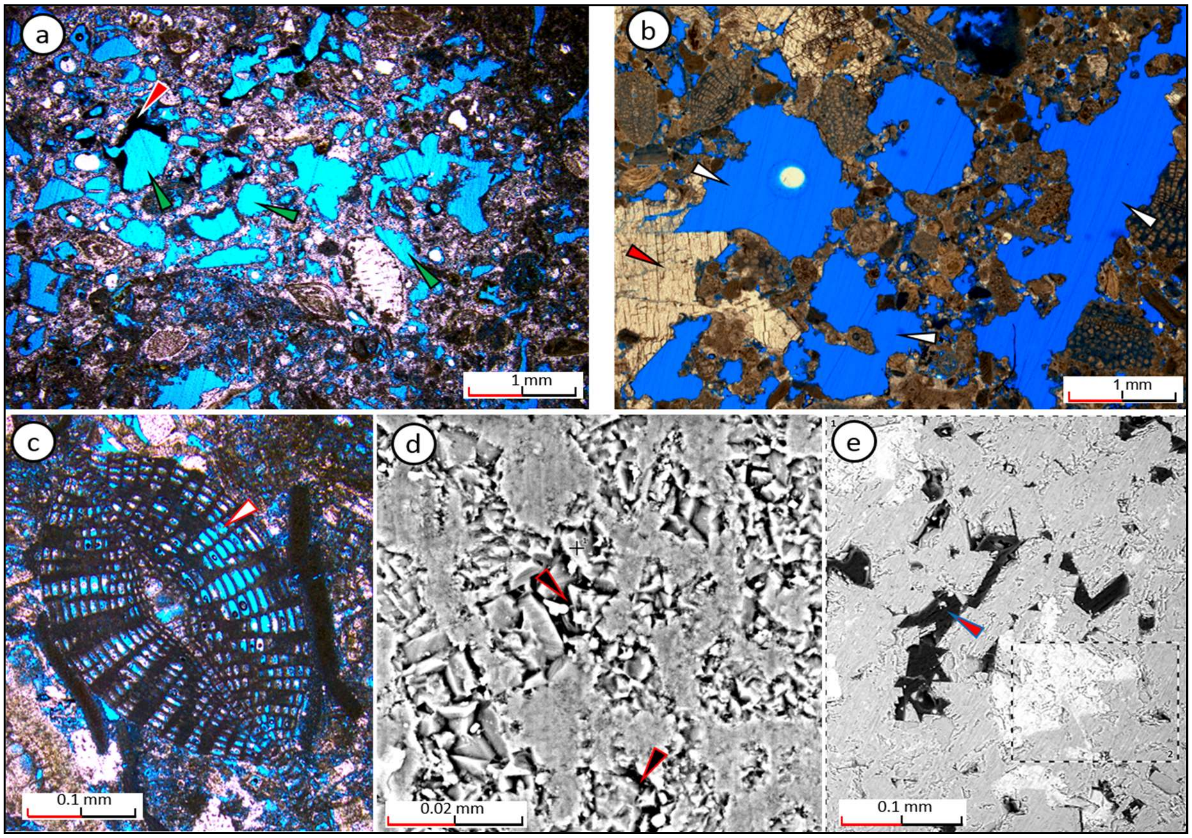

Figure 3.6. Porosity types observed in the Baturaja Formation succession. a. Moldic porosity (green arrows) resulted from dissolution of skeletal grains. Red arrow points to bitumen lining the moldic pore. b. Solution-enlarged vuggy pores (white arrows). Late blocky calcite mosaic cement is indicated by red arrow. c. Preserved intraskeletal porosity in the *Discocylina* sp. test chambers (white arrow). d. Microporosity shown with back-scattered electron (BSE) pointed by black arrows. e. Intercrystalline porosity occurs between type 2 dolomite crystals (red arrow). This BSE image shows that light grey is dolomite and white-spotted crystals are low-Mg calcite (LMC) based on the elemental mapping in the area indicated by dashed line.

Intraskeletal porosity occurs mostly within LBF (Figure 3.6c). This type of porosity is observed in skeletal-rich RFR and RPG facies from C-1 well. It has 7.5 to 25.7% porosity with an average of 14.2%.

Microporosity is seen in the SEM images within the microspar and carbonate mud for the muddy-sequence including wackestone (RLW) and packstone (RPG) facies. The diameter of this pore space ranges from 2 to 10 µm (Figure 3.6d). Microcrystalline texture is granular-subhedral based on the classification by Kaczmarek et al. (2015) characterized by a framework of calcitic microcrystals with curvilinear boundaries. Based on their microporosity typing, this granular-subhedral texture could have correlated to the highest porosity and permeability values.

Intercrystalline porosity occurs between planar dolomite crystals with 8.6 to 15% of pore volumes for W-1 and K-1 wells, respectively (Figure 3.6e). Dolomites in our samples is very rare, hence, it is considered to be an insignificant component for this succession (Tonkin et al., 1992; Carnel and Wilson, 2004). Consequently, its importance to the hydrocarbon exploration and production is negligible compared to the undolomitized carbonate as it has a low portion of expected intercrystalline porosity.

3.8. Discussion

Our data indicate that the hydrocarbon bearing intervals are dominated by dissolution porosity such as moldic and vuggy (Figures 3.6a, b). This result is similar to the Baturaja Formation study by Ardila (1982) and Djuanda (1985) for the offshore area. Porosity measurement from core samples results in the average of 15% (some intervals are up to 38%), with permeability between 5 and 300 mD (Djuanda, 1985; IIAPCO, 1986, Park et al., 1995). Additionally, minor occurrence of intercrystalline, interparticle-intraskeletal and rare fractures occurred in the succession for both offshore and onshore of the NW Java (IIAPCO, 1980; Ardila, 1982; Djuanda, 1985; Park et al., 1995; Setyowiyoto et al., 2007).

3.8.1. Paragenesis and diagenetic processes

We identify a series of diagenetic events in a paragenetic sequence that define diagenetic environments and the evolution of the porosity in the Oligocene-Miocene succession through time. This paragenetic sequence was created to help identifying porosity creation stages (Figure 3.7).

The earliest stage of diagenesis occurred shortly after the deposition of the succession and is characterized by marine cementation–micritization. These processes were followed by early meteoric diagenesis in vadose and phreatic realms. Sea-level fluctuations were clearly significant in the early stages of diagenesis especially in upper part of the succession and at the crest of the mounds. In contrast, the late-stage diagenesis is thought to have occurred in the burial diagenetic settings. These burial diagenetic events resulted in compaction, fracturing, pressure solution, burial dissolution, calcite cementation, and silicification.

Identification of diagenetic environments also is helped by the interpretation of stable isotope distributions (Figure 3.2). Here, negative values of $\delta^{18}O$ characterize a burial diagenesis while negative $\delta^{13}C$ could be related to a meteoric realm (Hudson, 1977; Veizer, 1992, Grossman, 1999). Clustering of values occurred and two major groups are shown: 1) minor to major burial with minor to no meteoric diagenesis, 2) minor to major burial with major meteoric diagenesis. The lowest value of $\delta^{18}O$ from S-1 well is possibly related to the higher temperature from the possible magmatic intrusion (Figure 2.6). Meanwhile, the lowest $\delta^{13}C$ from B-1 well is likely that the whole rock powdered-samples have a mixture with methane-derived cements (Figure 3.6a).

3.8.1.1. Marine diagenesis

Micritization of bioclasts, fibrous to bladed calcite cements filling shells, and the presence of dolomite, glauconite and pyrite are the lines of evidence of early marine phreatic diagenesis. Micritization (either complete or partial) has preferentially affected red algae, mollusc shells and LBF such as *Amphistegina* sp. by microboring, producing an irregular outline of micrite envelopes. This process generally takes place near the sediment–water interface in shallow marine waters (e.g. Bathurst 1966; Jacka 1977; Ellis 1986; Flügel 2004; Fournier et al., 2004). Early marine cements occur as thin isopachous rims of fibrous to bladed calcite crystals (Figure 3.8a). These cements are the first-generation marine products that were later occluded by late stage blocky calcite cements. These cements generally are associated with RPG facies.

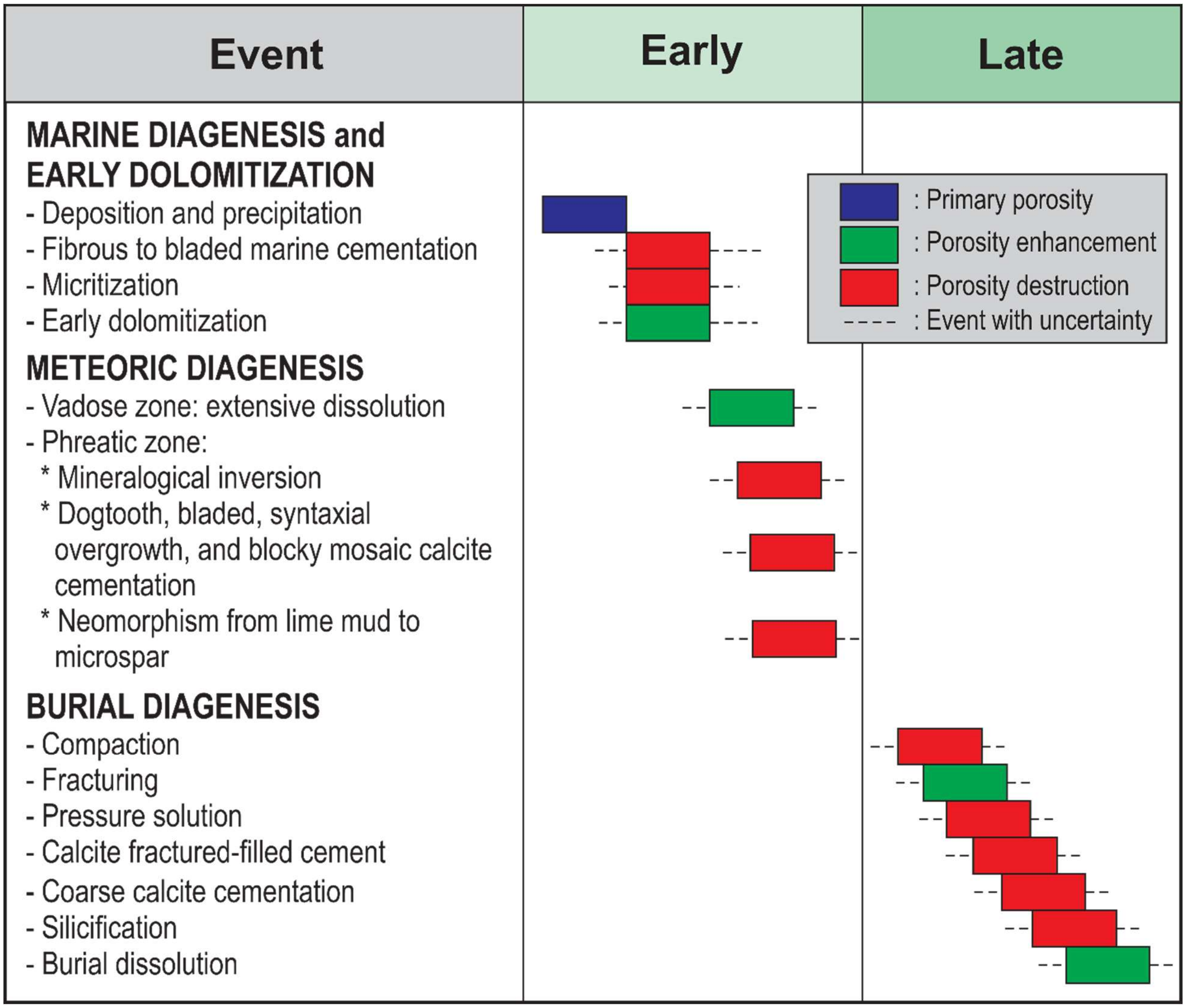

Figure 3.7. Schematic paragenesis of the Baturaja Formation. Diagenetic events for the succession can be classified to early and late diagenesis. Marine and meteoric diagenesis are categorized as early events whereas burial diagenesis is late process.

Dolomite in the Baturaja Formation is very fine to fine crystal sizes and could be related to syn-sedimentary processes. Stable isotope ratios are low negative to slightly positive for δ^{13}C (-2.1‰ to +1.2‰) that could be related to an organogenic model of dolomitization (Compton 1988; Mazzullo 2000). This model is promoted by bacterial sulfate reduction related with organic-matter diagenesis by a local light ^{12}C-enriched CO_2 to pore-fluids derived from bacterial degraded organic matter (Gregg et al. 1992; Perkins et al. 1994; Budd, 1997; Vasconcelos and McKenzie 1997; Mazzullo 2000; Vasconcelos et al. 2005). Trace element concentrations for Fe (151 to 2720 ppm) and Mn (55 to 70 ppm) are relatively low, common for this setting (Mazzullo, 2000). Slightly higher Sr value (87 to 287 ppm) could be from aragonite dissolution (Budd, 1997) in the previous meteoric setting before burial processes.

Spheroidal glauconite is rare in the Baturaja Formation (Figures 3.9a). This mineral likely formed at the sediment-water interface in a low-energy environment, possibly with very low detritus accumulation leads to sediment starvation, and high supply of Fe in an oxygenated to slightly reducing environment (Triplehorn, 1964; Chamley, 1989; Chafetz and Reid, 2000; Banerjee, 2016). The globular shape and absence of angular fragments indicate that this glauconite is authigenic (McConchie and Lewis, 1978). The enrichment of Fe in the samples could be related the presence of this mineral (Figure 3.10).

In the Baturaja Formation, pyrite occurs as framboidal and micro-nodule shapes (Figures 3.9b). This authigenic mineral formed by the reaction of reactive detrital iron with available dissolved sulfate produced by sulfate reduction bacteria (under anoxic condition) using sedimentary organic matter as reducing agent and energy source (Hudson, 1982; Berner, 1984; 1985, Wilkin et al., 1996; Brock et al., 2006). The pyrite in the Baturaja Formation likely formed a few centimeters below the sea-bed (Berner, 1984; 1985; Baird and Brett, 1986).

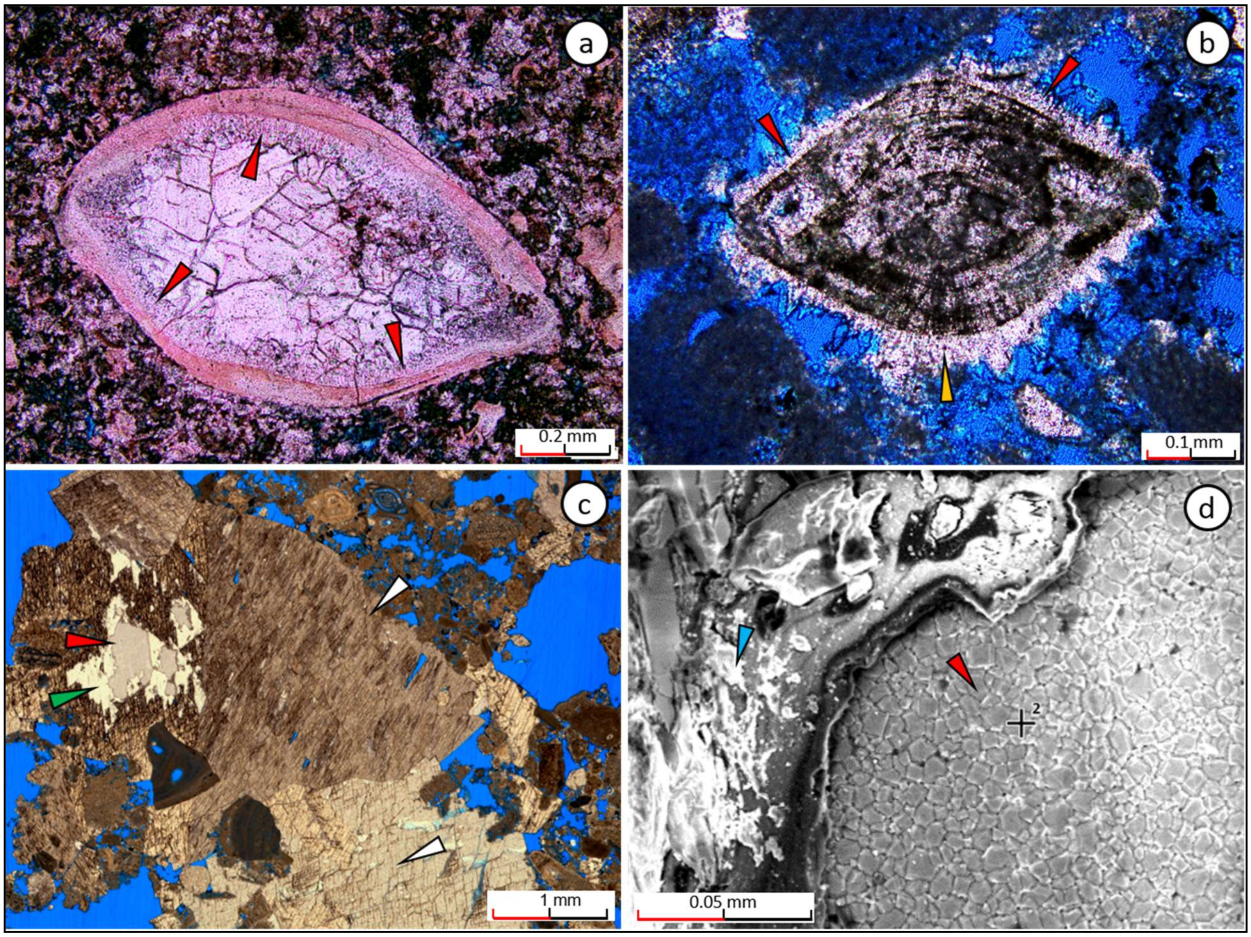

Figure 3.8. a. Fibrous cements (red arrows) lining inside an ostracod carapace; precipitated in a phreatic marine setting. The void was then occluded by coarse calcite cement precipitated in likely phreatic meteoric environment. b. Dogtooth cements (red arrows) grew around *Amphistegina* sp. Pendant-like cement (yellow arrow) also indicates a phreatic meteoric diagenesis. c. Blocky calcite mosaic cement (white arrows) with perpendicular to cross-cutting cleavages; occurs as pore filling cements. This cement is interpreted to have precipitated in a meteoric phreatic setting. Green arrow points to deeper burial calcite cement whereas red arrow indicates microcrystalline silica. d. Equant microcrystalline silica (red arrow) under SEM. Blue arrow shows late stage calcite cement.

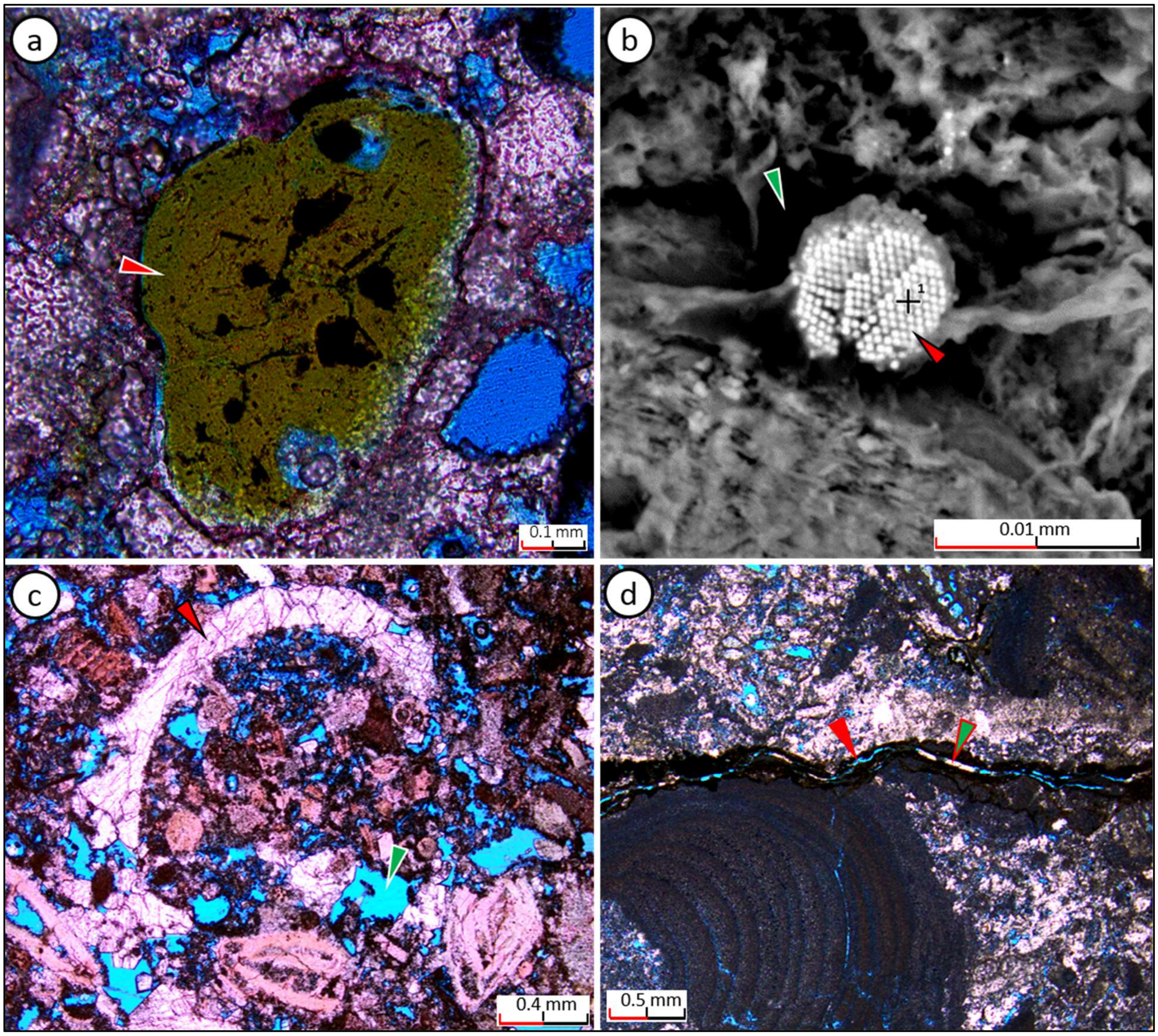

Figure 3.9. a. Globular shaped glauconite in (red arrow). b. SEM photomicrograph showing framboidal pyrite (red arrow) under the SEM filling the microporosity (green arrow). c. Dissolution processes dissolved skeletal grains of red algae and LBF, calcite cements and carbonate muds forming moldic and vuggy pores (green arrow). These non-fabric selective dissolution cuts across carbonate components. Calcite cements (red arrow) replaced possibly aragonitic bivalve shell. d. Enlargement of stylolite (red arrows) filled by calcite cements (green arrow) locally.

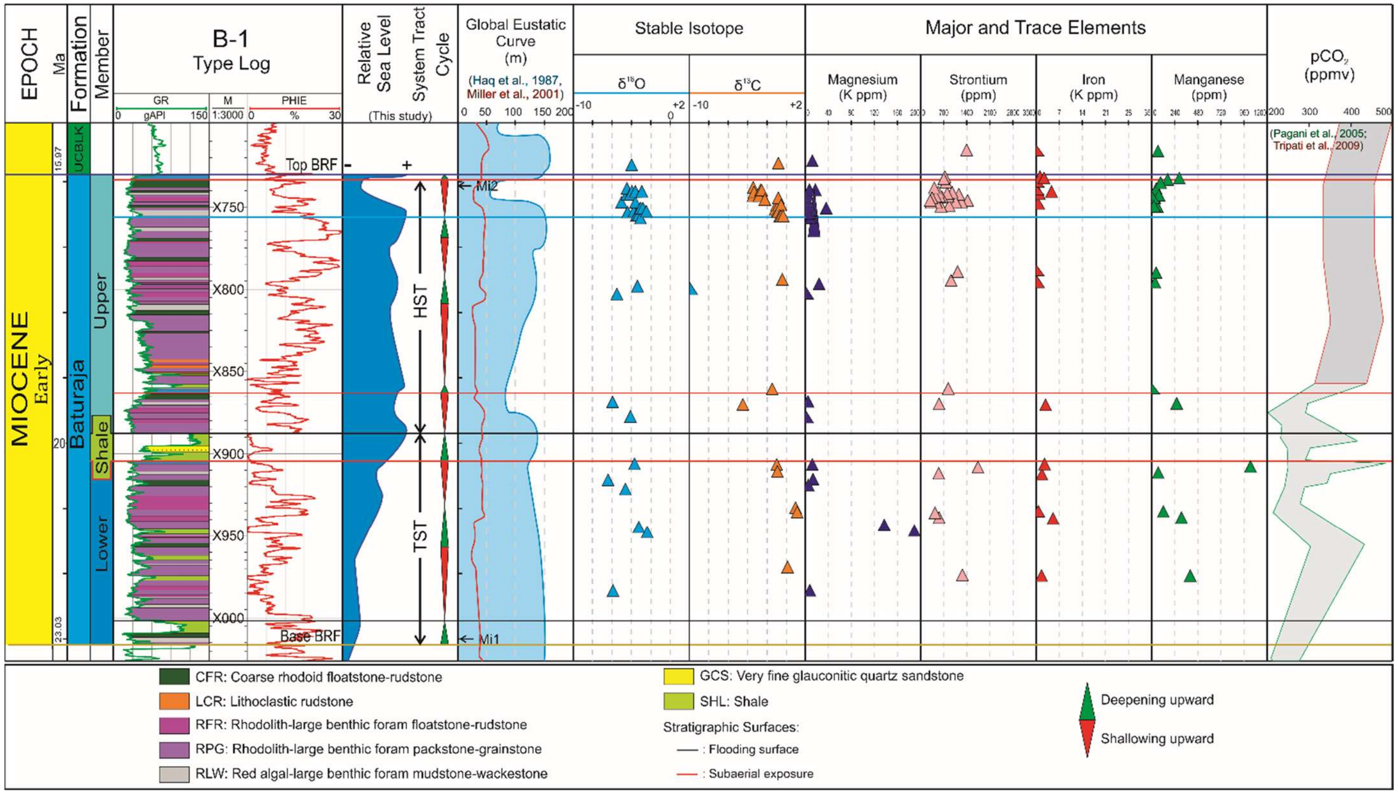

Figure 3.10. Type log of the Baturaja Formation and vertical composite plot of stable isotopes and major-trace elements. This carbonate formation can be distinguished into three members: lower, middle shale and upper. Color codes filling GR log represent facies that were predicted by neural network analysis based on the similarity of well log properties correlated to the specific facies defined from the sparse core data. A cyclicity of deepening and shallowing upward also is shown. System tracts are inferred from the interpreted relative sea level curve (relatively correlative with global eustatic curve). Negative shifts of $\delta^{13}C$ and $\delta^{18}O$ are related with possible subaerial exposure surfaces; supported by moderate Sr content just below these surfaces. Mg peaks represent dolomite content in the bulk samples whereas higher Fe could be related to glauconite. Higher Mn concentration indicates sub- to anoxic condition in burial setting. Miocene glaciation events of Mi1 and Mi2 are from Miller et al. (1991).

3.8.1.2. Early meteoric diagenesis

The early meteoric diagenesis is inferred from micrite recrystallization, distinctive negative shifts of vertical $\delta^{13}C$ plot, enrichment of Sr concentration, and cements. This diagenetic setting likely occurred occasionally during the deposition of the formation represented by probable exposure surfaces and shallowing-upward cycles for both upper and lower members of the Baturaja Formation (Figure 3.10).

Meteoric conditions are a common setting for the dissolution of skeletal grains, mud, and early cement in vadose environment and calcite cementation precipitated in the meteoric phreatic setting. Extensive meteoric dissolution produces extensive vuggy and moldic porosity that are noticeable in our samples (Figures 3.6a, b).

Aragonite was the original composition of coral skeletons and carbonate mud (Dodd 1966; Bathurst, 1971; Adams et al., 1984; Tucker and Wright, 1990) and this was dissolved by meteoric water flush and soil-derived CO_2 percolating through the rocks. Meteoric calcite cement later filled the pores, although in some cases the shells were calcitized and relics of the original aragonitic microstructure are still present (Tucker and Wright 1990). The dissolution-reprecipitation processes in this diagenetic setting reduces the original high Sr concentration but moderate Sr content is retained in the replacement crystals. The RPG and RFR facies, as an example for this case, have elevated Sr concentration up to 1429 ppm. Aragonitic coral skeletons were completely dissolved and filled by blocky calcite cements. In comparison, modern aragonite-rich mud in Florida Bay has ~4000 ppm of Sr whereas modern corals contain ~8000 ppm of Sr (Bathurst, 1971) that would likely be reduced during burial diagenesis and recrystallization through time.

Matrix recrystallization (neomorphism) is very common that the original carbonate mud transformed its crystal size, shape and crystal lattice orientation generally into coarser mosaic spar

(4-8 μm). This recrystallization is regarded as a product of meteoric diagenesis (Wiggins, 1986). Recrystallization of lime-mud matrix generally destroys microporosity (Pittman, 1971).

The interpretation of an early meteoric diagenetic event also is supported by the presence of calcite cements precipitated in this setting, which include dogtooth, syntaxial overgrowths of echinoid grains, and blocky cement. Cloudy fringing dogtooth cement (Figure 3.8b) precipitated and grew sharp, pointed, bladed calcite crystals around *Amphistegina* sp. In addition, pendant-like cement occurs as an asymmetrical shaped, pointed and thickening downward during precipitation by gravitational force. Even though dogtooth cement can be precipitated in a wide variety of diagenetic environments from meteoric to shallow burial settings (e.g. Flügel, 2004; Andrieu et al., 2018), formation of pendant-like cement leads to the interpretation of the likely meteoric vadose zone above the fresh-water table. Additionally, the sample containing this cement occurs at the 16 Ma probable subaerial exposure (Figure 3.10).

Syntaxial overgrowth cement is common for RPG, RFR and in some RLW facies. This cement is characterized by cloudy syntaxial calcite cement that grow in optical continuity with the substrate (typically echinoderm grains) of the same calcite mineralogy (Flügel, 2004). This type of cement is interpreted to be formed rapidly in the freshwater phreatic environment (Longman, 1980; Kaufman et al., 1988). Meanwhile, grayish cloudy blocky calcite mosaic cement is interpreted to have precipitated in meteoric phreatic realm.

Subaerial exposure events are inferred from our interpretation of depositional cycles and relative sea level curve based on the vertical facies association, porosity, and stable isotopic signatures especially the increasingly negative $\delta^{13}C$ below these surfaces (Figure 3.10). The distinctive negative shifts of $\delta^{13}C$ occurred episodically in the Early Miocene and are likely related to the meteoric affected event of subaerial exposures. Moderate Sr values at and right below these surfaces indicating aragonite dissolution caused by meteoric water flushing and possible neomorphism while retaining the moderate Sr values. There are at least three major subaerial exposure events, based on these shifts, i.e. at the boundary between lower member and middle shale member at 20.3 Ma, at the lower portion of the upper unit (19.2 Ma) and at the top of the Baturaja Formation (16 Ma). The latter event coincides with extensive dissolution of vuggy and moldic pores.

3.8.1.3. Burial diagenesis

A burial diagenesis is inferred from several lines of evidence including distinct trace element signatures, calcite cementation, stylolite formation with increasing burial depths, coarse calcite cement, silicification, burial dissolution, and calcite cement filling stylolites. Burial environments typically are characterized by a change to anoxic conditions after deposition and reflected by moderate concentrations of Fe and Mn (Tucker 1986) in the range of more than hundreds ppm, as the availability of dissolved Fe and Mn released from clays can easily substitute in the calcite lattice at low oxygen states (Budd 1997; Grossman 2012). Moderate values of these elements in the lower member support this interpretation (Figure 3.4).

As sediment overburden and pressure increase, mechanical compaction occurs in the succession, followed by fracturing and pressure solution. Deformation of shell fragments, cemented micro-fractures, grain re-orientation, and lithification occurred in the Baturaja Formation samples suggesting a transition to the burial environment. The compaction produced textural changes resulting in originally wackestone facies being altered into packstone as the carbonate mud was squeezed, skeletal grains were condensed, and intergranular spaces were filled by lime mudstone (Shinn and Robin, 1983; Choquette and James, 1987).

Pressure-solution occurs in many samples as stylolites. These irregular, serrated, interlocking, and suture-like contacts formed at the grain to grain contacts of mainly red algal and LBF (Figure 3.9d). Concentration of black insoluble residues (stylocumulates) along the stylolite surfaces are common. Approximately 40% of samples from the Melandong field have stylolite structures generally occurring in lime mud-dominated facies. Wackestone (RLW), packstone (RPG), and floatstone (RFR) in packstone matrix commonly contain this structure and support the interpretation that mud-rich facies were strongly affected by load and stress as the skeletal grains were less soluble than carbonate mud (Flügel, 2004). Other factors including clay content, the amount of the load/stress, water chemistry, pore-fluid pressure, mineralogy, host-rock porosity and permeability, degree of cementation, and rock resistance could also be major factors producing stylolites (Bathurst, 1972; Choquette and James, 1987; Buxton and Sibley 1981; Railsback 1993; Moore 1989; Flügel, 2004).

Limpid coarse mosaic calcite cement occurs in the sample (Figure 3.6b) and is expected to have negative $\delta^{18}O$ values reflecting increasing temperatures of the precipitating calcite supersaturated waters (Choquette and James, 1987). Higher Fe and Mn concentrations occurred (Figures 3.4, 3.5), as this cement was precipitated in anoxic and reducing conditions where significant Fe and Mn in the 2+ valence state formed (Choquette and James, 1987; Budd, 1997; Grossman, 2012).

Precipitation of microcrystalline silica occurs locally (Figure 3.8d). This kind of quartz consists of minute and slightly equant microcrystalline aggregates that preferentially replace coarse calcite cements. Decreasing pH in pore waters and accompanying decreasing silica solubility leads to increasing acidity and results in the silica precipitation (Birnbaum and Wireman, 1984; Noble and Stempvoort, 1989). Supersaturation of pore water with respect to silica also is considered without any changing saturation of the bulk host carbonate (Maliva and Siever, 1989) as there is no sign for carbonate dissolution adjacent to the silica. It seems that silicification in our sample occurred by the latter process since there is no evidence of calcite cement dissolution at the margin of conjoining silica and calcite cements.

Porosity and permeability in the carbonate succession normally are reduced significantly in response to compaction (both mechanical and chemical) by sediment loading, tectonic pressure, and cementation. However, dissolution processes may have occurred in the deeper burial setting and either enhanced pre-existing pores created in the previous diagenetic environments or created new pores. This diagenetic scenario is proposed to account for the presence of moldic and vuggy pores which occur primarily in samples from the inter-mound areas (Figures 3.6a, b). Since these inter-mound areas are a deeper depositional setting in the range of 150 to 300 m, it is unlikely that they were exposed during times of lower sea level thus rendering meteoric solution-enlargement of voids as unlikely.

Calcitic-rich solutions produced from dissolved carbonate materials by CO_2-rich burial fluids, precipitated calcite cement and locally filled opened stylolite (Figure 3.9d). The stylolite is inferred as a pathway for the movement of the dissolving fluids (Mazzullo and Harris, 1992). This cementation process postdates pressure-solution events likely occurred at hundreds of meters of burial depth.

3.8.2. Pore type analysis

Moldic porosity can form by fabric-selective leaching of skeletal components (Poppelreiter et al., 2005), controlled by the mineralogy (Moore, 1997), and possibly micro-structural difference between the solubility of individual skeletal grains, cements, and carbonate muds (Flugel, 2004). This type of porosity could occur in the meteoric-phreatic and also in burial settings (Flugel, 2004) and is characterized by non-fabric selective dissolution (Choquette and Pray, 1970; Choquette and James, 1987; Moore, 1997). Meanwhile, vuggy porosity was likely formed at the later stage after mineral stabilization (Moore, 1997). The Baturaja Formation samples show that this type of porosity was likely produced after stylolitization as the vugs locally cut across the stylolites in some thin sections.

The dissolution processes in our samples leached red algae, LBF, early calcitic cements and carbonate mud that have different crystal sizes, mineral compositions, and micro-textures indicating variations in relative solubility (Figures 3.9c, 3.11). The red algae mainly are composed of unstable high-magnesium calcite (HMC). LBF tests are mainly LMC calcite while carbonate muds might be dominantly aragonite that have changed to LMC calcite during mineral dissolution and re-precipitation in burial settings.

Perforated LBF, such as *Amphistegina* sp., *Assilina* sp., *Lepidocyclina* sp., and *Miogypsina* sp. (Bassi et al., 2007), are abundant in the Baturaja Formation. The distribution of these perforated LBF across the ramp is slightly different. B-1 well has more perforated foraminifera (89.1% of total LBF) than J-2 and K-1 wells (84.3%). In addition, ellipsoidal test shape of perforated LBF (such as *Amphistegina* sp. and *Miogypsina* sp.*)* shows similar trend being more abundant in B-1 well with 56.2% while J-2/K-1 wells show 46.8%. The richness trend toward more perforated LBF in the carbonate mound rather than the inter-mound area might be correlated to the more ellipsoidal moldic porosity observed in the B-1 well showing fabric-selective dissolution texture (Figures 3.3b, 3.11a). The perforated tests of the LBF likely served as micro-permeability conduits for the acidic fluids to dissolve the LBF.

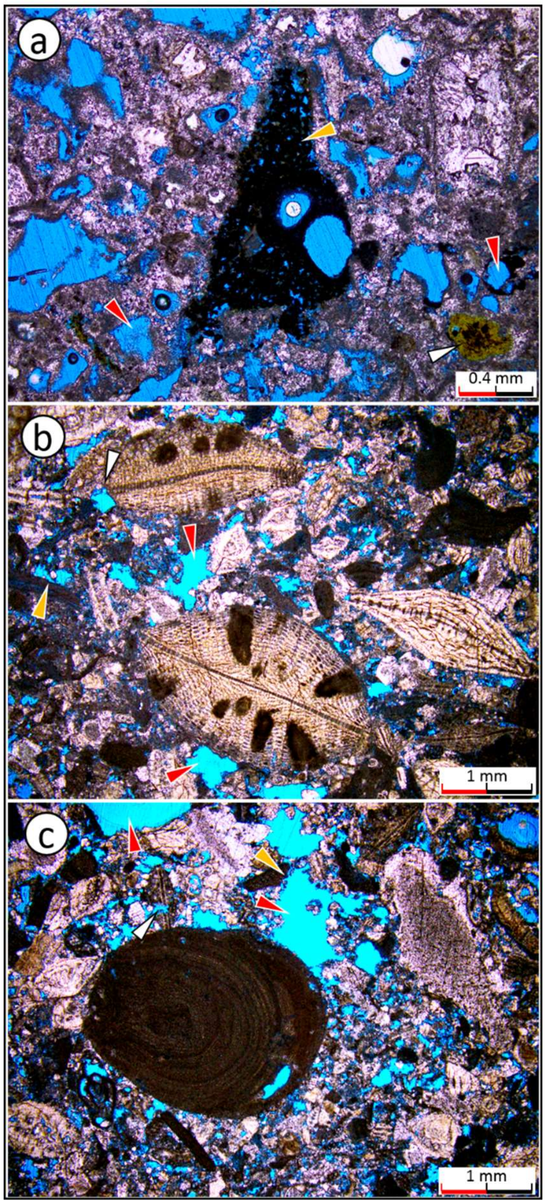

Figure 3.11. Extensive moldic and vuggy porosity in thin sections. a. Moldic porosity (red arrows) is likely produced by fabric-selective meteoric dissolution. Blacken and partially dissolved red algae (orange arrow) might indicate subaerial exposure event. Note glauconite indicated by white arrow. Sample is taken from B-1 well. b. Vuggy porosity (red arrows) resulted from partially dissolved skeletal grains of *Amphestigina* sp. and *Discocylina* sp. (white arrow), red algae (orange arrow), and calcite cements. Sample is from J-2 well. c. Similar vuggy porosity (red arrows) that cross-cut partially leached red algae (orange arrow), *Discocyclina* sp. (white arrow) and calcite

cements. Sample is from K-1 well. Burial dissolution by CO_2 was likely responsible for producing non-fabric selective pores in b and c.

At the inter-mound area, non-fabric selective dissolution texture (Figures 3.11b, c) occurs with slightly equal distribution of irregular pores of vuggy and ellipsoidal-shape of moldic porosity (Figure 3.3b). This texture is related to the water-controlled diagenesis indicating pore-water changes by increasing CO_2 concentrations (James and Jones, 2016) in a possible burial setting. In this diagenetic environment, the dissolution processes of the Baturaja Formation were likely controlled by micro-pores and micro-permeability (as in the perforated LBF) and crystal size (as in carbonate mud) different than this process being driven by original mineralogy (e.g. Larue, 1976; Ardila, 1982; IIAPCO, 1986; Tonkin et al., 1992; Park et al., 1995; Wicaksono, 1995).

The B-1 well from the mound area shows bulk porosity from image analysis of 2.3 to 26.3% with an average of 13.8% whereas an inter-mound area, represented by the J-2 well, has 3 to 29.2% porosity with an average of 14.8%. Furthermore, at the reservoir interval from the petrophysical analysis reports (Pertamina EP, 2014), B-1 has bigger effective porosity of 5.7 to 33.67% with an average of 17.2% whereas the J-2 well has 6.1 to 26.4% porosity with an average of 15.2%. These differences in the porosity may indicate micro-porosity in the succession that is not recognizable by image analysis.

3.8.3. Origin and evolution of the porosity

The Baturaja Formation has a quite simple burial history that after deposition, this succession was buried to the burial diagenetic setting after its deposition to Recent (Figure 3.12). Consequently, there are two possible scenarios of the origin of the moldic and vuggy dissolution porosity in the Baturaja Formation: 1) dissolution in meteoric setting or 2) burial dissolution based on CO_2 degassing from mantle through deep-seated fault conduits.

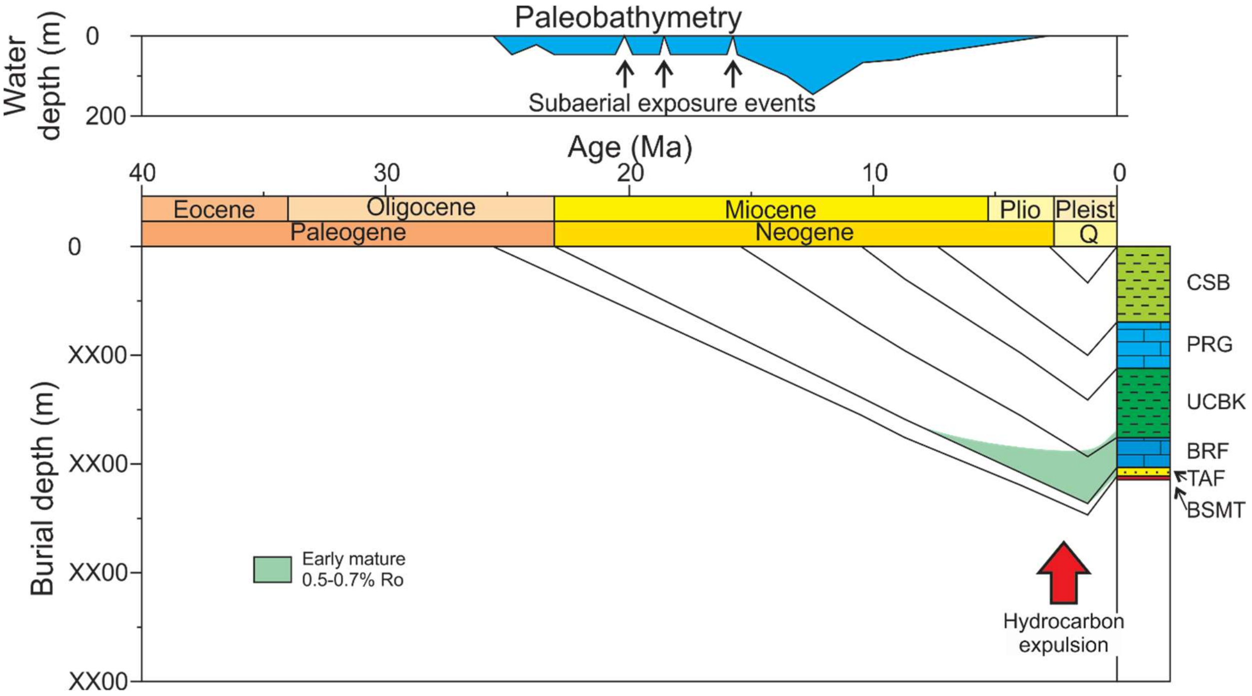

Figure 3.12. Paleobathymetry and burial diagram from B-1 well showing depositional environmental depth for the Baturaja Formation was maximum 40 m from paleontology analysis. Three subaerial exposure event occurred during deposition. Critical moment when hydrocarbon expelled for the well was during the Pliocene-Pleistocene (modified from LAPI ITB, 2012).

Meteoric diagenetic environments are prone to produce moldic and vuggy porosity that can provide high porosity-permeability intervals for hydrocarbon producing zones (Larue, 1976; Ardila, 1982; IIAPCO, 1986; Tonkin et al., 1992; Park et al., 1995; Wicaksono, 1995). When the carbonate sediments were exposed to meteoric environments during subaerial exposure, they were easily dissolved by freshwater that was undersaturated with respect to calcite and subsequently precipitate as LMC (Chave et al., 1962; Allan and Matthews, 1977; Tucker and Wright, 1990). The freshwater was acidified by atmospheric, soil-derived CO_2 and also soil acids (Tucker and Wright, 1990). Consequently, meteoric dissolution occurs more extensively in humid and tropical conditions where heavy rainfall and vegetation are common. In this diagenetic setting, the freshwater, decayed organic matter, and soils generally are enriched in δ^{12}C giving subaerially-exposed successions a distinctive negative δ^{13}C signature (Chave et al., 1962; Allan and Matthews, 1977; James and Choquette, 1984). Fabric-selective dissolution texture resulted from preferential dissolution of more soluble skeletal grains i.e. mainly red algae and ellipsoidal-shaped and perforated LBF that produced more moldic pores in the B-1 well at the carbonate mound area (Figures 3.3b, 3.11a).

We recognize that the main porous intervals are in the top of highstand upper member and are likely associated with a major sea-level fall. The isotopic data from the offshore area shows a depleted in ^{13}C for the calcite cement indicating meteoric influence (Park et al., 1995). Our stable isotope distribution shows similar trend of negative δ^{13}C values (Figures 3.1 and 3.2) for samples from B-1, P-1, C-1, and S-1 wells. The B-1 well located at the mound area on the paleotopographic high was most susceptible to sea-level fluctuations and prone to meteoric conditions when sea level lowered (Figure 3.2). The meteoric dissolution in this area resulted in moderate Sr concentration (Figures 3.3a, 3.10). Contrastingly, samples from the deeper inter-mound areas (J-2, K-1, and K-2) show more positive δ^{13}C and lower Sr values. This is attributed to the amplitude of sea level variations that were insufficient to expose the deeper areas.

In spite of this meteoric evidence there were variations of CO_2 content in gas production: 92% from B-1 production data at the mound area and 80% and 16% for S-1 and J-2 wells within the inter-mound areas. High CO_2 abundance could be related to several sources, including decomposition of organic material from biogenic processes, thermal breakdown of kerogen, mantle degassing, and metamorphic mineral reactions (Dai et al., 1996; Cooper et al., 1997; Noble et al., 1997). Data from a nearby well (PMK-2 with ~100% CO_2) at the Pamanukan High, located less than 3 km from our study area, has a mantle source of CO_2 from ^{3}He/^{4}He analysis (Cooper et al., 1997) and can be an analog to our data. Additionally, the position of the wells in the Melandong area is adjacent to deep-seated basement-involved faults (B-1 and J-2 wells) and magmatic intrusion-related faults (S-1 well) that could be correlated to a mantle- and magmatic-degassing interpretation. These faults were likely vertical conduits for CO_2 and brought this gas into contact with the Baturaja Formation (Figure 3.13). The deep-seated normal faults were produced by extensional tectonics (Irwin and Barnes, 1980; Giggenbach et al, 1993; Dai et al, 1996; Pinti and Marty, 2000; Liu et al., 2011; Castillo et al., 2017) during the early rifting in NW Java. Additionally, radial faults around the S-1 well (shown by high variance alignments) might be supplementary conduits for CO_2 gas expulsion from the magmatic intrusions and contribute to diagenetic fluids. The CO_2 gas likely affected carbonate sequences and significantly decreased the pH of diagenetic fluids and made corrosive brines that promoted the burial dissolution to create and expand pores. The dissolution in this burial setting likely result in non-fabric selective dissolution textures (Figure 3.11b, c). The very similar products of moldic and vuggy porosity might be produced by two distinctive processes of burial and meteoric dissolutions.

3.8.4. Implication for hydrocarbon exploration and production

Carbonate mounds were preferentially targeted as the Baturaja Formation hydrocarbon exploration play since the 1980s (Longman, 1994; Noble et al., 1997; Bishop, 2000; Suyono et al., 2005). The mounds, dominantly developed on paleotopographic-highs and uplifted fault blocks, show good secondary porosity and permeability and proved to form hydrocarbon producing reservoirs; both onshore and offshore. Hydrocarbon producing fields such as Krisna, Rama, and Bima in the offshore (IIAPCO, 1986; Woodling et al., 1991; Tonkin et al., 1992), Tugu, Tambun, Cilamaya, and Pegaden in the onshore area (Suyono et al., 2005) were targeting Baturaja Formation reservoirs. This conventional or traditional carbonate mound play of the Early Miocene

Baturaja Formation is largely exhausted (Netherwood, 2000); so, new exploration concepts are needed to increase reserve replacement ratio in this highly complex and heterogeneous porosity-permeability carbonate reservoir system.

Deeper structural concepts were explored and became vital since the degree of difficulty in petroleum exploration of shallow strata is increasing (Shen et al., 2016). Several structures were successfully discovered in NW Java Basin, such as Karangbaru (Suyono et al., 2005), and J structure at the Melandong complex, applying this deeper structural concept.

We propose the exploration play of the inter-mound located in the middle ramp setting (Figure 3.13). Here, deep-seated faults act as vertical conduits for CO_2 corrosive fluids. The J structure is proven to have good reservoirs in the Baturaja Formation producing oil and gas from this concept. This 3-way dip structure is located in the lower structural area and has deeper depositional setting. Bounded by deep-seated faults, this uplifted block was an objective for the drilling, at that time, targeting and exploring reservoir with meteoric-derived pores, despite its basinward setting. The disadvantage of this concept exploring burial dissolution pores in the lower structural areas is higher CO_2 content, as shown by well-test data. Corrosive CO_2 in the well production could signal increasing budgetary spending on downhole and surface facilities to prevent corroded pipes and high CO_2 removal processing costs.

While an understanding of the porosity creation mechanism is important, a complete subsurface dataset is required in order to accurately predict and describe the presence, geometry, and distribution of the secondary pores. High-resolution 3D seismic is a critical consideration for the further development phase in the mature field, like the Melandong area, to be able to map 3D geometry with its attribute analysis and to predict porosity-permeability system in carbonate succession. Integrated study of well data (logs and cores) and rock physics models are being conducted to identify and characterize pore types and their geometry (Agustianto, personal communication). The ability to describe pore heterogeneity laterally and vertically will lead to increased understanding of rock reservoir quality, especially in areas with limited core coverage.

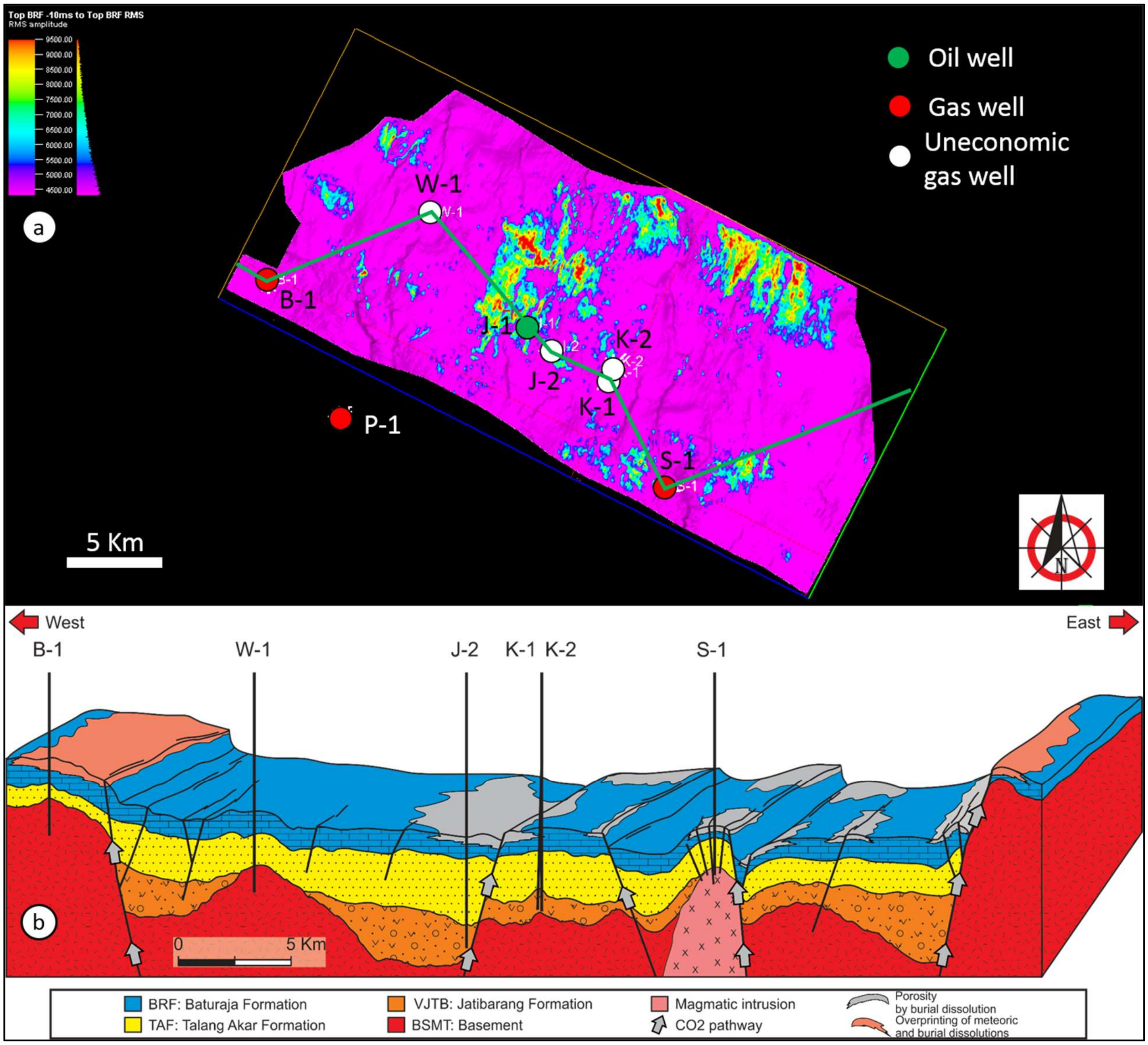

Figure 3.13. a. Amplitude slice map created by 0 to 10 ms window below the top Baturaja Formation horizon showing possible porosity distribution in the study area. Green polygon shows the direction of 3D model in b. b. Vertical conduit model for mantle- and magmatic-derived CO_2 affecting this deep buried succession. Moldic and vuggy porosity was created by the dissolution of the rock volume by this acidic gas. Inter-mound area is a locality where this porosity creation

is greatly affected by this burial dissolution process whereas at the mound region, overprinting to the porosity created by previous meteoric events should have occurred.

3.9. Conclusions

The Baturaja Formation has mixed porosity (moldic and vuggy) that was created by two main episodes: meteoric and burial processes, based on the following points:

1. Paragenesis for the Baturaja Formation succession in NW Java Basin, Indonesia shows early stage diagenesis began with marine diagenetic processes that were followed by occasional subaerial exposure events to meteoric settings. Rapid changes of diagenetic environments for these early events were clearly significant for the porosity creation, especially at the vadose meteoric zone. The late-stage burial diagenesis resulted in compaction, fracturing, pressure solution, burial dissolution, calcite cementation, and silicification.
2. Porosity types are dominated by moldic and vuggy secondary porosity. Intraskeletal, interparticle, intercrystalline, microporosity, and fracture porosity is minor to rare in the Baturaja Formation. More abundant moldic pores in the carbonate mound area are related to the fabric-selective meteoric dissolution of ellipsoidal shaped of perforated LBF and red algae whereas slightly equal portions of moldic and vuggy pores occurred in the inter-mound area related to non-fabric selective burial dissolution. Abundant perforated LBF with their micro-porosity and also micro-permeability might be factors influencing and controlling the differences in dissolution textures across the ramp.
3. The Baturaja Formation has prolific hydrocarbon reservoirs where its porosity system was widely interpreted previously by strong meteoric-dissolution events. Occasional meteoric exposures of the succession, for both lower and upper members, are indicated by the extensive dissolution of moldic and vuggy pores, in addition to ^{13}C-depleted intervals, caused by dissolution through meteoric processes in the succession within the mound area. This locality

was vulnerable to episodic subaerial exposure events. In the deeper inter-mound areas, burial dissolution might dominate porosity creation by dissolution of the rock volume by mantle-derived CO_2. Deep-seated faults were ascending pathways of these corrosive fluids. It is possible that this burial dissolution overprinted previous meteoric processes as the result of these two dissolution processes are similar in abundances, especially in the inter-mound area, i.e. moldic and vuggy pores.

4. The burial dissolution model emerges as an inter-mound exploration concept focusses on the muddy middle ramp setting. An area with the deep-rooted faults has a larger probability to have mantle-derived CO_2 to dissolve the rock and create secondary moldic and vuggy pore spaces.

CHAPTER 4

CONTROL ON DIAGENESIS AND DOLOMITIZATION OF PERITIDAL FACIES, EARLY CRETACEOUS LOWER EDWARDS GROUP, CENTRAL TEXAS, USA*

4.1 Overview

The Early Cretaceous Fort Terrett Formation of Mason County, central Texas, is a succession of subtidal to peritidal mud-dominated facies with minor intervals of bioclastic packstone-grainstone, rudist floatstone, and interbedded chert nodules. The strata conformably overlie the Hensel Formation, which was deposited unconformably on Precambrian basement. The Hensel Formation also contains a significant percentage of dolomite, precipitated within a fine-grained clayey matrix.

The Hensel and Fort Terrett Formations were deposited during a transgressive episode, which provided the conditions for the extensive shallow-water Comanche carbonate platform. Siliciclastic and carbonate sediments were deposited along the coastal margin in subtidal, intertidal to supratidal areas. Previous dolomitization models have suggested that high permeability layers are required for dolomitizing brines to flow through a carbonate succession. Although, interparticle porosity in muddy tidal-flat successions can be significant, it has a limited flow capacity. However, interconnected fenestral porosity can allow sufficient fluid flow to move dolomitizing fluids more efficiently through the succession. Thus, it is hypothesized that interconnected fenestral porosity

---

*Reprinted with permission from "Controls on diagenesis and dolomitization of peritidal facies, Early Cretaceous Lower Edwards Group, central Texas, USA" by Robet Wahyu Widodo and Juan Carlos Laya, 2017. Facies, v. 63, p. 23, Copyright 2017 by Springer-Verlag GmbH Germany could have had a significant impact on permeability within this muddy succession and provided the pathways and conduits for Mg-rich brines.

Four types of dolomite are recognized in the Fort Terrett succession. Three of these dolomite types formed largely by replacement and they occur throughout the succession. Features such as crystal size, crystal face geometry and zonation reflect the progressive development and recrystallization of the dolomite types. Only type 4 dolomite formed as a cement in void spaces during a late diagenetic stage. The direction of the dolomitizing fluid movement is difficult to determine, but it was likely downward in this case, controlled by a density head driving-mechanism generated by dense hypersaline fluids from an evaporating lagoon.

4.2. Keywords

Early Cretaceous, dolomite, dolomitization model, carbonate diagenesis, fenestral porosity

4.3. Introduction

Early dolomitization is a common process in peritidal carbonate deposits (e.g., Permian Tansill Formation, Cretaceous Edwards Group and Holocene carbonate sediment in the Bahamas) which has been attributed to several mechanisms including microbial activity, tidal pumping, seepage reflux and evaporation (Deffeyes et al. 1964; Vasconcelos and McKenzie 1997; Fisher and Rodda 1969; Saller and Henderson 2001; Machel 2004; Jones and Xiao 2005). Dolomitization models specifically for the Lower Edwards Group in Central Texas include seepage-reflux (Fisher and Rodda 1969) and evaporative pumping (Rose 1972). These mechanisms require sufficient permeability (minimum 240 millidarcies as calculated through a mass-balance method by Deffeyes et al. 1964 for the Pekelmeer lagoon in Bonaire, Netherlands Antilles) so that a Mg-rich brine can flow and deliver the large volume of fluid required for pervasive dolomitization (Machel 2004; Garcia-Fresca et al. 2012). However, fine-grained facies with few isolated packstone– grainstone layers dominate the Edwards Formation outcrops examined in Mason County; thus, it is difficult to see how muddy sediments with low permeability and limited high-permeability layers can allow brines to permeate for extensive dolomitization during early diagenesis.

In peritidal deposits, fenestrae and fenestral fabric are very common (Shinn 1968; Shinn and Robbin 1983) and these may have greatly affected primary permeability. However, the relationship between fenestral fabrics and dolomitization is poorly documented and understood, even though it is very common for dolomite units and fenestral fabrics to occur together in peritidal successions (Shinn and Robbin 1983; Abduslam 2012). It is proposed here that fenestral fabrics can play a significant role in the dolomitization of mud-dominated facies.

The Early Cretaceous Lower Edwards Group in Mason County, central Texas, was deposited unconformably over a Proterozoic granitic basement (Walker 1992) and is well exposed within The Mason Mountain Wildlife Management Area (MMWMA), 17.7 km north of Mason, Texas (Figure 4.1). Outcrops occur on the western flank of the Llano Uplift (Figure 4.1a) and the eastern extension of the Edwards Plateau (Barker and Ardis 1996; Anaya 2004).

Reddish conglomeratic sandstone to dolomitic sandstone of the Hensel Formation were deposited unconformably on basement rocks (Figure 4.1b) during the initial transgression (Payne and Scott 1982; Phelps et al. 2014). A peritidal mudstone to skeletal–fenestral wackestone succession of the Fort Terrett Formation contains minor intervals of bioclastic packstone–grainstone, isolated rudist floatstone, and thin evaporite deposits (Fisher and Rodda 1969; Rose 1972; Barker et al. 1994; Moore 2010).

4.4. Geological setting

The Llano Uplift region has a simple geological history that can be summarized in three major geological events: (1) Precambrian granite intrusion and metamorphism produced by the Laurentia and Rodinia collision event (Sellards et al. 1932; Walker 1992; Mosher 1998; Ewing 2005; Miall and Blakey 2008); (2) Early Mesozoic rifting followed by major Early Cretaceous transgression and formation of the shelf system, which led to the deposition of thick siliciclastic and carbonate successions; and (3) Late Oligocene-Early Miocene regional uplift along the Balcones Fault Zone, which caused the exposure of the Cretaceous strata in this area (Anaya 2004; Barker et al. 1994; Collins 1987; Ewing 2005; Lawton 2008; Maclay 1995; Phelps et al. 2014).

4.4.1. Regional depositional setting and stratigraphy of Early Cretaceous strata

Central Texas during the Early Cretaceous was located between 25° and 30° north paleolatitude, indicating a tropical environment for its successions (Scotese et al. 1999; Phelps et al. 2014). Additionally, a semi-arid to arid climatic regime was present (Payne and Scott 1982; Phelps et al. 2014). A second phase of tectonic activity led to the formation of a small island (Figure 4.1c) on the Comanche Platform (Fisher and Rodda 1969; Moore 2010). As the Early Cretaceous transgression covered the low-lying continental margin, the Hensel Formation was deposited in fluvial to coastal environments, onlapping the Proterozoic granitic basement (Barnes et al. 1972; Walker 1992; Moore 2010). As the transgression continued, carbonate sediments began to be deposited along the shoreline including peritidal areas (Moore 2010).

Sea-level fluctuations resulted in wide-ranging depositional environments including open-marine, shoals, shallow inner lagoon (known as the Kirschberg Lagoon) and interior peritidal systems located behind the Stuart City Reef to the south-southeast, and Central Texas Reef trend to the north-northeast. The carbonate succession on the platform is comprised of lime mudstone, miliolid foraminifera packstone-grainstone and rudist floatstone, interbedded with rare evaporites in the Fort Terrett Formation of the Edwards Group (Rose 1972; Barker et al. 1994).

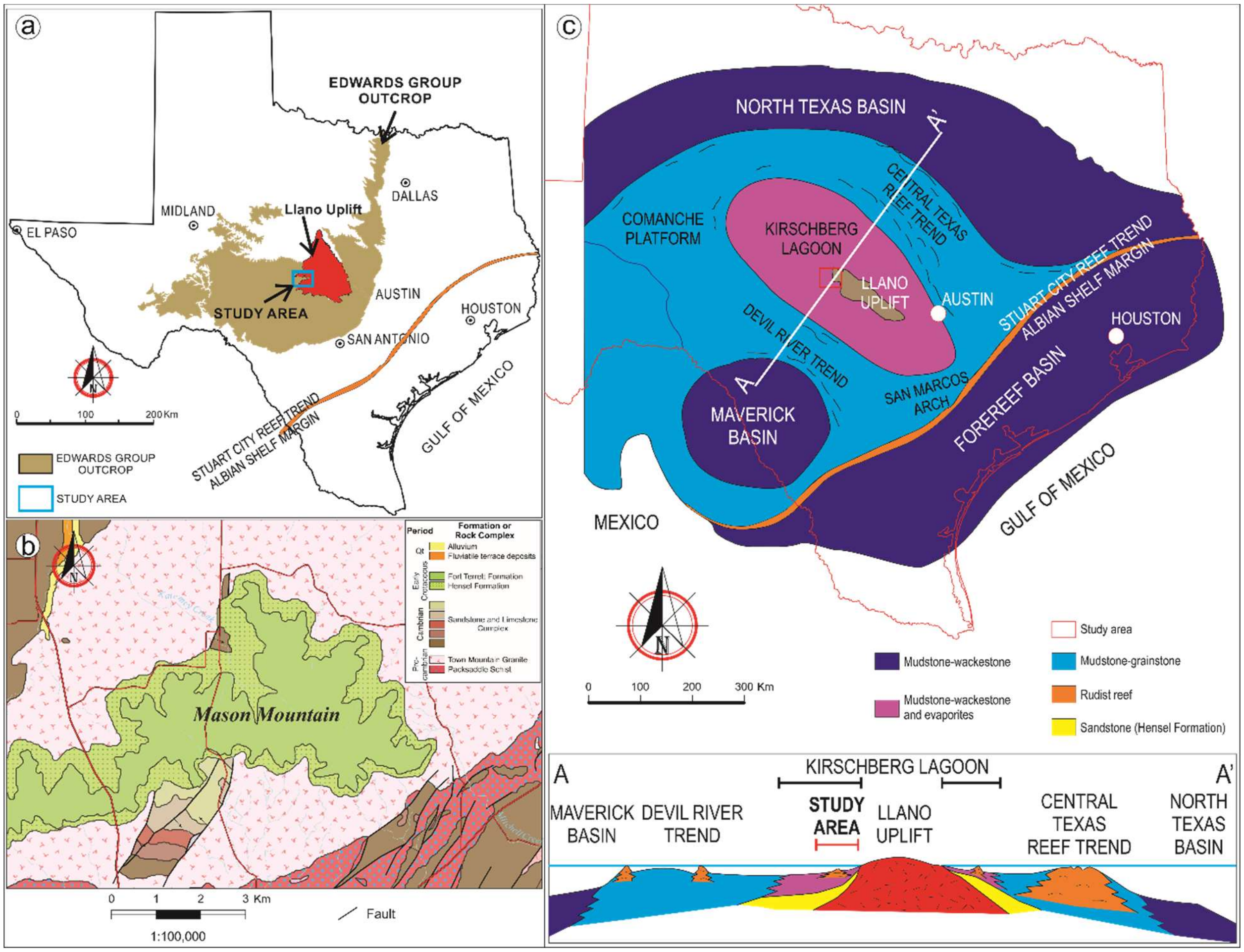

Figure 4.1. a. Location of the study outcrops in the eastern extension of the Edwards Plateau and the western flank of the Llano Uplift (modified from Bureau of Economic Geology 1992). b. Geological map of Mason Mountain Wildlife Management Area (MMWMA). The Early Cretaceous succession (in green colours) is surrounded by a Precambrian basement complex (modified from Helper 2006). c. Upper figure shows regional depositional setting of Texas during the Early Cretaceous-Albian stage (modified from Fisher and Rodda 1969). Study area in red box. Lower figure displays a schematic cross section of A–A' with the Kirschberg Lagoon deposits dominated by mudstone to skeletal–fenestral wackestone facies with scattered rudist biostromes (modified from Tucker and Wright 1990).

4.4.2. Description of the mason exposures in Central Texas

The Edwards Plateau covers approximately 61,500 km2 and consists of nearly flat-lying limestone and dolomite covered by modern soils (Barker et al. 1994). The study area (Figure 4.1b) has outcrops exposed along an elongate hill formed mainly of three stratigraphic units that are summarized in Figure 4.2. The Proterozoic basement is generally granite and metamorphic units overlain by a basal conglomerate and then a fining-upward succession of the Lower Cretaceous Hensel Formation (Figure 4.3a). The Fort Terrett Formation was deposited mostly conformably on the Hensel Formation with a little evidence of an erosional surface or paleosoil between the two. In the study area, the Fort Terrett Formation can be sub-divided into a lower member consisting of three, meter-scale depositional cycles (1, 2, and 3); a middle member consisting of cycles 4, 5, and 6, and an upper member consisting of cycles 7 and 8.

4.5. Methodology

Seven measured sections were described bed-by-bed using Dunham's (1962) classification. Total gamma-ray measurements were determined using a RS-230 handheld gamma-ray spectrometer at 30-cm increments. In addition, 67 hand-samples were collected for petrographic and geochemical analysis. Alizarin-red S was used to partially stain the thin-sections in order to distinguish dolomite (unstained) from calcite (red-stained).

High-resolution photomicrographs were obtained to illustrate sedimentological and diagenetic features. Dolomite crystal size was measured to determine textural maturity. ImageJ software with jPOR plug-ins was used to measure total thin-section porosity (Grove and Jerram 2011). Fenestrae observed in thin-section were also measured and quantified to determine initial porosity. Cathodoluminescence (CL) petrography was performed using a Technosyn Cold

Cathode Luminescence Model 8200 MKII to determine the dolomite compositional variation and crystal evolution.

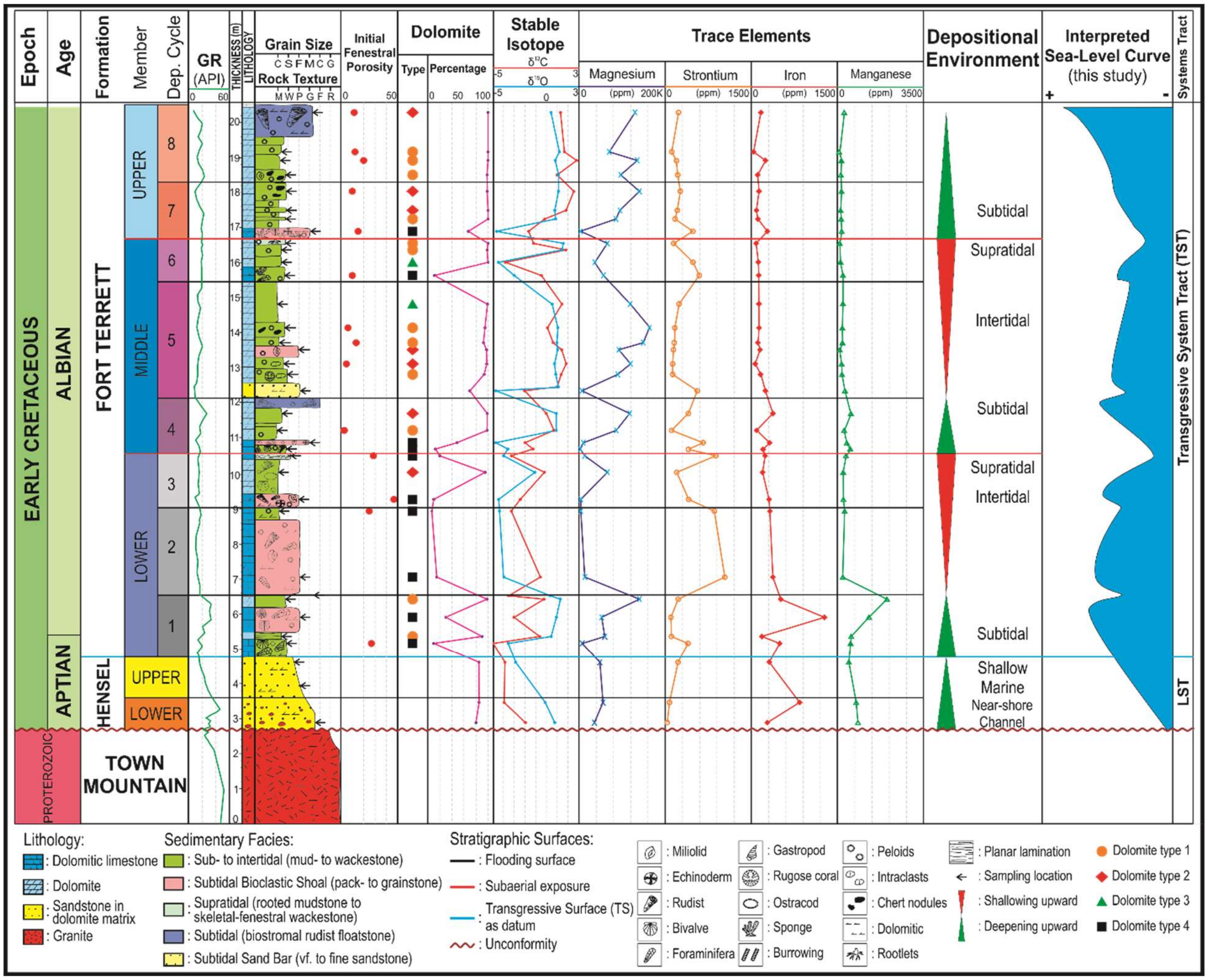

Figure 4.2. Composite measured section of the Mason succession, showing stratigraphy, dolomite percentage, initial fenestral porosity, geochemical analysis, and interpreted depositional environments and sea-level fluctuations. The frequency of initial fenestral porosity, geochemical analysis, and interpreted depositional environments and sea-level fluctuations. The frequency of initial fenestral porosity increases upwards in conjunction with an increase in dolomite percentage. Partially dolomitized beds are abundant in the lower part of the formation. Upward-decreasing Fe and Mn contents are also noticeable.

For stable isotope analysis, powdered whole-rock samples were analyzed for carbon ($\delta^{13}C$) and oxygen ($\delta^{18}O$) isotopes in a Kiel IV carbonate device coupled to a Thermo-Scientific MAT 253 isotope ratio mass spectrometer in the Stable Isotope Geosciences Facility at Texas A&M University. The results are reported in VPDB standard with analytical precision of 0.04‰ for $\delta^{13}C$ and 0.08‰ for $\delta^{18}O$.

Major and trace element analyses including strontium (Sr), manganese (Mn), and iron (Fe), reported in parts per million (ppm), were determined by an ICP-MS in the Radiogenic Isotope Geosciences Laboratory of Texas A&M University. Precision of major and trace element analysis was 0.001 ppm for Sr, 0.003 ppm for Mn and 0.03 ppm for Fe.

4.6. Facies analysis

Seven facies are described for the Hensel and Fort Terrett Formations based on lithological features such as composition, grain size, bedding characteristics, sedimentary structures, and fossil content, based on both field observations and petrographic analysis (Table 1). Interpreted depositional environments for each facies are presented.

4.6.1. Hensel Formation facies

The Hensel Formation is a fining-upward succession of conglomeratic to very fine sandstone that was deposited unconformably on the Proterozoic basement. Two facies are defined in this formation.

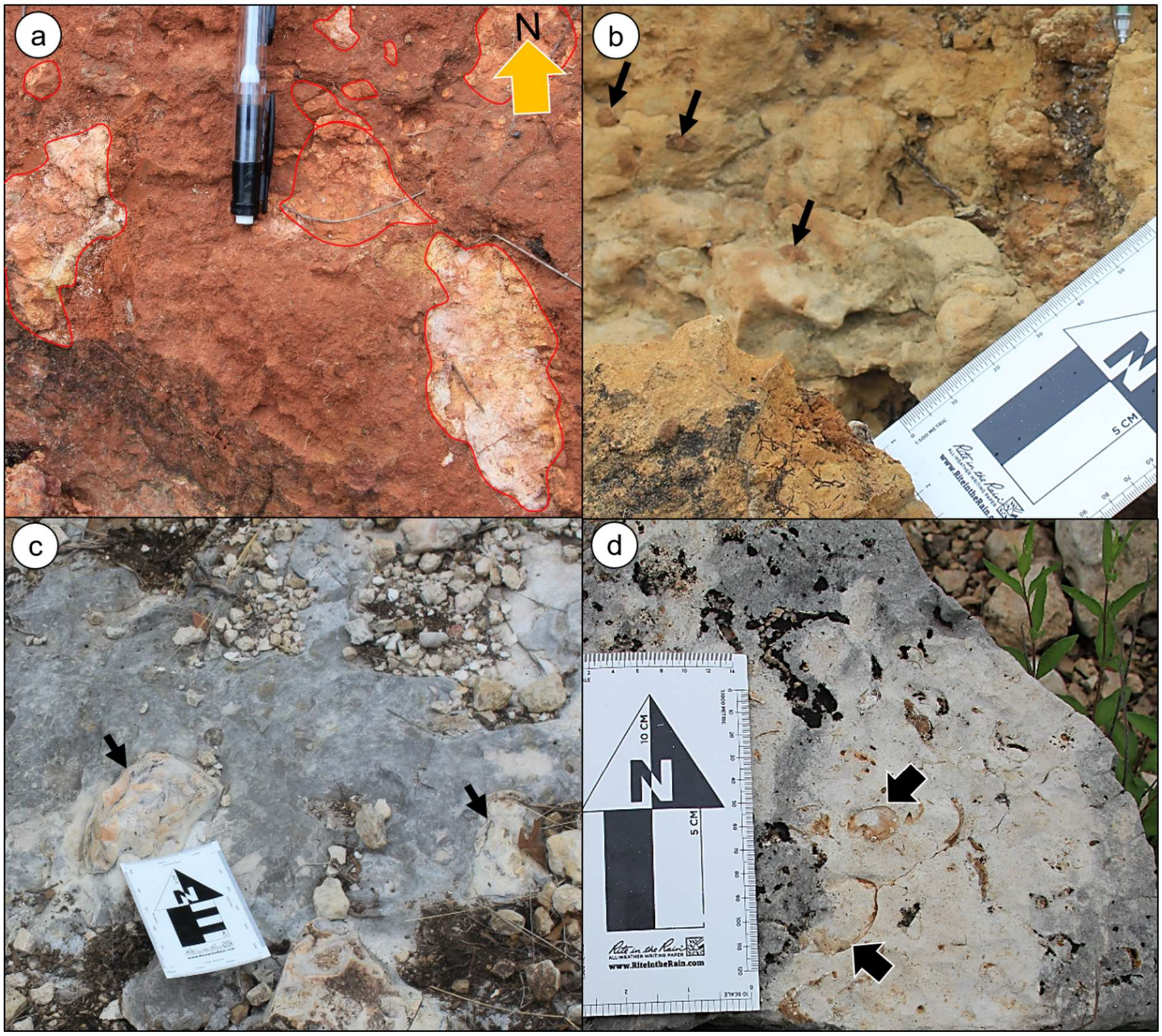

Figure 4.3. General view of Hensel and Fort Terrett Formations in Mason County. a. Fining-upward conglomeratic to dolomitic fine sandstone of the Hensel Formation. b. Burrows (black arrows) in shallow marine mudstone, base of the Fort Terrett Formation. C. Chert-nodule (arrows) in partially dolomitized mudstone to skeletal–fenestral wackestone facies. d. Rudist floatstone with moldic porosity mainly of *Exogyra texana* (arrows), floating in microcrystalline dolomite matrix.

4.6.1.1. Conglomeratic to medium sandstone (near-shore fluvial channel facies)

The lower member of the Hensel Formation is a brownish-grey, conglomeratic to medium sandstone whose thickness ranges from 1 to 1.1 m. Granule to pebble-size granitic and metamorphic rock fragments occur at the base of the succession immediately above the contact with the basement. The upper part of this unit consists of fine-to-medium, subangular to well-rounded quartz grains (~30%), floating in sucrosic crystalline dolomite. This facies has intercrystalline porosity up to 14% and is interpreted to have been deposited in a near-shore fluvial channel setting.

4.6.1.2. Very fine to medium sandstone (shallow-marine facies)

The upper member of the Hensel Formation is a brownish-grey, fining-upward unit of medium to very fine sandstone whose thickness ranges from 1 to 2.1 m. Petrographically, this unit consists of very fine to medium, subangular to well-rounded and poorly sorted quartz grains (~20%), floating in a mosaic of sucrosic crystalline dolomite with ~7% intercrystalline porosity. This member was deposited in a shallow-marine setting based on the finer grains floating in carbonate-mud that was later replaced by dolomite.

Table 4.1. Facies analysis, brief description, grain components, and interpreted depositional environments of the Hensel and Fort Terrett Formations

Facies Name	Description	Components	Interpreted Depositional Environment
Fort Terrett Formation			
Rooted mudstone to skeletal-fenestral wackestone	Light brown colour, partially to completely dolomitised, thickness 10 to 30 cm. Exposure features common.	Radiolitid rudist (~7%), ostracod (~5%), gastropod (~3%), miliolid (~1%), dasyclad green algae, planktonic foraminifera, rootlet structures and variously-sized peloids.	Intertidal-Supratidal
Skeletal-fenestral mudstone-wackestone	Dullish brown, relatively homogeneous with streaks of brownish orange, partially to completely dolomitised, thickness 10 to 240 cm. Chert nodules in the upper and middle member, bioturbation and parallel lamination on the base of the formation.	Radiolitid rudist (~12%), miliolid (~7%), gastropod (~5%), dasyclad green algae, equivalved-megalodontid bivalve, foraminiferas, peloids (~10%), aggregate grains and very fine to fine quartz (~3%)	Intertidal-subtidal
Rudist floatstone	Brownish grey, completely dolomitised, thickness 50 to 200 cm.	*Exogyra texana* and radiolitid rudist common floating in very fine to fine sucrosic dolomite matrix	Subtidal
Skeletal packstone-grainstone	Dullish to milky brown, thickness 10 to 260 cm and partially to completely dolomitised.	Radiolitid rudist (~15%), ostracod (~10%), miliolids (~7%), echinoderm (~3%), foraminifera (~2%), peloids (~5%) and aggregate grains (~30%), intraclasts and very fine to fine quartz (~1%).	High-energy subtidal shoal
Very fine to fine sandstone	Brownish grey with thickness 18 cm, parallel lamination.	Very fine to fine quartz (~30%) floating in dolomite microcrystalline cement, subangular to well-rounded, poorly sorted and loose packing.	Subtidal sand-bar
Hensel Formation			
Very fine to medium sandstone	Fining-upward, brownish grey to brownish red, subangular to well-rounded quartz shape, poorly sorted.	Very fine to medium quartz (~20%), floating in dolomite microcrystalline cement	Shallow marine
Conglomeratic to medium sandstone	Fining-upward, brownish grey, granule to pebble size of granite clasts on the contact to the basement. Subangular to well-rounded quartz shape, poorly sorted and loose packing.	Fine to coarse quartz grains (~30%), floating in dolomite microcrystalline cement	Near-shore fluvial channel

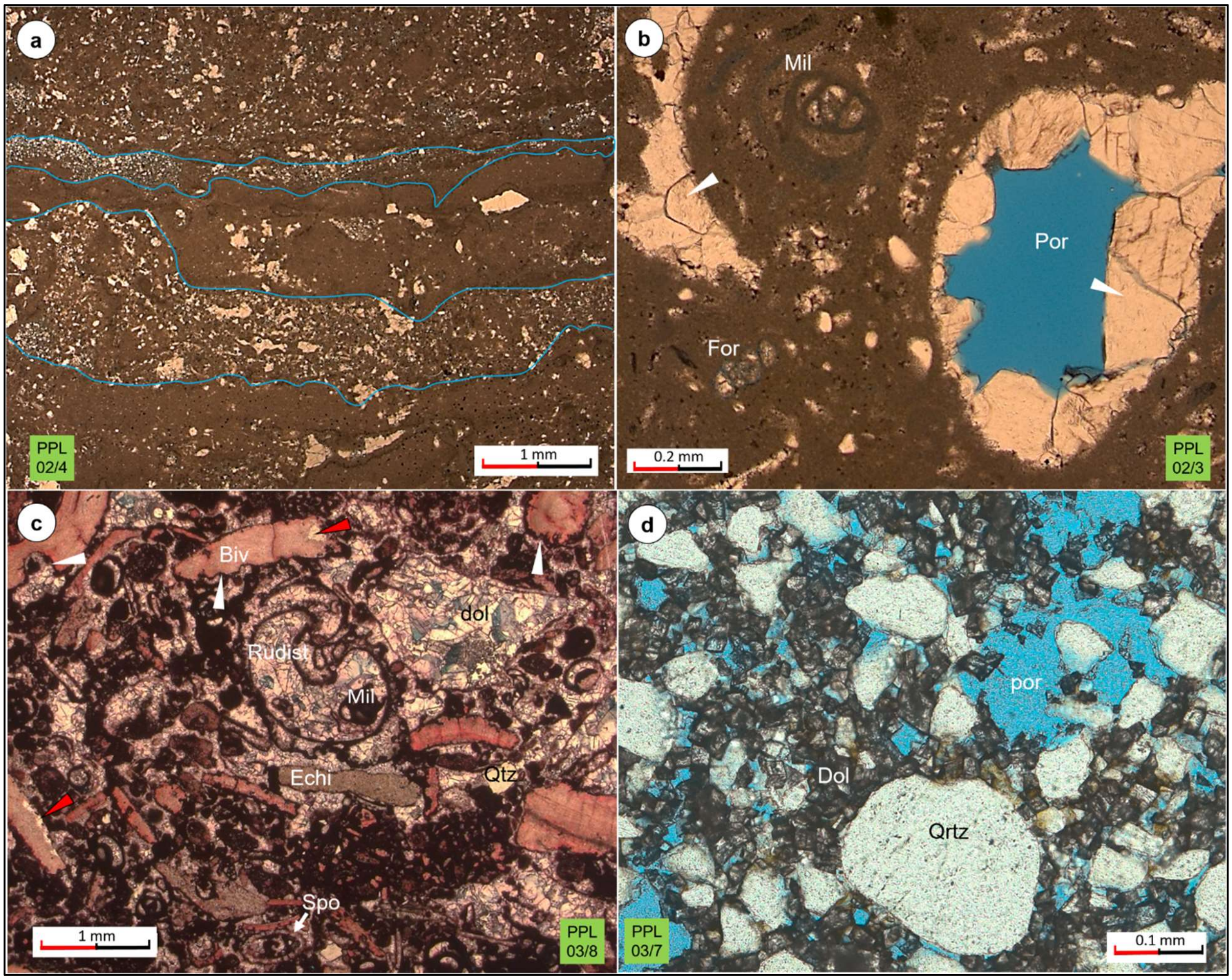

Figure 4.4. Photomicrographs of the Fort Terrett Formation facies. a. Fenestrae filled by internal sediment and dolomite (delineated by blue polygons) in partially dolomitized wackestone. b. Blocky mosaic dolomite cement (white arrows) partially to completely filling moldic pores in partially dolomitized skeletal–fenestral wackestone. Micrite-walled miliolid foraminifera (Mil) and foraminifera (For) are partially dissolved. c. Skeletal grainstone shows calcitic bivalve shell (Biv) fragments with irregular micrite envelopes (white arrows) caused by microboring organisms. Void within a rudist shell filled by miliolid foraminifera (Mil) and dolomite cement. Other grains are echinoderm (Echi), sponge (Spo), and quartz grains (Qtz) cemented by dolomite. d. Subangular to well-rounded, poorly sorted, very fine to fine quartz grains (Qtz) floating in dolomite cement. Note that slides c and d are stained by alizarin Red S. Por porosity, dol dolomite, XPL cross-polarized light, PPL plain-polarized light.

4.6.2. Fort Terrett Formation facies

The Fort Terrett Formation has five carbonate facies dominated by fenestral mudstone–wackestone that are grouped into five facies associations. It also has minor intervals of bioclastic packstone–grainstone.

4.6.2. 1. Rooted mudstone to skeletal–fenestral wackestone (intertidal–supratidal facies)

This facies is light brown, partially to completely dolomitized skeletal wackestone, consisting mainly of carbonate mud with minor bioclastics such as calcitic radiolitid rudists (~7%), ostracods (~5%), gastropods (~3%), miliolid foraminifera (~1%), a few *Dasyclad* green algae (<1%) and planktic foraminifera. This facies also contains variously sized peloids and rootlets. This facies ranges in thickness from 10 to 30 cm. Fine to very fine dolomite crystals occur in partially dolomitized skeletal wackestone as planar to non-planar porphyrotopic cement, whereas completely dolomitized wackestone shows rootlets (~4% by volume) and peloids as grains floating in sucrosic dolomite.

Micrite envelopes and dolomite replacement (partially or completely) of calcitic rudists, miliolid foraminifera, ostracods, and planktic foraminifera are common and dolomite cementation occurred in some skeletal chambers. The chambers of micritic rootlets were filled by dolomite cement.

Porosity in this facies consists of primary porosity, such as elongate well-connected fenestral pores (15%), and secondary porosity including moldic and fracture porosity. Initial voids were partially or completely filled by muddy or silty sediment and then cemented by dolomite with planar crystal boundaries (Figure 4.4a). Intercrystalline porosity up to 10% occurs in completely dolomitized skeletal wackestone.

The presence of rare rootlets indicates subaerial exposure long enough to develop terrestrial plants with well-established root systems. Bioclastic fragments in this facies indicate that seawater intermittently flooded the area. The association of fenestral fabrics, rootlets and assorted bioclastic grains suggests that deposition occurred in an intertidal– supratidal setting susceptible to episodic dry and wet periods.

4.6.2.2. Skeletal-fenestral mudstone-wackestone (intertidal-subtidal facies)

Skeletal–fenestral mudstone–wackestone facies is dullish brown, relatively homogeneous with streaks of brownish orange oxidation and partially to completely dolomitized (Figure 4.4b). The thickness of this facies varies from 10 to 240 cm. Irregular chert nodules ranging from 4 to 15 cm in diameter occur in the middle and upper members. Bioturbated mudstone near the base of the formation contains rare Teichichnus ichnogenera in addition to rare parallel lamination. Moldic (14%) and fenestral (12%) porosity is common in this facies.

The skeletal grains in this facies include calcitic rudist fragments (~12%), miliolid foraminifera (~7%), gastropods (~5%), and minor (<1%) dasyclad green algae, calcitic bivalves, and multi-chambered-uniserial foraminifera. Non-skeletal grains consist of variously sized peloids (~10%), aggregate grains, and fine quartz grains (~3%) in a muddy carbonate matrix. Very fine to coarse dolomite crystals (5–250 μm) with planar to non-planar porphyrotopic crystal boundaries are scattered in the mud. The depositional environment of this facies is interpreted to have been a low-energy, intertidal to shallow subtidal zone with a muddy substrate (Flügel 2004).

4.6.2.3. Rudist floatstone (subtidal facies)

Rudist floatstone is brownish-grey, completely dolomitized and occurs as an isolated unit, 50–200 cm thick. Common *Exogyra texana* and radiolitid rudists occur as the main bioclasts in this facies, floating in a fine to very fine sucrosic dolomite matrix (Figure 4.3d). Porosity types in this facies are predominantly moldic (~12%) and intercrystalline (13%). Biomoldic porosity was formed by rudist shell dissolution with molds locally filled by dolomite cement. The distribution of this facies indicates that the rudist colonies grew in relatively small, isolated, and scattered areas in a shallow subtidal setting within a lagoon with a water depth probably no more than 5 m; this resulted in an isolated biostromal facies.

4.6.2.4. Skeletal packstone-grainstone (high-energy subtidal shoal facies)

The skeletal packstone–grainstone is dull to milky brown and partially to completely dolomitized; bed thickness ranges from 10 to 260 cm. The packstone consists of mixed skeletal grains and fragments: rudists (~15%), miliolid foraminifera (~7%), rare benthic–planktic foraminifera and non-skeletal grains, peloids (~5%) and a few aggregate grains, within a minor carbonate matrix. Selective silica replacement of aragonitic rudist shells occurs in this facies.

The skeletal grainstone is composed of radiolitid rudists (~12%), ostracods (~10%), miliolid foraminifera (~7%), echinoderms (~3%), planktic foraminifera (~2%), and unidentifiable skeletal grains. Non-skeletal grains are peloids (~30%), aggregate grains (~5%), intraclasts and very fine to fine quartz grains (~1%). All grains are cemented by dolomite.

Micrite envelopes occur on some bioclasts produced by microborers whereas other grains show partially to complete dolomite replacement. Dolomite cement fills some skeletal chambers (Figure 4.4c). Peloids are mainly composed of calcitic mud and locally were replaced by dolomite whereas others were dissolved to give a moldic porosity. Very fine to coarse dolomite crystals (4–670 μm) are scattered with planar to non-planar crystal boundaries and a porphyrotopic texture in some samples. Common porosity types for this facies are fenestral (14%), intercrystalline (12%), moldic (3%), and fracture (<1%), and these pores were partially to completely filled by dolomite cement with planar crystal boundaries. These packstone and grainstone facies were deposited in a high-energy subtidal shoal, based on the abundance and diversity of the skeletal grains and the lack of mud.

4.6.2.5. Very fine to fine sandstone (subtidal sand-bar facies)

A single bed of brownish-grey sandstone (18 cm thick and less than 15 m in lateral extent) contains very fine to fine quartz grains (~30%), floating in a dolomite crystalline matrix. The grains are subangular to well-rounded, poorly sorted with a loose packing; there is an intercrystalline porosity up to 11% (Figure 4.4d).

4.7. Dolomite types

The textural classification proposed by Sibley and Gregg (1987) and adapted by Machel (2004) was used to identify different types of dolomite in the Fort Terrett Formation. In addition, a modified grain-size scale for authigenic constituents was applied to determine the dolomite crystal size (Folk 1974). For consistency in this article, the term aphanocrystalline is modified to micro, for crystals less than 0.004 mm or 4 μm. The criteria used to classify dolomite components in the Hensel and Fort Terrett Formations are crystal size, distribution and boundary shape. These elements were chosen with the purpose of characterizing dolomite crystal maturity (Tables 2 and 3).

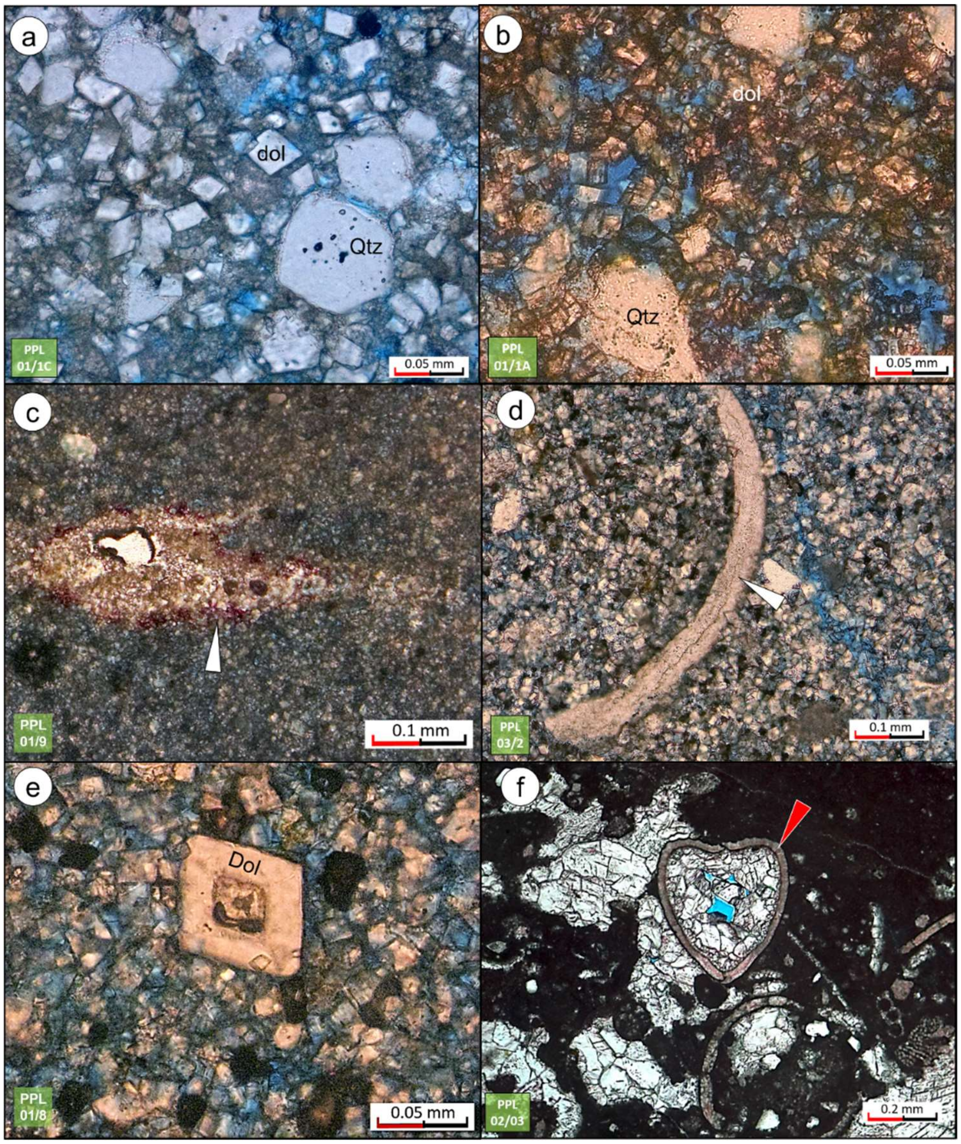

Figure 4.5. Dolomite within the Hensel (a, b) and Fort Terrett Formations (c–f). a. Micro- to fine dolomite crystals in fine to medium sandstone of the upper member of the Hensel Formation. b. Very fine to medium dolomite crystals in conglomeratic to medium sandstone of the Lower Hensel Formation. c. Type 1 dolomite shows a micro- to very fine crystal size with calcite cement around the fenestrae (white arrow). d. Type 2 dolomite has a very fine to fine crystal size with selective preservation of a low-Mg calcitic bivalve (white arrow). e. Type 3 dolomite shows very fine to medium overgrowths with multiple internal zones. f. Type 4 dolomite is a cement with a micro- to coarse crystal size filling voids inside a high-Mg calcite bivalve (red arrow) and within the lime-mud. Note that slides b, c, and f are stained with alizarin Red S. PPL plane-polarized light, Qtz quartz, dol dolomite.

4.7.1. Hensel Formation dolomite

The Hensel Formation shows very fine to coarse quartz grains floating in a sucrosic mosaic dolomite of micro to medium size, a polymodal crystal-size distribution, of planar euhedral to subhedral crystal boundaries, locally having cloudy centers and CL-zoning (Table 2). The conglomeratic lower Hensel Formation has a fine to medium sandstone and dolomite matrix with crystal size ranging from 3 to 30 μm. In contrast, the upper member of the Hensel Formation has very similar features but a much coarser dolomite crystal size of 6–80 μm and crystals with cloudy centers caused by mineral inclusions and CL-zoning (Figure 4.5a, b).

4.7.2. Fort Terrett Formation dolomite

Dolomite in the Fort Terrett Formation can be classified into four types (Table 4.3). The main criteria to identify textural maturity is the increasing crystal size (Table 4.3, lower figure), which can be interpreted to indicate decreasing saturation state of dolomitizing brines (Sibley and Gregg 1987). Type 1 dolomite is the most common and it is normally abundant in fully dolomitized facies (Figure 4.2). In contrast, type 3 is scarce in the succession.

Table 4.2. Dolomite characterization of the Lower and Upper members of the Hensel Formation.

		Fort Terrett Formation			
No	**Category**	**Type 1**	**Type 2**	**Type 3**	**Type 4**
1	Dolomite Classification and Evolution	Micro to very fine dolomite	Very fine to fine dolomite	Very fine to medium overgrowth dolomite	Micro to coarse dolomite cement
2	Crystal size (μm)*				
	- Minimum	1.5	2	5	2
	- Maximum	35	40	65	670
	- Mean	7	10	21	50
3	Crystal size category	micro to fine	very fine to fine	very fine to medium	micro to coarse
4	Crystal size distribution	polymodal	polymodal	polymodal	polymodal
5	Crystal boundary shape	planar subhedral to nonplanar anhedral	planar euhedral to subhedral	planar euhedral to subhedral	planar to nonplanar porphyrotopic to planar cement
6	Mimetic vs nonmimetic	nonmimetic to mimetic	mimetic	mostly nonmimetic	-
8	Cloudy center	No	No	mostly cloudy center	No
9	Mean porosity (%)				
	- Intercrystalline	10	13	13	-
	- Moldic	9	4	11	-
	- Fenestral	8	9	-	21.5
10	Others	calcite cement around the moldic pores	calcitic shell and fragment are preserved	zoning (cement overgrowth), completely dolomitized	pores filled by dolomite cement

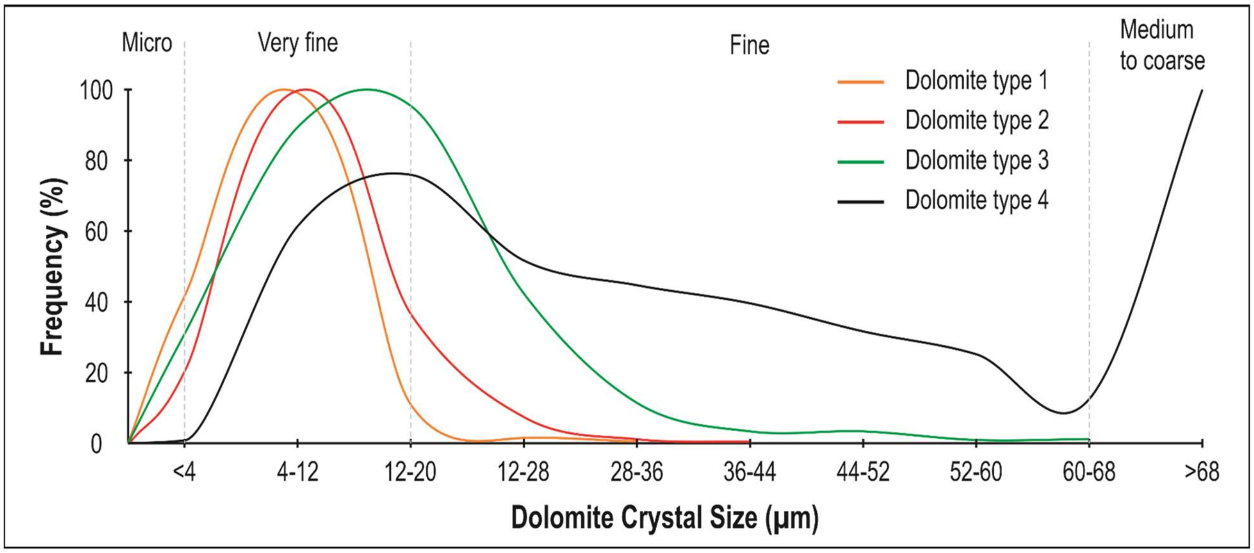

Table 4.3.Upper table of dolomite characterization for the Fort Terrett Formation shows increasing maturity of texture and evolution. Lower figure exhibits the distribution of dolomite crystal size for all dolomite types; increasing crystal size is shown by the increasing peak of frequency towards a coarser crystal size.

		Fort Terrett Formation			
No	**Category**	**Type 1**	**Type 2**	**Type 3**	**Type 4**
1	Dolomite Classification and Evolution	Micro to very fine dolomite	Very fine to fine dolomite	Very fine to medium overgrowth dolomite	Micro to coarse dolomite cement
2	Crystal size (μm)*				
	- Minimum	1.5	2	5	2
	- Maximum	35	40	65	670
	- Mean	7	10	21	50
3	Crystal size category	micro to fine	very fine to fine	very fine to medium	micro to coarse
4	Crystal size distribution	polymodal	polymodal	polymodal	polymodal
5	Crystal boundary shape	planar subhedral to nonplanar anhedral	planar euhedral to subhedral	planar euhedral to subhedral	planar to nonplanar porphyrotopic to planar cement
6	Mimetic vs nonmimetic	nonmimetic to mimetic	mimetic	mostly nonmimetic	-
8	Cloudy center	No	No	mostly cloudy center	No
9	Mean porosity (%)				
	- Intercrystalline	10	13	13	-
	- Moldic	9	4	11	-
	- Fenestral	8	9	-	21.5
10	Others	calcite cement around the moldic pores	calcitic shell and fragment are preserved	zoning (cement overgrowth), completely dolomitized	pores filled by dolomite cement

4.7.2.1. Type 1: first stage of dolomitization

The initial dolomite crystals have a micro- to fine crystal size (1.5–35 μm with a mean of 7 μm), a polymodal size distribution, planar subhedral to non-planar anhedral crystal boundaries, and mimetic to non-mimetic fabric preservation (Figure 4.5c). This is the most common dolomite type within the succession and is normally associated with mudstone to skeletal wackestone facies. This dolomite was likely the initial product of an early replacement dolomitization (cf. Saller and Henderson 2001; Jones and Xiao 2005).

4.7.2.2. Type 2: second stage of dolomitization

The second-stage dolomite crystals are very fine to fine crystals (2–40 µm with mean of 10 µm) that have a polymodal crystal-size distribution, planar euhedral to planar subhedral crystal boundaries, and mimetic fabric preservation. Crystal appearance is clean with no cloudy centers or zonation (Figure 4.5d). The larger crystal size of this dolomite type is likely the result of the continuation of the replacement process of the initial stage (cf. Saller and Henderson 2001; Jones and Xiao 2005).

4.7.2.3. Type 3: overgrowth dolomite

Overgrowth dolomite has a very fine to medium crystal size (5–65 µm with mean of 21 µm), polymodal size distribution, planar euhedral to planar subhedral crystal boundaries, and a mostly non-mimetic texture. This type of dolomite commonly has recognizable fluid inclusion-rich cloudy centers with multiple CL-overgrowth zones (Figure 4.5e). This type of dolomite may represent a post-replacement or overdolomitization process (cf. Saller and Henderson 2001; Jones and Xiao 2005).

4.7.2.4. Type 4: coarse dolomite cement

Coarse dolomite cements have a micro- to coarse crystal size (2–670 µm with a mean of 50 µm), and polymodal crystal-size distribution; they fill voids and pore spaces, mainly intraskeletal and fenestrae (Figure 4.5f). This type of dolomite is common in partially dolomitized skeletal wackestone to grainstone facies.

4.8. Geochemistry

4.8.1. Stable isotope geochemistry

$\delta^{18}O$ values for the Hensel and Fort Terrett Formations range from −4.7 to +1.7‰ and $\delta^{13}C$ varies from −5.0 to +2.6‰ (Figure 4.7a). Dolomite crystals from both lower and upper members of the Hensel Formation have negative $\delta^{13}C$ values of −3.9 to −1.1‰.

Isotopic data for the Fort Terrett Formation show a distinct clustering of values that can be assigned to two groups. Group 1 dolomites (red polygon, Figure 4.7a) have negative values in both $\delta^{18}O$ (−4.7 to −3.1‰) and $\delta^{13}C$ (−5.0 to −0.3‰), and consist dominantly of type 4 dolomite (dolomite cement). Group 2 dolomites (blue polygon) show more scattered positive values in $\delta^{18}O$ (−0.1 to +1.7‰) and a large variation in $\delta^{13}C$ (−4.0 to +2.6‰).

$\delta^{13}C$ values of type 1 dolomite range from −2.3 to +1.9‰. Type 2 dolomite is enriched in ^{13}C with values ranging from +1.1 to +2.5‰. Type 3 dolomite has a broad range of carbon isotopic values from −3.6 to +2.6‰. Type 4 dolomite has a narrow range from +1.2 to +1.4‰.

4.8.2. Major and trace element data

The dolomites of the Lower Edwards Group have distinct Fe and Mn concentrations from 36 to 1273 ppm Fe and 62 to 3279 ppm Mn (Figure 4.7b), which in the cross-plot, show a positive correlation. On average, there is nearly two times more Fe within the Hensel Formation dolomites (average 462 ppm, range 278–842 ppm) compared to the Fort Terrett Formation (average 240 ppm, range 36–1273 ppm), whereas nearly three times more Mn in the Hensel Formation dolomites (average 1170 ppm, range 754–2224 ppm) than the Fort Terrett Formation (average 363 ppm, range 62–3279 ppm).

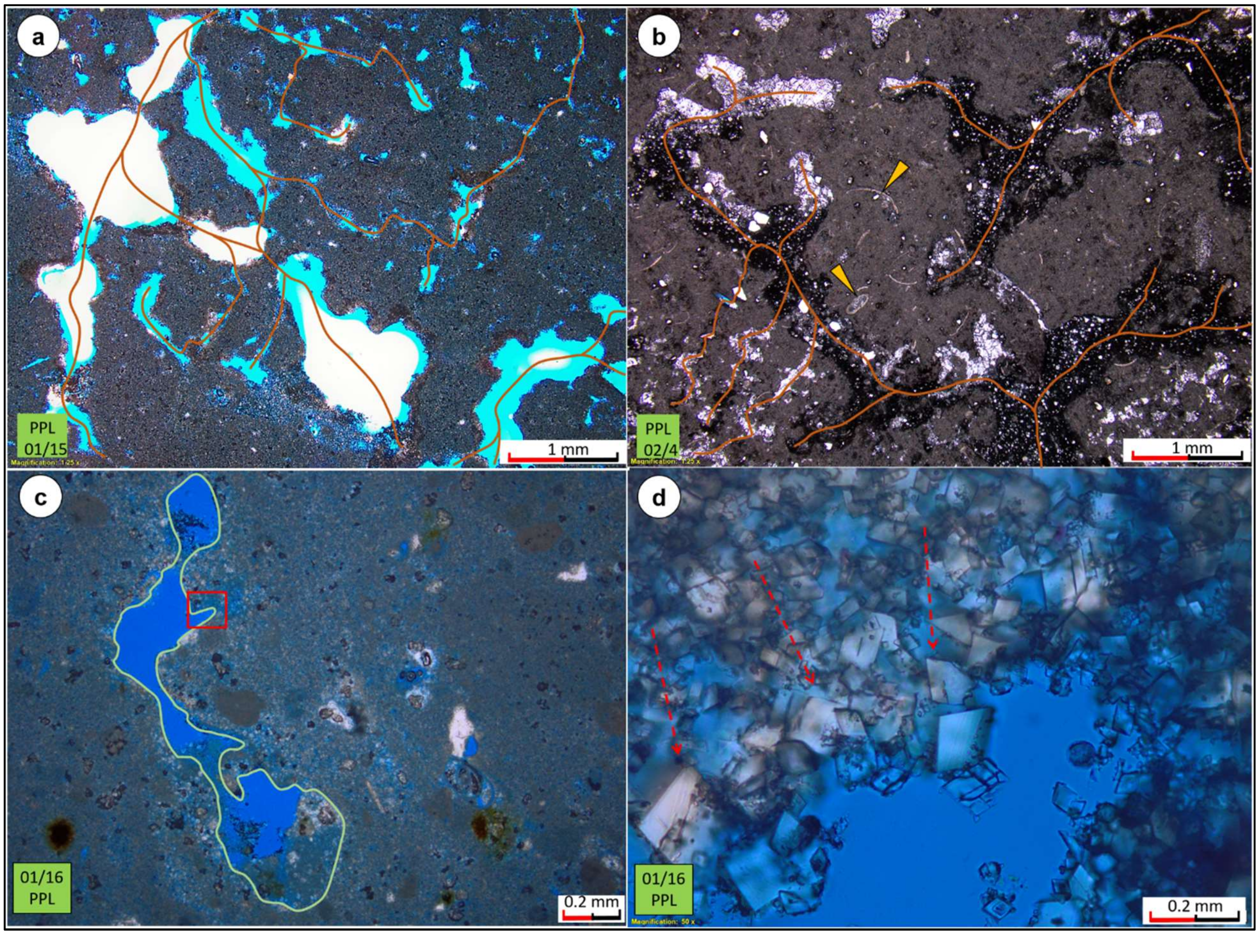

Figure 4.6. a. Photomicrographs from the upper member of Fort Terrett Formation shows 26% fenestrae and 100% dolomite. b. Fenestrae filled by mud to silt sediment (darker color in the fenestrae) and cemented by dolomite (white to grey in the fenestrae). It shows initial porosity of 23% with 8% dolomite. c. Photomicrograph of fenestral (light green polygon) and moldic (orange polygon) porosity. The red box contains a detailed view of the area for image d. d. Increasing dolomite crystal size from 1–4 to 9–25 µm towards the fenestral porosity (pointed by red arrows). Note that slides a and b are stained with alizarin Red S. The orange lines are possible flow paths of dolomitizing brines through fenestral bodies. PPL plain-polarized light.

Sr concentrations are in the typical range for dolomite forming from marine fluids which is up to 600 ppm (Land 1973), although, there is one high value of 1039 ppm for skeletal packstone facies. The average value of the Fort Terrett Formation is 295 ppm, nearly three times that of the Hensel Formation (average 109 ppm). Plotting Sr against Fe + Mn concentrations suggests an enrichment of Sr concentration for dolomite type 4, up to 1039 ppm (Figure 4.7c). A negative correlation (in red polygons) indicates that Sr was lost during diagenesis (Veizer 1983; Grossman 2012).

4.9. Discussion

4.9.1. Depositional facies and stratigraphy

A stratigraphic cross section of the Hensel and Fort Terrett Formations (Figure 4.8) in Mason County shows westward thickening strata, interpreted cycles, unconformities, stacking patterns, facies variations, and a transgressive surface (TS). The Hensel Formation has two fining-upward sandstone cycles that are differentiated by grain size. These sandstones were deposited in a coastal to nearshore marine environment; the carbonate-rich muddy matrix of the sandstone was later replaced by dolomite. The basal conglomeratic sandstone of this unit only occurs in local topographic lows.

Eight, mostly shallowing-upward meter-scale cycles (Figs. 2, 8) can be recognized in the Fort Terrett succession based on muddy-grainy facies variation and the fluctuation of total GR log. These cycles consist of peritidal facies with supra-, inter-, and subtidal deposits. Muddy facies contain bioclasts of gastropod, miliolid foraminifera, and other foraminifera. Bioturbation, fenestrae, and rootlet structures in this facies indicate deposition in a tidal-flat environment.

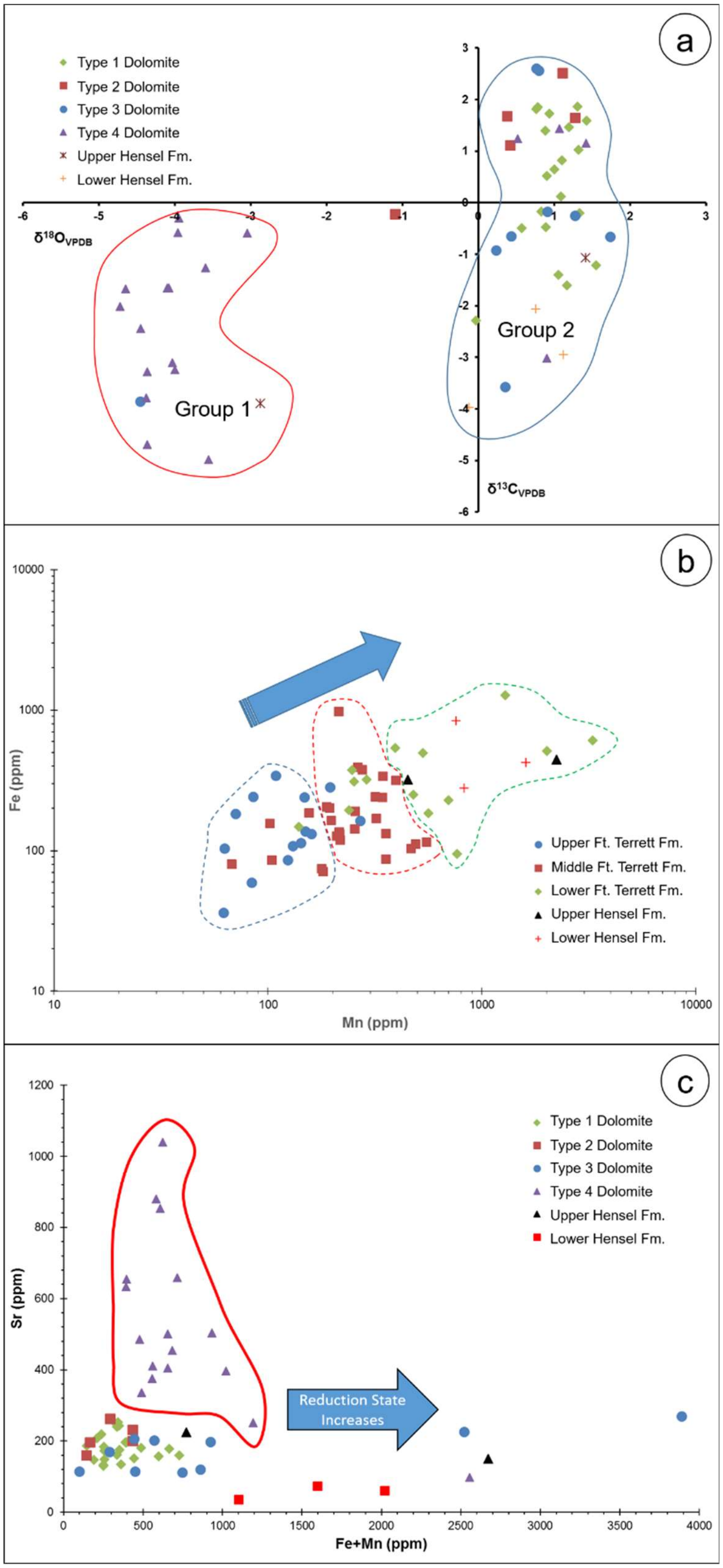
a
Type 1 Dolomite
Type 2 Dolomite
Type 3 Dolomite
Type 4 Dolomite
Upper Hensel Fm.
Lower Hensel Fm.
Group 1
Group 2
δ18OVPDB
δ13CVPDB
-6
-5
-4
-3
-2
-1
0
1
2
3
-6
-5
-4
-3
-2
-1
0
1
2
3
b
Upper Ft. Terrett Fm.
Middle Ft. Terrett Fm.
Lower Ft. Terrett Fm.
Upper Hensel Fm.
Lower Hensel Fm.
Fe (ppm)
Mn (ppm)
10
100
1000
10000
10
100
1000
10000
c
Type 1 Dolomite
Type 2 Dolomite
Type 3 Dolomite
Type 4 Dolomite
Upper Hensel Fm.
Lower Hensel Fm.
Reduction State Increases
Sr (ppm)
Fe+Mn (ppm)
0
200
400
600
800
1000
1200
0
500
1000
1500
2000
2500
3000
3500
4000

Figure 4.7. a. Cross-plot of $\delta^{18}O$ and $\delta^{13}C$ values from the Hensel and Fort Terrett Formations. Group 1 (red polygon) relates to Miocene to Recent diagenetic products and group 2 (blue polygon) indicates Cretaceous diagenetic effects. b. Fe and Mn cross-plot of Hensel and Fort Terrett Formations showing covarying values. The lower member of the Fort Terrett Formation (green polygon) is more enriched in Fe and Mn compared to the Middle (red polygon) and Lower members (blue polygon). c. Cross-plot of Sr against Fe + Mn showing negative correlation (in red polygons) which implies that Sr was being lost with burial. Note the elevated Sr concentrations for type 4 dolomite (in red polygon).

Multiple flooding surfaces in the Fort Terrett Formation suggest that there were numerous low-amplitude sea-level variations during deposition of this unit, which is typical for the greenhouse times of the Cretaceous. Much of the study area was located within a low-energy lagoon, which repeatedly developed supratidal–intertidal facies where fenestral porosity and vegetation formed during subaerial exposure. Intertidal facies grade upward to the rudist floatstone, suggesting the area was locally deepening to a subtidal setting. Interbedded within the succession, a fine-grained sandbar facies is present, indicating a local sea-level fall with sporadic siliciclastic sediment input from nearby exposed Precambrian basement.

4.9.2. Porosity systems

4.9.2.1. Initial porosity system

It was not possible to quantify or assess the initial interparticle porosity (microporosity in the muddy facies) since most of this type of porosity was lost during compaction or early lithification. Fenestrae are common features in peritidal deposits and during deposition and shallow burial, before compaction, these structures created significant pore space. In this succession, this type of porosity was mostly filled by cement or fine-grained sediment, but locally the pore-space remained open (Figure 4.6). Fenestrae have different geometries including laminar-elongate, spherical and irregular shapes that locally are interconnected (Shinn 1968; Shinn and

Robbin 1983; Choquette and Pray 1970; Grover and Read 1978; Bain and Kindler 1994; Scholle and Ulmer-Scholle 2003; Mazzullo and Birdwell 1989; Mazzullo 2004; Flügel 2004). It is suggested here that fenestral porosity may have had a significant impact in the passage and flow of dolomitizing fluids through the sediment. For this reason, image analysis was used to calculate initial fenestral porosity to quantify original void percentage; this ranged from 2 to 46%.

4.9.2.2. Secondary porosity system

Two main types of secondary porosity, intercrystalline and moldic, occur in the Fort Terrett Formation. Intercrystalline porosity was identified in all dolomitic intervals of the Hensel and Fort Terrett Formations. The lower member of the Hensel Formation has a porosity from 7.5 to 14%, whereas the upper member has 5.5–7%. Conversely, the Fort Terrett Formation has a highly variable porosity, ranging from 1 to 22% with an average of 12%. The pore size is also very variable from micron-scale to several hundreds of microns. Moldic porosity in the Fort Terrett Formation ranges from 1 to 19% with an average of 7%. This type of porosity was a result of the dissolution of rudists, gastropods, miliolid foraminifera, and peloids that produced voids with a spherical shape, common in the skeletal–fenestral wackestone to grainstone facies.

4.9.3. Diagenetic processes and paragenesis

Paragenesis can be interpreted from different approaches including petrography and geochemistry, especially stable isotope analysis (Figure 4.7a). The interpretation here is similar to previous studies concerning diagenetic alteration of Edwards Group sediments (Mench et al. 1980; Ellis 1986). The isotope data show a clustering into two groups, one with positive $\delta^{18}O$ and relatively scattered $\delta^{13}C$. This group can be interpreted as the result of diagenetic alteration, probably during marine to shallow-burial in the Late Cretaceous. The second cluster, with more negative $\delta^{18}O$ and $\delta^{13}C$, was likely associated with Miocene-Recent burial and subsequent uplift.

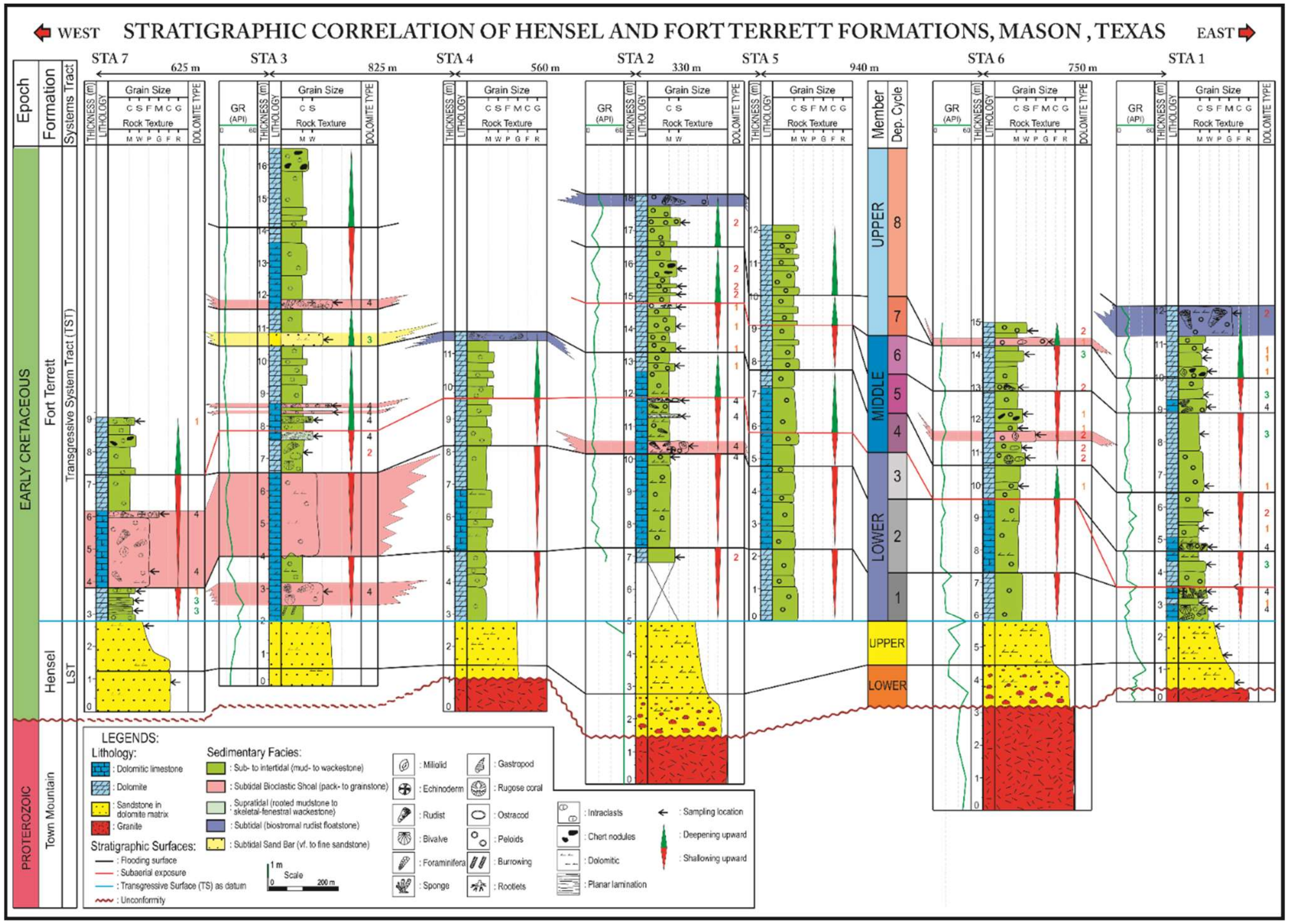

Figure 4.8. Stratigraphic correlation of the Hensel and Fort Terrett Formations in Mason County. The strata thicken to the west. The Fort Terrett Formation is divided into Lower, Middle, and Upper members on the basis of sub-, inter-, and supratidal cycles. These are defined by flooding surfaces, which indicate frequent sea-level fluctuations affecting deposition of the various facies and early diagenetic processes. The basal conglomeratic sandstone with angular granitic clasts of the lower member of the Hensel Formation only occurs in local topographic lows.

During the Early Cretaceous to Oligocene (before the Balcones Fault Zone uplift), several diagenetic processes sequentially affected the strata, beginning with marine cementation–micritization and initial dolomitization, followed by early meteoric vadose and phreatic and finally shallow burial dissolution and cementation. Sea-level fluctuations were clearly significant in the early stages, resulting in rapid changes in diagenetic environment (Figure 4.2).

Late-stage diagenesis of post-Miocene age is linked to the exhumation (telogenesis) that resulted in further dissolution, dedolomitization, and production of oxidation features. The schematic paragenesis of the Fort Terrett Formation (Figure 4.9) shows the evolution of the strata from the Early Cretaceous deposition through burial to post-Miocene to Recent telogenesis.

4.9.3.1. Marine diagenesis

The evidence for marine diagenesis includes micritization and bladed calcite cements. External layers of rudist, miliolid foraminifera, and gastropod and bivalve shells were affected by microboring, producing an irregular outline of micrite envelopes. These features are common for skeletal shells and the process generally takes place in shallow-marine waters close to the sediment–water interface, in low-energy subtidal to intertidal environments (Bathurst 1966; Jacka 1977; Ellis 1986; Flügel 2004). Thin isopachous rims of bladed calcite crystals around and within bioclasts are the firstgeneration marine products; these were later replaced by dolomite in some cases (Figure 4.10b).

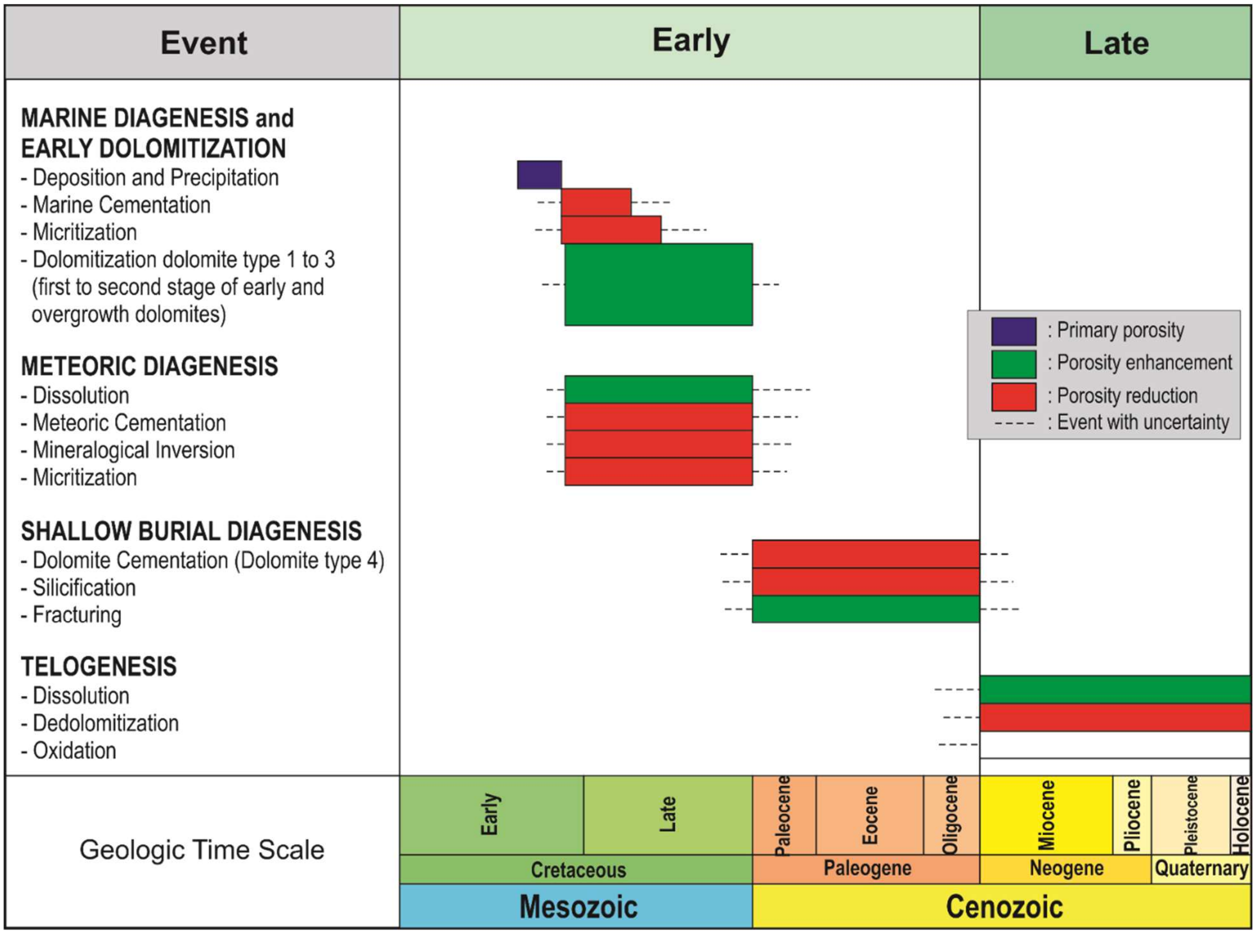

Figure 4.9. Schematic paragenesis of the Fort Terrett Formation. Early diagenetic processes likely occurred during the Late Cretaceous to Paleogene whereas late diagenesis took place in the Neogene to Recent.

4.9.3.2. Early meteoric diagenesis

Early meteoric diagenesis affected the succession when it was exposed during the Early Cretaceous. This diagenetic phase is best preserved in shallowing-upward cycles in the Middle Member of the Fort Terrett Formation, which are bounded by subaerial exposure surfaces with common evidence of plant roots. These surfaces are marked by dissolution of aragonite and probably high-Mg calcite (HMC) grains in vadose and phreatic environments and pore-filling calcite cement precipitated in the meteoric phreatic environment (Ellis 1986).

Aragonite was the original composition of parts of rudist, gastropod shells, and carbonate mud (Dodd 1966; Steuber and Löser 2000; Pascual-Cebrian et al. 2016) and this was dissolved by meteoric water flushing. Meteoric calcite spar then filled empty voids, although in some cases the shells were calcitized and relics of the original aragonitic microstructure are still present (Tucker and Wright 1990).

Aragonite grains and cements typically have high Sr contents (up to 10,000 ppm), but on diagenetic alteration and replacement by calcite (calcitization) these values are reduced. However, a 'memory' of that high Sr may be retained in replacement crystals in the form of moderate Sr values, much higher than in a calcite cement. The type 4 dolomite cement has an elevated Sr value reaching 1036 ppm (Figure 4.7c). Early seawater dolomite would be expected to have ~600 ppm Sr (Tucker and Wright 1990), but this would likely be reduced on burial recrystallization. The high Sr content of type 4 dolomite could indicate replacement of early aragonite cement precipitated in the marine setting.

Plant roots (Figure 4.10a) indicate subaerial exposure (Halley and Rose 1977; Tucker and Wright 1990) and a pause in sedimentation, associated with rhizogenic calcretes. Later, calcretes were flooded and subjected to meteoric phreatic conditions where the voids were filled by blocky calcite cement and then later replaced by dolomite.

Thin calcitic cement rims around fenestrae (as shown by red-stained rims in Figure 4.5c) can be interpreted as meteoric phreatic precipitates. Later, dolomite cements occluded any remaining pore space in the fenestrae. These two different cement phases indicate a changing pore-fluid chemistry from a meteoric to shallow-burial setting.

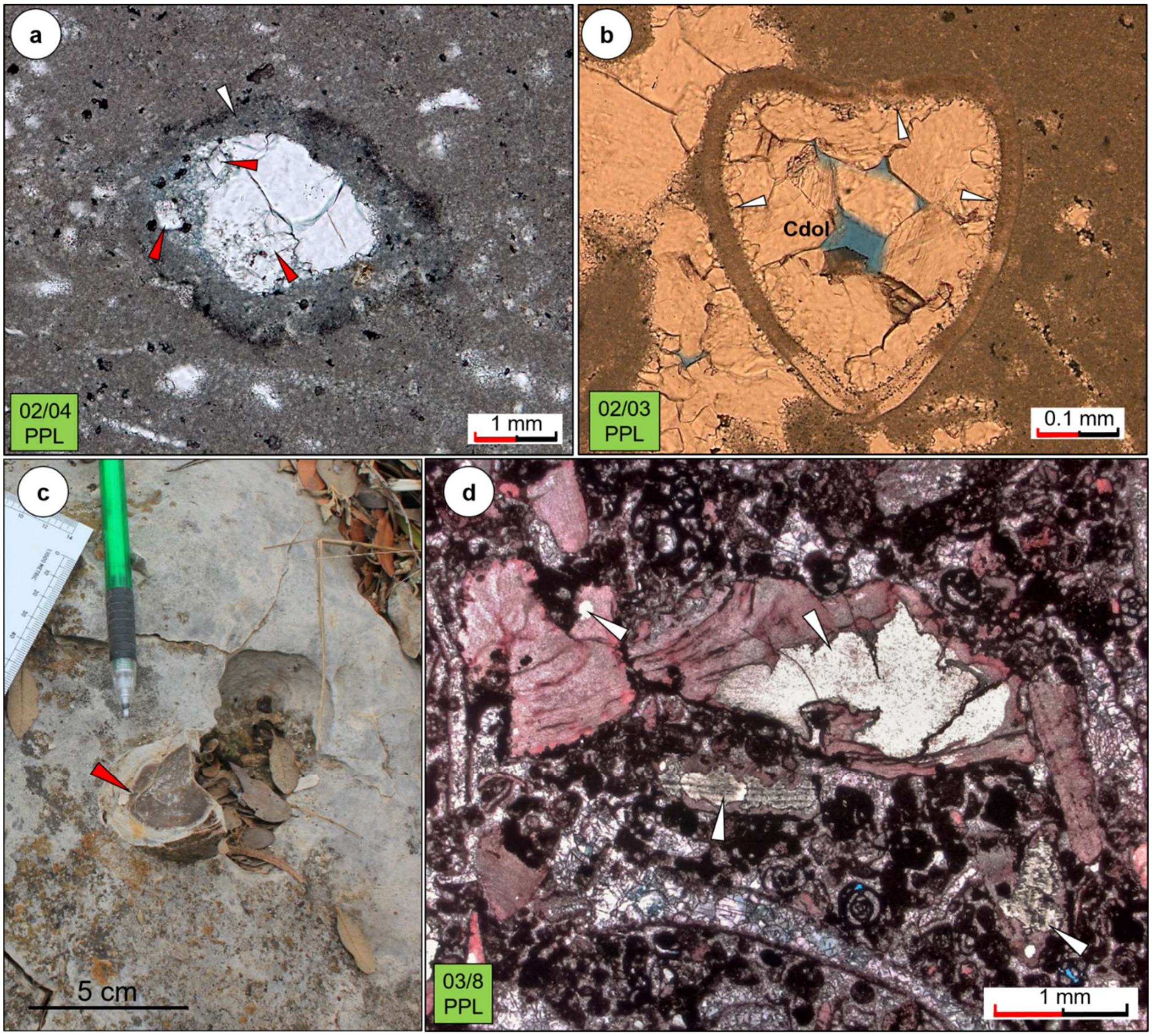

Figure 4.10. a. Rootlet in partially dolomitized skeletal–fenestral wackestone facies. The rootlet wall was micritized (white arrow) and the initial void was filled by an early generation of dolomite cement. Planar euhedral dolomite can be observed (red arrows). b. Thin rim of marine calcite cement (white arrows) lining the inside of a bivalve shell. This cement later was replaced by dolomite and the remaining void was filled by a second generation of blocky dolomite cement (Cdol). c. Chert-nodules (red arrows) in partially dolomitized mudstone to skeletal–fenestral wackestone facies. d. Chert (white arrows) in partially dolomitized skeletal grainstone forming selective replacement of calcitic-bivalve shell fragments (rudist). Note that slide d is stained by alizarin Red S. PPL plain polarized light.

4.9.3.3. Shallow‐burial diagenesis

The Comanche Platform was submerged in the Late Washita time (Albian) and buried by younger sediments of the Segovia Formation (Ellis 1986). In the Mason County area, several features suggest a slightly deeper burial diagenetic environment, i.e., the moderate Fe and Mn contents indicating a dysoxic environment, presence of fractures and silicification in a form of chert nodules, and selective microcrystalline silica replacement of rudist fragments.

Moderate concentrations of Fe and Mn (Figure 4.7b) indicate a change to sub-dysoxic conditions after deposition, and this is typical of a burial environment (Tucker 1986), as the availability of dissolved Fe and Mn released from clays can easily substitute calcium in the calcite lattice at low oxygen states (Budd 1997; Grossman 2012). Fractures were filled by dolomite cement, and the lack of offset along fractures indicates a shallow-burial origin, where limited overburden did not have enough pressure to offset the fractures. A shallow burial depth, probably to a few tens of meters, is also indicated by the absence of stylolites in the succession. The chemical compaction and pressure solution to form stylolites is thought to begin at an overburden of several hundred meters and depend on lithofacies, carbonate fabric, mud content, degree of cementation, and susceptibility to pressure solubility and resistance (Buxton and Sibley 1981; Railsback 1993).

Irregular chert nodules range from 4 to 15 cm in diameter and commonly appear in skeletal–fenestral wackestone to skeletal packstone facies of the middle and upper members of the Fort Terrett Formation (Figure 4.10c). These features indicate that silica-supersaturated fluids passed through the different stratal units to form nodules (Jacka 1977), as an event after an early stage of dolomitization from the evidence of dolomite rhombs within the chert nodules (Pittman 1959).

Selective silica replacement of calcitic (probably HMC) rudist shell fragments occurs locally (Figure 4.10d), with the silica source being either biogenic (such as sponge spicules and radiolarians) or inorganic (Pittman 1959; Knauth 1979; Maliva and Siever 1989; Hesse 1988, 1989). The inorganic silica source is indicated here from dissolved detrital silicates, which consist mainly of quartz. Chert precipitation occurs when the pH decreases, which could have been induced by organic matter decomposition followed by hypersaline conditions (Hesse 1988, 1989). The inorganic model seems appropriate in this case because of the absence of sponge spicules in the Edwards Group succession (Pittman 1959).

4.9.3.4. Telogenesis

Movement on the Balcones Fault Zone in the Oligo-Miocene uplifted, exposed and eroded the Edwards Group including the Fort Terrett Formation after tens to hundreds of meters of burial. This process has continued from the Miocene to the present time (Anaya 2004) and resulted in a late-stage meteoric diagenesis. Telogenesis in the study area is characterized by several processes related to oxidation and exposure. Brownish-orange oxidation bands occur at several horizons. The absence of gypsum and other evaporate minerals in this succession indicates their dissolution or removal during the initial fresh-water flushing (Fisher and Rodda 1969).

Geochemical trends, including the negative correlation of Sr against Fe and Mn content for type 4 dolomite could be related to decreasing Sr concentration caused by meteoric water flushing through time (Figure 4.7c). This contact with freshwater may also have affected the stable isotope values, such that the type 4 dolomite has quite negative $\delta^{18}O$ (Figure 4.7a), typical for a meteoric influence (Hudson 1977; Grossman 2012).

4.9.4. Dolomitization and dolomite evolution

Two dolomitization models, seepage-reflux and evaporative pumping, have been discussed for the Edwards Group of Mason County (e.g., Fisher and Rodda 1969; Rose 1972). The seepage-reflux model hypothesizes that hypersaline fluids flow downwards due to their higher density and are recharged by variations in tidal currents and possibly storms, leading to dolomite replacement of peritidal and subtidal carbonates (Fisher and Rodda 1969). The evaporative pumping mechanism suggests Mg-rich brines were induced to flow through porous sediments by an upward decrease of hydrodynamic potential during evaporation (Rose 1972). In this model, the path of the fluid-flow is opposite to that in the seepage-reflux model. These two models require an understanding of fluid-flow patterns in mud-dominated deposits. Carbonate mud should have a permeability of at least 240 mD for fluid-flow (Deffeyes et al. 1964), but this is relatively high since modern carbonate mud from the tidal flats of the Bahamas has permeabilities in the range of 1–100 mD (Gebelein et al. 1980). The average for all Holocene carbonate sediments of Florida (and the Bahamas), which includes those dominated by grains, is the order of 230 mD (Enos and Sawatsky 1981). Thus, muddy successions need sufficient permeability for the flow of the Mg-rich brines and for a significant period of time so that the succession can be dolomitized.

The Edwards Group succession is dominated by mudstone and skeletal–fenestral wackestone facies with limited fluid-flow capability and has only scarce and isolated skeletal packstone–grainstone facies (Figure 4.8). All units should contain high permeability layers to allow dolomitizing brines to flow through the muddy facies (Machel 2004). For this reason, other factors may have been involved to provide the additional permeability necessary for the passage of brines through this mud-dominated succession. Fenestrae occur throughout the succession, and are common in many dolomitized peritidal deposits in the rock record (Figures 4.2, 4.6). It is suggested here that this fenestral structure at the time of dolomitization may have had a significant impact on an initial permeability, thus allowing Mg-rich brines to enter the mud-dominated facies. Interconnected fenestral fabrics are abundant in the succession as possible flow-paths for the dolomitizing brine (Figure 4.6a, b).

Coarsening of dolomite crystals (Figure 4.6d) is associated with fenestral porosity with overgrowths developed on the parts of crystals that were protruding into the fenestral pores (Figs. 9, 10). These voids served as initial space within which dolomite could precipitate and grow, fed by brine fluids moving through the pores in a similar process suggested by Choquette and Hiatt (2008).

Multiple zones of dolomite cortex overgrowth are distinguishable by cathodoluminescence petrography for the Fort Terrett and Hensel Formations (Figure 4.11). Concentric zonation of bright orange and then dull red luminescence is a feature of type 3 dolomite. Cyclic zonation in dolomites of the Upper Hensel Formation reflects repetitive episodes of Mg-rich brine flushing through with different bulk fluid chemistry and variable Fe and Mn contents (Machel 2000).

Dolomitizing brines should have moved from the source downwards, driven by density and producing replacement dolomite in the first stage (Saller and Henderson 1998, 2001; Jones and Xiao 2005). Progressively, dolomitizing fronts would have continued but would have become less saturated and precipitated less dolomite than the earlier stage. In addition, the sediment closer to the brine source would have suffered “overdolomitization”, that is the precipitation of overgrowths on dolomite crystals (a cement stage rather than a replacement of original sediment) (Saller and Henderson 1998, 2001).

The textural evolution of dolomites in Fort Terrett Formation shows a pattern of maturation including crystal-size coarsening, crystal face development, and fabric preservation in conjunction with decreasing porosity (Figure 4.12). This evolution is also reflected in the geochemical data whereby isotope values become increasingly negative and trace element contents are reduced.

Type 1 dolomite shows a micro- to fine- crystal size related to the first stage of dolomitization, which was likely associated with syn-sedimentary processes (Longman and Mench 1978; Budd 1997; Machel 2004). It was a direct pore-precipitation process resulting from evaporitic conditions in a supratidal setting, typical of a warm and arid environment (Warren 2000; Machel 2004). This type of dolomite is usually poorly ordered (Figure 4.5c) and mostly Ca-rich (Mazzullo 2000; Machel 2004).

Concentrations of Fe and Mn for this type 1 dolomite are 59–194 ppm and 63–269 ppm, respectively (Figure 4.7b). These contents are relatively low compared to the other types of dolomite. Low Fe and Mn concentrations could be related to the oxic conditions, which would have reduced the availability of Fe (and also Mn) to be incorporated into the crystal lattice (Elderfield 1981; Burdige 1993; Mazzullo 2000).

Stable isotope ratios for type 1 dolomite are low positive for $\delta^{18}O$, between 0.0 and +1.6‰ (Figure 4.7a), a typical range for evaporitic conditions (Hudson 1977; Grossman 2012; Swart 2015). The $\delta^{13}C$ values show a range between –2.3 and +1.9‰, which could be linked to an organogenic model of dolomitization (Compton 1988; Mazzullo 2000) that is influenced or perhaps promoted by bacterial sulfate reduction related with organic-matter diagenesis resulting in the depletion of ^{13}C. This model occurs at surface temperature and at the near sediment-seawater interface and probably up to tens of meters burial depth. Low Fe, Mn and Sr concentrations are common for this model; as seen in Figure 4.7c. The low negative values of $\delta^{13}C$ may be caused by the addition of light ^{12}C-enriched CO_2 to pore-fluids derived from bacterial degraded organic matter (Gregg et al. 1992; Perkins et al. 1994; Vasconcelos and McKenzie 1997; Mazzullo 2000; Vasconcelos et al. 2005). This type 1 dolomite may provide nuclei or initial cortex for the next stage of dolomites.

Type 2 dolomite has a slightly increased crystal size (very fine to fine); it also shows mimetic fabric preservation and selective calcitic-shell replacement (Figure 4.5d). Mimetic fabric forms during dolomitization at a lower saturation state and it may have been controlled by mineralogy (Sibley and Gregg 1987). Meanwhile, selective replacement occurs as a result of an interplay between dolomitizing brine and mineralogy. Changes in dolomitizing brine from a supersaturated to an undersaturated fluid can control rates of precipitation, while a dominantly high-Mg calcite sediment could be more prone to replacement (Sibley and Gregg 1987; Tucker and Wright 1990). The supersaturated brine replaces precursor carbonate minerals by dolomite and the solution, later, becomes undersaturated so that replacement of the remaining carbonate minerals does not take place (Murray and Lucia 1967; Tucker and Wright 1990).

Type 2 dolomite formed in a shallow-burial setting as indicated by slight enrichment in Fe and Mn concentrations compared to type 1 dolomite (Figure 4.7b). The concentrations range from 71 to 251 ppm and 67 to 487 ppm, respectively. These concentrations are attributed to dysoxic conditions that are dominant in shallow-burial settings (Tucker 1986).

In terms of isotopes, the values of $\delta^{18}O$ are low negative and $\delta^{13}C$ low positive for type 2 dolomite (Figure 4.7a), in comparison with type 1 dolomite. Increasing temperature during shallow burial is the main factor controlling the negative $\delta^{18}O$ for this type 2 dolomite. Meanwhile, the positive $\delta^{13}C$ is a normal-marine signal, with values commonly +1‰ higher than marine calcite (Swart 2015).

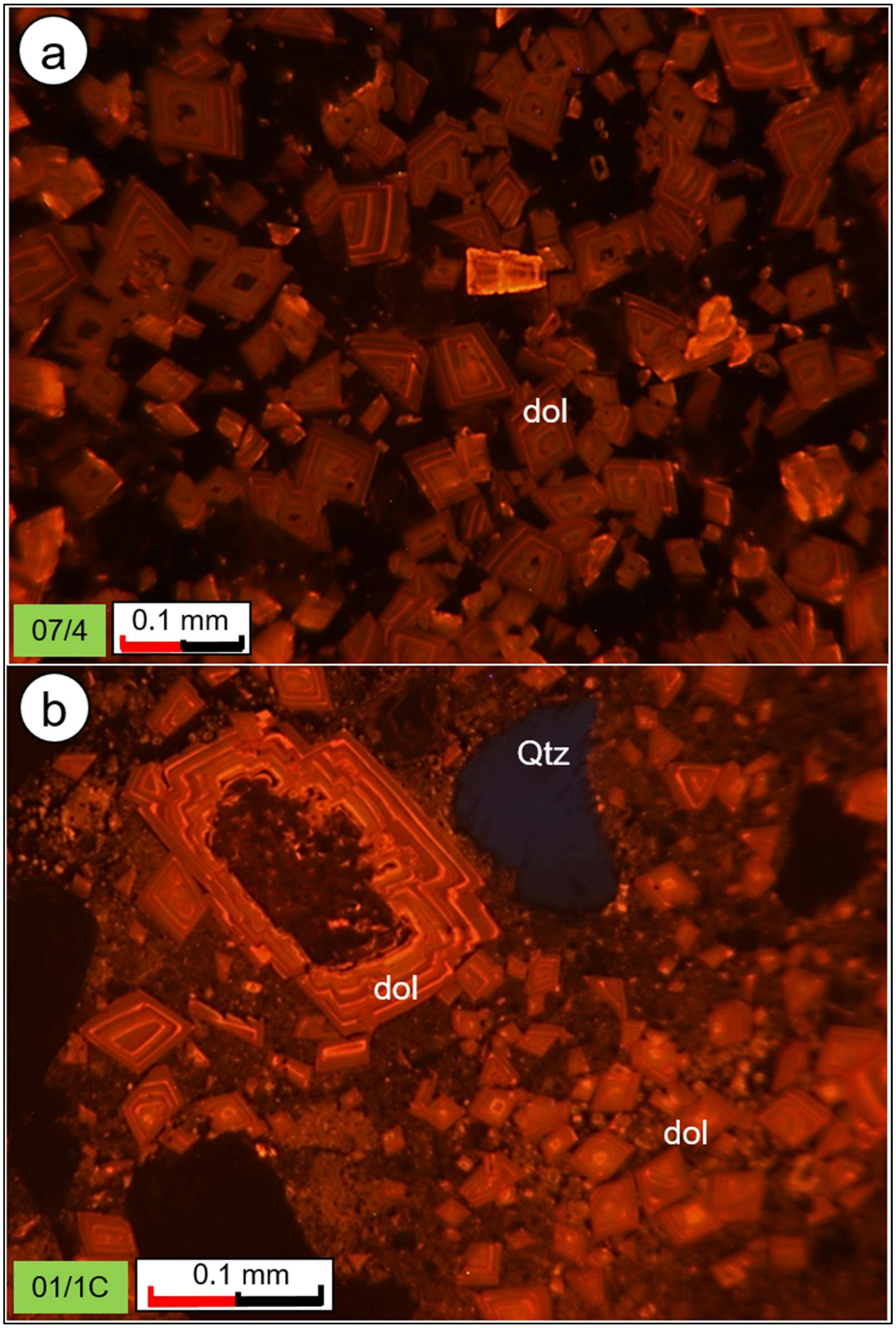

Figure 4.11. Multiple zones within the cortex overgrowth of dolomite crystals in CL. a. Concentric zonation of type 3 dolomite of the Fort Terrett Formation. b. Cyclic zonation of dolomite cement of the upper member of the Hensel Formation.

Type 3 dolomite has extensive crystal coarsening and cortex growth up to medium crystal size (Figure 4.5e) and is associated with increasing fabric maturity caused by dolomite overgrowths, which record repeated development of the dolomite rhombs. The overgrowths are related to constant episodes of Mg-rich brine flushing (Katz 1971; Longman and Mench 1978; Sibley and Gregg 1987; Choquette and Hiatt 2008). This type of dolomite is characterized by subhedral to euhedral rhombic crystals with the presence of some cloudy residual inclusion-rich cores. It is likely that in this stage, dolomitization was occurring during sediment compaction resulting from increasing burial depth (Shinn and Robbin 1983; Katz 1971; Longman and Mench 1978; Choquette and Hiatt 2008). Extensive enrichment of Fe and Mn also indicates increasing burial (Figure 4.7b).

Type 4 dolomite is a cement, which precipitated in bioclast molds, voids, fenestral pores and fractures within precursor lime mud (Figure 4.5f). Several episodes of Mg-rich brine flushing are responsible for the coarser dolomite crystals in these settings.

Dolomitizing fluids moving downwards can cause generation of different types of dolomite (Saller and Henderson 2001; Jones and Xiao 2005). The initial process produced fine crystalline dolomite of types 1 and 2 in this study. Later, the dolomitization front would have continued basinwards and the dolomitizing brine would have flowed through the earlier precipitated dolomite causing overgrowths (dolomite type 3). Finally, fluids would have kept moving and precipitated a dolomite (type 4) cement, filling remaining pore spaces.

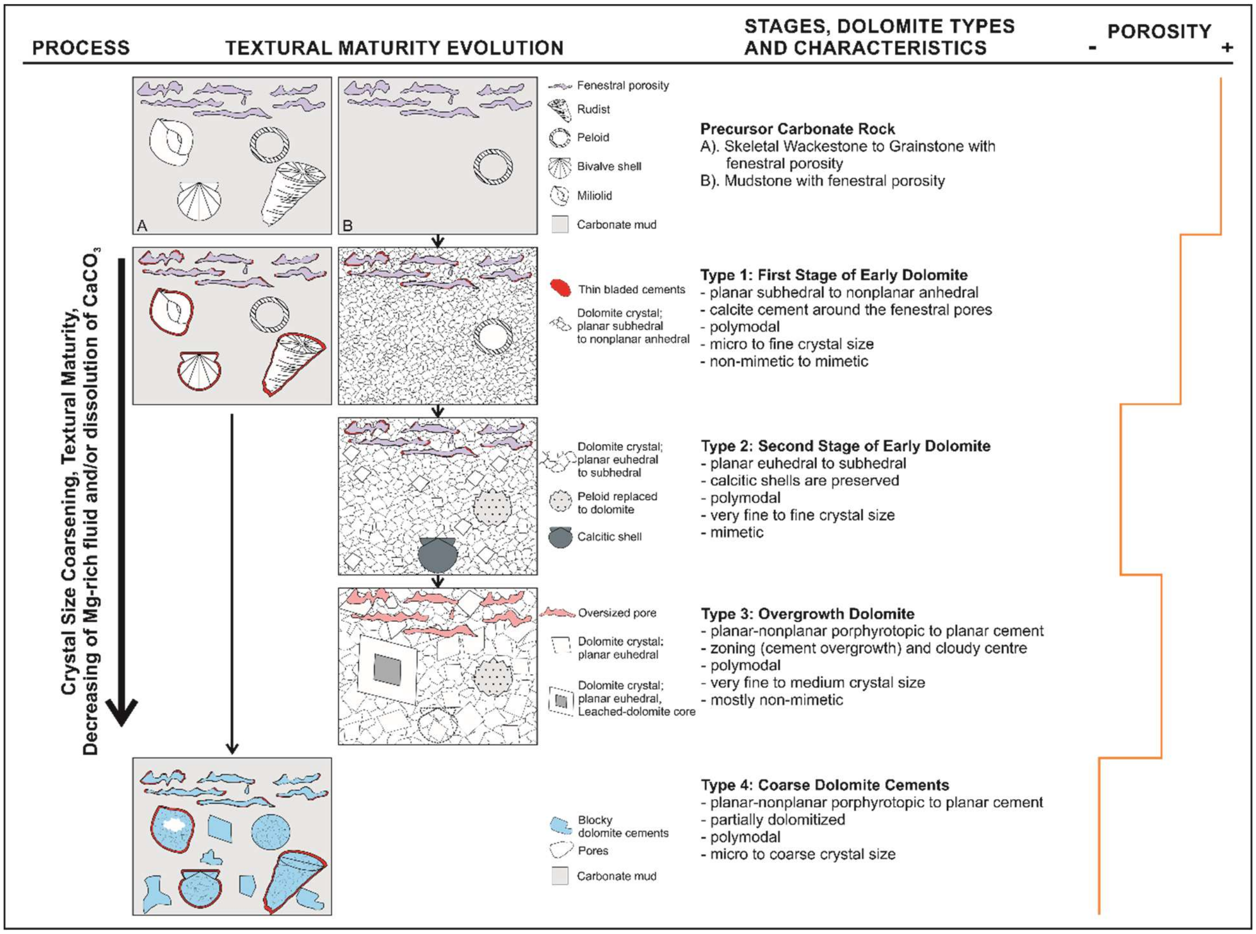

Figure 4.12. Textural development of the dolomite in the Fort Terrett Formation (adapted and modified from Sibley and Gregg 1987; Choquette and Hiatt 2008). The figure shows the stages of maturation including crystal-size coarsening within sequences, crystal face development, and fabric preservation in conjunction with decreasing porosity from two different precursor carbonate rocks.

The main diagenetic process operating on uplift (telogenesis) of the Edwards Group in post-Oligocene–Miocene time, related to movement on the Balcones Fault Zone, is calcitization of dolomite (dedolomitization). This was caused by circulating fresh-water dissolving gypsum, which elevated the Ca/Mg ratio of the pore-water and resulted in the replacement of dolomite by calcite (cf. Evamy 1967; Abbott 1974; Longman and Mench, 1978; Ellis 1986; Barker and Ardis 1996). Leached dolomite cores (hollow) are observed (Figure 4.5e), since the core would originally have been less stable or poorly ordered and so susceptible to dissolution; the dolomite cortex on the other hand is preserved.

4.9.5. Fluid‑flow mechanism

This Early Cretaceous succession was deposited above the Precambrian basement and it had a very simple burial history; the diagenetic processes are well constrained into a narrow range of environments, which make the interpretation of fluid-flow quite simple. There are probably three possible scenarios of fluid-flow directions in this succession: (1) dolomitizing fluids that flowed downwards (a density head mechanism), (2) fluids that flowed upwards due to evaporative pumping, and (3) fluids that flowed upwards from the basement or through the basal Edwards layers, which would suggest compaction-driven fluid-flow from the Maverick Basin or a thermal component due to the higher thermal conductivity of the granitic basement.

The most likely scenario for dolomitizing fluid flow in this succession is the downward model (Figure 4.13). This model invokes a density-head driving-mechanism whereby evaporation generates denser fluids than normal seawater, which then sink within the formation through gravity, so facilitating the initiation of dolomitization (Budd 1997; Saller and Henderson 1998; Saller and Henderson 2001; Whitaker et al. 2004; Jones and Xiao 2005). Eventually, fluid density reaches equilibrium at a certain depth as the Mg-rich brines are mixed with relatively Mg-depleted pore water. This situation would have triggered lateral or outward flow of the mixed pore water. In this model, dolomite crystal size and maturity should decrease downwards. However, in the Fort Terrett Formation, the dolomite crystal sizes show a scattered distribution, perhaps due to a more complex flow system controlled by different stratigraphic horizons with different properties. Initially, fluid flow may have operated through interconnected fenestral porosity (Figure 4.6) and isolated skeletal packstone–grainstone layers operating as permeable pathways.

The Fort Terrett Formation is not entirely dolomitized (Figure 4.2, 4.8). Completely dolomitized beds dominate in the upper part (dolomite ranges from 12 to 100%), whereas partially dolomitized mudstone to skeletal packstone predominate in the lower part of the formation (8 to 24% dolomite). Although, in the upper part of the succession there is only an average of 15% initial fenestral porosity, the fabric appears more commonly, which could have resulted in a higher connectivity, allowing fluids to move farther than in the lower part where higher dolomite percentages only occur in isolated samples (Figure 4.2). It is suggested here that initial fenestral porosity could have provided the permeability pathways for the dolomitizing brines, which moved downward from a surface source (such as an evaporating lagoon or evaporative tidal flat), developed especially during deposition of the upper part of the formation, into sediments below, previously deposited.

At the base of the succession, the Hensel Formation presents a much simpler porosity-permeability system and the decreasing crystal size from the top layers downwards toward the basement (Figure 4.5a, b) supports the hypothesis of gravity-driven dolomitization. The downward flow then became lateral flow when the dolomitizing brines reached the granitic basement as this rock has extremely low permeability. This fluid-flow situation allows more extensive dolomite cortex overgrowths to be precipitated around the dolomite cores in the Upper Hensel Formation, resulting in coarser dolomite crystals in conjunction with decreasing porosity (Figure 4.12). Mg-rich brines allowed the dolomitizing processes to act from the depositional surface downwards, and then for the depleted brines to move farther downward and laterally.

There are other mechanisms that could have driven dolomitizing fluids upward through the succession including geothermal heat (Simms 1985; Land 1985; Budd 1997; Machel 2004) and compaction-drive from the nearest basin (Machel 2004; Whitaker et al. 2004). Both mechanisms could produce a burial or hydrothermal dolomite such as saddle dolomite. However, there is no evidence that these textures occur in the Edwards Group in Mason County. Another mechanism, i.e., evaporative pumping, draws dolomitizing fluids upward but since a decreasing dolomite crystal size is observed in the Hensel Formation, it is inferred that this model was unlikely to have been operating in the study area.

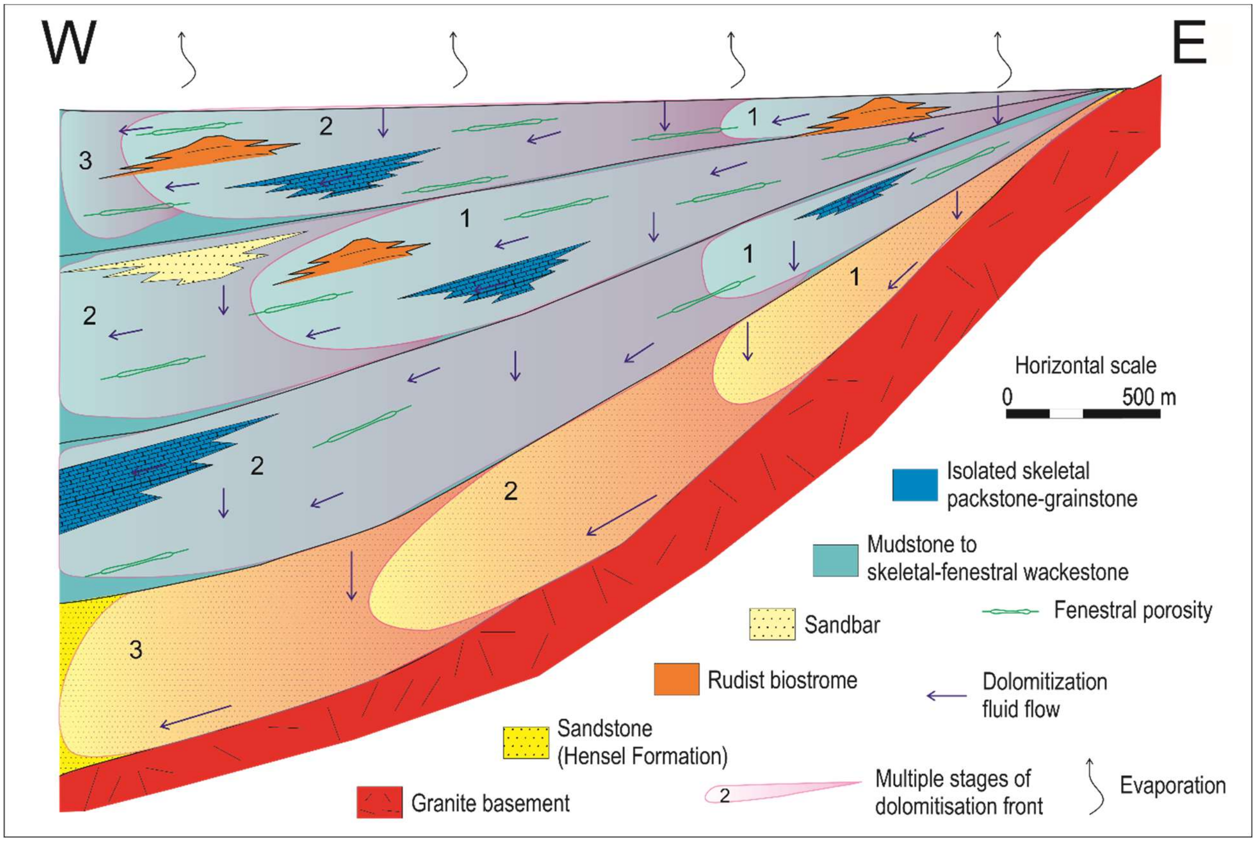

Figure 4.13. The multiple stages of a downward fluid-flow model or density-head driving-mechanism through mainly fenestral porosity as the permeability pathway for dolomitization of the Edwards Group carbonates in Mason County. Note the decreasing frequency of fenestral porosity downwards and the large vertical exaggeration to show the interconnected fenestral porosity.

4.10. Conclusions

1. Through detailed analysis including sedimentological, petrographical, and geochemical approaches, this study is contributing towards the understanding of porosity types as a control on dolomitization and diagenetic evolution of the Early Cretaceous Hensel and Fort Terrett Formations in the Edwards Group of Mason County, Texas.
2. The results of this study suggest that interconnected fenestral porosity could have played a major role in the flow of dolomitizing fluids through mud-dominated facies with limited permeability.
3. The Lower Cretaceous Edwards Group in Mason County was subjected to a simple burial history followed by uplift related to the Balcones Fault Zone in the Miocene. The diagenetic sequence consists of early marine cementation and micritization, meteoric dissolution and cementation, and near-surface to shallow moderate burial dolomitization, followed by telogenesis, involving dedolomitization.
5. Four types of dolomite have been recognized and they reflect textural evolution and maturity through increasing crystal size from dolomite overgrowth and cementation. Type 1 dolomite was the result of direct pore-precipitation and sediment replacement and/or organogenic precipitation; type 2 dolomite has a slightly larger crystal size, is a replacement type, and is probably linked to a shallow-burial setting; type 3 dolomite has a larger crystal size still, and is likely precipitated at a deeper burial depth; type 4 dolomite is a late-stage cement precipitated in voids, bioclast molds, and fenestrae.

6. The interpreted fluid-flow model applicable for the Edwards Group of Mason County is a density-driven, downward-flux mechanism related to the sinking of dense dolomitizing brines derived by evaporation within the Kirschberg Lagoon. Interaction with lower Mg-saturated pore water to reach an equilibrium initiated outward flow through fenestral porosity. A more complex porosity–permeability system in the Fort Terrett Formation resulted in a more scattered distribution of dolomite crystal size, whereas a much simpler flow system in the Hensel Formation resulted in a decreasing dolomite crystal size towards the underlying Precambrian.

CHAPTER 5

CONCLUSION

We have investigated and defined facies, reservoir geometry and stratigraphy, global Early Miocene events, carbonate factory, paleogeography, morphology of the carbonate platform, depositional model, paragenetic sequences, porosity types and their evolution for the Baturaja Formation. In addition, we have conducted similar methodology and interpretation for the Mason data. This chapter compiles all the key findings of our study.

Main results and implications

Chapter 2 discussed the facies distribution in which the red algae and LBF dominate the skeletal grains in the Baturaja Formation succession as the main carbonate producer. This skeletal association contributed to the significant reservoir rock volumes as the Baturaja reservoirs are composed of mainly red algae and LBF packstone-grainstone facies. Meanwhile, corals occured in small, isolated and scattered colonies. This new fact rejects a common interpretation that suggests corals dominated the Oligocene-Miocene carbonate producer and reef builder; as common evidence in the modern world. In addition, we have presented several global events during the Early Miocene, including an overall global warming trend and higher nutrient level. It is suggested that combination of these global events affecting and controlling the abundant red algae and LBF. Regional paleogeography has been proposed using this carbonate producers' context to explain facies distribution along the inner, middle and outer ramp. Depositional model for the Melandong area has been recommended to improve reservoir distribution and prediction capability. This model explains how the distribution of facies belts in the area significantly contribute to the reservoir rock volume; in the mound and in the deeper inter-mound areas.

Chapter 3 presented paragenetic sequences constructed from a combination of cement stratigraphy, diagenetic analysis, and process characterization from petrography and geochemical analysis that lead to the interpretation of the diagenetic environment. Extensive leaching of red algae and perforated-LBF characterizes early meteoric diagenesis forming extensive moldic porosity and showing fabric-selective dissolution. Several lines of evidence including distinctive negative shifts of $\delta^{13}C$, moderate Sr values, and such dogtooth, syntaxial overgrowth of echinoid grains, and blocky cements. Possible occasional sea level lows during the deposition of the Baturaja Formation were indicated by exposure surfaces and shallowing-upward cycles for both upper and lower members. These features were the case for the mound setting develop on the paleo-topographic highs which was very likely vulnerable to the sea level fluctuations. Meanwhile, in the deeper inter-mound depositional area, the porosity creation pointed out by the presence of burial CO_2 gas. This corrosive gas leached all the carbonate components forming non-fabric selective dissolution texture. We present cements filling late-stage stylolite as evidence for this interpretation. This new analysis gives an idea to explore deeper depositional setting as traditional carbonate mound play has been discovered. An accurate prediction to identify and characterize pore types and geometry of the burial pores are needed using integration of well data (logs and cores) and rock physics models for further development of the mature oil fields.

Chapter 4 investigated fenestrae and fenestral fabric and their relationship to the dolomite units; a common case occurred in peritidal deposits that suitable for the Fort Terrett Formation in Mason, central Texas. Through facies identification, dolomite typing, and geochemistry analysis we could establish an understanding of this correlation to control dolomitization and diagenetic evolution. Four dolomite types have been defined showing textural maturity to the increasing dolomite crystal size. The formation, dominated by mudstone-wackestone facies, has limited fluid-flow capability as it has only scarce and isolated skeletal packstone–grainstone beds. We suggested that the interconnected fenestral structure at the time of dolomitization may have had a significant impact on an initial permeability; allowing Mg-rich brines to enter the mud-dominated facies. Eventually, we were able to define and propose fluid flow mechanism for the succession involving dolomitizing fluids that flowed downwards. This model invokes a density-head driving-mechanism whereby evaporation generates denser fluids than normal seawater, which then sink within the formation through gravity, so facilitating the initiation of dolomitization. The process itself initially was enabled by the interconnected fenestral porosity and isolated skeletal packstone-grainstone layers operating as permeable pathways.

Future Work

This study presents a new perspective in term of Early Miocene carbonate producers. Instead of corals domination, we provide evidence that red algae and LBF are the major carbonate producers and reef builders at this time. Our data are compiled from the published papers, conference proceedings, and internal reports in combination with the dataset from the Melandong area, an onshore part of the NW Java Basin. We realize that it would be constructively important to have more dataset within the basin (both onshore and offshore) to strengthen our interpretation. It also is useful to have a study in the Baturaja Formation locality in Baturaja, South Sumatra, using this new perspective as a starting point to the other Oligocene-Miocene carbonate succession around Indonesia and more importantly around the world.

An interpretation of burial dissolutions in chapter 3 needs gas data analysis, especially from the wells producing high content CO_2 from the Baturaja Formation reservoirs. The gas analysis, including $\delta^{13}C$ and $^3He/^4He$, could support our interpretation. Carbon isotope is indicative for corrosive gas sources; i.e. –3.41 to –8.44‰ and the helium gas ratio >1 characterize mantle sources. Micro-drilled sampling is also needed to get samples from the calcite cements filling late-stage stylolite.

REFERENCES

Abbott, P. L., 1974, Calcitization of Edwards Group dolomites in the Balcones Fault Zone aquifer, south-central Texas: Geology, v. 2, p. 359-362.

Abduslam, A., 2012, Reservoir characterization and enhanced oil recovery potential in Middle Devonian Dundee Limestone reservoirs, Michigan Basin, USA, Western Michigan University, Michigan.

Adams, A., W. MacKenzie, and C. Guilford, 1988, Atlas of sedimentary rocks under the microscope. Great Britain, Longman Group UK Ltd.

Adey, W. H., and I. Macintyre, 1973, Crustose coralline algae: a re-evaluation in the geological sciences: Geological Society of America Bulletin, v. 84, p. 883-904.

Ageng, C., D. H. Hairunnisa, D. Nugroho, and N. I. Basuki, 2014, Facies Analysis, Rock Type, and Property Distribution in Upper Interval of Baturaja Formation, Krisna Field, Sunda Basin: Indonesian Petroleum Association 38th Annual Convention and Exhibition Proceeedings.

Allan, J., and R. Matthews, 1977, Carbon and oxygen isotopes as diagenetic and stratigraphic tools: surface and subsurface data, Barbados, West Indies: Geology, v. 5, p. 16-20.

Allen, R., A. Foggo, K. Fabricius, A. Balistreri, and J. M. Hall-Spencer, 2017, Tropical CO2 seeps reveal the impact of ocean acidification on coral reef invertebrate recruitment: Marine pollution bulletin, v. 124, p. 607-613.

Alsharhan, A., 2003, Petroleum geology and potential hydrocarbon plays in the Gulf of Suez rift basin, Egypt: AAPG bulletin, v. 87, p. 143-180.

Anaya, R., 2004, Conceptual model for the Edwards-Trinity (Plateau) aquifer system, Texas, *in* R.

E. Mace, E. S. Angle, and I. William F. Mullican, eds., Aquifers of the Edwards Plateau, Austin, Texas, Texas Water Development Board Report, p. 21-62.

Anderson, T. F., and M. A. Arthur, 1983, Stable isotopes of oxygen and carbon and their application to sedimentologic and paleoenvironmental problems: Stable Isotopes in Sedimentary Geology, v. 10, p. 1-151.

Andrieu, S., B. Brigaud, J. Barbarand, and E. Lasseur, 2017, The complex diagenetic history of discontinuities in shallow-marine carbonate rocks: New insights from high-resolution ion microprobe investigation of δ18O and δ13C of early cements: Sedimentology.

Apel, J. R., 1987, Principles of ocean physics: International Geophysics Series, v. 38, Academic Press, 631 p.

Ardila, L. E., 1982, The Krisna High: Its Geologic Setting and Related Hydrocarbon Accumulations, Proceedings of the South East Asia Petroleum Exploration Society, Society of Petroleum Engineers, p. 10-23.

Arpandi, D., and S. Patmosukismo, 1975, The Cibulakan Formation as one of the most prospective stratigraphic units in the north-west Java basinal area: Indonesian Petroleum Association 4th Annual Convention and Exhibition Proceeedings.

Ayers, J. M., P. G. Strutton, V. J. Coles, R. R. Hood, and R. J. Matear, 2014, Indonesian throughflow nutrient fluxes and their potential impact on Indian Ocean productivity: Geophysical Research Letters, v. 41, p. 5060-5067.

Bain, R. J., and P. Kindler, 1994, Irregular fenestrae in Bahamian eolianites: a rainstorm-induced origin: Jounal of Sedimentary Research, v. A64, p. 140-146.

Baird, G. C., and C. E. Brett, 1986, Erosion on an anaerobic seafloor: significance of reworked pyrite deposits from the Devonian of New York State: Palaeogeography, Palaeoclimatology, Palaeoecology, v. 57, p. 157-193.

Banerjee, S., U. Bansal, K. Pande, and S. Meena, 2016, Compositional variability of glauconites within the Upper Cretaceous Karai Shale Formation, Cauvery Basin, India: implications for evaluation of stratigraphic condensation: Sedimentary Geology, v. 331, p. 12-29.

Banerjee, S., U. Bansal, and A. V. Thorat, 2016, A review on palaeogeographic implications and temporal variation in glaucony composition: Journal of Palaeogeography, v. 5, p. 43-71.

Barker, R. A., and A. F. Ardis, 1992, Configuration of the base of the Edwards-Trinity Aquifer System and hydrogeology of the underlying pre-Cretaceous Rocks, west-central Texas, Water-resources inverstigations report 91–4071, Austin, Texas, US Geological Survey.

Barker, R. A., and A. F. Ardis, 1996, Hydrogeologic framework of the Edwards-Trinity aquifer system, West-Central Texas: Washington, U.S. Geological Survey.

Barker, R. A., P. W. Bush, and E. T. Baker, 1994, Geologic history and hydrogeologic setting of the Edwards-Trinity aquifer system, west-central Texas, Water-resources investigations report 91–4071, Austin, Texas, US Geological Survey.

Barnes, V. E., W. C. Bell, S. E. Clabaugh, P. E. Cloud Jr., R. V. McGehee, P. U. Rodda, and K. Young, 1972, Geology of the Llano region and Austin area: Field excursion: Austin, Texas, University of Texas at Austin, 77 p.

Bassi, D., L. Hottinger, and J. H. Nebelsick, 2007, Larger foraminifera from the Upper Oligocene of the Venetian area, north-east Italy: Palaeontology, v. 50, p. 845-868.

Bathurst, R., 1966, Boring algae, micrite envelopes and lithification of molluscan biosparites: Geological Journal, v. 5, p. 15-32.

Bathurst, R. G., 1972, Carbonate sediments and their diagenesis, v. 12, Elsevier.

Ben-Avraham, Z., and K. O. Emery, 1973, Structural framework of Sunda shelf: AAPG Bulletin,

v. 57, p. 2323-2366.

Berner, R., 1985, Sulphate reduction, organic matter decomposition and pyrite formation: Phil. Trans. R. Soc. Lond. A, v. 315, p. 25-38.

Berner, R. A., 1984, Sedimentary pyrite formation: an update: Geochimica et cosmochimica Acta, v. 48, p. 605-615.

Bhattacharya, J. P., 2006, Deltas, *in* H. W. Posamentier, and R. G. Walker, eds., Facies Model Revisited: Tulsa, Oklahoma, USA, Society for Sedimentary Geology, p. 237-292.

Birnbaum, S. J., and J. W. Wireman, 1984, Bacterial sulfate reduction and pH: implications for early diagenesis: Chemical Geology, v. 43, p. 143-149.

Bishop, M. G., 2000, Petroleum systems of the northwest Java province, Java and offshore southeast Sumatra, Indonesia, Denver, Colorado, USGS, p. 34.

Bosellini, F. R., and C. Perrin, 2008, Estimating Mediterranean Oligocene–Miocene sea-surface temperatures: an approach based on coral taxonomic richness: Palaeogeography, Palaeoclimatology, Palaeoecology, v. 258, p. 71-88.

Bosence, D., 2005, A genetic classification of carbonate platforms based on their basinal and tectonic settings in the Cenozoic: Sedimentary Geology, v. 175, p. 49-72.

Brandano, M., I. Cornacchia, and L. Tomassetti, 2017, Global versus regional influence on the carbonate factories of Oligo-Miocene carbonate platforms in the Mediterranean area: Marine and Petroleum Geology, v. 87, p. 188-202.

Brock, F., R. J. Parkes, and D. E. Briggs, 2006, Experimental pyrite formation associated with decay of plant material: Palaios, v. 21, p. 499-506.

Budd, D., 1997, Cenozoic dolomites of carbonate islands: their attributes and origin: Earth-Science Reviews, v. 42, p. 1-47.

Bullen, S. B., and D. F. Sibley, 1984, Dolomite selectivity and mimic replacement: Geology, v. 12, p. 655-658.

Burbury, J. E., 1977, Seismic expression of carbonate buildups northwest Java basin: Indonesian Petroleum Association 6th Annual Convention Proceeedings, p. 239-268.

Burdige, D. J., 1993, The biogeochemistry of manganese and iron reduction in marine sediments: Earth-Science Reviews, v. 35, p. 249-284.

Buxton, T. M., and D. F. Sibley, 1981, Pressure Solution Features in a Shallow Burled Limestone: Journal of Sedimentary Research, v. 51, p. 19-26.

Cane, M. A., and P. Molnar, 2001, Closing of the Indonesian seaway as a precursor to east African aridification around 3–4 million years ago: Nature, v. 411, p. 157.

Carannante, G., M. Esteban, J. Milliman, and L. Simone, 1988, Carbonate lithofacies as paleolatitude indicators: problems and limitations: Sedimentary Geology, v. 60, p. 333-346.

Carnell, A. J. H., and M. E. J. Wilson, 2004, Dolomites in SE Asia — varied origins and implications for hydrocarbon exploration: Geological Society, London, Special Publications, v. 235, p. 255-300.

Castillo, V., L. Benkovics, C. Cobos, D. Demuro, and A. Franco, 2017, Perla Field: The Largest Discovery Ever in Latin America.

Chafetz, H., and A. Reid, 2000, Syndepositional shallow-water precipitation of glauconitic minerals: Sedimentary Geology, v. 136, p. 29-42.

Chamley, H., 1989, Clay sedimentology, Springer-Verlag.

Chave, K., K. Deffeyes, P. Weyl, R. Garrels, and M. Thompson, 1962, Observations on the solubility of skeletal carbonates in aqueous solutions: Science, v. 137, p. 33-34.

Choquette, P. W., and E. E. Hiatt, 2008, Shallow-burial dolomite cement: a major component of many ancient sucrosic dolomites: Sedimentology, v. 55, p. 423-460.

Choquette, P. W., and N. P. James, 1987, Diagenesis# 12. Diagenesis in Limestones-3. The deep burial environment: Geoscience Canada, v. 14.

Choquette, P. W., and L. C. Pray, 1970, Geologic nomenclature and classification of porosity in sedimentary carbonates: AAPG bulletin, v. 54, p. 207-250.

Clements, B., and R. Hall, 2007, Cretaceous to late Miocene stratigraphic and tectonic evolution of west Java: Indonesian Petroleum Association 31st Annual Convention and Exhibition Proceeedings.

Clements, B., R. Hall, H. R. Smyth, and M. A. Cottam, 2009, Thrusting of a volcanic arc: a new structural model for Java: Petroleum Geoscience, v. 15, p. 159.

Cohen, K. M., S. C. Finney, P. L. Gibbard, and J.-X. Fan, 2013; updated, The ICS International Chronostratigraphic Chart, v. Episodes 36, p. 199-204.

Collins, E. W., 1987, Characterization of fractures in limestones, northern segment of the Edwards aquifer and Balcones fault zone, central Texas: Gulf Coast Association of Geological Societies Transactions, v. 37, p. 43-54.

Compton, J. S., 1988, Degree of supersaturation and precipitation of organogenic dolomite: Geology, v. 16, p. 318-321.

Cooper, B., M. Raven, and L. Samuel, 1997, Origin and geological controls on subsurface CO2 distribution with examples from western Indonesia.

Cooper, B., M. Raven, and L. Samuel, 1997, Origin and geological controls on subsurface CO_2 distribution with examples from western Indonesia: Indonesian Petroleum Association Proceedings of an International Conference on Petroleum Systems of SE Asia and

Australasia.

Corda, L., and C. Palmiotto, 2015, Rhodalgal–foramol facies in equatorial carbonates: Insights from Miocene tectonic islands of the central Atlantic: Palaeogeography, Palaeoclimatology, Palaeoecology, v. 428, p. 21-30.

Dai, J.-x., Y. Song, C.-s. Dai, and D.-r. Wang, 1996, Geochemistry and accumulation of carbon dioxide gases in China: AAPG bulletin, v. 80, p. 1615-1625.

Daly, M. C., M. A. Cooper, I. Wilson, D. G. Smith, and B. G. D. Hooper, 1991, Cenozoic plate tectonics and basin evolution in Indonesia: Marine and Petroleum Geology, v. 8, p. 2-21.

Deffeyes, K., F. J. Lucia, and P. Weyl, 1964, Dolomitizanon of Recent and Plio-Pleistocene sediments by marine evaporite waters on Bonaire Netherlands Antilles: SEPM Special Publication, v. 13, p. 71-88.

Djuanda, H., 1985, Facies distribution in the Nurbani carbonate build-up, Sunda Basin: Indonesian Petroleum Association 14th Annual Convention Proceedings, p. 507-533.

Dodd, J. R., 1966, Processes of conversion of aragonite to calcite with examples from the Cretaceous of Texas: Journal of Sedimentary Research, v. 36, p. 733-741.

Doust, H., and R. A. Noble, 2008, Petroleum systems of Indonesia: Marine and Petroleum Geology, v. 25, p. 103-129.

Dunham, R. J., 1962, Classification of carbonate rocks according to depositional textures, *in* W. E. Ham, ed., AAPG Memoir 1: Classification of Carbonate Rocks-A Symposium: Tulsa, Oklahoma, The American Association of Petroleum Geologists, p. 108-121.

Elderfield, H., 1981, Metal-organic associations in interstitial waters of Narragansett Bay sediments: American Journal of Science, v. 281, p. 1184-1196.

Ellis, P. M., 1986, Post-Miocene Carbonate Diagenesis of the Lower Cretaceous Edwards Group in the Balcones Fault Zone Area, South-Central Texas, *in* P. L. Abbott, and C. M. J. Woodruff, eds., The Balcones Escarpment: San Antonio, Texas, Geological Society of America Annual Meeting, p. 101-114.

Embry, A. F., and J. E. Klovan, 1971, A late Devonian reef tract on northeastern Banks Island, N.W.T: Bulletin of Canadian Petroleum Geology, v. 19, p. 730-781.

Enos, P., and L. H. Sawatsky, 1981, Pore networks in Holocene carbonate sediments: Journal of Sedimentary Petrology, v. 51, p. 961-985.

Epting, M., 1980, Sedimentology of Miocene carbonate buildups, central Luconia, offshore Sarawak: Bulletin of the Geological Society of Malaysia, v. 12, p. 17-30.

Evamy, B., 1967, Dedolomitization and the development of rhombohedral pores in limestones: Journal of Sedimentary Petrology, v. 37, p. 1204-1215.

Ewing, T. E., 2005, Phanerozoic development of the Llano uplift: Bulletin of South Texas Geological Society, v. 45, p. 15-25.

Fisher, W. L., and P. U. Rodda, 1969, Edwards Formation (Lower Cretaceous), Texas: dolomitization in a carbonate platform system: AAPG Bulletin, v. 53, p. 55-72.

Flower, B. P., 1999, Palaeoclimatology: Warming without high CO 2?: Nature, v. 399, p. 313.

Flügel, E., 2004, Microfacies of carbonate rocks: analysis, interpretation and application: London, Springer, 984 p.

Flügel, E., 2010, Microfacies of carbonate rocks: analysis, interpretation and application: London, Springer, 984 p.

Folk, R. L., 1974, Petrology of the sedimentary rocks: Austin, Texas, Hemphil Publishing Company, 184 p.

Fournier, F., L. Montaggioni, and J. Borgomano, 2004, Paleoenvironments and high-frequency cyclicity from Cenozoic South-East Asian shallow-water carbonates: a case study from the Oligo-Miocene buildups of Malampaya (Offshore Palawan, Philippines): Marine and Petroleum Geology, v. 21, p. 1-21.

Gaina, C., and D. Müller, 2007, Cenozoic tectonic and depth/age evolution of the Indonesian gateway and associated back-arc basins: Earth-Science Reviews, v. 83, p. 177-203.

Gallagher, S. J., M. W. Wallace, C. L. Li, B. Kinna, J. T. Bye, K. Akimoto, and M. Torii, 2009, Neogene history of the West Pacific Warm Pool, Kuroshio and Leeuwin currents: Paleoceanography, v. 24, p. n/a-n/a.

Garcia-Fresca, B., F. J. Lucia, J. M. S. Jr., and C. Kerans, 2012, Outcrop-constrained hydrogeological simulations of brine reflux and early dolomitization of the Permian San Andres Formation: AAPG Bulletin, v. 96, p. 1757-1781.

Gat, J., and C. Bowser, 1991, The heavy isotope enrichment of water in coupled evaporative systems: Stable Isotope Geochemistry: A Tribute to Samuel Epstein, v. 3, p. 159-168.

Gebelein, C., R. Steinen, P. Garrett, E. Hoffman, J. Queen, and L. Plummer, 1980, Subsurface dolomitization beneath the tidal flats of central west Andros Island, Bahamas: SEPM Special Publication, v. 28, p. 31-49.

Geology, B. o. E., 1992, Geology of Texas: The University of Texas at Austin.

Geoservices, 2013, Rock description, biostratigraphy and geochemistry report, p. 293.

Gibson-Robinson, C., and H. Soedirdja, 1986, Transgressive development of Miocene reefs, Salawati Basin, Irian Jaya: Indonesian Petroleum Association 15th Annual Convention Proceedings.

Giggenbach, W., Y. Sano, and H. Wakita, 1993, Isotopic composition of helium, and CO2 and CH4 contents in gases produced along the New Zealand part of a convergent plate boundary: Geochimica et cosmochimica acta, v. 57, p. 3427-3455.

Giles, M. R., and J. D. Marshall, 1986, Constraints on the development of secondary porosity in the subsurface: re-evaluation of processes: Marine and Petroleum Geology, v. 3, p. 243-255.

Godfrey, J. S., 1996, The effect of the Indonesian throughflow on ocean circulation and heat exchange with the atmosphere: A review: Journal of Geophysical Research: Oceans, v. 101, p. 12217-12237.

Gómez, F., 2012, A checlist and classification of living Dinoflagellates (Dinoflagellata, Alveolata): CICIMAR Oceánides, v. 27, p. 65-140.

Gordon, A. L., 2005, Oceanography of the Indonesian seas and their throughflow: Oceanography v. 18, p. 14–27.

Goreau, T. F., 1963, Calcium carbonate deposition by coralline algae and corals in relation to their roles as reef-builders: Annals of the New York Academy of Sciences, v. 109, p. 127-167.

Gothmann, A. M., J. Stolarski, J. F. Adkins, B. Schoene, K. J. Dennis, D. P. Schrag, M. Mazur, and M. L. Bender, 2015, Fossil corals as an archive of secular variations in seawater chemistry since the Mesozoic: Geochimica et Cosmochimica Acta, v. 160, p. 188-208.

Gregg, J. M., S. A. Howard, and S. Mazzullo, 1992, Early diagenetic recrystallization of Holocene (< 3000 years old) peritidal dolomites, Ambergris Cay, Belize: Sedimentology, v. 39, p. 143-160.

Gresko, M., C. Suria, and S. Sinclair, 1995, Basin evolution of the Ardjuna rift system and its implications for hydrocarbon exploration, offshore Northwest Java, Indonesia: Indonesian Petroleum Association 24th Annual Convention and Exhibition Proceeedings, p. 147-161.

Grossman, E. L., 1999, Oxygen isotopes *in* C. P. Marshall, and R. W. Fairbridge, eds., The encyclopedia of geochemistry Lancaster, Kluwer Academic Publishers, p. 469-474.

Grossman, E. L., 2012, Applying Oxygen Isotope Paleothermometry in Deep Time, *in* L. C. Ivany, and B. T. Huber, eds., Reconstructing Earth's Deep-Time Climate—The State of the Art in 2012, v. Paleontological Society Short Course, The Paleontological Society Papers, p. 39-67.

Grove, C., and D. A. Jerram, 2011, jPOR: An ImageJ macro to quantify total optical porosity from blue-stained thin sections: Computers & Geosciences, v. 37, p. 1850-1859.

Grover Jr, G., and J. Read, 1978, Fenestral and associated vadose diagenetic fabrics of tidal flat carbonates, Middle Ordovician New Market Limestone, southwestern Virginia: Journal of Sedimentary Petrology, v. 48, p. 453-473.

Guillem, M.-V., P. Hallock, and M. Brandano, 2008, A depositional model and paleoecological reconstruction of the lower Tortonian distally steepened ramp of Menorca (Balearic Islands, Spain): Palaios, v. 23, p. 465-481.

Hackett, J. D., D. M. Anderson, D. L. Erdner, and D. Bhattacharya, 2004, Dinoflagellates: a remarkable evolutionary experiment: American Journal of Botany, v. 91, p. 1523-1534.

Hadi, T., and B. Simbolon, 1976, The carbonate rocks of the Baturaja formation in its locality, Baturaja - south Sumatra: Indonesian Petroleum Association Proceedings of the Carbonate Seminar, p. 67-78.

Halfar, J., and M. Mutti, 2005, Global dominance of coralline red-algal facies: a response to Miocene oceanographic events: Geology, v. 33, p. 481-484.

Hall, R., 2002, Cenozoic geological and plate tectonic evolution of SE Asia and the SW Pacific: computer-based reconstructions, model and animations: Journal of Asian Earth Sciences, v. 20, p. 353-431.

Hall, R., 2012, Late Jurassic–Cenozoic reconstructions of the Indonesian region and the Indian Ocean: Tectonophysics, v. 570-571, p. 1-41.

Halley, R. B., and P. R. Rose, 1977, Significance of Fresh-Water Limestone in Marine Carbonate Successions of Pleistocene and Cretaceous Age, *in* D. G. Bebout, and R. G. Loucks, eds., Cretaceous Carbonates of Texas and Mexico, Application to Subsurface Exploration: Austin, Texas, Bureu of Economic Geology The University of Texas at Austin, p. 206-215.

Hallock, P., 1999, Symbiont-bearing foraminifera, *in* B. K. S. Gupta, ed., Modern foraminifera, Springer, p. 123-139.

Haq, B. U., J. Hardenbol, and P. R. Vail, 1987, Chronology of Fluctuating Sea Levels Since the Triassic: Science, v. 235, p. 1156-1167.

Helper, M., 2006, Geologic map of north-central Mason County, Texas (1:100,000): The University of Texas at Austin.

Hesse, R., 1988, Diagenesis #13 Origin of chert: diagenesis of biogenic siliceous sediments: Geoscience Canada, v. 15, p. 171-192.

Hesse, R., 1989, Silica diagenesis: origin of inorganic and replacement cherts: Earth-Science Reviews, v. 26, p. 253-284.

Hsü, K. J., and C. Siegenthaler, 1969, Preliminary experiments on hydrodynamic movement induced by evaporation and their bearing on the dolomite problem: Sedimentology, v. 12, p. 11-25.

Hudson, J., 1977, Stable isotopes and limestone lithification: Journal of the Geological Society, v. 133, p. 637-660.

Hudson, J., 1982, Pyrite in ammonite-bearing shales from the Jurassic of England and Germany: Sedimentology, v. 29, p. 639-667.

IIAPCO, 1986, Pertamina - IIAPCO offshore southeast Sumatra contract area Sunda basin re-evaluation study: Phase two, Jakarta, Indonesia, IIAPCO, p. 1-207.

Illing, L., 1959, 2 Deposition and Diagenesis of Some Upper Palaeozoic Carbonate Sediments in Western Canada: 5th World Petroleum Congress.

Irwin, W. P., and I. Barnes, 1980, Tectonic relations of carbon dioxide discharges and earthquakes: Journal of Geophysical Research: Solid Earth, v. 85, p. 3115-3121.

Jacka, A. D., 1977, Deposition and Diagenesis of the Fort Terrett Formation (Edwards Group) in the Vicinity of Junction, Texas, *in* D. G. Bebout, and R. G. Loucks, eds., Cretaceous Carbonates of Texas and Mexico, Application to Subsurface Exploration: Austin, Texas, Bureu of Economic Geology, The University of Texas at Austin, p. 182-199.

James, N. P., and P. W. Choquette, 1984, Diagenesis 9. Limestones-the meteoric diagenetic environment: Geoscience Canada, v. 11.

James, N. P., and B. Jones, 2015, Origin of Carbonate Rocks, John Wiley & Sons.

Johnson, M. D., and R. C. Carpenter, 2012, Ocean acidification and warming decrease calcification in the crustose coralline alga Hydrolithon onkodes and increase susceptibility to grazing: Journal of Experimental Marine Biology and Ecology, v. 434, p. 94-101.

Jones, B., and I. G. Hunter, 1994, Evolution of an isolated carbonate bank during Oligocene, Miocene and Pliocene times, Cayman Brac, British west Indies: Facies, v. 30, p. 25-50.

Jones, G. D., and Y. Xiao, 2005, Dolomitization, anhydrite cementation, and porosity evolution in a reflux system: Insights from reactive transport models: AAPG Bulletin, v. 89, p. 577-601.

Kaczmarek, S. E., S. M. Fullmer, and F. J. Hasiuk, 2015, A universal classification scheme for the microcrystals that host limestone microporosity: Journal of Sedimentary Research, v. 85,

p. 1197-1212.

Kah, L. C., J. K. Bartley, and D. A. Teal, 2012, Chemostratigraphy of the Late Mesoproterozoic Atar Group, Taoudeni Basin, Mauritania: Muted isotopic variability, facies correlation, and global isotopic trends: Precambrian Research, v. 200, p. 82-103.

Kaplan, I., K. Emery, and S. Rittenbebg, 1963, The distribution and isotopic abundance of sulphur in recent marine sediments off southern California: Geochimica et Cosmochimica Acta, v. 27, p. 297-331.

Katz, A., 1971, Zoned dolomite crystals: The Journal of Geology, v. 79, p. 38-51.

Kaufman, J., H. S. Cander, L. D. Daniels, and W. J. Meyers, 1988, Calcite cement stratigraphy and cementation history of the Burlington-Keokuk Formation (Mississippian), Illinois and Missouri: Journal of Sedimentary Research, v. 58.

Knauth, L. P., 1979, A model for the origin of chert in limestone: Geology, v. 7, p. 274-277.

Koesoemadinata, R. P., and A. Pulunggono, 1974, Offshore Tertiary sedimentary basins in Indonesia: Proceedings ITB, p. 91-108.

Kovacs, P. P., 1982, Rama Reservoir Model Study, Offshore South East Asia 82 Conference, Society of Petroleum Engineers.

Kuhnt, W., A. Holbourn, R. Hall, M. Zuvela, and R. Käse, 2004, Neogene history of the Indonesian throughflow, *in* P. Clift, W. Kuhnt, P. Wang, and D. Hayes, eds., Continent-ocean interactions within east Asian marginal seas: Geophysical Monograph Series, v. 149: Washington, D. C., American Geophysical Union, p. 337.

Land, L., 1973, Contemporaneous Dolomitization of Middle Pleistocene Reefs by Meteoric Water, North Jamaica: Bulletin of Marine Science, v. 23, p. 64-92.

Land, L. S., 1985, The origin of massive dolomite: Journal of Geological Education, v. 33, p. 112-

125.

LAPI-ITB, 2012, A study on the petroleum geochemistry of northwest and north central Java, p. 240.

Larue, R., 1976, The Baturaja formation of the Sunda sub-basin area: Indonesian Petroleum Association, Proceedings of the carbonate seminar, p. 118.

Lawton, T. S., 2008, Laramide sedimentary basins, *in* A. D. Miall, ed., Sedimentary basins of the world, v. 5: Amsterdam, Elsevier, p. 429-450.

Lemigas, 1990, Full core photography of C-1 well

Linthout, K., H. Helmers, and J. Sopaheluwakan, 1997, Late Miocene obduction and microplate migration around the southern Banda Sea and the closure of the Indonesian Seaway: Tectonophysics, v. 281, p. 17-30.

Liu, W., Y. Xu, M. Tao, and X. Zhang, 2011, Helium and argon isotope geochemistry of natural gases in China's petroliferous basins: Chinese Journal of Geochemistry, v. 30, p. 19-32.

Longman, M. W., 1980, Carbonate diagenetic textures from nearsurface diagenetic environments: AAPG bulletin, v. 64, p. 461-487.

Longman, M. W., 1994, Characteristics of tertiary carbonate reservoirs in Southeast Asia: HGS Dinner Meeting, p. 11.

Longman, M. W., and P. A. Mench, 1978, Diagenesis of Cretaceous limestones in the Edwards aquifer system of south-central Texas: a scanning electron microscope study: Sedimentary Geology, v. 21, p. 241-276.

Lowenstam, H. A., 1950, Niagaran Reefs of the Great Lakes Area: The Journal of Geology, v. 58, p. 430-487.

LPPM-ITB, and Pertamina-EP, 2006, Studi sedimentasi dan karakterisasi sesar daerah KRB-

MLB-TTM, p. 1-121.

Lucia, F. J., 1962, Diagenesis of a crinoidal sediment: Journal of Sedimentary Petrology, v. 32, p. 848-865.

Machel, H. G., 2000, Application of cathodoluminescence to carbonate diagenesis, *in* M. Pagel, V. Barbin, and P. Blanc, eds., Cathodoluminescence in geosciences: Berlin, Springer-Verlag, p. 271-301.

Machel, H. G., 2004, Concepts and models of dolomitization: a critical reappraisal: Geological Society, London, Special Publications, v. 235, p. 7-63.

Machel, H. G., 2005, Investigations of burial diagenesis in carbonate hydrocarbon reservoir rocks: Geoscience Canada, v. 32.

Maclay, R. W., 1995, Geology and hydrology of the Edwards Aquifer in the San Antonio area, Texas, Water-resources investigations 95-4186, Austin, Texas, US Geological Survey, p. 1-64.

Maliva, R. G., and R. Siever, 1989, Nodular chert formation in carbonate rocks: The Journal of Geology, v. 97, p. 421-433.

Manaf, N. A., 2017, The exploration challenges and opportunities left in the mature of the west Java basin area, Indonesia: Search and Discovery Article #90291 AAPG Annual Convention and Exhibition

Mattes, B. W., and E. W. Mountjoy, 1980, Burial dolomitization of the upper devonian miette buildup, Jasper National Park, Alberta.

Mazzullo, S., 2000, Organogenic dolomitization in peritidal to deep-sea sediments: Journal of Sedimentary Research, v. 70, p. 10-23.

Mazzullo, S., 2004, Overview of porosity evolution in carbonate reservoirs: Kansas Geological

Society Bulletin, v. 79, p. 20-28.

Mazzullo, S., and B. A. Birdwell, 1989, Syngenetic formation of grainstones and pisolites from fenestral carbonates in peritidal settings: Journal of Sedimentary Petrology, v. 59, p. 605-611.

Mazzullo, S., and P. Harris, 1992, Mesogenetic dissolution: its role in porosity development in carbonate reservoirs (1): AAPG bulletin, v. 76, p. 607-620.

McConchie, D., J. Ward, V. McCann, and D. Lewis, 1979, A Mossbauer investigation of glauconite and its geological significance: CLAYS CLAY MINER. Clays Clay Miner., v. 27, p. 339.

Mench, P. A., J. Pearson, F.J., and R. G. Deike, 1980, Stable isotope evidence for modern freshwater diagenesis of the Cretaceous Edwards Limestone, San Antonio area, Texas (abstract): AAPG Bulletin, v. 64, p. 749.

Meyers, G., 1996, Variation of Indonesian throughflow and the El Niño-Southern Oscillation: Journal of Geophysical Research: Oceans, v. 101, p. 12255-12263.

Meyers, W. J., 1991, Calcite cement stratigraphy: an overview.

Miall, A. D., and R. C. Blakey, 2008, The Phanerozoic Tectonic and Sedimentary Evolution of North America, *in* A. D. Miall, ed., Sedimentary Basins of the World, v. 5: Amsterdam, Elsevier, p. 1-29.

Miller, K. G., J. D. Wright, and R. G. Fairbanks, 1991, Unlocking the ice house: Oligocene-Miocene oxygen isotopes, eustasy, and margin erosion: Journal of Geophysical Research: Solid Earth, v. 96, p. 6829-6848.

Miller, N. R., and J. G. Kaldi, 1990, Strontium isotope chronostratigraphy and diagenesis of the Batu Raja Limestone, offshore Northwest Java, Indonesia (abstract), AAPG Search and

Discovery Article #90999.

Moore, C. H., 1989, Carbonate diagenesis and porosity, v. 46, Elsevier.

Moore, D. W., 2010, Geologic map of the Edwards aquifer and related rocks in northeastern Kinney and southernmost Edwards counties, south-central Texas: Reston, Virginia, US Geological Survey.

Mosher, S., 1998, Tectonic evolution of the southern Laurentian Grenville orogenic belt: Geological Society of America Bulletin, v. 110, p. 1357-1375.

Murray, R., and F. Lucia, 1967, Cause and control of dolomite distribution by rock selectivity: Geological Society of America Bulletin, v. 78, p. 21-36.

Nash, M., U. Troitzsch, B. Opdyke, J. Trafford, B. Russell, and D. Kline, 2011, Biomineralization of dolomite and magnesite discovered in tropical coralline algae: a biological solution to the geological dolomite problem.

Nash, M. C., B. N. Opdyke, U. Troitzsch, B. D. Russell, W. H. Adey, A. Kato, G. Diaz-Pulido, C. Brent, M. Gardner, and J. Prichard, 2013, Dolomite-rich coralline algae in reefs resist dissolution in acidified conditions: Nature Climate Change, v. 3, p. 268.

Nash, M. C., S. Uthicke, A. P. Negri, and N. E. Cantin, 2015, Ocean acidification does not affect magnesium composition or dolomite formation in living crustose coralline algae, <i>Porolithon onkodes</i> in an experimental system: Biogeosciences, v. 12, p. 5247-5260.

Nelson, C. S., and A. M. Smith, 1996, Stable oxygen and carbon isotope compositional fields for skeletal and diagenetic components in New Zealand Cenozoic nontropical carbonate sediments and limestones: a synthesis and review: New Zealand Journal of Geology and Geophysics, v. 39, p. 93-107.

Netherwood, R., 2000, A geological overview of Indonesia: Indonesia Reservoir Optimization Conference, p. 173-277.

Netherwood, R., 2000, A geological overview of Indonesia: Overview of Indonesia's oil and gas industry - Geology, p. 174-.

Nishimura, S., and S. Suparka, 1997, Tectonic approach to the Neogene evolution of Pacific-Indian Ocean seaways: Tectonophysics, v. 281, p. 1-16.

Noble, J., and D. Van Stempvoort, 1989, Early burial quartz authigenesis in Silurian platform carbonates, New Brunswick, Canada: Journal of Sedimentary Research, v. 59.

Noble, R. A., K. H. Pratomo, K. Nugrahanto, A. M. T. Brahim, I. Prasetya, N. Mujahidin, C. H. Wu, and J. V. C. Howes, 1997, Petroleum systems of northwest Java, Indonesia: Indonesian Petroleum Association Proceedings of the Petroleum Systems of SE Asia and Australasia Conference.

Noisette, F., H. Egilsdottir, D. Davoult, and S. Martin, 2013, Physiological responses of three temperate coralline algae from contrasting habitats to near-future ocean acidification: Journal of Experimental Marine Biology and Ecology, v. 448, p. 179-187.

Padmono, J., E. Hartanto, A. Sukmatiawan, A. Prasetyo, A. Prasetya, A. Krisnandya, T. Hendriansyah, and N. Yudhandono, 2008, Tectonic Fractures Analysis of Carbonate Baturaja Formation, Pondok Tengah Field Using Coherence Attributes.

Padmono, J., E. Hartanto, A. Sukmatiawan, A. Prasetyo, A. Prasetya, A. Krisnandya, T. Hendriansyah, and N. Yudhandono, 2008, Tectonic fractures analysis of carbonate Baturaja formation, Pondok Tengah field using coherence attributes: Indonesian Petroleum Association 32nd Annual Convention and Exhibition Proceeedings.

Pagani, M., J. C. Zachos, K. H. Freeman, B. Tipple, and S. Bohaty, 2005, Marked decline in atmospheric carbon dioxide concentrations during the Paleogene: Science, v. 309, p. 600-603.

Pandey, V. K., and A. C. Pandey, 2006, Heat transport through Indonesian throughflow: Indian Geophysical Union, v. 10, p. 273-277.

Park, R. K., P. D. Crevello, and W. Hantoro, 2010, Equatorial carbonate depositional systems of Indonesia, *in* W. A. Morgan, A. D. George, P. M. Harris, J. A. Kupecz, and J. F. Sarg, eds., Cenozoic Carbonate Systems of Australasia SEPM Special Publication, v. 95, SEPM (Society for Sedimentary Geology), p. 41–77.

Park, R. K., A. Matter, and P. C. Tonkin, 1995, Porosity evolution in the Baturaja carbonates of the Sunda basin - Windows of opportunity: Indonesian Petroleum Association 24th Annual Convention Proceeedings.

Park, R. K., C. T. Siemers, and A. A. Brown, 1992, Holocene carbonate sedimentation, Pulau Seribu, Java Sea—the third dimension: Indonesian Petroleum Association Carbonate Rocks and Reservoirs of Indonesia: A Core Workshop.

Pascual-Cebrian, E., S. Götz, T. Bover-Arnal, P. W. Skelton, E. Gili, R. Salas, and W. Stinnesbeck, 2016, Calcite/aragonite ratio fluctuations in Aptian rudist bivalves: Correlation with changing temperatures: Geology, v. 44, p. 135-138.

Patmosukismo, S., and I. Yahya, 1974, The basement configuration of the north west Java area: Indonesian Petroleum Association 3rd Annual Convention Proceedings, p. 129-152.

Payne, J. H., and A. J. Scott, 1982, Facies analysis of the Cretaceous Hensel formation, response of a fluvial system to a marine transgression: Gulf Coast Association of Geological Societies Transactions, v. 32, p. 92-100.

Perkins, R. D., G. S. Dwyer, D. B. Rosoff, P. A. Fuller, and R. M. Lloyd, 1994, Salina

Sedimentation and Diagenesis: West Caicos Island, British West Indies, *in* B. Purser, M. E. Tucker, and D. Zenger, eds., Dolomites: A Volume in Honour of Dolomieu, v. Special Publication, The International Association of Sedimentologists: Oxford, London, The International Association of Sedimentologists, p. 35-54.

Pertamina, and BEICIP, 1985, Hydrocarbon potential of western Indonesia, Pertamina, p. 1-70.

Pertamina EP, 2014, Petrophysical evaluation of J-2 well

Phelps, R. M., C. Kerans, R. G. Loucks, R. O. Da Gama, J. Jeremiah, and D. Hull, 2014, Oceanographic and eustatic control of carbonate platform evolution and sequence stratigraphy on the Cretaceous (Valanginian–Campanian) passive margin, northern Gulf of Mexico: Sedimentology, v. 61, p. 461-496.

PHE-ONWJ, and Pertamina-EP, 2015, Regional geological cross section transition zone.

Pinti, D. L., and B. Marty, 2000, Noble gases in oil and gas fields: origins and processes: Fluids Basin Evolution, p. 160-196.

Pittman, E. D., 1971, Microporosity in carbonate rocks: AAPG Bulletin, v. 55, p. 1873-1878.

Pittman Jr, J., 1959, Silica in Edwards Limestone, Travis County, Texas: Society of Economic Paleontologists and Mineralogists, v. Silica in Sediments (SP7), p. 121-134.

Pochon, X., J. I. Montoya-Burgos, B. Stadelmann, and J. Pawlowski, 2006, Molecular phylogeny, evolutionary rates, and divergence timing of the symbiotic dinoflagellate genus Symbiodinium: Molecular Phylogenetics and Evolution, v. 38, p. 20-30.

Pomar, L., 2001, Types of carbonate platforms: a genetic approach: Basin Research, v. 13, p. 313-334.

Pomar, L., J. I. Baceta, P. Hallock, G. Mateu-Vicens, and D. Basso, 2017, Reef building and carbonate production modes in the west-central Tethys during the Cenozoic: Marine and

Petroleum Geology, v. 83, p. 261-304.

Pomar, L., M. Brandano, and H. Westphal, 2004, Environmental factors influencing skeletal grain sediment associations: a critical review of Miocene examples from the western Mediterranean: Sedimentology, v. 51, p. 627-651.

Pomar, L., M. Esteban, W. Martinez, D. Espino, V. C. de Ott, L. Benkovics, and T. C. Leyva, 2015, Oligocene–Miocene carbonates of the Perla Field, Offshore Venezuela: Depositional model and facies architecture.

Pomar, L., and P. Hallock, 2007, Changes in coral-reef structure through the Miocene in the Mediterranean province: Adaptive versus environmental influence: Geology, v. 35, p. 899-902.

Pomar, L., and P. Hallock, 2008, Carbonate factories: a conundrum in sedimentary geology: Earth-Science Reviews, v. 87, p. 134-169.

Pomar, L., G. Mateu-Vicens, M. Morsilli, and M. Brandano, 2014, Carbonate ramp evolution during the late Oligocene (Chattian), Salento Peninsula, southern Italy: Palaeogeography, Palaeoclimatology, Palaeoecology, v. 404, p. 109-132.

Pomar, L., M. Morsilli, P. Hallock, and B. Bádenas, 2012, Internal waves, an under-explored source of turbulence events in the sedimentary record: Earth-Science Reviews, v. 111, p. 56-81.

Ponto, C. V., C. H. Wu, A. Pranoto, and W. H. Stinson, 1988, Improved interpretation of the Talang Akar formation depositional environment as and aid to hydrocarbon exploration in the ARII offshore northwest Java contract area: Indonesian Petroleum Association 17th Annual Convention Proceeedings.

Pppelreiter, M., M. A. Balzarini, P. De Sousa, S. Engel, M. Galarraga, B. Hansen, X. Marquez, J.

Morell, R. Nelson, and F. Rodriguez, 2005, Structural control on sweet-spot distribution in a carbonate reservoir: Concepts and 3-D models (Cogollo Group, Lower Cretaceous, Venezuela): AAPG bulletin, v. 89, p. 1651-1676.

Pratt, B. R., 2010, Peritidal carbonates, *in* N. P. James, and R. W. Dalrymple, eds., Facies Models 4: Geotext 6: Canada, Geological Association of Canada, p. 401-420.

Pulunggono, A., 1976, Tertiary carbonates distribution and oil potential in Indonesia: Indonesian Petroleum Association Proceedings of the Carbonate Seminar, p. 6-12.

Quaranta, F., L. Tomassetti, G. Vannucci, and M. Brandano, 2012, Coralline algae as environmental indicators: a case study from the Attard member (Chattian, Malta): Geodiversitas, v. 34, p. 151-166.

Railsback, L. B., 1993, Lithologic controls on morphology of pressure-dissolution surfaces (stylolites and dissolution seams) in Paleozoic carbonate rocks from the mideastern United States: Journal of Sedimentary Petrology, v. 63, p. 513-522.

Rao, R., and S. Talukdar, 1980, Petroleum geology of Bombay high field, India, *in* M. T. Halbouty, ed., Giant Oil and Gas Fields of the Decade 1968-1978, v. 30: Tulsa, Oklahoma The American Association of Petroleum Geologists, p. 487-506.

Reeder, R. J., 1991, An overview of zoning in carbonate minerals, *in* C. E. Barker, and O. C. Kopp, eds., SEPM Short Course Notes Luminescence Microscopy and Spectroscopy: Qualitative and Quantitative Applications (SC25), v. 25: Dallas, Texas, SEPM, p. 77-82.

Riding, R., 2002, Structure and composition of organic reefs and carbonate mud mounds: concepts and categories: Earth-Science Reviews, v. 58, p. 163-231.

Ries, J. B., 2006, Mg fractionation in crustose coralline algae: geochemical, biological, and sedimentological implications of secular variation in the Mg/Ca ratio of seawater:

Geochimica et Cosmochimica Acta, v. 70, p. 891-900.

Ries, J. B., 2011, Skeletal mineralogy in a high-CO 2 world: Journal of Experimental Marine Biology and Ecology, v. 403, p. 54-64.

Rodgers, K. B., M. Latif, and S. Legutke, 2000, Sensitivity of equatorial Pacific and Indian Ocean watermasses to the position of the Indonesian Throughflow: Geophysical Research Letters, v. 27, p. 2941-2944.

Rose, P. R., 1972, Edwards group, surface and subsurface, central Texas: Austin, Texas, Bureu of Economic Geology, The University of Texas at Austin.

Saller, A. H., and N. Henderson, 1998, Distribution of porosity and permeability in platform dolomites: insight from the Permian of west Texas: AAPG Bulletin, v. 82, p. 1528-1550.

Saller, A. H., and N. Henderson, 2001, Distribution of porosity and permeability in platform dolomites: Insight from the Permian of west Texas: Reply: AAPG Bulletin, v. 85, p. 530-532.

Santodomingo, N., W. Renema, and K. G. Johnson, 2016, Understanding the murky history of the Coral Triangle: Miocene corals and reef habitats in East Kalimantan (Indonesia): Coral Reefs, v. 35, p. 765-781.

Satyana, A. H., 2005, Oligo-Miocene carbonates of Java, Indonesia: tectonic-volcanic setting and petroleum implications: Indonesian Petroleum Association 30th Annual Convention Proceeedings, p. 217-249.

Satyana, A. H., C. Armandita, B. Raharjo, and I. Syafri, 2002, New observations on the evolution of the Bogor basin, west Java: Opportunities for turbidite hydrocarbon play: Buletin Geologi Institut Teknologi Bandung – Edisi Khusus, p. 1-16.

Satyana, A. H., and M. E. M. Purwaningsih, 2003, Oligo-Miocene carbonates of Java: Tectonic setting and effects of volcanims: The 32nd IAGI and 28th HAGI Annual Convention and Exhibition Proceedings of Joint Convention.

Satyana, A. H., and M. E. M. Purwaningsih, 2013, Variability of Paleogene source facies of circum-Sundaland basins, western Indonesia: Tectonic, sedimentary and geochemical constraints - Implication for oil characteristic: Indonesian Petroleum Association 37th Annual Convention and Exhibition Proceeedings.

Schlager, W., 2005, Carbonate sedimentology and sequence stratigraphy, SEPM Soc for Sed Geology.

Schlanger, S. O., and H. Jenkyns, 2007, Cretaceous oceanic anoxic events: causes and consequences: Netherlands Journal of Geosciences/Geologie en Mijnbouw, v. 55, p. 179-184.

Scholle, P. A., and D. S. Ulmer-Scholle, 2003, A color guide to the petrography of carbonate rocks: grains, textures, porosity, diagenesis: AAPG Memoir 77: Tulsa, Oklahoma, The American Association of Petroleum Geologists.

Schuhmacher, H., and H. Zibrowius, 1985, What is hermatypic?: Coral Reefs, v. 4, p. 1-9.

Scotese, C., A. Boucot, and W. McKerrow, 1999, Gondwanan palaeogeography and paleoclimatology: Journal of African Earth Sciences, v. 28, p. 99-114.

Sellards, E. H., W. S. Adkins, and F. B. Plummer, 1932, The Geology of Texas: Stratigraphy, v. The University of Texas Bulletin: Austin, Texas, Bereu of Economic Geology.

Semesi, I. S., J. Kangwe, and M. Björk, 2009, Alterations in seawater pH and CO2 affect calcification and photosynthesis in the tropical coralline alga, Hydrolithon sp.(Rhodophyta): Estuarine, Coastal and Shelf Science, v. 84, p. 337-341.

Setyowiyoto, J., B. E. B. Nurhandoko, A. Samsuri, B. Widjanarkko, and Thurisina, 2007, Influence of porosity and facies of Baturaja carbonate to the seismic wave velocity: case study of Tambun field west Java: Indonesian Petroleum Association 31st Annual Convention and Exhibition Proceeedings.

Setyowiyoto, J., B. E. B. Nurhandoko, A. Samsuri, and B. Widjanarko, 2007, Influence of Porosity and Facies of Baturaja Carbonate to the Seismic Wave Velocity: Case Study of Tambun Field West Java.

Shen, A., M. She, A. Hu, L. Pan, and J. Lu, 2016, Scale and distribution of marine carbonate burial dissolution pores: Journal of Natural Gas Geoscience, v. 1, p. 187-193.

Shinn, E. A., 1968, Practical significance of birdseye structures in carbonate rocks: Journal of Sedimentary Petrology, v. 38, p. 215-223.

Shinn, E. A., and D. M. Robbin, 1983, Mechanical and chemical compaction in fine-grained shallow-water limestones: Journal of Sedimentary Petrology, v. 53, p. 595-618.

Sibley, D. F., and J. M. Gregg, 1987, Classification of dolomite rock textures: Journal of Sedimentary Petrology, v. 57, p. 967-975.

Simms, M. A., 1985, Diagenesis by Kohout Convection in Carbonate Platform Margins: Gulf Coast Association of Geological Societies Transactions (abstract), v. 35, p. 493.

Sprintall, J., and A. Révelard, 2014, The Indonesian Throughflow response to Indo-Pacific climate variability: Journal of Geophysical Research: Oceans, v. 119, p. 1161-1175.

Sribudiyani, N. Muchsin, R. Ryacudu, T. Kunto, P. Astono, I. Prasetya, B. Sapiie, S. Asikin, A. H. Harsolumakso, and I. Yulianto, 2003, The collision of the east Java microplate and its implication for hydrocarbon occurences in the east Java basin: Indonesian Petroleum Association 29th Annual Convention and Exhibition Proceeedings.

Stanley, S. M., and L. A. Hardie, 1998, Secular oscillations in the carbonate mineralogy of reef-building and sediment-producing organisms driven by tectonically forced shifts in seawater chemistry: Palaeogeography, Palaeoclimatology, Palaeoecology, v. 144, p. 3-19.

Steneck, R. S., 1986, The ecology of coralline algal crusts: convergent patterns and adaptative strategies: Annual review of ecology and systematics, v. 17, p. 273-303.

Steuber, T., and H. Löser, 2000, Species richness and abundance patterns of Tethyan Cretaceous rudist bivalves (Mollusca: Hippuritacea) in the central-eastern Mediterranean and Middle East, analysed from a palaeontological database: Palaeogeography, Palaeoclimatology, Palaeoecology, v. 162, p. 75-104.

Sudamono, S. T., and B. Eza, 1997, Paleogene basin development in Sundaland and its role to the petroleum systems in western Indonesia: Indonesian Petroleum Association Proceedings of the Petroleum Systems of SE Asia and Australasia Conference, p. 545-560.

Sukmono, S., D. Santoso, A. Samodra, W. Waluyo, and S. Tjiptoharsono, 2006, Integrating seismic attributes for reservoir characterization in Melandong Field, Indonesia: The Leading Edge, v. 25, p. 532-538.

Suyono, K. Sahudi, and I. Prasetya, 2005, Exploration in west Java: Play concepts in the past, present and future, efforts to maintain reserves growth: Indonesian Petroleum Association 30th Annual Convention and Exhibition Proceeedings, p. 267-281.

Swart, P. K., 2015, The geochemistry of carbonate diagenesis: The past, present and future: Sedimentology, v. 62, p. 1233-1304.

Taylor, F. J. R., M. Hoppenrath, and J. F. Saldarriaga, 2008, Dinoflagellate diversity and distribution: Biodiversity & Conservation, v. 17, p. 407-418.

Tonkin, P. C., A. Temansji, and R. K. Park, 1992, Reef complex lithofacies and reservoir, Rama field, Sunda basin, southeast Sumatra, Indonesia: Indonesian Petroleum Association

Carbonate Rocks and Reservoirs of Indonesia: A Core Workshop, p. 7-1 - 7-32.

Tripati, A. K., C. D. Roberts, and R. A. Eagle, 2009, Coupling of CO2 and ice sheet stability over major climate transitions of the last 20 million years: science, v. 326, p. 1394-1397.

Triplehorn, D., 1965, Origin and significance of glauconite in the geologic sequence: Tulsa Geological Society Digest, v. 33, p. 282-283.

Tsuchi, R., 1997, Marine climatic responses to Neogene tectonics of the Pacific Ocean seaways: Tectonophysics, v. 281, p. 113-124.

Tucker, M. E., 1986, Formerly aragonitic limestones associated with tillites in the late Proterozoic of Death Valley, California: Journal of Sedimentary Petrology, v. 56, p. 818-830.

Tucker, M. E., and V. P. Wright, 1990, Carbonate sedimentology: Malden, Massachusetts, Blackwell Science Ltd., 482 p.

Turner, N., and H. Zhong, 1996, The Lower Miocene Liuhua Carbonate Reservoir, Pearl River Mouth Basin, Offshore Peoples Republic of China: Circum-Pacific Energy and Mineral Resources Conference Transactions, p. 657-666.

Udgata, D., 2007, Glauconite as an indicator of sequence stratigraphic packages in a lower Paleocene passive-margin shelf succession, Central Alabama: Thesis thesis, Auburn University, Auburn, Alabama, 124 p.

van Buchem, F. S. P., T. L. Allan, G. V. Laursen, M. Lotfpour, A. Moallemi, S. Monibi, H. Motiei, N. A. H. Pickard, A. R. Tahmasbi, V. Vedrenne, and B. Vincent, 2010, Regional stratigraphic architecture and reservoir types of the Oligo-Miocene deposits in the Dezful Embayment (Asmari and Pabdeh Formations) SW Iran: Geological Society, London, Special Publications, v. 329, p. 219-263.

Vasconcelos, C., and J. A. McKenzie, 1997, Microbial mediation of modern dolomite precipitation and diagenesis under anoxic conditions (Lagoa Vermelha, Rio de Janeiro, Brazil): Journal of sedimentary Research, v. 67, p. 378-390.

Vasconcelos, C., J. A. McKenzie, R. Warthmann, and S. M. Bernasconi, 2005, Calibration of the $\delta^{18}O$ paleothermometer for dolomite precipitated in microbial cultures and natural environments: Geologi, v. 33, p. 317-320.

Veizer, J., 1983, Chemical diagenesis of carbonates: theory and application of trace element technique: SEPM Stable Isotope in Sedimentary Geology (SC10), v. 10, p. 1-100.

Veizer, J., 1992, Depositional and diagenetic history of limestones: stable and radiogenic isotopes, *in* N. Clauer, and S. Chauduri, eds., Isotopic signatures and sedimentary records: Lecture Notes in Earth Sciences, v. 43: Berlin, Germany, Springer, p. 13-48.

Vranes, K., A. L. Gordon, and A. Ffield, 2002, The heat transport of the Indonesian Throughflow and implications for the Indian Ocean heat budget: Deep Sea Research Part II: Topical Studies in Oceanography, v. 49, p. 1391-1410.

Walker, N., 1992, Middle Proterozoic Geologic Evolution of Llano Uplift, Texas: Evidence from U-Pb zircon Geochronometry: Geological Society of America Bulletin, v. 104, p. 494-504.

Warren, J., 2000, Dolomite: occurrence, evolution and economically important associations: Earth-Science Reviews, v. 52, p. 1-81.

Welch, C. L., 2001, Petrography and geochemistry of dolomites in the lower Cretaceous Edwards Formation, Taylor County, Texas, Texas Tech University, 116 p.

Whitaker, F. F., P. L. Smart, and G. D. Jones, 2004, Dolomitization: from conceptual to numerical model, *in* C. J. R. Braithwaite, G. Rizzi, and G. Darke, eds., The geometry and petrogenesis of dolomite hydrocarbon reservoirs: Special Publications, v. 235: London, Geological Society, p. 99-139.

Whitaker, F. F., P. L. Smart, and G. D. Jones, 2004, Dolomitization: from conceptual to numerical models, *in* C. J. R. Braithwaite, G. Rizzl, and G. Darke, eds., The geometry and petrogenesis of dolomite hydrocarbon reservoir, v. 235: London, Geological Society of London, p. 99-139.

Wibowo, A. W., A. Pujianto, W. Hindadari, R. Raguwanti, and Y. F. Yushendri, 2013, Density analysis to predict carbonate reservoirs in volcanic clastic environment, implications for field development: AAPG Search and Discovery Article #90166 International Conference & Exhibition.

Wicaksono, P., A. M. R. Wight, W. R. Lodwick, R. E. Netherwood, B. Budiarto, and D. Hanggoro, 1995, Use of sequence stratigraphy in carbonate exploration : Sunda basin, Java sea, Indonesia: Indonesian Petroleum Association Proceeedings of the International Symposium on Sequence Stratigraphy in SE Asia, p. 197-229.

Widodo, R. W., and J. C. Laya, 2017, Controls on diagenesis and dolomitization of peritidal facies, Early Cretaceous Lower Edwards Group, central Texas, USA: Facies, v. 63, p. 23.

Wieckzorek, J., 1979, Geopetal structures as indicators of top and bottom: Rocznik Polskiego Towarzystwa Geologicznego Annales de la Societe Geologique de Pologne, p. 215-221.

Wiggins, W. D., 1986, Geochemical signatures in carbonate matrix and their relation to deposition and diagenesis, Pennsylvanian Marble Falls Limestone, central Texas: Journal of Sedimentary Research, v. 56.

Wight, A., H. Friestad, I. Anderson, P. Wicaksono, and C. Reminton, 1997, Exploration history of the offshore Southeast Sumatra PSC, Java Sea, Indonesia: Geological Society, London, Special Publications, p. 121-142.

Wight, A., and I. A. Sudarmono, 1986, Stratigraphic response to structural evolution in a tensional back-arc setting and its exploratory significance: Sunda Basin, West Java Sea: Indonesian Petroleum Association 15th Annual Convention and Exhibition Proceeedings, p. 77-100.

Wilkin, R., H. Barnes, and S. Brantley, 1996, The size distribution of framboidal pyrite in modern sediments: an indicator of redox conditions: Geochimica et cosmochimica acta, v. 60, p. 3897-3912.

Wilson, M. E., 2000, Tectonic and volcanic influences on the development and diachronous termination of a Tertiary tropical carbonate platform: Journal of Sedimentary Research, v. 70, p. 310-324.

Wilson, M. E., R. Hall, W. Morgan, A. George, P. Harris, J. Kupecz, and J. Sarg, 2010, Tectonic influences on SE Asian carbonate systems and their reservoir development: Cenozoic Carbonate Systems of Australasia: SEPM, Special Publication, v. 95, p. 13-40.

Wilson, M. E., and S. W. Lokier, 2002, Siliciclastic and volcaniclastic influences on equatorial carbonates: insights from the Neogene of Indonesia: Sedimentology, v. 49, p. 583-601.

Wilson, M. E. J., 2002, Cenozoic carbonates in Southeast Asia: implications for equatorial carbonate development: Sedimentary Geology, v. 147, p. 295-428.

Wilson, M. E. J., 2008, Global and regional influences on equatorial shallow-marine carbonates during the Cenozoic: Palaeogeography, Palaeoclimatology, Palaeoecology, v. 265, p. 262-274.

Wilson, M. E. J., and A. Vecsei, 2005, The apparent paradox of abundant foramol facies in low latitudes: their environmental significance and effect on platform development: Earth-Science Reviews, v. 69, p. 133-168.

Woodling, G. S., J. G. Kaldi, R. C. Roe, and K. I. Oentarsih, 1991, Multidisciplinary reservoir study of the Bima field, offshore N.W. Java, Indonesia: Multidisciplinary studies, *in* R.

Sneider, W. Massell, R. Mathis, D. Loren, and P. Wichmann, eds., The Integration of Geology, Geophysics, Petrophysics and Petroleum Engineering in Reservoir Delineation, Description and Management AAPG Special Publications, v. 26: Tulsa, Oklahoma, U.S.A, AAPG, p. 1-36.

Woodling, G. S., J. G. Kaldi, R. C. Roe, and K. I. Oentarsih, 1991, Multidisciplinary Reservoir Study of the Bima Field, Offshore NW Java, Indonesia: Multidisciplinary Studies.

Wu, C.-H. C., 1991, Depositional environments and source rock investigations of the Oligocene to middle Miocene deposits in the Ardjuna basin, offshore northwest Java basin, Indonesia: Dissertation thesis, The University of Texas at Dallas, Dallas, 194 p.

Young, K., 1972, Cretaceous paleogeography: implications of endemic ammonite faunas: Geological Circular 72-2, p. 1-13.

Young, R., W. E. Harmony, G. Juniarto, and B. Thomas, 1991, Widuri field offshore southeast Sumatra: sandbody geometries and the reservoir model: Indonesian Petroleum Association 20th Annual Convention Proceeedings.

Zachos, J., M. Pagani, L. Sloan, E. Thomas, and K. Billups, 2001, Trends, rhythms, and aberrations in global climate 65 Ma to present: Science, v. 292, p. 686-693.

Zahirovic, S., M. Seton, and R. D. Müller, 2014, The Cretaceous and Cenozoic tectonic evolution of Southeast Asia: Solid Earth, v. 5, p. 227-273.

APPENDIX 1

NOMENCLATURE

3D	three-dimensional
CFR	coral floatstone-rudstone
CL	cathodoluminescence
CSB	Cisubuh Formation
EDX	energy-dispersive X-ray
EMCM	Early Miocene Carbon Maximum
GQS	glauconitic quartz sandstone
HMC	high-magnesium calcite
ICP-MS	inductively-coupled plasma mass spectrometry
LBF	large benthic foraminifera
LMC	low-magnesium calcite
MFS	maximum flooding surface
Mg	magnesium
Mg/Ca	magnesium/calcium ratio
MMCO	Mid-Miocene Climatic Optimum
Mn	manganese
N-S	north-south
NW	northwest
pCO_2	partial pressure of carbon dioxide in the ocean and atmosphere
pH	a figure expressing the acidity or alkalinity of a seawater

ppm	parts per million
PRG	Parigi Formation
RFR	rhodoid-LBF floatstone-rudstone
RLW	red algal-LBF mudstone-wackestone
RPG	rhodoid/red algal-LBF packstone-grainstone
SE	south east
SEM	scanning electron microscope
SHL	shale
Sr	strontium
SST	sea surface temperature
SWC	side-wall core
TAF	Talang Akar Formation
UCBL	Upper Cibulakan Formation
VJTB	Jatibarang Formation

APPENDIX 2

CORE DESCRIPTIONS OF THE MELANDONG DATASET

Examination on the conventional cores has been done on the 3 wells, C-1, J-2, and P-1, with a total length of more than 27 m. Critical information of sedimentological and diagenetic analysis was then plotted and noted on a graphic log format, including lithology, type of contact between lithologies, thickness, sedimentary structure, skeletal content, facies, fracture, diagenetic feature, and relative porosity. The cores are described and classified using Dunham's (1962) classification and expanded one from Embry and Klovan (1971). Figure A1 shows the key symbols for the core descriptions.

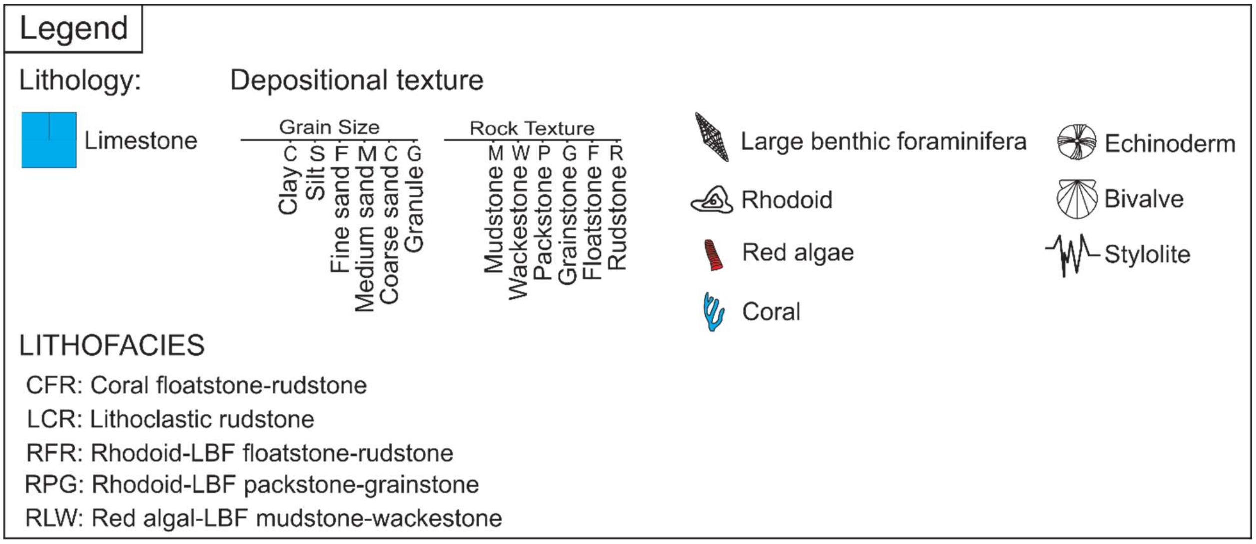

Figure A1. Legend for the symbols used in the core description logs.

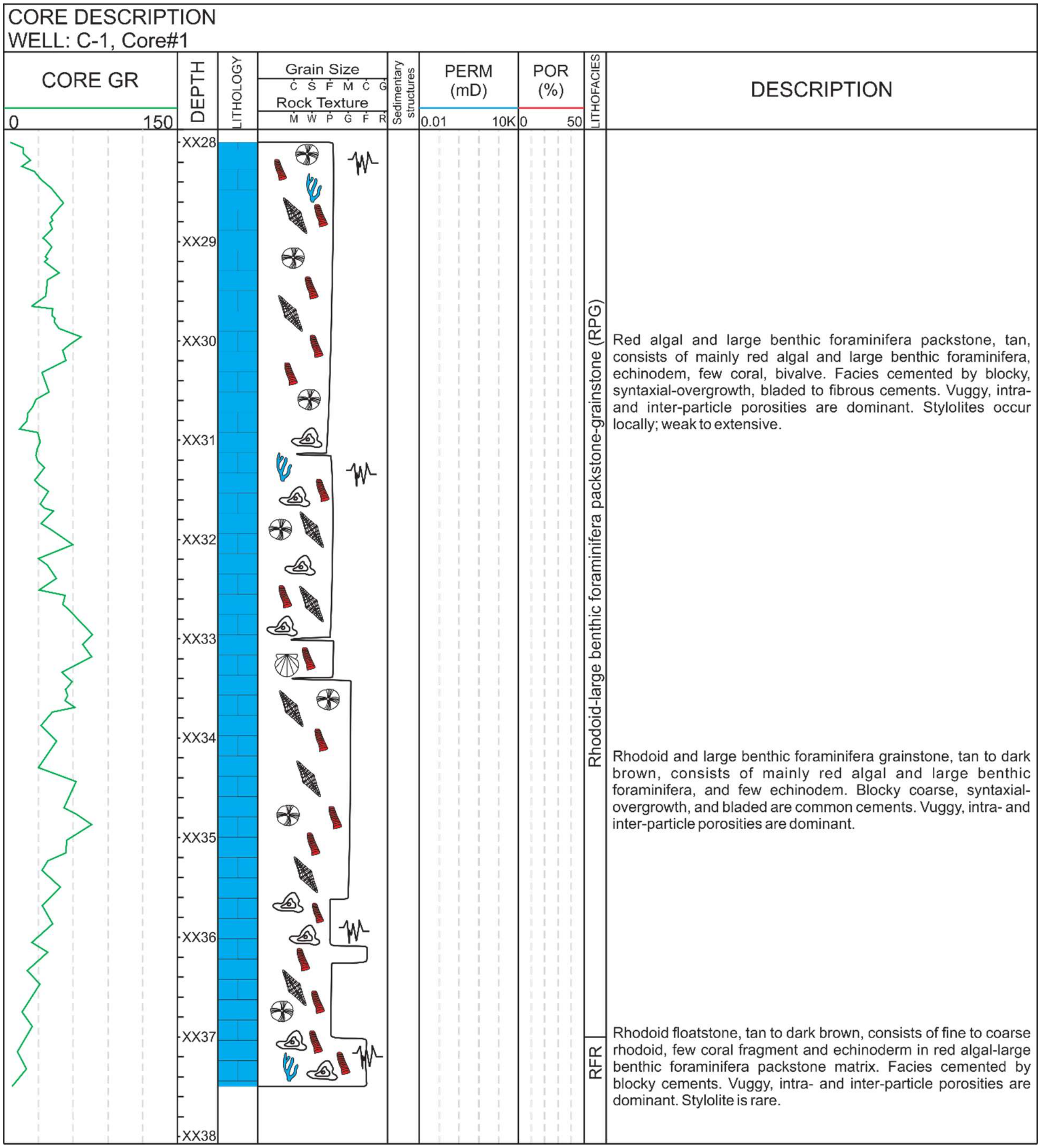

Red algal and large benthic foraminifera packstone, tan, consists of mainly red algal and large benthic foraminifera, echinodem, few coral, bivalve. Facies cemented by blocky, syntaxial-overgrowth, bladed to fibrous cements. Vuggy, intra- and inter-particle porosities are dominant. Stylolites occur locally; weak to extensive.

Rhodoid and large benthic foraminifera grainstone, tan to dark brown, consists of mainly red algal and large benthic foraminifera, and few echinodem. Blocky coarse, syntaxial-overgrowth, and bladed are common cements. Vuggy, intra- and inter-particle porosities are dominant.

Rhodoid floatstone, tan to dark brown, consists of fine to coarse rhodoid, few coral fragment and echinoderm in red algal-large benthic foraminifera packstone matrix. Facies cemented by blocky cements. Vuggy, intra- and inter-particle porosities are dominant. Stylolite is rare.

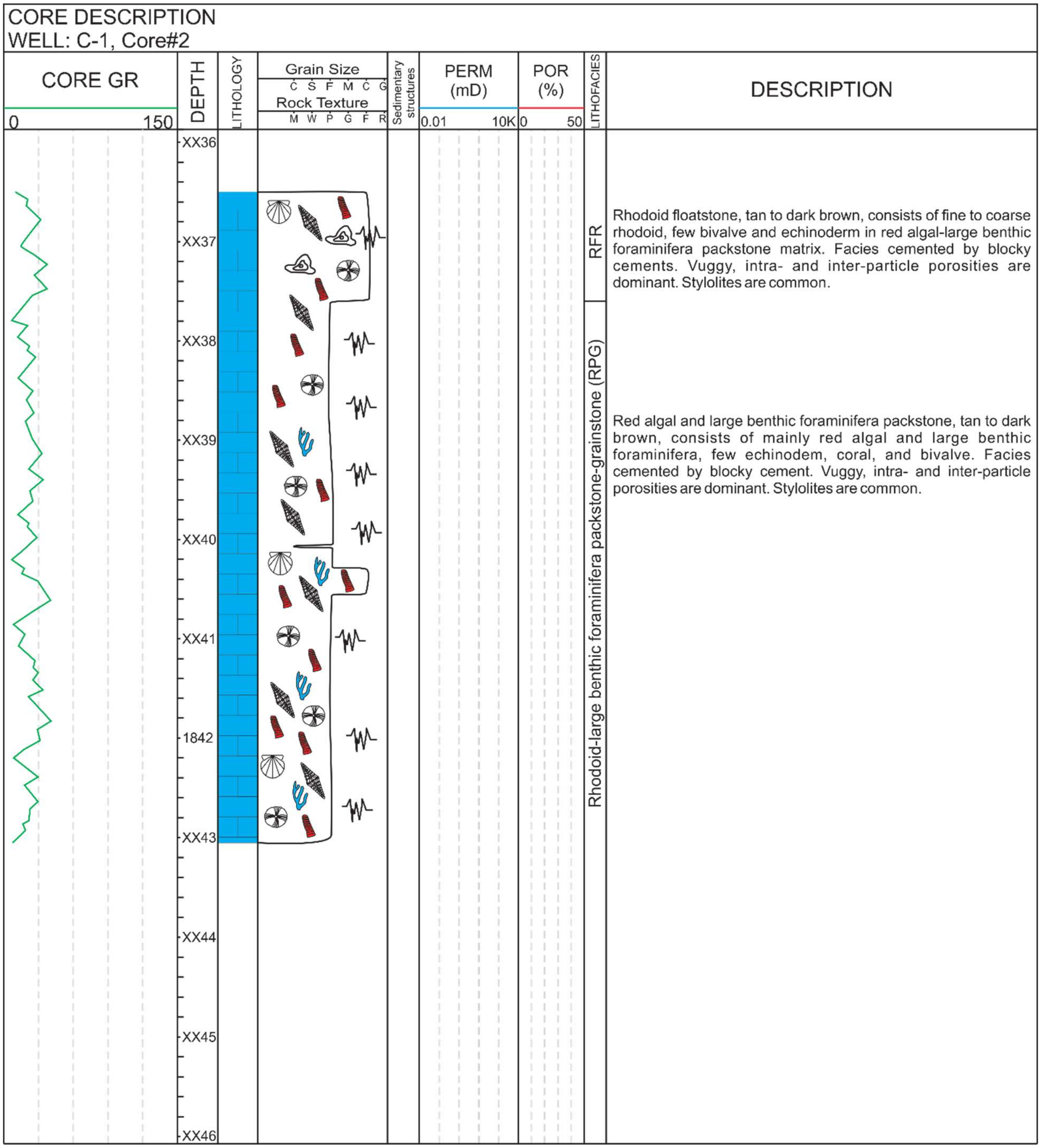

Rhodoid floatstone, tan to dark brown, consists of fine to coarse rhodoid, few bivalve and echinoderm in red algal-large benthic foraminifera packstone matrix. Facies cemented by blocky cements. Vuggy, intra- and inter-particle porosities are dominant. Stylolites are common.

Red algal and large benthic foraminifera packstone, tan to dark brown, consists of mainly red algal and large benthic foraminifera, few echinodem, coral, and bivalve. Facies cemented by blocky cement. Vuggy, intra- and inter-particle porosities are dominant. Stylolites are common.

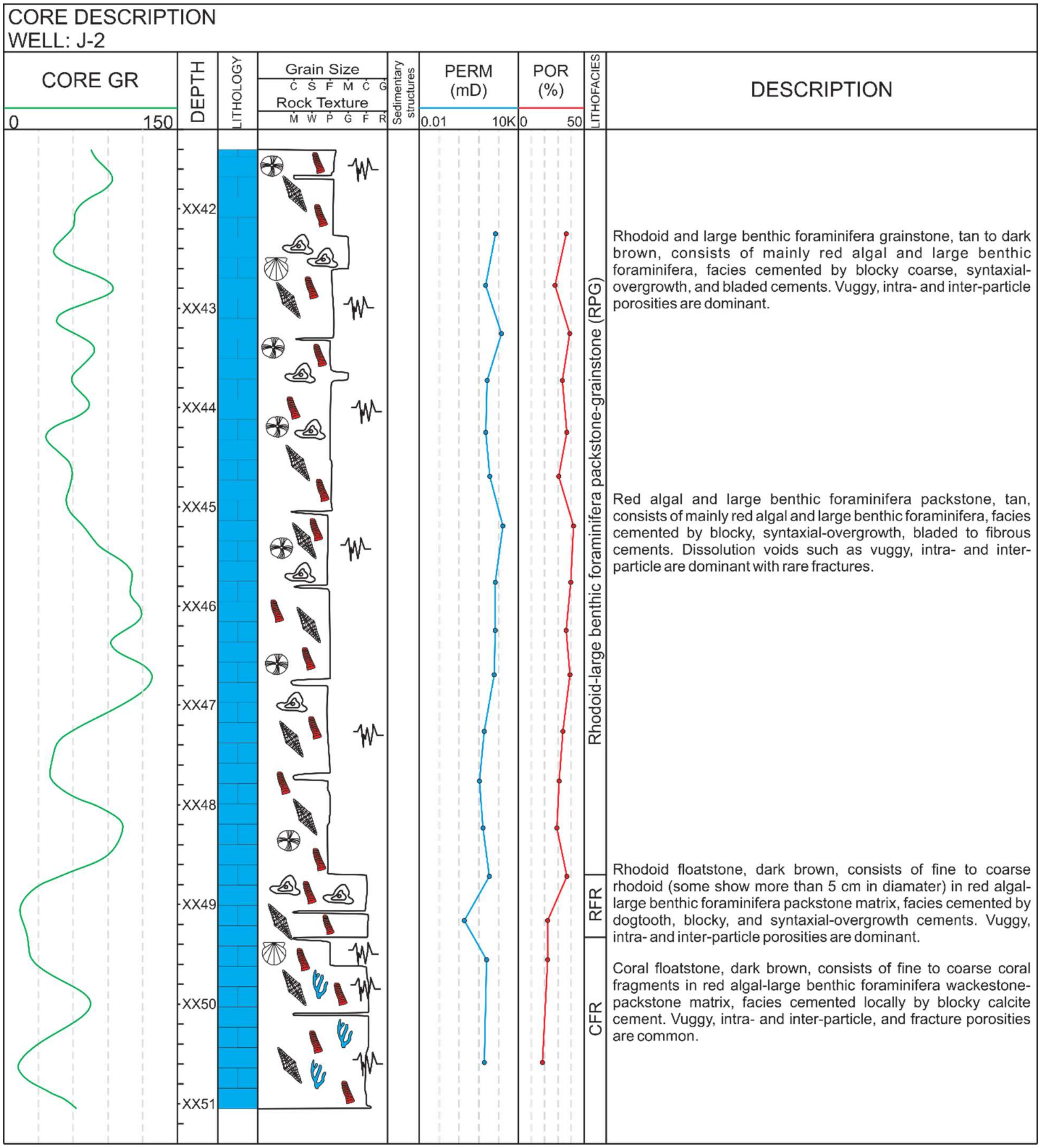

Rhodoid and large benthic foraminifera grainstone, tan to dark brown, consists of mainly red algal and large benthic foraminifera, facies cemented by blocky coarse, syntaxial-overgrowth, and bladed cements. Vuggy, intra- and inter-particle porosities are dominant.

Red algal and large benthic foraminifera packstone, tan, consists of mainly red algal and large benthic foraminifera, facies cemented by blocky, syntaxial-overgrowth, bladed to fibrous cements. Dissolution voids such as vuggy, intra- and inter-particle are dominant with rare fractures.

Rhodoid floatstone, dark brown, consists of fine to coarse rhodoid (some show more than 5 cm in diamater) in red algal-large benthic foraminifera packstone matrix, facies cemented by dogtooth, blocky, and syntaxial-overgrowth cements. Vuggy, intra- and inter-particle porosities are dominant.

Coral floatstone, dark brown, consists of fine to coarse coral fragments in red algal-large benthic foraminifera wackestone-packstone matrix, facies cemented locally by blocky calcite cement. Vuggy, intra- and inter-particle, and fracture porosities are common.

CORE DESCRIPTION
WELL: P-1

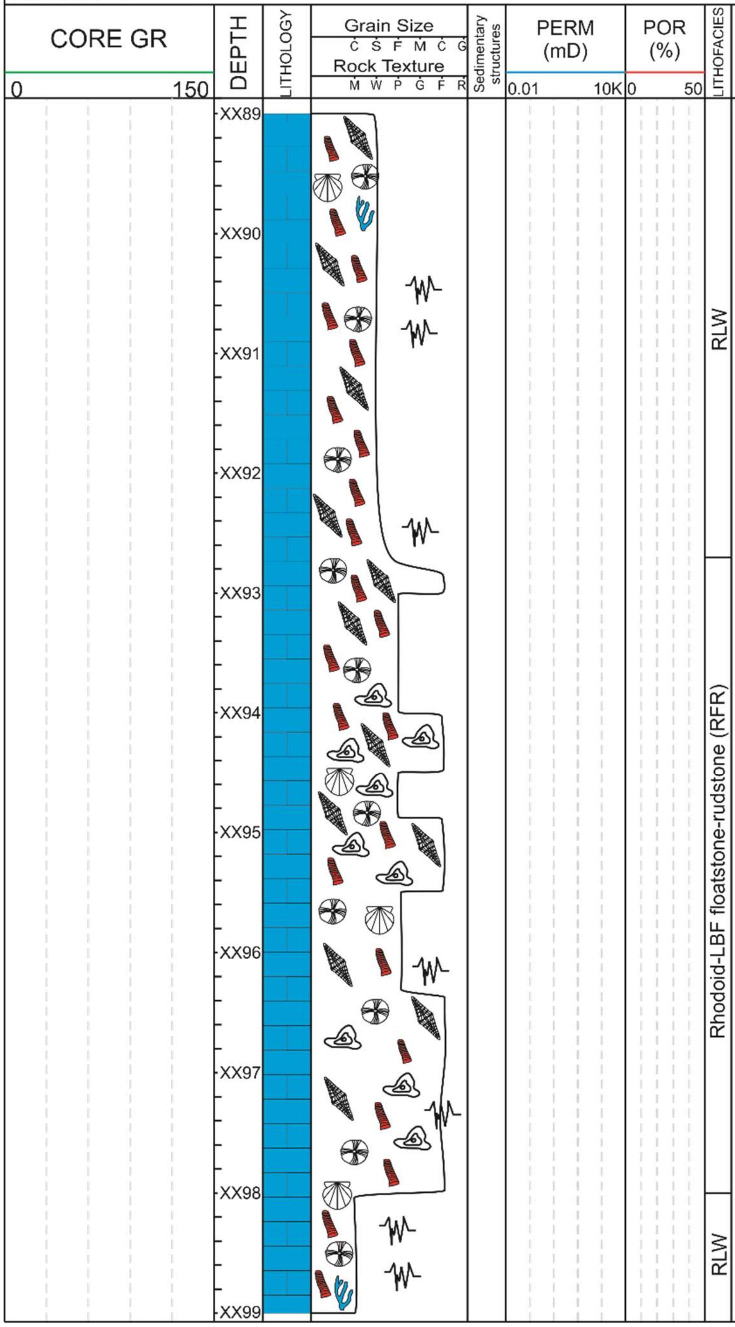

DESCRIPTION

Red algal and large benthic foraminifera wackestone, tan to dark brown, consists of mainly red algal and large benthic foraminifera, echinodem, few coral and bivalve. Facies cemented by blocky, syntaxial-overgrowth to bladed cements. Vuggy, intra- and inter-particle porosities are dominant with few fractures. Stylolites are common.

Alternation of rhodoid-LBF floatstone and red algal-LBF packstone, tan to dark brown. Rhodoid-LBF floatstone consists of fine to coarse rhodoid, few coral fragment and echinoderm in red algal-large benthic foraminifera packstone matrix. Red algal-LBF packstone comprises of dominantly red algae, LBF with few echinoderm and bivalve shell. Facies cemented by blocky, syntaxial overgrowth, bladed to fibrous cements. Vuggy, intra- and inter-particle porosities are dominant. Stylolite is rare.

Red algal and large benthic foraminifera wackestone, tan to dark brown, consists of mainly red algal and large benthic foraminifera, echinodem, few coral and bivalve. Facies cemented by blocky cement. Vuggy, intra- and inter-particle porosities are dominant with few fractures. Stylolites are common.

APPENDIX 3

PETROGRAPHIC ANALYSIS OF THE MELANDONG DATASET

A number of 111 blue-impregnated thin sections from the Melandong area are used for this conventional petrographic methodology utilizing the Olympus BX53MTRF petrographic microscope. Alizarin-red S was used to stain the thin-sections for mineralogical identification. Quantitative point-counting approach was conducted on the petrographic image using JMicroVision v1.2.7 software. A threshold of 300 counting was set in a random grid selection.

						Large benthic foram								Plaktic foram													
Well	**Depth**	**Bivalve**	**Gastropod**	**Coral**	**Echinodem**	***Amphestigina***	***Assilina***	***Discocyclina***	***Fusulinid***	***Lepidocyclina***	***Miliolid***	***Miogypsina***	***Operculina***	***Globigerina***	***Heterohelix***	***Globorotalia***	**Red Algae**	**Rhodoid**	**Lithoclast**	**Ooid**	**Peloid**	**Unidentifiable grains**	**Cement**	**Carbonate muds**	**Quartz**	**Glauconite**	**Dolomite**
B-1	17XX.8				1					19	1		3				12					16	12	37			
B-1	17XX	1		8	1					8	1		2				1		7				32	40			
B-1	17XX.15	3								18			4	1			19						46	9			
B-1	17XX.4	1		7	1			1		7	1		1	1			2					12	25	41			
B-1	17XX.8	1		8	1					14			2	1			15						27	31			
B-1	17XX.13							1		15			1	1			18						31	33			
B-1	17XX.6				1					13			4	1			23						24	35			
B-1	17XX.03				2					20		4	4	1			12						35	23			
B-1	17XX.5				3				1	10	1	2	5	1			17						26	34			
B-1	17XX.85				1				1	16	4		3				26						28	22			
B-1	17XX.5	1			1				1	8	1	1	1	1			14						31	40			
B-1	17XX.9			62						1							5						32				
B-1	17XX.91	1			1					10	1		3	1			21						26	36			
B-1	17XX.95	1							1	2	1		1				11		1				19	63			
B-1	17XX.2	1		3	2					16	1	1	10				21						19	26			
B-1	17XX.8				1					2	1	26	4	1			44						22				
B-1	17XX.2	1			1					6	1	5	6				57						17	6			
B-1	17XX.52				2	7	4			10		17	2				18						19	22			
B-1	17XX.92				1	3	1			3		20	1				51						20				
B-1	17XX.35				1	4	1					25	6				36						16	11			
B-1	17XX.8				1	6	2	1		3		28	4				35						16	5			
B-1	17XX.2	1			1	7	7	1				35	3				19			1			13	11			
B-1	17XX.3																					13	82	5			

						Large benthic foram								Plaktic foram													
Well	**Depth**	**Bivalve**	**Gastropod**	**Coral**	**Echinodem**	***Amphestigina***	***Assilina***	***Discocyclina***	***Fusulinid***	***Lepidocyclina***	***Miliolid***	***Miogypsina***	***Operculina***	***Globigerina***	***Heterohelix***	***Globorotalia***	**Red Algae**	**Rhodoid**	**Lithoclast**	**Ooid**	**Peloid**	**Unidentifiable grains**	**Cement**	**Carbonate muds**	**Quartz**	**Glauconite**	**Dolomite**
B-1	17XX				1	9	8			2		31	4	1			9	1					16	17			
B-1	17XX.5				1	6	8			6		28	2				13	1					20	15			
P-1	18XX				3		2	2		6		4					21						10	52			
P-1	18XX.95	1		2	1		1	1		2							13	1					15	63			
P-1	18XX.25				1		3	4		2		1					17						11	62			
P-1	18XX.9						2	2		2							10	1					7	75			
P-1	18XX.1				1		1	1		4							8						6	79			
P-1	18XX.8				1		1	1		4		1					7						5	79			
P-1	18XX.7				4		5	3		22		13					11						6	36			
P-1	18XX				3		4	6		17		31					17	1					10	11			
P-1	18XX.6				5		8	6		20		18					17						7	19			
P-1	18XX				1			6		1		52					15						16	9			
P-1	18XX.55				2		2	5		4		42					18	1					10	15			
P-1	18XX.85	1			1			3		1		65					11						8	10			
P-1	18XX.5				1			1		1		53					12	2					21	8			
P-1	18XX.7	1			1		1	4		1		64					7						8	14			
P-1	18XX.3	1			2			4		1		61					4						7	21			
P-1	1897.25				2			5				56					19	1					7	11			
P-1	18XX				1		1	2		1		48					13	1					16	17			
P-1	18XX.3	1			1		1	1		4		1					30						12	50			
P-1	18XX			4	1		1	1		2		1					23	1					9	57			
C-1	18XX.81																		91				9				
C-1	18XX.31	4	1	8	1	1	1			1		1		14	1	1	2						12	53			

								Large benthic foram						Plaktic foram													
Well	**Depth**	**Bivalve**	**Gastropod**	**Coral**	**Echinodem**	***Amphestigina***	***Assilina***	***Discocyclina***	***Fusulinid***	***Lepidocyclina***	***Miliolid***	***Miogypsina***	***Operculina***	***Globigerina***	***Heterohelix***	***Globorotalia***	**Red Algae**	**Rhodoid**	**Lithoclast**	**Ooid**	**Peloid**	**Unidentifiable grains**	**Cement**	**Carbonate muds**	**Quartz**	**Glauconite**	**Dolomite**
C-1	18XX.34			3		1				1	1	1		11		1	1		11		8		10	51			
C-1	18XX				3	3	8	1		30		2			1		18	1					15	19			
C-1	18XX.37			1	2	2	4	12		11		2					27						14	24			
C-1	18XX.3				7		3	21		14		3	1			1	27						10	14			
C-1	18XX.03				3		2	8		1		19	1				44						10	12			
C-1	18XX.1			1	2		1	4		2		2					33	1					6	47			
C-1	18XX.16			1	1			3				1	1				43	2					9	40			
C-1	18XX.46				1			6					1				42	1					8	41			
C-1	18XX.18				2			11					4				47	2					23	12			
C-1	18XX.78				3			3				5	1				52	3					16	19			
C-1	18XX.13				2			3				11	1				52	3					12	16			
C-1	18XX.43	1			1			2	1		1	20					38					2	33				
C-1	18XX.3	1			2		1	2	1	1	6	22					39	1					24				
C-1	18XX.6	1			2		1	27				25					36	2					7				
C-1	18XX.91				3		1	21				33					32	2					8				
C-1	18XX.21				3		4	10		3		17					28	2					11	22			
C-1	18XX.91				1		3	5		1		28					30	1					17	15			
C-1	18XX.05				4		4	10		1		17	1				42						9	12			
C-1	18XX.35			3	3		3	5		3		5	1				48	2					11	16			
C-1	18XX.03				3		1	7	1	6		15					45	1					8	13			
C-1	18XX.6	1			2		1	5		2		14					39	2					14	20			
C-1	18XX.8				5		2	15		2		25					32						9	10			
C-1	18XX.2			1	2		1	5	1	1		26					41	1					10	12			

						Large benthic foram								**Plaktic foram**													
Well	**Depth**	**Bivalve**	**Gastropod**	**Coral**	**Echinodem**	***Amphestigina***	***Assilina***	***Discocyclina***	***Fusulinid***	***Lepidocyclina***	***Miliolid***	***Miogypsina***	***Operculina***	***Globigerina***	***Heterohelix***	***Globorotalia***	**Red Algae**	**Rhodoid**	**Lithoclast**	**Ooid**	**Peloid**	**Unidentifiable grains**	**Cement**	**Carbonate muds**	**Quartz**	**Glauconite**	**Dolomite**
C-1	18XX.5				3		4	6		1		32					27	1					10	16			
C-1	18XX	1		1	2			3		2		41					29	1					8	13			
C-1	18XX.3	1		8	2		1	1	1	1		24	1				30	1					11	18			
C-1	18XX.6	1		3	2		1	1	1	2		25					29	1					22	14			
C-1	18XX.2			1	2		2	13	1	6		21					28	1					11	14			
C-1	18XX.04			1	1		1	9	1	3		21					32	1					20	10			
C-1	18XX.34	1		1	1		1	10	1	2	1	22					25						21	16			
C-1	18XX.09	1		1	1			23	1	2		19					26	1					11	14			
J-2	23XX.75				2	1	1	15		1		27					30						8	14			
J-2	23XX.15	1		1	3			3		5	1	17					34	1					19	16			
J-2	23XX.58				1		3	5		5		11					35	3					37				
J-2	23XX	1		1	6			4		17		14					25	2					19	11			
J-2	23XX.35	1			8		1	1		29		20					11	1					8	20			
J-2	23XX.7	1			2		3	1		11	1	9					32	2					24	13			
J-2	23XX.25				4		3	1	1	12		20					30	1					11	17			
J-2	23XX.5				5		1			7		31					29	1					14	11			
J-2	23XX.65				6		7			13		37					15						9	14			
J-2	23XX.4			1	6					9		33					31	1					9	11			
J-2	23XX.8				5		1			12		30					34	2					9	7			
J-2	23XX.4				3		4			19		31					22	1					9	10			
J-2	23XX.65				12		1	6	1	16		23					24						8	11			
J-2	23XX.1				6		11	5		16		19					20	5					6	11			
J-2	23XX.5				5		3	8		10		24					27	1					10	12			

						Large benthic foram								**Plaktic foram**													
Well	**Depth**	**Bivalve**	**Gastropod**	**Coral**	**Echinodem**	***Amphestigina***	***Assilina***	***Discocyclina***	***Fusulinid***	***Lepidocyclina***	***Miliolid***	***Miogypsina***	***Operculina***	***Globigerina***	***Heterohelix***	***Globorotalia***	**Red Algae**	**Rhodoid**	**Lithoclast**	**Ooid**	**Peloid**	**Unidentifiable grains**	**Cement**	**Carbonate muds**	**Quartz**	**Glauconite**	**Dolomite**
J-2	23XX.6				5		4	4	1	12		15					35						8	18			
J-2	23XX.2				2		3	11		7		9					36						14	18			
J-2	23XX.7				6		6	8		9		12					34						8	18			
J-2	23XX.85				3		4	7		16		12					34	1					7	16			
J-2	23XX.3				1		3	3	1	6	1	1					33	1					6	44			
J-2	23XX.6	1		35	1		1	1		1		1					8	2					9	39			
J-2	23XX.05			6			12	5		3		1					18						10	46			
J-2	23XX.46			12			3	4		3		1					1						13	65			
J-2	23XX.65			23			7	5		7		2					12		1				12	31			
J-2	23XX.1			12			11	1		8	1						14						7	46			
K-1	23XX			26	1		5	4		8		2					14						17	24			
K-1	24XX																5						2				93
K-1	25XX				1		5	5		2							6						20	61			
K-2	24XX																15					6	46	33			
K-2	24XX				3		2	3		9		6					8						44	24			
K-2	24XX									5							31						17	47			
W-1	22XX																								85	15	
W-1	23XX						1	6		1		2											38				52

APPENDIX 4

POROSITY MEASUREMENT OF THE MASON DATASET

Sample	Formation	Cycle	Dolomite type	Dolomite crystal size (µm)	Porosity		
					Inter-crystalline	Moldic	Fenestral
01/14	Upper Ft. Terrett Fm.	8	1	6.03		14.64	
01/15		8	1	7.45	9.13		20.44
01/16		8	1	6.26	13.06		12.51
06/9		8	1	4.27	7.34		16
01/17		8	2	14.46	13.27	12.10	
02/14		8	2	6.49	5.99	4.65	
06/10		8	2	10.52	16.57	3.66	
02/11		7	2	13.04	15.98		
02/12		7	2	6.45	19.34		
02/13		7	2	11.03	16.98		9.98
01/13	Middle Ft. Terrett Fm.	6	1	4.58	12.31	1.66	
06/7		6	2	12.41	17.26	6.85	9.02
01/12		6	3	20.05	21.60	4.82	
06/8		6	3	26.29	14.75	4.14	
01/11		6	4	23.59			9.58
03/8		6	4	28.98			14.66
01/9		5	1	4.58	9.31		7.16
02/7		5	1	6.41	3.63		
02/8		5	1	5.77	12.28		2.05
02/9		5	1	4.96	7.68		
02/10		5	1	7.59	7.44		
06/4		5	2	6.46	12.52	3.81	

Sample	Formation	Cycle	Dolomite type	Dolomite crystal size (µm)	Porosity		
					Inter-crystalline	Moldic	Fenestral
06/5		5	1	5.42	14.9		13.71
06/6		5	1	2.83	1.15		7.71
06/2		5	2	7.08	11.77	1.24	
06/3		5	2	9.68	11.85	1.82	5.33
01/10		5	3	19.2	15.11	19.02	
03/7		5	3	17.87	11.06		
01/7		4	1	8.76	5.12	1.15	3.01
02/6		4	1	8.32	10.94		
06/1		4	1	6.25	15.33		3.73
07/8		4	1	5.66	8.65	17.24	
01/8		4	2	5.59	16.53		
01/6		4	4	101.37			
03/4		4	4	28.89			28.63
03/5		4	4	49.64	12.14		
03/6		4	4	50.65			
01/5	Lower Ft. Terrett Fm.	3	3	24.75	18.57		
02/3		3	4	91.1			46.37
02/4		3	4	60.47			28.57
03/3		3	4	45.33			28.54
02/2		2	4	20.57			24.91
07/6		2	4	63.52			
07/7		2	4	40.3			
01/2		1	1	13.22	12.25		
07/5		1	1	4.86	5.75	4.86	4.01
02/1		1	2	13.06	1.04		
07/3		1	3	15.7	11.95		

Sample	**Formation**	**Cycle**	**Dolomite type**	**Dolomite crystal size (µm)**	**Porosity**		
					Inter-crystalline	**Moldic**	**Fenestral**
07/4		1	3	23.56	13.92		
01/1		1	4	49.57			27.37
01/3		1	4	23.37			28.97
03/1		1	4	16.14			
01/1C	Upper Hensel Formation			19.4	5.54		
				21.24	5.85		
07/2				16.00	7.01		
				18.21	6.808		
01/1A	Lower Hensel Formation			13.54	14.01		
01/1B				8.95	11.83		
				9.89	12.32		
07/1				12.24	10.92		

APPENDIX 5

STABLE ISOTOPE AND TRACE ELEMENT OF THE MELANDONG DATASET

Well	Depth (m)	$\delta^{13}C$ (VPDB)	$\delta^{18}O$ (VPDB)	Mg (ppm)	Sr (ppm)	Fe (ppm)	Mn (ppm)
B-1	17XX.8	-0.79	-5.96	12097.23	1394.39	216.90	65.05
B-1	17XX	-2.63	-4.90	17205.49	736.15	987.25	287.86
B-1	17XX	-3.42	-6.42	6958.99	710.51	2151.41	166.50
B-1	17XX	-3.33	-6.14				
B-1	17XX	-3.42	-5.57	4185.89	769.43	215.31	93.50
B-1	17XX	-2.20	-6.99	2656.69	410.55	136.68	46.83
B-1	17XX	-0.81	-5.47				
B-1	17XX.15	-0.75	-5.59	4809.92	951.13	4469.69	39.80
B-1	17XX.8	-0.84	-5.56				
B-1	17XX.4			4059.55	547.07	67.01	40.24
B-1	17XX.6	-0.53	-4.78	6019.16	810.63	174.29	54.59
B-1	17XX.13			6480.52	812.94	685.65	60.83
B-1	17XX.03	-0.77	-5.32	35972.58	1164.23	186.25	76.59
B-1	17XX.5	-0.86	-5.05				
B-1	17XX.85	-0.97	-5.72				
B-1	17XX.5	-0.80	-5.41	6276.27	840.46	15.22	28.74
B-1	17XX.9	-0.81	-4.45	3316.11	345.42	69.06	18.14
B-1	17XX.2	-0.89	-5.29				
B-1	17XX.2	-0.60	-5.04	10689.71	1428.87	191.27	62.35
B-1	17XX.52	-0.56	-5.46				
B-1	17XX.92	-0.65	-5.19	15295.16	1240.60	347.74	59.35
B-1	17XX.35	-0.51	-5.29	14460.02	1060.19	29.96	38.45
B-1	17XX.8	-0.54	-5.35	7626.07	480.49	167.59	21.82
B-1	17XX	-0.33	-5.08				

Well	Depth (m)	$\delta^{13}C$ (VPDB)	$\delta^{18}O$ (VPDB)	Mg (ppm)	Sr (ppm)	Fe (ppm)	Mn (ppm)
B-1	17XX.2			12150.98	856.24	340.21	58.37
B-1	17XX.5	-0.40	-5.38	8468.01	620.87	0.51	24.27
B-1	18XX.5	-1.44	-7.93	2923.19	923.24	333.71	33.88
B-1	18XX	-4.47	-6.07				
B-1	18XX	-1.76	-5.65	3004.96	564.04	2609.03	261.50
B-1	19XX	-0.95	-8.40	11959.96	1830.73	3209.27	759.13
B-1	19XX.5	-0.89	-6.58	12944.81	1734.73	2399.01	1025.33
B-1	19XX.5	0.96	-5.22	4326.24	549.21	1584.29	67.51
B-1	19XX.5	1.13	-4.34	136909.71	435.37	585.39	122.30
B-1	19XX.5			188264.54	566.20	4941.65	311.37
B-1	19XX	0.15	-7.87	7533.60	1272.71	1514.30	402.66
C-1	18XX.81	-0.20	-5.78	3951.10	808.40	1309.97	378.14
C-1	18XX.31	-0.10	-5.46	3051.16	547.28	2353.66	278.47
C-1	18XX.34	-0.14	-5.44	2881.08	550.82	1048.78	309.61
C-1	18XX	-0.31	-5.26	15604.36	458.67	256.70	5.91
C-1	18XX.37	-0.32	-5.27	15741.45	434.56	235.43	6.76
C-1	18XX.3	-0.19	-5.54	11168.76	542.05	583.59	5.10
C-1	18XX.03	-0.18	-5.34	14059.93	614.85	546.53	6.77
C-1	18XX.1	-0.49	-6.74	14168.02	515.16	623.07	28.01
C-1	18XX.16	-0.64	-6.74	15425.73	533.46	980.93	39.87
C-1	18XX.46	-0.63	-6.82	8339.93	273.49	411.35	10.98
C-1	18XX.18	-0.23	-5.61	20616.93	633.04	1266.99	49.10
C-1	18XX.78	-0.53	-6.59	7021.05	335.25	347.93	24.42
C-1	18XX.13	-0.52	-6.69	13636.32	532.15	1059.95	49.39
C-1	18XX.43	-0.53	-6.28	3206.86	436.15	437.30	39.75
C-1	18XX.3	-0.85	-5.83	2413.81	593.45	126.68	9.78
C-1	18XX.6	-0.45	-6.27	8075.10	513.00	263.02	27.06
C-1	18XX.9	-0.40	-6.02	12045.95	515.93	345.09	22.35

Well	Depth (m)	$\delta^{13}C$ (VPDB)	$\delta^{18}O$ (VPDB)	Mg (ppm)	Sr (ppm)	Fe (ppm)	Mn (ppm)
C-1	18XX.21	-0.41	-6.16	19103.40	855.34	1151.56	43.14
C-1	18XX.91	-0.21	-5.30	15134.59	588.91	409.65	26.05
C-1	18XX.05	-0.17	-5.14	12967.76	654.03	727.52	16.88
C-1	18XX.35	-0.11	-5.06	32598.93	587.50	755.68	10.85
C-1	18XX.03	-0.20	-5.35	15213.99	654.76	601.77	6.56
C-1	18XX.6	-0.20	-5.34	15099.20	605.25	471.49	7.75
C-1	18XX.8	-0.24	-5.83	12500.12	585.39	512.27	21.83
C-1	18XX.2	-0.18	-5.47	13535.32	640.45	696.07	22.15
C-1	1839.5	-0.23	-5.26	15814.98	636.78	884.25	17.36
C-1	18XX	-0.21	-5.37	12653.46	520.59	528.68	6.02
C-1	18XX.3	-0.15	-5.18	11668.49	601.95	1016.16	5.95
C-1	18XX.6	-0.26	-5.60	7313.15	515.72	646.63	1.42
C-1	18XX.2	-0.18	-5.43	8243.44	566.02	809.58	2.20
C-1	18XX.04	-0.22	-5.38	7810.19	651.42	1175.26	9.73
C-1	18XX.34	-0.17	-5.42	5886.02	616.28	738.41	13.36
C-1	18XX.09	-0.20	-5.43	7945.62	655.39	1692.62	11.02
J-2	23XX.75	0.32	-3.68	4293.58	325.96	151.08	194.67
J-2	23XX.15	0.24	-4.14	3225.43	269.84	131.86	182.91
J-2	23XX.58	0.18	-4.28	4174.42	283.28	116.25	128.94
J-2	23XX	0.09	-4.41	6107.30	382.66	175.44	159.79
J-2	23XX.35	0.02	-5.33	6236.64	521.65	178.98	123.91
J-2	23XX.7	0.09	-5.06	8880.30	426.46	183.63	100.12
J-2	23XX.25	0.14	-4.23	5680.16	469.66	96.70	84.94
J-2	23XX.5	0.12	-5.13	3124.67	265.10	55.75	55.66
J-2	23XX.65	0.21	-4.79	3693.37	331.98	81.27	59.65
J-2	23XX.4	0.18	-4.95	2919.19	260.44	46.72	43.46
J-2	23XX.8	0.19	-4.61	4823.50	342.57	62.69	63.49
J-2	23XX.4	0.21	-4.54	4565.73	350.44	52.81	52.43

Well	Depth (m)	$\delta^{13}C$ (VPDB)	$\delta^{18}O$ (VPDB)	Mg (ppm)	Sr (ppm)	Fe (ppm)	Mn (ppm)
J-2	2346.65	0.16	-4.92	11253.44	442.53	194.25	67.18
J-2	23XX.1	0.11	-5.08	5635.85	435.24	73.63	90.73
J-2	23XX.5	0.23	-4.91	5153.83	354.50	76.88	90.05
J-2	23XX.6	0.22	-4.73	7343.11	529.21	118.62	109.85
J-2	23XX.2	0.37	-4.22	6703.10	387.79	202.62	78.19
J-2	23XX.7	0.85	-0.23	5461.17	422.05	106.03	87.29
J-2	23XX.85	0.40	-4.01	3780.28	281.95	28.48	60.22
J-2	23XX.3	0.37	-4.00	4048.71	305.63	14.51	79.85
J-2	23XX.6	0.63	-3.62	5032.21	366.53	11.24	119.65
J-2	23XX.05	1.05	-3.52				
J-2	23XX.46	1.15	-3.67	2190.13	166.42	16.86	65.69
J-2	23XX.65	0.91	-4.26	2247.42	174.82	75.80	61.30
J-2	23XX.1	0.76	-6.27	3255.75	457.50	272.10	144.78
K-1	23XX	1.00	-3.24	5666.92	413.49	1590.97	291.39
K-1	24XX.5	0.92	-5.63	4267.96	297.67	514.20	256.56
K-1	24XX			4049.61	570.27	2153.76	233.06
K-1	24XX	1.23	-7.04	94933.66	286.96	2721.10	70.26
K-1	25XX.5	0.76	-5.04	2387.01	249.31	718.84	55.05
K-1	25XX	-0.45	-6.06	6219.53	613.65	2028.36	235.04
K-1	25XX	0.72	-5.65	5272.19	656.42	11958.32	250.73
K-1	25XX	-0.59	-6.44	4963.01	340.93	860.19	224.13
K-1	25XX	0.50	-4.93	3807.71	283.42	291.76	187.36
K-2	24XX	-0.18	-5.30	4093.77	525.16	4552.18	134.28
K-2	24XX	-0.16	-5.10	4758.54	437.48	1794.35	113.13
K-2	24XX	-0.06	-5.93	3979.14	326.93	737.13	144.38
K-2	24XX	0.56	-6.31	4904.25	415.09	651.28	83.19
K-2	24XX	0.59	-3.53	5674.60	399.22	770.52	135.95
K-2	24XX	0.46	-3.32	4418.94	309.40	558.32	286.21

Well	Depth (m)	$\delta^{13}C$ (VPDB)	$\delta^{18}O$ (VPDB)	Mg (ppm)	Sr (ppm)	Fe (ppm)	Mn (ppm)
K-2	24XX	0.00	-5.16	5573.41	456.77	1895.44	157.47
K-2	24XX.5	0.85	-4.45	4029.36	341.46	1028.60	137.55
K-2	24XX	0.11	-4.26	5497.81	549.82	4757.00	314.22
K-2	24XX.5	0.92	-6.17	5786.31	313.60	875.43	418.05
K-2	24XX.5	0.90	-3.93	5661.86	388.56	1756.06	130.09
K-2	24XX	-0.10	-3.94	4490.47	305.88	550.13	186.65
K-2	24XX	0.90	-3.08	6222.24	393.44	858.07	287.34
K-2	24XX	0.28	-4.84	3961.37	294.13	759.97	174.65
K-2	24XX.57	1.07	-4.79	4494.53	283.34	545.25	249.83
K-2	25XX	-0.54	-5.45	11762.35	368.47	5105.94	150.04
K-2	25XX			6913.26	652.01	812.91	181.78
K-2	25XX			6765.57	104.31	34750.66	1100.54
K-2	25XX	0.21	-3.77	823.34	95.61	4767.77	35.75
P-1	18XX	-0.82	-6.21				
P-1	18XX	-0.51	-5.55				
P-1	18XX	-0.33	-5.73	3533.77	561.58	813.75	5.06
P-1	18XX	-1.30	-7.13	3513.13	473.07	620.16	2.06
P-1	18XX	-0.83	-6.10	3679.38	663.59	2234.28	51.30
P-1	18XX	-0.30	-5.83	4336.58	492.91	251.84	37.35
P-1	18XX.95	-0.26	-5.94	3824.57	504.81	379.22	48.35
P-1	1890.25	-0.27	-5.96	3359.95	446.27	981.64	47.94
P-1	18XX.9	-0.26	-5.83	2622.00	354.00	677.24	38.41
P-1	18XX.1	-0.31	-5.89	2096.40	272.82	422.26	32.07
P-1	18XX.8	-0.28	-5.86	2310.03	319.66	588.62	45.98
P-1	18XX.7	-0.32	-5.30	3708.60	679.03	126.44	8.46
P-1	18XX	-0.33	-5.41	4773.94	380.80	107.50	10.27
P-1	18XX.6	-0.28	-5.16	3837.09	296.72	145.66	9.72
P-1	18XX	-0.31	-5.65	4928.40	448.77	199.72	4.91

Well	Depth (m)	$\delta^{13}C$ (VPDB)	$\delta^{18}O$ (VPDB)	Mg (ppm)	Sr (ppm)	Fe (ppm)	Mn (ppm)
P-1	18XX.55	-0.29	-5.47	5088.87	379.20	121.88	11.16
P-1	18XX.85	-0.29	-5.35	6656.02	383.43	156.78	3.52
P-1	18XX.5	-0.37	-5.98	9240.73	459.36	96.96	9.69
P-1	18XX.7	-0.41	-5.94				
P-1	18XX.3	-0.33	-5.20	4325.10	441.33	219.90	7.39
P-1	18XX.6	-0.38	-5.79	2322.63	274.66	102.24	4.77
P-1	18XX.25	-0.58	-6.29	4523.34	412.30	78.17	3.18
P-1	18XX.55	-0.10	-4.68	2596.73	264.67	401.16	6.91
P-1	18XX	-0.38	-5.32	3225.24	332.24	288.22	6.76
P-1	18XX.3	-0.11	-5.47	2545.91	315.29	521.78	42.66
P-1	18XX	-0.18	-5.76	2397.87	292.70	993.93	34.16
P-1	19XX	-0.14	-5.61	2582.60	271.51	1260.25	54.70
P-1	20XX.5	-0.06	-6.38				
S-1	21XX.5	-0.96	-5.00	8833.27	586.69	3387.13	233.51
S-1	21XX.3	-1.61	-4.60	3549.28	268.09	377.20	163.44
S-1	21XX.5	-0.84	-4.03	5106.02	217.90	24.96	126.48
S-1	21XX	-4.69	-9.04	964.70	84.30	15.06	38.19
S-1	21XX	-3.02	-7.90	81762.64	252.04	1311.54	269.30
S-1	21XX	-0.60	-4.96	8977.80	35.22	51.93	18.19
S-1	21XX	-3.63	-7.60	70017.74	128.86	2607.41	206.78
S-1	22XX	-0.56	-4.95	9197.26	28.12	28.91	12.61
S-1	21XX	-0.90	-4.21	10801.96	546.46	507.12	64.90
S-1	22XX	-0.80	-6.66	3306.51	156.57	129.99	39.80
S-1	22XX	-1.30	-6.52	3411.29	231.03	111.35	56.40
S-1	22XX	-0.96	-6.55	4271.34	510.57	414.32	58.56
S-1	22XX.5	-1.00	-5.68	2306.89	201.73	92.40	27.93
S-1	22XX	-3.58	-9.50	6154.29	30.30	75.81	9.60
S-1	22XX	-0.94	-3.57	6277.82	32.16	145.55	17.17

Well	**Depth (m)**	**$\delta^{13}C$ (VPDB)**	**$\delta^{18}O$ (VPDB)**	**Mg (ppm)**	**Sr (ppm)**	**Fe (ppm)**	**Mn (ppm)**
S-1	22XX	-2.37	-5.62	7989.35	36.11	46.43	15.93
S-1	22XX	-2.06	-10.54	5308.81	204.81	131.09	104.50
S-1	22XX	-2.02	-5.63	14193.61	434.60	375.82	121.87
S-1	22XX.5	-1.35	-7.52	5288.26	473.50	409.12	63.34
S-1	22XX	-1.76	-7.86	7684.27	105.31	78.63	38.63
S-1	22XX	-1.38	-7.01	25643.38	269.40	260.42	124.40
S-1	21XX	-1.28	-7.70	10718.83	91.85	349.97	23.45
S-1	22XX	-1.12	-7.49	14136.57	150.88	219.10	29.28
S-1	22XX.5	-1.81	-8.12	5462.45	222.86	114.08	63.03
S-1	22XX	-0.44	-5.99	3246.62	148.40	183.92	123.99
S-1	22XX.5	-1.90	-6.11	4879.43	485.52	313.18	49.45
S-1	22XX	-2.94	-7.30	23176.99	46.23	398.41	103.32
S-1	22XX			1116.23	20.29	240.43	4.81
W-1	23XX	-2.13	-0.21	3512.51	87.42	150.67	55.13

APPENDIX 6

STABLE ISOTOPE AND TRACE ELEMENT OF THE MASON DATASET

Sample	**Formation**	**Cycle**	**Dolomite type**	**$\delta^{13}C$ (VPDB)**	**$\delta^{18}O$ (VPDB)**	**Sr (ppm)**	**Fe (ppm)**	**Mn (ppm)**
01/14	Upper Ft. Terrett Fm.	8	1	0.82	1.10	196.00	240.68	147.66
01/15		8	1	2.57	0.79	113.99	36.30	61.87
01-16		8	1	1.47	1.19			
01/17		8	2	1.11	0.42	231.88	163.75	269.39
02/14		8	2	1.65	1.27	159.82	59.13	83.95
06/10		8	2	1.86	1.30			
06/9		8	1	1.15	1.42	249.31	242.58	85.07
02/11		7	2	-0.18	0.83	172.12	113.43	142.03
02/12		7	2	1.81	0.76	207.97	85.86	123.78
02/13		7	2	2.52	1.11	261.90	131.89	159.31
06/8	Middle Ft. Terrett Fm.	6	3	2.60	0.76	113.85	342.17	108.24
01/11		6	4	-0.59	-3.05			
01/12		6	3	-3.85	-4.45	611.98	137.90	149.61
01/13		6	1	1.59	1.43	218.33	108.56	130.51
06/7		6	2	1.68	0.38	195.91	103.92	62.62
03/8		6	4	-1.67	-4.65	485.49	283.66	194.30
02/10		5	1	-1.21	1.55			
01/10		5	3	1.24	0.52	206.27	190.09	254.47
01/9		5	1	1.03	1.32	243.42	132.14	215.70
02/7		5	1	-2.28	-0.03	196.96	143.63	253.23
02/8		5	1	-1.40	1.05	253.25	186.48	155.07
02/9		5	1	-0.20	1.33	147.41	85.68	103.97
06/2		5	2	1.39	0.88	134.44	164.87	196.44
06/3		5	2	1.85	0.78	132.52	70.93	180.21

Sample	Formation	Cycle	Dolomite type	$\delta^{13}C$ (VPDB)	$\delta^{18}O$ (VPDB)	Sr (ppm)	Fe (ppm)	Mn (ppm)
06/4		5	2	1.43	1.07	147.98	156.26	101.63
06/5		5	1	0.64	1.00	160.80	119.04	216.31
06/6		5	1	0.12	1.09	174.56	136.18	214.71
01/6		4	4	-4.69	-4.36	404.37	379.21	274.82
01/7		4	1	0.52	0.90	177.32	115.22	549.46
01/8		4	2	-0.18	0.91	201.82	104.21	464.65
02/4		4	4	-3.24	-4.00	880.38	239.55	341.54
02/5		4	4	-1.65	-4.10	454.89	339.69	342.87
02/6		4	1	-0.47	0.89	180.49	133.31	354.77
03/3		4	4	-3.78	-4.37	633.55	205.03	187.59
03/4		4	4	-1.26	-3.60	374.97	242.17	316.21
03/5		4	4	-1.65	-4.08	336.52	169.53	319.90
03/6		4	4	-2.02	-4.72	659.10	318.92	395.90
06/1		4	1	-1.60	1.17	156.54	111.95	487.36
07/8		4	1	1.72	0.94	186.69	80.32	67.30
01/5	Lower Ft. Terrett Fm.	3	3	-3.57	0.35	119.48	94.76	765.39
02/3		3	4	-2.45	-4.45	410.66	309.46	251.57
03/2		3	2	-0.22	-1.09	200.51	194.29	239.46
02/2		2	4	-3.28	-4.36	852.94	319.59	288.30
07/6		2	4	-0.58	-3.96	1039.03	376.03	246.43
07/7		2	4	-0.30	-3.94	501.43	394.31	261.72
01/1		1	4	-4.98	-3.56	396.87	494.80	528.14
01/2		1	1	-0.65	1.73	270.14	608.99	3279.06
01/3		1	4	-3.10	-4.03	503.94	537.83	393.77
02/1		1	2	-0.25	1.28	225.53	510.17	2009.63
03/1		1	4	-3.02	0.90	97.98	1273.32	1280.76
07/3		1	3	-0.65	0.43	111.44	184.70	560.70

Sample	**Formation**	**Cycle**	**Dolomite type**	**δ13C (VPDB)**	**δ18O (VPDB)**	**Sr (ppm)**	**Fe (ppm)**	**Mn (ppm)**
07/4		1	3	-0.93	0.23	198.27	228.93	695.54
07/5		1	1	-0.49	0.57	160.16	251.07	475.95
01/1C	Upper Hensel Formation			-3.89	-2.87	225.17	320.64	450.57
07/2				-1.07	1.41	149.35	446.33	2224.09
01/1B	Middle Hensel Formation			-3.97	-0.12	74.00	842.09	753.95
07/1				-2.95	1.12	61.22	424.53	1597.38
01/1A	Lower Hensel Formation			-2.06	0.75	35.88	277.76	824.10

APPENDIX 7

PUBLISHED ARTICLE

Facies (2017) 63:23
DOI 10.1007/s10347-017-0503-2

ORIGINAL PAPER

Controls on diagenesis and dolomitization of peritidal facies, Early Cretaceous Lower Edwards Group, central Texas, USA

Robet Wahyu Widodo[1] · **Juan Carlos Laya**[1]

Received: 2 December 2016 / Accepted: 22 June 2017

Abstract The Early Cretaceous Fort Terrett Formation of Mason County, central Texas, is a succession of subtidal to peritidal mud-dominated facies with minor intervals of bioclastic packstone–grainstone, rudist floatstone, and interbedded chert nodules. The strata conformably overlie the Hensel Formation, which was deposited unconformably on Precambrian basement. The Hensel Formation also contains a significant percentage of dolomite, precipitated within a fine-grained clayey matrix. The Hensel and Fort Terrett Formations were deposited during a transgressive episode, which provided the conditions for the extensive shallow-water Comanche carbonate platform. Siliciclastic and carbonate sediments were deposited along the coastal margin in subtidal, intertidal to supratidal areas. Previous dolomitization models have suggested that high permeability layers are required for dolomitizing brines to flow through a carbonate succession. Although, interparticle porosity in muddy tidal-flat successions can be significant, it has a limited flow capacity. However, interconnected fenestral porosity can allow sufficient fluid flow to move dolomitizing fluids more efficiently through the succession. Thus, it is hypothesized that interconnected fenestral porosity could have had a significant impact on permeability within this muddy succession and provided the pathways and conduits for Mg-rich brines. Four types of dolomite are recognized in the Fort Terrett succession. Three of these dolomite types formed largely by replacement and they occur throughout the succession. Features such as crystal size, crystal face geometry and zonation reflect the progressive development and recrystallization of the dolomite types. Only type 4 dolomite formed as a cement in void spaces during a late diagenetic stage. The direction of the dolomitizing fluid movement is difficult to determine, but it was likely downward in this case, controlled by a density-head driving-mechanism generated by dense hypersaline fluids from an evaporating lagoon.

Keywords Early Cretaceous · Dolomite · Dolomitization model · Carbonate diagenesis · Fenestral porosity

Introduction

Early dolomitization is a common process in peritidal carbonate deposits (e.g., Permian Tansill Formation, Cretaceous Edwards Group and Holocene carbonate sediment in the Bahamas) which has been attributed to several mechanisms including microbial activity, tidal pumping, seepage-reflux and evaporation (Deffeyes et al. 1964; Vasconcelos and McKenzie 1997; Fisher and Rodda 1969; Saller and Henderson 2001; Machel 2004; Jones and Xiao 2005). Dolomitization models specifically for the Lower Edwards Group in Central Texas include seepage-reflux (Fisher and Rodda 1969) and evaporative pumping (Rose 1972). These mechanisms require sufficient permeability (minimum 240 millidarcies as calculated through a mass-balance method by Deffeyes et al. 1964 for the Pekelmeer lagoon in Bonaire, Netherlands Antilles) so that a Mg-rich brine can flow and deliver the large volume of fluid required for pervasive dolomitization (Machel 2004; Garcia-Fresca et al. 2012). However, fine-grained facies with few isolated packstone–grainstone layers dominate the Edwards Formation outcrops examined in Mason County; thus, it is difficult to

---

✉ Robet Wahyu Widodo
rbtwidodo@tamu.edu

[1] Department of Geology and Geophysics, Texas A&M University, 3115 TAMU, College Station, TX 77843-3115, USA

see how muddy sediments with low permeability and limited high-permeability layers can allow brines to permeate for extensive dolomitization during early diagenesis.

In peritidal deposits, fenestrae and fenestral fabric are very common (Shinn 1968; Shinn and Robbin 1983) and these may have greatly affected primary permeability. However, the relationship between fenestral fabrics and dolomitization is poorly documented and understood, even though it is very common for dolomite units and fenestral fabrics to occur together in peritidal successions (Shinn and Robbin 1983; Abduslam 2012). It is proposed here that fenestral fabrics can play a significant role in the dolomitization of mud-dominated facies.

The Early Cretaceous Lower Edwards Group in Mason County, central Texas, was deposited unconformably over a Proterozoic granitic basement (Walker 1992) and is well exposed within The Mason Mountain Wildlife Management Area (MMWMA), 17.7 km north of Mason, Texas (Fig. 1). Outcrops occur on the western flank of the Llano Uplift (Fig. 1a) and the eastern extension of the Edwards Plateau (Barker and Ardis 1996; Anaya 2004).

Reddish conglomeratic sandstone to dolomitic sandstone of the Hensel Formation were deposited unconformably on basement rocks (Fig. 1b) during the initial transgression (Payne and Scott 1982; Phelps et al. 2014). A peritidal mudstone to skeletal–fenestral wackestone succession of the Fort Terrett Formation contains minor intervals of bioclastic packstone–grainstone, isolated rudist floatstone, and thin evaporite deposits (Fisher and Rodda 1969; Rose 1972; Barker et al. 1994; Moore 2010).

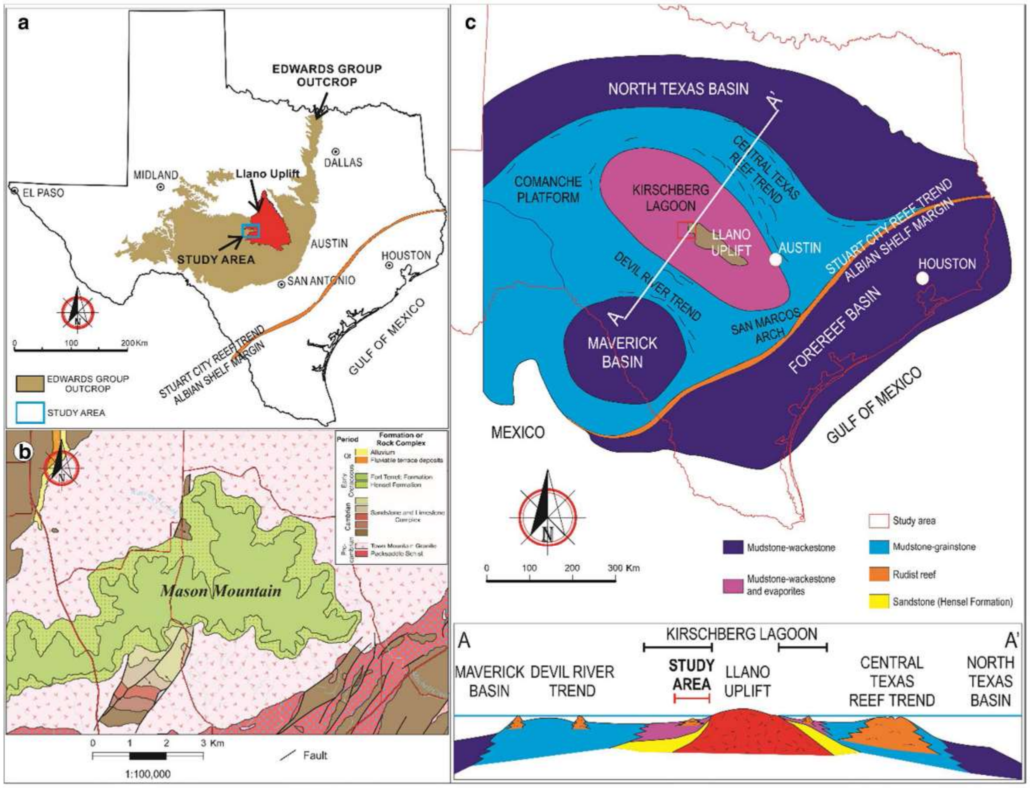

Fig. 1 **a** Location of the study outcrops in the eastern extension of the Edwards Plateau and the western flank of the Llano Uplift (modified from Bureau of Economic Geology 1992). **b** Geological map of Mason Mountain Wildlife Management Area (MMWMA). The Early Cretaceous succession (in *green* colors) is surrounded by a Precambrian basement complex (modified from Helper 2006). **c** Upper figure shows regional depositional setting of Texas during the Early Cretaceous-Albian stage (modified from Fisher and Rodda 1969). Study area in *red box*. Lower figure displays a schematic cross section of *A–A'* with the Kirschberg Lagoon deposits dominated by mudstone to skeletal–fenestral wackestone facies with scattered rudist biostromes (modified from Tucker and Wright 1990)

Geological setting

The Llano Uplift region has a simple geological history that can be summarized in three major geological events: (1) Precambrian granite intrusion and metamorphism produced by the Laurentia and Rodinia collision event (Sellards et al. 1932; Walker 1992; Mosher 1998; Ewing 2005; Miall and Blakey 2008); (2) Early Mesozoic rifting followed by major Early Cretaceous transgression and formation of the shelf system, which led to the deposition of thick siliciclastic and carbonate successions; and (3) Late Oligocene—Early Miocene regional uplift along the Balcones Fault Zone, which caused the exposure of the Cretaceous strata in this area (Anaya 2004; Barker et al. 1994; Collins 1987; Ewing 2005; Lawton 2008; Maclay 1995; Phelps et al. 2014).

Regional depositional setting and stratigraphy of Early Cretaceous strata

Central Texas during the Early Cretaceous was located between 25° and 30° north paleolatitude, indicating a tropical environment for its successions (Scotese et al. 1999; Phelps et al. 2014). Additionally, a semi-arid to arid climatic regime was present (Payne and Scott 1982; Phelps et al. 2014). A second phase of tectonic activity led to the formation of a small island (Fig. 1c) on the Comanche Platform (Fisher and Rodda 1969; Moore 2010). As the Early Cretaceous transgression covered the low-lying continental margin, the Hensel Formation was deposited in fluvial to coastal environments, onlapping the Proterozoic granitic basement (Barnes et al. 1972; Walker 1992; Moore 2010). As the transgression continued, carbonate sediments began to be deposited along the shoreline including peritidal areas (Moore 2010).

Sea-level fluctuations resulted in wide-ranging depositional environments including open-marine, skeletal shoals, shallow inner lagoon (known as the Kirschberg Lagoon) and interior peritidal systems located behind the Stuart City Reef to the south-southeast, and Central Texas Reef trend to the north-northeast. The carbonate succession on the platform is comprised of lime mudstone, miliolid foraminifera packstone–grainstone and rudist floatstone, interbedded with rare evaporites in the Fort Terrett Formation of the Edwards Group (Rose 1972; Barker et al. 1994).

Description of the mason exposures in Central Texas

The Edwards Plateau covers approximately 61,500 km^2 and consists of nearly flat-lying limestone and dolomite covered by modern soils (Barker et al. 1994). The study area (Fig. 1b) has outcrops exposed along an elongate-hill formed mainly of three stratigraphic units that are summarized in Fig. 2. The Proterozoic basement is generally granite and metamorphic units overlain by a basal conglomerate and then a fining-upward succession of the Lower Cretaceous Hensel Formation (Fig. 3a). The Fort Terrett Formation was deposited mostly conformably on the Hensel Formation with little evidence of an erosional surface or paleosoil between the two. In the study area, the Fort Terrett Formation can be sub-divided into a lower member consisting of three, meter-scale depositional cycles (1, 2, and 3); a Middle Member consisting of cycles 4, 5, and 6, and the upper member consisting of cycles 7 and 8.

Methodology

Seven measured sections were described bed-by-bed using Dunham's (1962) classification. Total gamma-ray measurements were determined using a RS-230 handheld gamma-ray scintillometer at 30-cm increments. In addition, 67 hand-samples were collected for petrographic and geochemical analysis. Alizarin-red S was used to partially stain the thin-sections in order to distinguish dolomite (unstained) from calcite (red-stained).

High-resolution photomicrographs were obtained to illustrate sedimentological and diagenetic features. Dolomite crystal size was measured to determine textural maturity. ImageJ software with jPOR plug-ins was used to measure total thin-section porosity (Grove and Jerram 2011). Fenestrae observed in thin-section were also measured and quantified to determine initial porosity. Cathodoluminescence (CL) petrography was performed using a Technosyn Cold Cathode Luminescence Model 8200 MKII to determine the dolomite compositional variation and crystal evolution.

For stable isotope analysis, powdered whole-rock samples were analyzed for carbon (δ^{13}C) and oxygen (δ^{18}O) isotopes in a Kiel IV carbonate device coupled to a Thermo-Scientific MAT 253 isotope ratio mass spectrometer in the Stable Isotope Geosciences Facility at Texas A&M University. The results are reported in VPDB standard with analytical precision of 0.04‰ for δ^{13}C and 0.08‰ for δ^{18}O.

Major and trace element analyses including strontium (Sr), manganese (Mn), and iron (Fe), reported in parts per million (ppm), were determined by an ICP-MS in the Radiogenic Isotope Geosciences Laboratory of Texas A&M University. Precision of major and trace element analysis was 0.001 ppm for Sr, 0.003 ppm for Mn and 0.03 ppm for Fe.

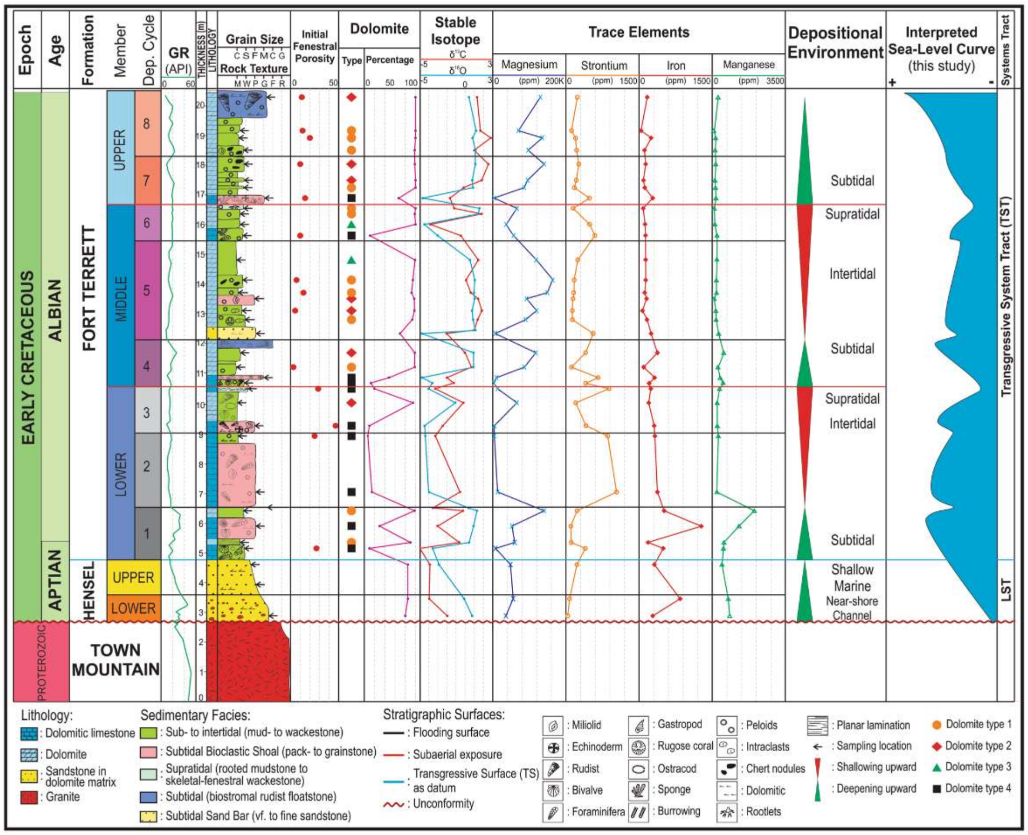

Fig. 2 Composite measured section of the Mason succession, showing stratigraphy, dolomite percentage, initial fenestral porosity, geochemical analysis, and interpreted depositional environments and sea-level fluctuations. The frequency of initial fenestral porosity increases upwards in conjunction with an increase in dolomite percentage. Partially dolomitized beds are abundant in the lower part of the formation. Upward-decreasing Fe and Mn contents are also noticeable

Facies analysis

Seven facies are described for the Hensel and Fort Terrett Formations based on lithological features such as composition, grain size, bedding characteristics, sedimentary structures, and fossil content, based on both field observations and petrographic analysis (Table 1). Interpreted depositional environments for each facies are presented.

Hensel Formation facies

The Hensel Formation is a fining-upward succession of conglomeratic to very fine sandstone that was deposited unconformably on the Proterozoic basement. Two facies are defined in this formation.

Conglomeratic to medium sandstone (near-shore fluvial channel facies)

The lower member of the Hensel Formation is a brownish-grey, conglomeratic to medium sandstone whose thickness ranges from 1 to 1.1 m. Granule to pebble-size granitic and metamorphic rock fragments occur at the base of the succession immediately above the contact with the basement. The upper part of this unit consists of fine-to-medium, subangular to well-rounded quartz grains (~30%), floating in sucrosic crystalline dolomite. This facies has intercrystalline porosity up to 14% and is

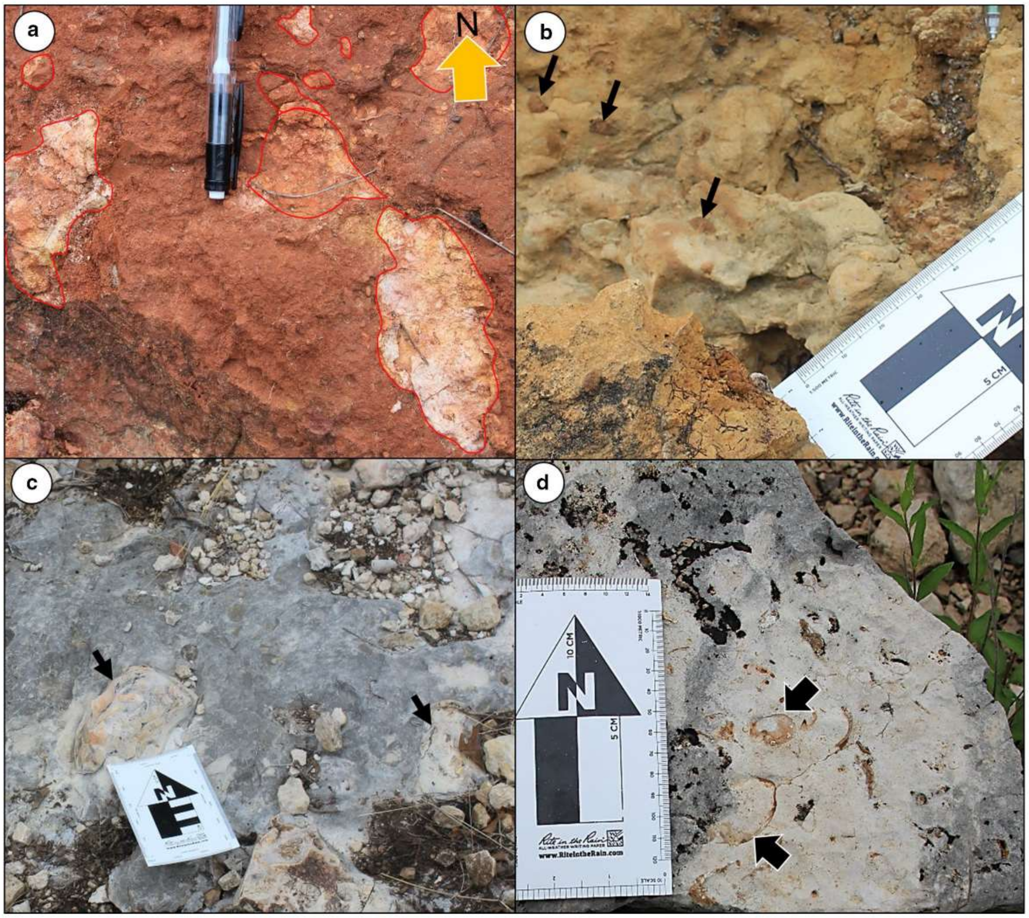

Fig. 3 General view of Hensel and Fort Terrett Formations in Mason County. **a** Fining-upward conglomeratic to dolomitic fine sandstone of the Hensel Formation. **b** Burrows (*black arrows*) in shallow-marine mudstone, base of the Fort Terrett Formation. **c** Chert-nodule (*arrow*) in partially dolomitized mudstone to skeletal–fenestral wackestone facies. **d** Rudist floatstone with moldic porosities mainly of *Exogyra texana* (*arrows*), floating in microcrystalline dolomite matrix

interpreted to have been deposited in a near-shore fluvial channel setting.

Very fine to medium sandstone (shallow-marine facies)

The upper member of the Hensel Formation is a brownish-grey, fining-upward unit of medium to very fine sandstone whose thickness ranges from 1 to 2.1 m. Petrographically, this unit consists of very fine to medium, subangular to well-rounded and poorly sorted quartz grains (~20%), floating in a mosaic of sucrosic crystalline dolomite with ~7% intercrystalline porosity. This member was deposited in a shallow-marine setting based on the finer grains floating in carbonate-mud that was later replaced by dolomite.

Fort Terrett Formation facies

The Fort Terrett Formation has five carbonate facies dominated by fenestral mudstone–wackestone that are grouped into five facies associations. It also has minor intervals of bioclastic packstone–grainstone.

Table 1 Facies analysis, brief description, grain components, and interpreted depositional environments of the Hensel and Fort Terrett Formations

Facies name	Description	Components	Interpreted depositional environment
Fort Terrett Formation			
Rooted mudstone to skeletal-fenestral wackestone	Light brown colour, partially to completely dolomitised, thickness 10–30 cm. Exposure features common	Radiolitid rudist (~7%), ostracod (~5%), gastropod (~3%), miliolid (~1%), dasyclad green algae, planktonic foraminifera, rootlet structures and variously-sized peloids.	Intertidal–Supratidal
Skeletal–fenestral mudstone–wackestone	Dullish brown, relatively homogeneous with streaks of brownish orange, partially to completely dolomitised, thickness 10–240 cm. Chert nodules in the upper and middle member, bioturbation and parallel lamination on the base of the formation	Radiolitid rudist (~12%), miliolid (~7%), gastropod (~5%), dasyclad green algae, equivalved-megalodontid bivalve, foraminiferas, peloids (~10%), aggregate grains and very fine to fine quartz (~3%).	Intertidal–subtidal
Rudist floatstone	Brownish grey, completely dolomitised, thickness 50–200 cm.	*Exogyra texana* and radiolitid rudist common floating in very fine to fine sucrosic dolomite matrix.	Subtidal
Skeletal packstone–grainstone	Dullish to milky brown, thickness 10–260 cm and partially to completely dolomitised.	Radiolitid rudist (~15%), ostracod (~10%), miliolids (~7%), echinoderm (~3%), foraminifera (~2%), peloids (~5%) and aggregate grains (~30%), intraclasts and very fine to fine quartz (~1%)	High-energy subtidal shoal
Very fine to fine sandstone	Brownish grey with thickness 18 cm, parallel lamination.	Very fine to fine quartz (~30%) floating in dolomite microcrystalline cement, subangular to well-rounded, poorly sorted and loose packing	Subtidal sand-bar
Hensel Formation			
Very fine to medium sandstone	Fining-upward, brownish grey to brownish red, subangular to well-rounded quartz shape, poorly sorted	Very fine to medium quartz (~20%), floating in dolomite microcrystalline cement	Shallow marine
Conglomeratic to medium sandstone	Fining-upward, brownish grey, granule to pebble size of granite clasts on the contact to the basement. Subangular to well-rounded quartz shape, poorly sorted and loose packing	Fine to coarse quartz grains (~30%), floating in dolomite microcrystalline cement	Near-shore fluvial channel

Rooted mudstone to skeletal–fenestral wackestone (intertidal–supratidal facies)

This facies is light brown, partially to completely dolomitized skeletal wackestone, consisting mainly of carbonate mud with minor bioclastics such as calcitic radiolitid rudists (~7%), ostracods (~5%), gastropods (~3%), miliolid foraminifera (~1%), a few dasyclad green algae (<1%) and planktic foraminifera. This facies also contains variously sized peloids and rootlets. This facies ranges in thickness from 10 to 30 cm. Fine to very fine dolomite crystals occur in partially dolomitized skeletal wackestone as planar to non-planar porphyrotopic cement, whereas completely dolomitized wackestone shows rootlets (~4% by volume) and peloids as grains floating in sucrosic dolomite.

Micrite envelopes and dolomite replacement (partially or completely) of calcitic rudists, miliolid foraminifera, ostracods, and planktic foraminifera are common and dolomite cementation occurred in some skeletal chambers. The chambers of micritic rootlets were filled by dolomite cement.

Porosity in this facies consists of primary porosity, such as elongate well-connected fenestral pores (15%), and secondary porosity including moldic and fracture porosity. Initial voids were partially or completely filled by muddy or silty sediment and then cemented by dolomite with planar crystal boundaries (Fig. 4a). Intercrystalline porosity up to 10% occurs in completely dolomitized skeletal wackestone.

The presence of rare rootlets indicates subaerial exposure long enough to develop terrestrial plants with well-established root systems. Bioclastic fragments in this facies indicate that seawater intermittently flooded the area. The association of fenestral fabrics, rootlets and assorted bioclastic grains suggests that deposition occurred in an intertidal–supratidal setting susceptible to episodic dry and wet periods.

Skeletal–fenestral mudstone–wackestone (intertidal–subtidal facies)

Skeletal–fenestral mudstone–wackestone facies is dullish brown, relatively homogeneous with streaks of brownish orange oxidation and partially to completely dolomitized (Fig. 4b). The thickness of this facies varies from 10 to 240 cm. Irregular chert nodules ranging from 4 to 15 cm in diameter occur in the middle and upper members. Bioturbated mudstone near the base of the formation contains rare *Teichichnus* ichnogenera in addition to rare parallel lamination. Moldic (14%) and fenestral (12%) porosity is common in this facies.

The skeletal grains in this facies include calcitic rudist fragments (~12%), miliolid foraminifera (~7%), gastropods (~5%), and minor (<1%) dasyclad green algae, calcitic bivalves, and multi-chambered-uniserial foraminifera. Non-skeletal grains consist of variously sized peloids (~10%), aggregate grains, and fine quartz grains (~3%) in a muddy carbonate matrix. Very fine to coarse dolomite crystals (5–250 μm) with planar to non-planar porphyrotopic crystal boundaries are scattered in the mud. The depositional environment of this facies is interpreted to have been a low-energy, intertidal to shallow subtidal zone with a muddy substrate (Flügel 2004).

Rudist floatstone (subtidal facies)

Rudist floatstone is brownish-grey, completely dolomitized and occurs as an isolated unit, 50–200 cm thick. Common *Exogyra texana* and radiolitid rudists occur as the main bioclasts in this facies, floating in a fine to very fine sucrosic dolomite matrix (Fig. 3d). Porosity types in this facies are predominantly moldic (~12%) and intercrystalline (13%). Biomoldic porosity was formed by rudist shell dissolution with molds locally filled by dolomite cement. The distribution of this facies indicates that the rudist colonies grew in relatively small, isolated, and scattered areas in a shallow subtidal setting within a lagoon with a water depth probably no more than 5 m; this resulted in an isolated biostromal facies.

Skeletal packstone–grainstone (high-energy subtidal shoal facies)

The skeletal packstone–grainstone is dull to milky brown and partially to completely dolomitized; bed thickness ranges from 10 to 260 cm. The packstone consists of mixed skeletal grains and fragments: rudists (~15%), miliolid foraminifera (~7%), rare benthic–planktic foraminifera and non-skeletal grains, peloids (~5%) and a few aggregate grains, within a minor carbonate matrix. Selective silica replacement of aragonitic rudist shells occurs in this facies.

The skeletal grainstone is composed of radiolitid rudists (~12%), ostracods (~10%), miliolid foraminifera (~7%), echinoderms (~3%), planktic foraminifera (~2%), and unidentifiable skeletal grains. Non-skeletal grains are peloids (~30%), aggregate grains (~5%), intraclasts and very fine to fine quartz grains (~1%). All grains are cemented by dolomite.

Micrite envelopes occur on some bioclasts produced by microborers whereas other grains show partially to complete dolomite replacement. Dolomite cement fills some skeletal chambers (Fig. 4c). Peloids are mainly composed of calcitic mud and locally were replaced by dolomite whereas others were dissolved to give a moldic porosity. Very fine to coarse dolomite crystals (4–670 μm) are scattered with planar to non-planar crystal boundaries and a porphyrotopic texture in some samples. Common porosity types for this facies are

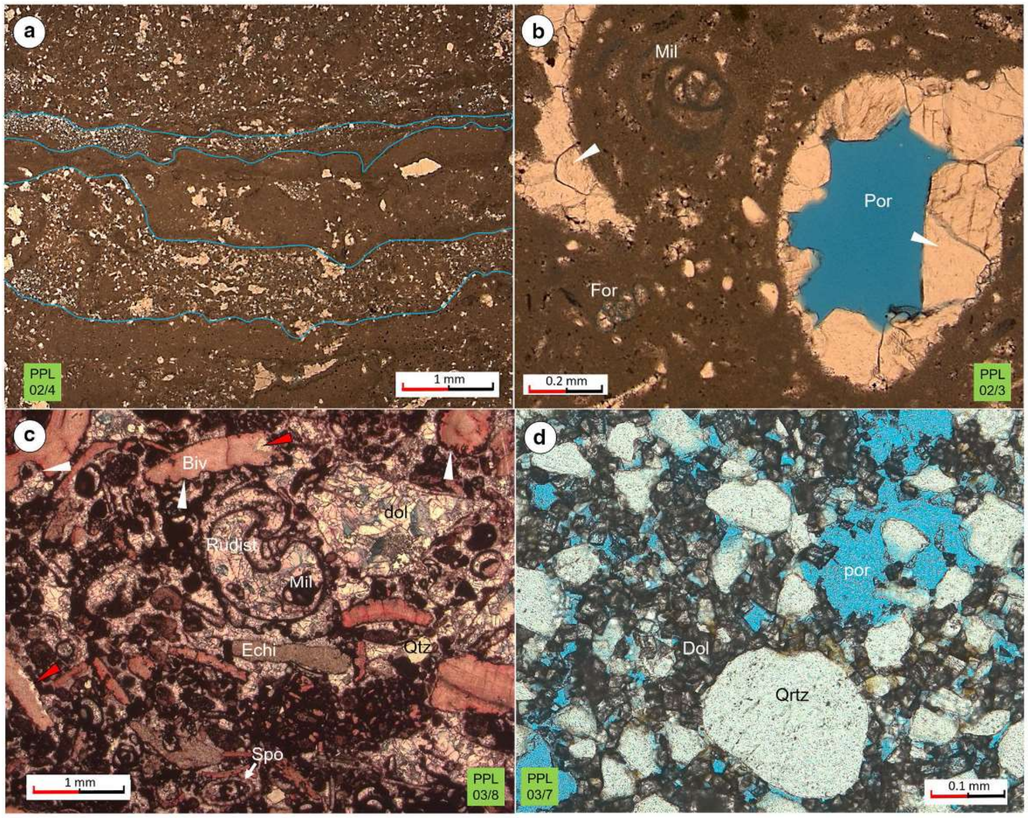

Fig. 4 Photomicrographs of the Fort Terrett Formation facies. **a** Fenestrae filled by internal sediment and dolomite (delineated by *blue polygons*) in partially dolomitized wackestone. **b** Blocky mosaic dolomite cement (*white arrows*) partially to completely filling moldic pores in partially dolomitized skeletal–fenestral wackestone. Micrite-walled miliolid foraminifera (Mil) and foraminifera (For) are partially dissolved. **c** Skeletal grainstone shows calcitic bivalve shell (Biv) fragments with irregular micrite envelopes (*white arrows*) caused by microboring organisms. Void within a rudist shell filled by miliolid foraminifera (Mil) and dolomite cement. Other grains are echinoderm (Echi), sponge (Spo), and quartz grains (Qtz) cemented by dolomite. **d** Subangular to well-rounded, poorly sorted, very fine to fine quartz grains (Qtz) floating in dolomite cement. Note that slides **c** and **d** are stained by alizarin *Red* S. *Por* porosity, *dol* dolomite, *XPL* cross-polarized light, *PPL* plain-polarized light

fenestral (14%), intercrystalline (12%), moldic (3%), and fracture (<1%), and these pores were partially to completely filled by dolomite cement with planar crystal boundaries. These packstone and grainstone facies were deposited in a high-energy subtidal shoal, based on the abundance and diversity of the skeletal grains and the lack of mud.

Very fine to fine sandstone (subtidal sand-bar facies)

A single bed of brownish-grey sandstone (18 cm thick and less than 15 m in lateral extent) contains very fine to fine quartz grains (~30%), floating in a dolomite crystalline matrix. The grains are subangular to well-rounded, poorly sorted with a loose packing; there is an intercrystalline porosity up to 11% (Fig. 4d).

Dolomite types

The textural classification proposed by Sibley and Gregg (1987) and adapted by Machel (2004) was used to identify different types of dolomite in the Fort Terrett Formation.

In addition, a modified grain-size scale for authigenic constituents was applied to determine the dolomite crystal size (Folk 1974). For consistency in this article, the term *aphanocrystalline* is modified to *micro*, for crystals less than 0.004 mm or 4 µm. The criteria used to classify dolomite components in the Hensel and Fort Terrett Formations are crystal size, distribution and boundary shape. These elements were chosen with the purpose of characterizing dolomite crystal maturity (Tables 2 and 3).

Hensel Formation dolomite

The Hensel Formation shows very fine to coarse quartz grains floating in a sucrosic mosaic dolomite of micro to medium size, a polymodal crystal-size distribution, of planar euhedral to subhedral crystal boundaries, locally having cloudy centers and CL-zoning (Table 2). The conglomeratic lower Hensel Formation has a fine to medium sandstone and dolomite matrix with crystal size ranging from 3 to 30 µm. In contrast, the upper member of the Hensel Formation has very similar features but a much coarser dolomite crystal size of 6–80 µm and crystals with cloudy centers caused by mineral inclusions and CL-zoning (Fig. 5a, b).

Fort Terrett Formation dolomite

Dolomite in the Fort Terrett Formation can be classified into four types (Table 3). The main criteria to identify textural maturity is the increasing crystal size (Table 3, lower figure), which can be interpreted to indicate decreasing saturation state of dolomitizing brines (Sibley and Gregg 1987). Type 1 dolomite is the most common and it is normally abundant in fully dolomitized facies (Fig. 2). In contrast, type 3 is scarce in the succession.

Type 1: first stage of dolomitization

The initial dolomite crystals have a micro- to fine crystal-size (1.5–35 µm with a mean of 7 µm), a polymodal size distribution, planar subhedral to non-planar anhedral crystal boundaries, and mimetic to non-mimetic fabric preservation (Fig. 5c). This is the most common dolomite type within the succession and is normally associated with mudstone to skeletal wackestone facies. This dolomite was likely the initial product of early replacement dolomitization (cf. Saller and Henderson 2001; Jones and Xiao 2005).

Type 2: second stage of dolomitization

The second-stage dolomite crystals are very fine to fine crystals (2–40 µm with mean of 10 µm) that have a polymodal crystal-size distribution, planar euhedral to planar subhedral crystal boundaries, and mimetic fabric preservation. Crystal appearance is clean with no cloudy centers or zonation (Fig. 5d). The larger crystal size of this dolomite type is likely the result of the continuation of the replacement process of the initial stage (cf. Saller and Henderson 2001; Jones and Xiao 2005).

Type 3: overgrowth dolomite

Overgrowth dolomite has a very fine to medium crystal size (5–65 µm with mean of 21 µm), polymodal size distribution, planar euhedral to planar subhedral crystal boundaries, and a mostly non-mimetic texture. This type of dolomite

Table 2 Dolomite characterization of the Lower and Upper members of the Hensel Formation

No	Category	Hensel formation	
		Lower	Upper
1	Dolomite classification	Crystalline dolomite	Crystalline dolomite
2	Crystal size (µm)		
	Minimum	3	6
	Maximum	30	80
	Mean	12	20
3	Crystal size category	Micro to fine	Micro to medium
4	Crystal size distribution	Polymodal	Polymodal
5	Crystal boundary shape	Planar euhedral to subhedral	Planar euhedral to subhedral
6	Mimetic vs nonmimetic	Nonmimetic	Nonmimetic
7	Cloudy centre	No	Cloudy centre and zoning in some crystals
8	Pore-type dominated	Intercrystalline	Intercrystalline
9	Porosity (%)	7.5 to 14%	5.5 to 7%

Note the decreasing crystal size with increasing intercrystalline porosity observed towards the Lower Member

Table 3 Upper table of dolomite characterization for the Fort Terrett Formation shows increasing maturity of texture and evolution

No	Category	Fort Terrett Formation			
		Type 1	Type 2	Type 3	Type 4
1	Dolomite classification	First stage of early dolomite	Second stage of early dolomite	Overgrowth dolomite	Coarse dolomite cement
2	Crystal size (µm)				
	Minimum	1.5	2	5	2
	Maximum	35	40	65	670
	Mean	7	10	21	50
3	Crystal size category	Micro to fine	Very fine to fine	Very fine to medium	Micro to coarse
4	Crystal size distribution	Polymodal	Polymodal	Polymodal	Polymodal
5	Crystal boundary shape	Planar subhedral to non-planar anhedral	Planar euhedral to subhedral	Planar euhedral to subhedral	Planar-nonplanar porphyrotopic to planar cement
6	Mimetic vs nonmimetic	Nonmimetic to mimetic	Mimetic	Mostly nonmimetic	–
7	Cloudy centre	No	No	Mostly cloudy centre	No
8	Mean porosity (%)				
	Intercrystalline	10	13	13	–
	Moldic	9	4	11	–
	Fenestral	8	9	–	21.5
9	Others	Calcite cement around the fenestrae	Calcitic shells are preserved	Zoning, completely dolomitised	Partially dolomitised

Lower figure exhibits the distribution of dolomite crystal size for all dolomite types; increasing crystal size is shown by the increasing peak of frequency towards a coarser crystal size

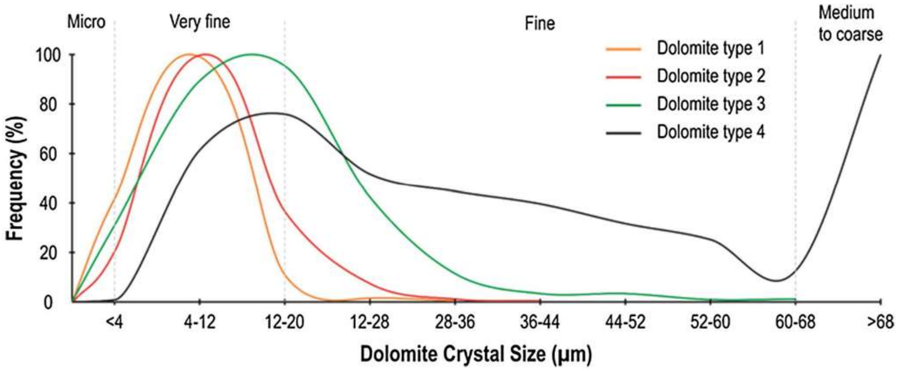

commonly has recognizable fluid inclusion-rich cloudy centers with multiple CL-overgrowth zones (Fig. 5e). This type of dolomite may represent a post-replacement or over-dolomitization process (cf. Saller and Henderson 2001; Jones and Xiao 2005).

Type 4: coarse dolomite cement

Coarse dolomite cements have a micro- to coarse crystal size (2–670 µm with a mean of 50 µm), and polymodal crystal-size distribution; they fill voids and pore spaces, mainly intraskeletal and fenestrae (Fig. 5f). This type of dolomite is common in partially dolomitized skeletal wackestone to grainstone facies.

Geochemistry

Stable isotope geochemistry

$\delta^{18}O$ values for the Hensel and Fort Terrett Formations range from −4.7 to +1.7‰ and $\delta^{13}C$ varies from −5.0 to

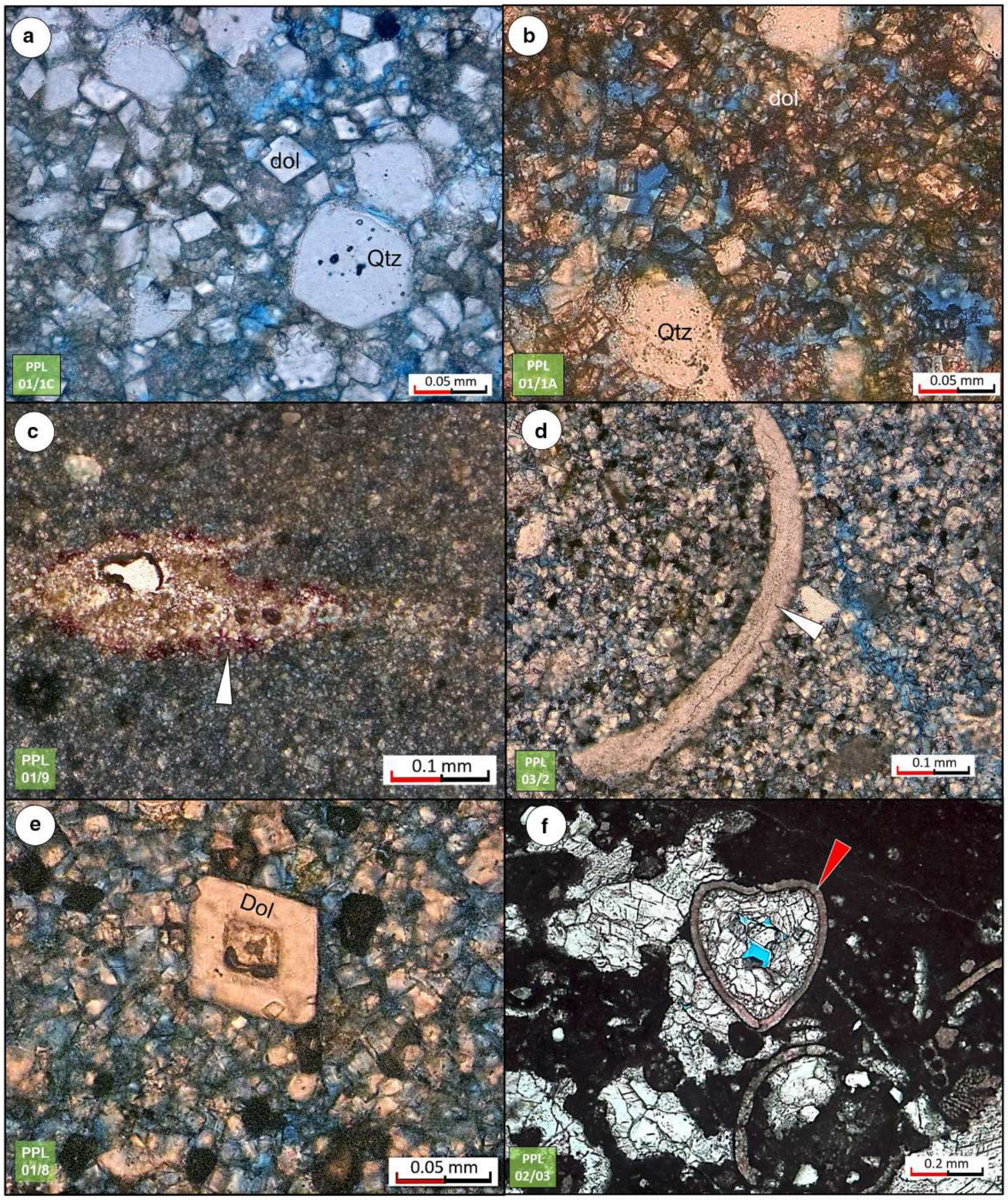

Fig. 5 Dolomite within the Hensel (**a**, **b**) and Fort Terrett Formations (**c**–**f**). **a** Micro- to fine dolomite crystals in fine to medium sandstone of the upper member of the Hensel Formation. **b** Very fine to medium dolomite crystals in conglomeratic to medium sandstone of the Lower Hensel Formation. **c** Type 1 dolomite shows a micro- to very fine crystal size with calcite cement around the fenestrae (*white arrow*). **d** Type 2 dolomite has a very fine to fine crystal size with selective preservation of a low-Mg calcitic bivalve (*white arrow*). **e** Type 3 dolomite shows very fine to medium overgrowths with multiple internal zones. **f** Type 4 dolomite is a cement with a micro- to coarse crystal size filling voids inside a high-Mg calcite bivalve (*red arrow*) and within the lime-mud. Note that slides **b**, **c**, and **f** are stained with alizarin Red S. *PPL* plane-polarized light, *Qtz* quartz, *dol* dolomite

+2.6‰ (Fig. 7a). Dolomite crystals from both lower and upper members of the Hensel Formation have negative $\delta^{13}C$ values of −3.9 to −1.1‰.

Isotopic data for the Fort Terrett Formation show a distinct clustering of values that can be assigned to two groups. Group 1 dolomites (red polygon, Fig. 7a) have negative values in both $\delta^{18}O$ (−4.7 to −3.1‰) and $\delta^{13}C$ (−5.0 to −0.3‰), and consist dominantly of type 4 dolomite (dolomite cement). Group 2 dolomites (blue polygon) show more scattered positive values in $\delta^{18}O$ (−0.1 to +1.7‰) and a large variation in $\delta^{13}C$ (−4.0 to +2.6‰).

$\delta^{13}C$ values of type 1 dolomite range from −2.3 to +1.9‰. Type 2 dolomite is enriched in ^{13}C with values ranging from +1.1 to +2.5‰. Type 3 dolomite has a broad range of carbon isotopic values from −3.6 to +2.6‰. Type 4 dolomite has a narrow range from +1.2 to +1.4‰.

Major and trace element data

The dolomites of the Lower Edwards Group have distinct Fe and Mn concentrations from 36 to 1273 ppm Fe and 62 to 3279 ppm Mn (Fig. 7b), which in the cross-plot, show a positive correlation. On average, there is nearly two times more Fe within the Hensel Formation dolomites (average 462 ppm, range 278–842 ppm) compared to the Fort Terrett Formation (average 240 ppm, range 36–1273 ppm), whereas nearly three times more Mn in the Hensel Formation dolomites (average 1170 ppm, range 754–2224 ppm) than the Fort Terrett Formation (average 363 ppm, range 62–3279 ppm).

Sr concentrations are in the typical range for dolomite forming from marine fluids which is up to 600 ppm (Land 1973), although, there is one high value of 1039 ppm for skeletal packstone facies. The average value of the Fort Terrett Formation is 295 ppm, nearly three times that of the Hensel Formation (average 109 ppm). Plotting Sr against Fe + Mn concentrations suggests an enrichment of Sr concentration for dolomite type 4, up to 1039 ppm (Fig. 7c). A negative correlation (in red polygons) indicates that Sr was lost during diagenesis (Veizer 1983; Grossman 2012).

Discussion

Depositional facies and stratigraphy

A stratigraphic cross section of the Hensel and Fort Terrett Formations (Fig. 8) in Mason County shows westward-thickening strata, interpreted cycles, unconformities, stacking patterns, facies variations, and a transgressive surface (TS). The Hensel Formation has two fining-upward sandstone cycles that are differentiated by grain size. These sandstones were deposited in a coastal to nearshore marine environment; the carbonate-rich muddy matrix of the sandstone was later replaced by dolomite. The basal conglomeratic sandstone of this unit only occurs in local topographic lows.

Eight, mostly shallowing-upward meter-scale cycles (Figs. 2, 8) can be recognized in the Fort Terrett succession based on muddy-grainy facies variation and the fluctuation of total GR log. These cycles consist of peritidal facies with supra-, inter-, and subtidal deposits. Muddy facies contain bioclasts of gastropod, miliolid foraminifera, and other foraminifera. Bioturbation, fenestrae, and rootlet structures in this facies indicate deposition in a tidal-flat environment.

Multiple flooding surfaces in the Fort Terrett Formation suggest that there were numerous low-amplitude sea-level variations during deposition of this unit, which is typical for the greenhouse times of the Cretaceous. Much of the study area was located within a low-energy lagoon, which repeatedly developed supratidal–intertidal facies where fenestral porosity and vegetation formed during subaerial exposure. Intertidal facies grade upward to the rudist floatstone, suggesting the area was locally deepening to a subtidal setting. Interbedded within the succession, a fine-grained sandbar facies is present, indicating a local sea-level fall with sporadic siliciclastic sediment input from nearby exposed Precambrian basement.

Porosity systems

Initial porosity system

It was not possible to quantify or assess the initial interparticle porosity (microporosity in the muddy facies) since most of this type of porosity was lost during compaction or early lithification. Fenestrae are common features in peritidal deposits and during deposition and shallow burial, before compaction, these structures created significant pore space. In this succession, this type of porosity was mostly filled by cement or fine-grained sediment, but locally the pore-space remained open (Fig. 6). Fenestrae have different geometries including laminar-elongate, spherical and irregular shapes that locally are interconnected (Shinn 1968; Shinn and Robbin 1983; Choquette and Pray 1970; Grover and Read 1978; Bain and Kindler 1994; Scholle and Ulmer-Scholle 2003; Mazzullo and Birdwell 1989; Mazzullo 2004; Flügel 2004). It is suggested here that fenestral porosity may have had a significant impact in the passage and flow of dolomitizing fluids through the sediment. For this reason, image analysis was used to calculate initial fenestral porosity to quantify original void percentage; this ranged from 2 to 46%.

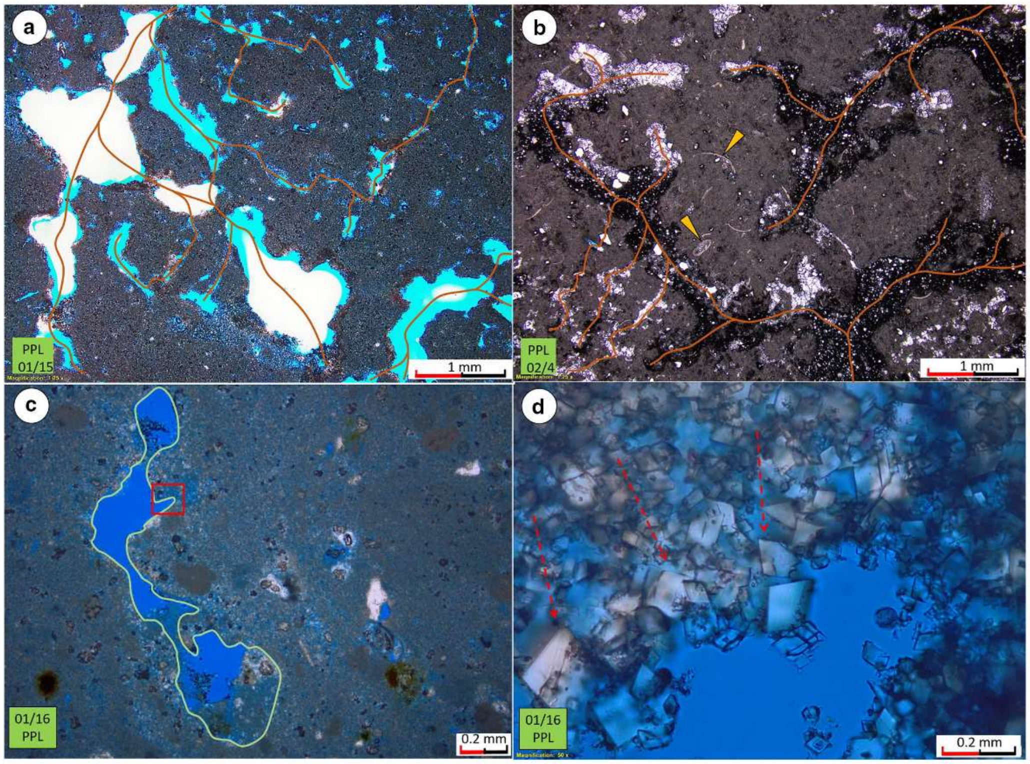

Fig. 6 **a** Photomicrographs from the upper member of Fort Terrett Formation shows 26% cement-filled fenestrae and 100% dolomite. **b** Fenestrae filled by mud to silt sediment (*darker color* in the fenestrae) and cemented by dolomite (*white* to *grey* in the fenestrae). It shows initial porosity of 23% with 8% dolomite. **c** Photomicrograph of fenestral (*light green* polygon) and moldic (*orange polygon*) porosity. The *red box* contains a detailed view of the area for image **d**. **d** Increasing dolomite crystal size from 1–4 to 9–25 μm towards the fenestral porosity (pointed by *red arrows*). Note that slides **a** and **b** are stained with alizarin Red S. The *orange lines* are possible flow paths of dolomitizing brines through fenestral bodies. *PPL* plain-polarized light

Secondary porosity system

Two main types of secondary porosity, intercrystalline and moldic, occur in the Fort Terrett Formation. Intercrystalline porosity was identified in all dolomitic intervals of the Hensel and Fort Terrett Formations. The lower member of the Hensel Formation has a porosity from 7.5 to 14%, whereas the upper member has 5.5–7%. Conversely, the Fort Terrett Formation has a highly variable porosity, ranging from 1 to 22% with an average of 12%. The pore size is also very variable from micron-scale to several hundreds of microns. Moldic porosity in the Fort Terrett Formation ranges from 1 to 19% with an average of 7%. This type of porosity was a result of the dissolution of rudists, gastropods, miliolid foraminifera, and peloids that produced voids with a spherical shape, common in the skeletal–fenestral wackestone to grainstone facies.

Diagenetic processes and paragenesis

Paragenesis can be interpreted from different approaches including petrography and geochemistry, especially stable isotope analysis (Fig. 7a). The interpretation here is similar to previous studies concerning diagenetic alteration of Edwards Group sediments (Mench et al. 1980; Ellis 1986). The isotope data show a clustering into two groups, one with positive $\delta^{18}O$ and relatively scattered $\delta^{13}C$. This group can be interpreted as the result of diagenetic alteration, probably during marine to shallow-burial in the Late Cretaceous. The second cluster, with more negative $\delta^{18}O$ and

Fig. 7 **a** Cross-plot of δ^{18}O and δ^{13}C values from the Hensel and Fort Terrett Formations. Group 1 (*red polygon*) relates to Miocene to Recent diagenetic products and group 2 (*blue polygon*) indicates Cretaceous diagenetic effects. **b** Fe and Mn cross-plot of Hensel and Fort Terrett Formations showing covarying values. The lower member of the Fort Terrett Formation (*green polygon*) is more enriched in Fe and Mn compared to the Middle (*red polygon*) and Lower members (*blue polygon*). **c** Cross-plot of Sr against Fe + Mn showing negative correlation (in *red polygons*) which implies that Sr was being lost with burial. Note the elevated Sr concentrations for type 4 dolomite (in *red polygon*)

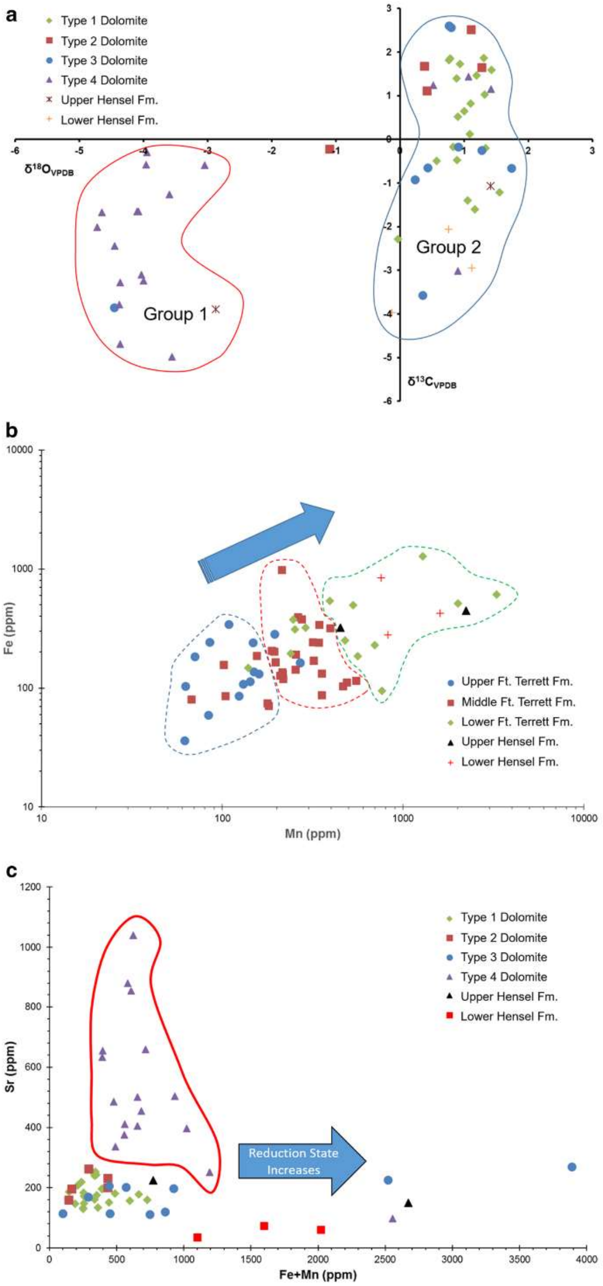

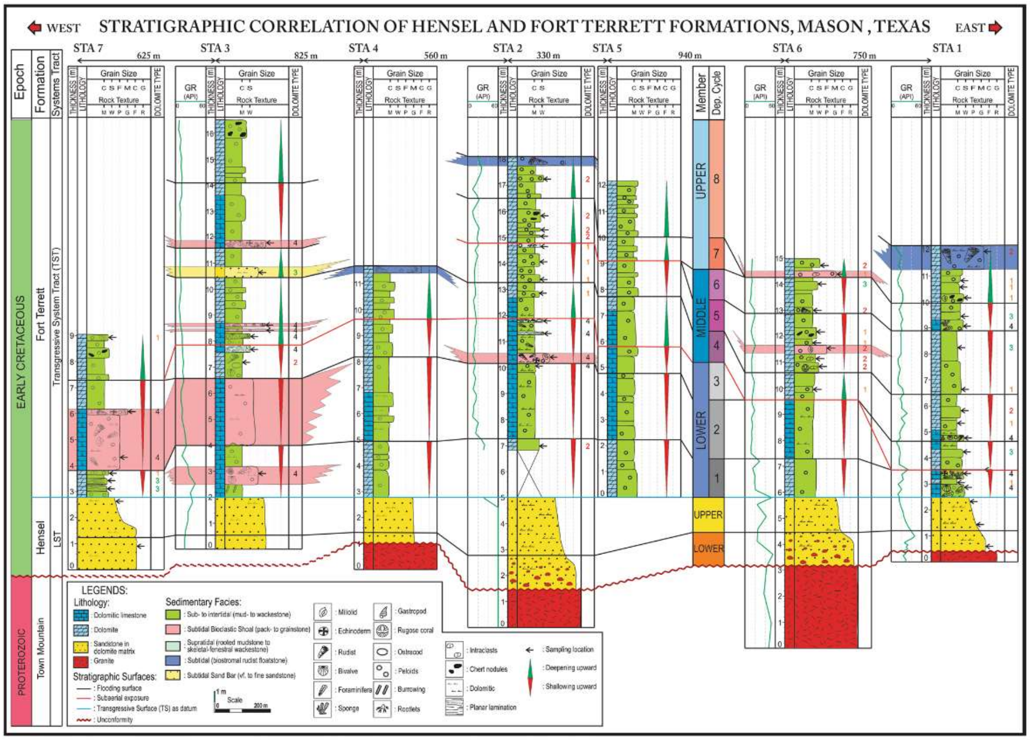

Fig. 8 Stratigraphic correlation of the Hensel and Fort Terrett Formations in Mason County. The strata thicken to the west. The Fort Terrett Formation is divided into Lower, Middle, and Upper members on the basis of sub-, inter-, and supratidal cycles. These are defined by flooding surfaces, which indicate frequent sea-level fluctuations affecting deposition of the various facies and early diagenetic processes. The basal conglomeratic sandstone with angular granitic clasts of the lower member of the Hensel Formation only occurs in local topographic lows

δ^{13}C, was likely associated with Miocene-Recent burial and subsequent uplift.

During the early Cretaceous to Oligocene (before the Balcones Fault Zone uplift), several diagenetic processes sequentially affected the strata, beginning with marine cementation–micritization and initial dolomitization, followed by early meteoric vadose and phreatic and finally shallow burial dissolution and cementation. Sea-level fluctuations were clearly significant in the early stages, resulting in rapid changes in diagenetic environment (Fig. 2).

Late-stage diagenesis of post-Miocene age is linked to the exhumation (telogenesis) that resulted in further dissolution, dedolomitization, and production of oxidation features. The schematic paragenesis of the Fort Terrett Formation (Fig. 9) shows the evolution of the strata from early Cretaceous deposition through burial to post-Miocene to Recent telogenesis.

Marine diagenesis

The evidence for marine diagenesis includes micritization and bladed calcite cements. External layers of rudists, miliolid foraminifera, and gastropod and bivalve shells were affected by microboring, producing an irregular outline of micrite envelopes (Bathurst 1966). These features are common for skeletal shells and the process generally takes place in shallow-marine waters close to the sediment–water interface, in low-energy subtidal to intertidal environments (Bathurst 1966; Jacka 1977;

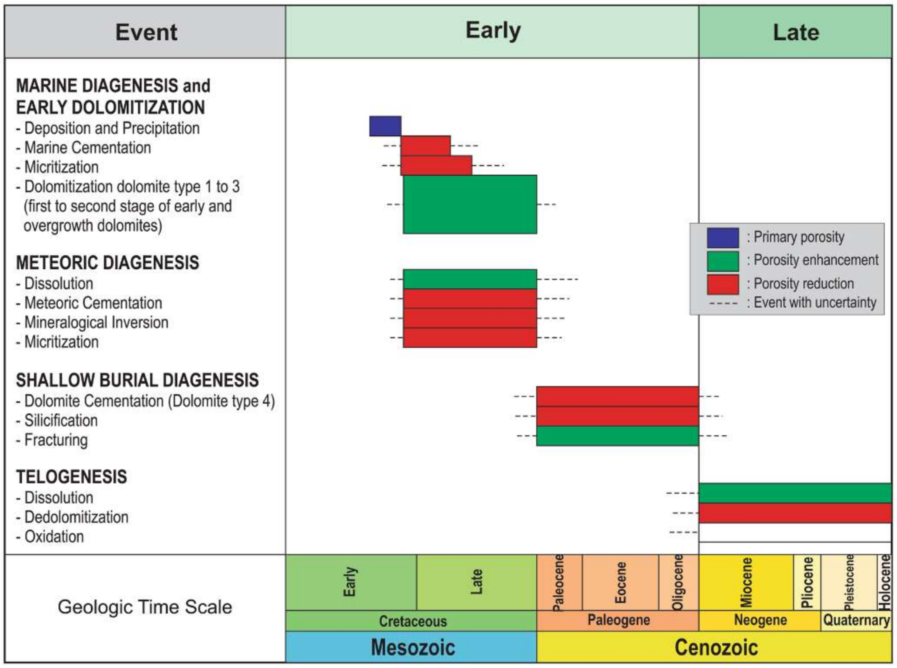

Fig. 9 Schematic paragenesis of the Fort Terrett Formation. Early diagenetic processes likely occurred during the Late Cretaceous to Paleogene whereas late diagenesis took place in the Neogene to Recent

Ellis 1986; Flügel 2004). Thin isopachous rims of bladed calcite crystals around and within bioclasts are the first-generation marine products; these were later replaced by dolomite in some cases (Fig. 10b).

Early meteoric diagenesis

Early meteoric diagenesis affected the succession when it was exposed during the early Cretaceous. This diagenetic phase is best preserved in shallowing-upward cycles in the Middle Member of the Fort Terrett Formation, which are bounded by subaerial exposure surfaces with common evidence of plant roots. These surfaces are marked by dissolution of aragonite and probably high-Mg calcite (HMC) grains in vadose and phreatic environments and pore-filling calcite cement precipitated in the meteoric phreatic environment (Ellis 1986).

Aragonite was the original composition of parts of rudist shells, gastropod shells, and carbonate mud (Dodd 1966; Steuber and Löser 2000; Pascual-Cebrian et al. 2016), and this was dissolved by meteoric water flushing. Meteoric calcite spar then filled empty voids, although in some cases the shells were calcitized and relics of the original aragonitic microstructure are still present (Tucker and Wright 1990).

Aragonite grains and cements typically have high Sr contents (up to 10,000 ppm), but on diagenetic alteration and replacement by calcite (calcitization) these values are reduced. However, a 'memory' of that high Sr may be retained in replacement crystals in the form of moderate Sr values, much higher than in a calcite cement. The type 4 dolomite cement has an elevated Sr value reaching 1036 ppm (Fig. 7c). Early seawater dolomite would be expected to have ~600 ppm Sr (Tucker and Wright 1990), but this would likely be reduced on burial recrystallization. The high Sr content of type 4 dolomite could indicate replacement of early aragonite cement precipitated in the marine setting.

Plant roots (Fig. 10a) indicate subaerial exposure (Halley and Rose 1977; Tucker and Wright 1990) and a pause in sedimentation, associated with rhizogenic

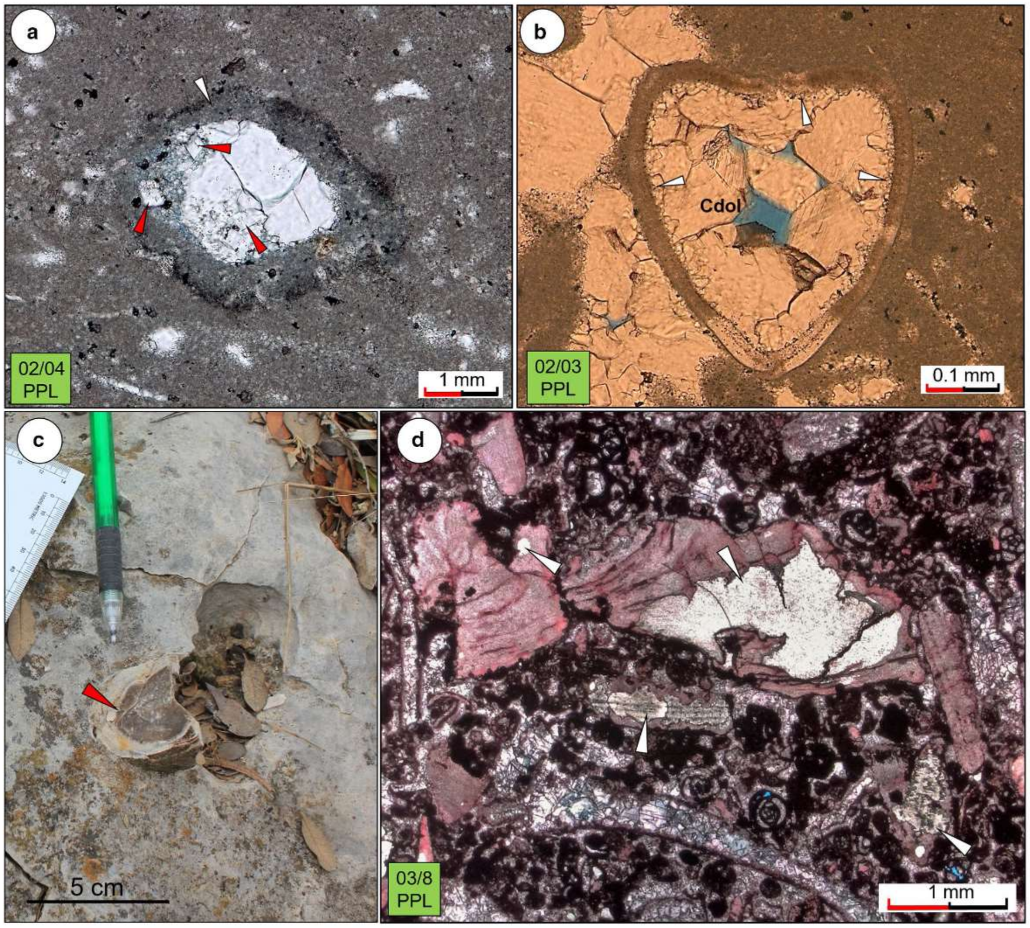

Fig. 10 **a** Rootlet in partially dolomitized skeletal–fenestral wackestone facies. The rootlet wall was micritized (*white arrow*) and the initial void was filled by an early generation of dolomite cement. Planar euhedral dolomite can be observed (*red arrows*). **b** Thin rim of marine calcite cement (*white arrows*) lining the inside of a bivalve shell. This cement later was replaced by dolomite and the remaining void was filled by a second generation of blocky dolomite cement (Cdol). **c** Chert-nodules (*red arrows*) in partially dolomitized mudstone to skeletal–fenestral wackestone facies. **d** Chalcedony (*white arrows*) in partially dolomitized skeletal grainstone forming selective replacement of calcitic-bivalve shell fragments (rudist). Note that slide **d** is stained by alizarin Red S. *PPL* plain polarized light

calcretes. Later, calcretes were flooded and subjected to meteoric phreatic conditions where the voids were filled by blocky calcite cement and then later replaced by dolomite.

Thin calcitic cement rims around fenestrae (as shown by red-stained rims in Fig. 5c) can be interpreted as meteoric phreatic precipitates. Later, dolomite cements occluded any remaining pore space in the fenestrae. These two different cement phases indicate a changing pore-fluid chemistry from a meteoric to shallow-burial setting.

Shallow-burial diagenesis

The Comanche Platform was submerged in Late Washita time (Albian) and buried by younger sediments of the Segovia Formation (Ellis 1986). In the Mason County area, several features suggest a slightly deeper burial diagenetic environment, i.e., the moderate Fe and Mn contents indicating a dysoxic environment, presence of fractures, and silicification in a form of chert nodules and selective quartz replacement of rudist fragments.

Moderate concentrations of Fe and Mn (Fig. 7b) indicate a change to sub-dysoxic conditions after deposition, and this is typical of a burial environment (Tucker 1986), as the availability of dissolved Fe and Mn released from clays can easily substitute in the calcite lattice at low oxygen states (Budd 1997; Grossman 2012). Fractures were filled by dolomite cement, and the lack of offset along fractures indicates a shallow-burial origin, where limited overburden did not have enough pressure to offset the fractures. A shallow burial depth, probably to a few tens of meters, is also indicated by the absence of stylolites in the succession. The chemical compaction and pressure dissolution to form stylolites is thought to begin at an overburden of several hundred meters and depend on lithofacies, carbonate fabric, mud content, degree of cementation, and susceptibility to pressure solubility and resistance (Buxton and Sibley 1981; Railsback 1993).

Irregular chert nodules range from 4 to 15 cm in diameter and commonly appear in skeletal–fenestral wackestone to skeletal packstone facies of the middle and upper members of the Fort Terrett Formation (Fig. 10c). These features indicate that silica-supersaturated fluids passed through the different stratal units to form nodules (Jacka 1977), as an event after an early stage of dolomitization from the evidence of dolomite rhombs within the chert nodules (Pittman 1959).

Selective silica replacement of calcitic (probably HMC) rudist shell fragments occurs locally (Fig. 10d), with the silica source being either biogenic (such as sponge spicules and radiolarians) or inorganic (Pittman 1959; Knauth 1979; Maliva and Siever 1989; Hesse 1988, 1989). The inorganic silica source is indicated here from dissolved detrital silicates, which consist mainly of quartz. Chert precipitation occurs when the pH decreases, which could have been induced by organic matter decomposition followed by hypersaline conditions (Hesse 1988, 1989). The inorganic model seems appropriate in this case because of the absence of sponge spicules in the Edwards Group succession (Pittman 1959).

Telogenesis

Movement on the Balcones Fault Zone in the Oligo-Miocene uplifted, exposed and eroded the Edwards Group including the Fort Terrett Formation after tens to hundreds of meters of burial. This process has continued from the Miocene to the present time (Anaya 2004) and resulted in late-stage meteoric diagenesis. Telogenesis in the study area is characterized by several processes related to oxidation and exposure. Brownish-orange oxidation bands occur at several horizons. The absence of gypsum and other evaporite minerals in this succession indicates their dissolution or removal during the initial fresh-water flushing (Fisher and Rodda 1969).

Geochemical trends, including the negative correlation of Sr against Fe and Mn content for type 4 dolomite could be related to decreasing Sr concentration caused by meteoric water flushing through time (Fig. 7c). This contact with freshwater may also have affected the stable isotope values, such that the type 4 dolomite has quite negative $\delta^{18}O$ (Fig. 7a), typical for a meteoric influence (Hudson 1977; Grossman 2012).

Dolomitization and dolomite evolution

Two dolomitization models, seepage-reflux and evaporative pumping, have been discussed for the Edwards Group of Mason County (e.g., Fisher and Rodda 1969; Rose 1972). The seepage-reflux model hypothesizes that hypersaline fluids flow downwards due to their higher density and are recharged by variations in tidal currents and possibly storms, leading to dolomite replacement of peritidal and subtidal carbonates (Fisher and Rodda 1969). The evaporative pumping mechanism suggests Mg-rich brines were induced to flow through porous sediments by an upward decrease of hydrodynamic potential during evaporation (Rose 1972). In this model, the path of the fluid-flow is opposite to that in the seepage-reflux model. These two models require an understanding of fluid-flow patterns in mud-dominated deposits. Carbonate mud should have a permeability of at least 240 mD for fluid-flow (Deffeyes et al. 1964), but this is relatively high since modern carbonate mud from the tidal flats of the Bahamas has permeabilities in the range of 1–100 mD (Gebelein et al. 1980). The average for all Holocene carbonate sediments of Florida (and the Bahamas), which includes those dominated by grains, is the order of 230 mD (Enos and Sawatsky 1981). Thus, muddy successions need sufficient permeability for the flow of the Mg-rich brines and for a significant period of time so that the succession can be dolomitized.

The Edwards Group succession is dominated by mudstone and skeletal–fenestral wackestone facies with limited fluid-flow capability and has only scarce and isolated skeletal packstone–grainstone facies (Fig. 8). All units should contain high permeability layers to allow dolomitizing brines to flow through the muddy facies (Machel 2004). For this reason, other factors may have been involved to provide the additional permeability necessary for the passage of brines through this mud-dominated succession. Fenestrae occur throughout the succession, and are common in many dolomitized peritidal deposits in the rock record (Figs. 2, 6). It is suggested here that this fenestral structure at the time of dolomitization may have had a significant impact on permeability, thus allowing Mg-rich

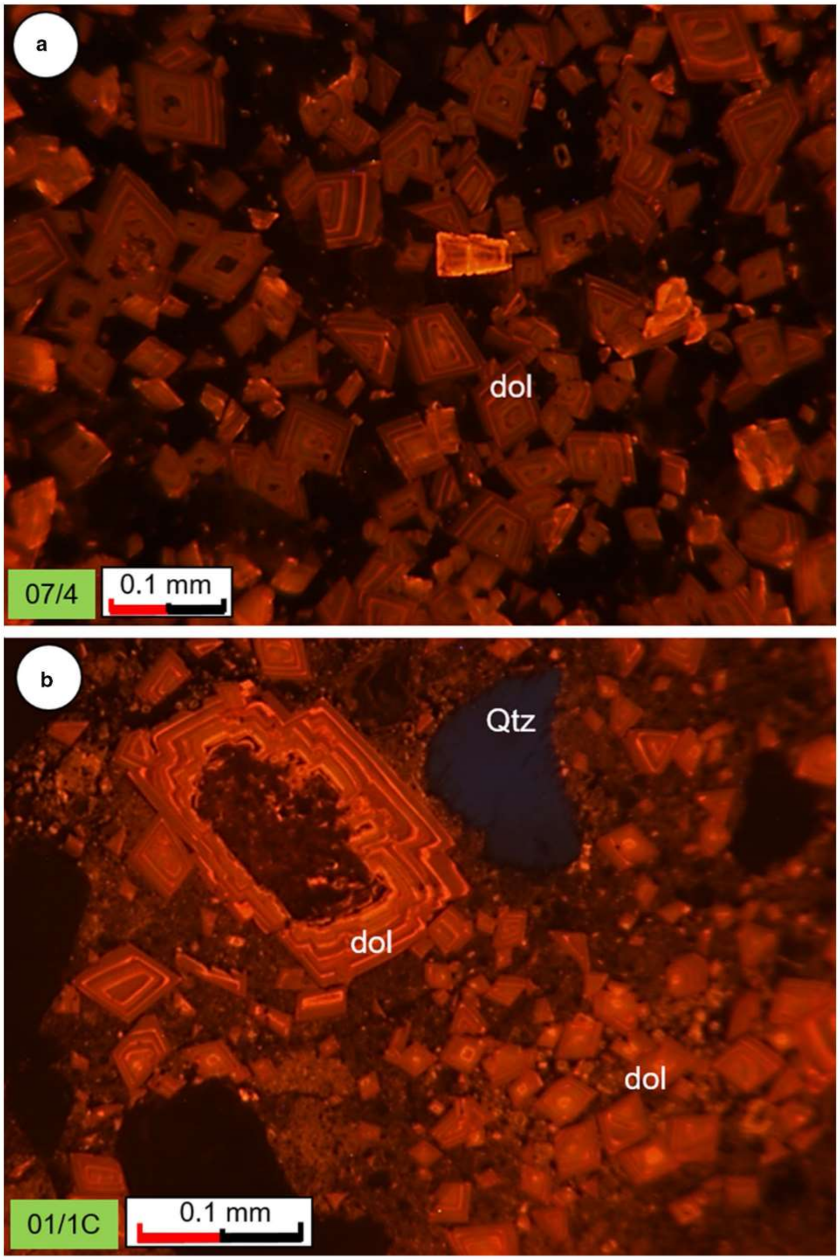

Fig. 11 Multiple zones within the cortex overgrowth of dolomite crystals in CL. **a** Concentric zonation of type 3 dolomite of the Fort Terrett Formation. **b** Cyclic zonation of dolomite cement of the upper member of the Hensel Formation

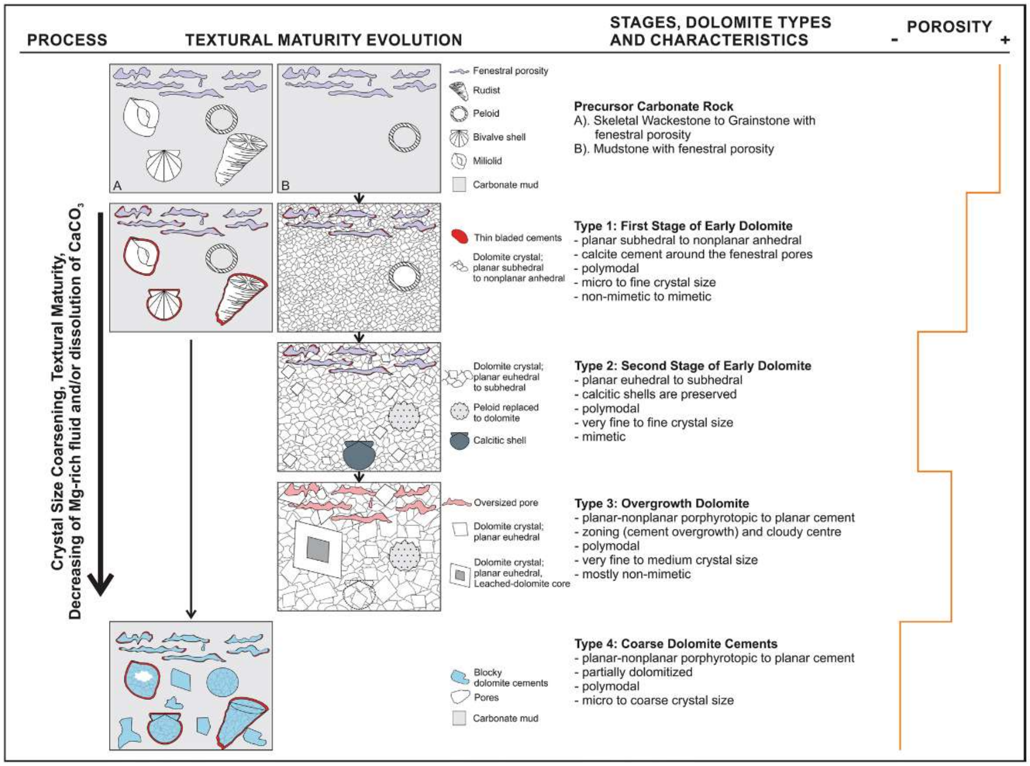

Fig. 12 Textural development of the dolomite in the Fort Terrett Formation (adapted and modified from Sibley and Gregg 1987; Choquette and Hiatt 2008). The figure shows the stages of maturation including crystal-size coarsening within sequences, crystal face development, and fabric preservation in conjunction with decreasing porosity from two different precursor carbonate rocks

brines to enter the mud-dominated facies. Interconnected fenestral fabrics are abundant in the succession as possible flow-paths for the dolomitizing brine (Fig. 6a, b).

Coarsening of dolomite crystals (Fig. 6d) is associated with fenestral porosity with overgrowths developed on the parts of crystals that were protruding into the fenestral pores (Figs. 9, 10). These voids served as initial space within which dolomite could precipitate and grow, fed by brine fluids moving through the pores in a similar process suggested by Choquette and Hiatt (2008).

Multiple zones of dolomite cortex overgrowth are distinguishable by cathodoluminescence petrography for the Fort Terrett and Hensel Formations (Fig. 11). Concentric zonation of bright orange and then dull red luminescence is a feature of type 3 dolomite. Cyclic zonation in dolomites of the Upper Hensel Formation reflects repetitive episodes of Mg-rich brine flushing through with different bulk fluid chemistry and variable Fe and Mn contents (Machel 2000).

Dolomitizing brines should have moved from the source downwards, driven by density and producing replacement dolomite in the first stage (Saller and Henderson 1998, 2001; Jones and Xiao 2005). Progressively, dolomitizing fronts would have continued but would have become less supersaturated and precipitated less dolomite than the earlier stage. In addition, the sediment closer to the brine source would have suffered "overdolomitization", that is the precipitation of overgrowths on dolomite crystals (a cement stage rather than a replacement of original sediment) (Saller and Henderson 1998, 2001).

The textural evolution of dolomites in Fort Terrett Formation shows a pattern of maturation including crystal-size coarsening, crystal face development, and fabric preservation in conjunction with decreasing porosity (Fig. 12). This evolution is also reflected in the geochemical data whereby isotope values become increasingly negative and trace element contents are reduced.

Type 1 dolomite shows a micro- to fine- crystal size related to the first stage of dolomitization, which was likely associated with syn-sedimentary processes (Longman and Mench 1978; Budd 1997; Machel 2004). It was a direct pore-precipitation process resulting from evaporitic conditions in a supratidal setting, typical of a warm and arid environment (Warren 2000; Machel 2004). This type of dolomite is usually poorly ordered (Fig. 5c) and mostly Ca-rich (Mazzullo 2000; Machel 2004).

Concentrations of Fe and Mn for this type 1 dolomite are 59–194 ppm and 63–269 ppm, respectively (Fig. 7b). These contents are relatively low compared to the other types of dolomite. Low Fe and Mn concentrations could be related to the oxic conditions, which would have reduced the availability of Fe to be incorporated into the crystal lattice (Elderfield 1981; Burdige 1993; Mazzullo 2000).

Stable isotope ratios for type 1 dolomite are low positive for $\delta^{18}O$, between 0.0 and +1.6‰ (Fig. 7a), a typical range for evaporitic conditions (Hudson 1977; Grossman 2012; Swart 2015). The $\delta^{13}C$ values show a range between –2.3 and +1.9‰, which could be linked to an organogenic model of dolomitization (Compton 1988; Mazzullo 2000) that is influenced or perhaps promoted by bacterial sulfate reduction related with organic-matter diagenesis resulting in the depletion of ^{13}C. This model occurs at surface temperature and at the near sediment–seawater interface and probably up to tens of meters burial depth. Low Fe, Mn and Sr concentrations are common for this model; as seen in Fig. 7c. The low negative values of $\delta^{13}C$ may be caused by the addition of light ^{12}C-enriched CO_2 to pore-fluids derived from bacterial-degraded organic matter (Gregg et al. 1992; Perkins et al. 1994; Vasconcelos and McKenzie 1997; Mazzullo 2000; Vasconcelos et al. 2005). This type 1 dolomite may provide nuclei or initial cortex for the next stage of dolomites.

Type 2 dolomite has a slightly increased crystal size (very fine to fine); it also shows mimetic fabric preservation and selective calcitic-shell replacement (Fig. 5d). Mimetic fabric forms during dolomitization at a lower saturation state and it may have been controlled by mineralogy (Sibley and Gregg 1987). Meanwhile, selective replacement occurs as a result of an interplay between dolomitizing brine and mineralogy. Changes in dolomitizing brine from a supersaturated to an undersaturated fluid can control rates of precipitation, while a dominantly high-Mg calcite sediment could be more prone to replacement (Sibley and Gregg 1987; Tucker and Wright 1990). The supersaturated brine replaces precursor carbonate minerals by dolomite and the solution, later, becomes undersaturated so that replacement of the remaining carbonate minerals does not take place (Murray and Lucia 1967; Tucker and Wright 1990).

Type 2 dolomite formed in a shallow-burial setting as indicated by slight enrichment in Fe and Mn concentrations compared to type 1 dolomite (Fig. 7b). The concentrations range from 71 to 251 ppm and 67 to 487 ppm, respectively. These concentrations are attributed to dysoxic conditions that are dominant in shallow-burial settings (Tucker 1986).

In terms of isotopes, the values of $\delta^{18}O$ are low negative and $\delta^{13}C$ low positive for type 2 dolomite (Fig. 7a), in comparison with type 1 dolomite. Increasing temperature during shallow burial is the main factor controlling the negative $\delta^{18}O$ for this type 2 dolomite. Meanwhile, the positive $\delta^{13}C$ is a normal-marine signal, with values commonly +1‰ higher than marine calcite (Swart 2015).

Type 3 dolomite has extensive crystal coarsening and cortex growth up to medium crystal size (Fig. 5e) and is associated with increasing fabric maturity caused by dolomite overgrowths, which record repeated development of the dolomite rhombs. The overgrowths are related to constant episodes of Mg-rich brine flushing (Katz 1971; Longman and Mench 1978; Sibley and Gregg 1987; Choquette and Hiatt 2008). This type of dolomite is characterized by subhedral to euhedral rhombic crystals with the presence of some cloudy residual inclusion-rich cores. It is likely that in this stage, dolomitization was occurring during sediment compaction resulting from increasing burial depth (Shinn and Robbin 1983; Katz 1971; Longman and Mench 1978; Choquette and Hiatt 2008). Extensive enrichment of Fe and Mn also indicates increasing burial (Fig. 7b).

Type 4 dolomite is a cement, which precipitated in bioclast molds, voids, fenestral pores and fractures within precursor lime mud (Fig. 5f). Several episodes of Mg-rich brine flushing are responsible for the coarser dolomite crystals in these settings.

Dolomitizing fluids moving downwards can cause generation of different types of dolomite (Saller and Henderson 2001; Jones and Xiao 2005). The initial process produced fine crystalline dolomite of types 1 and 2 in this study. Later, the dolomitization front would have continued basinwards and the dolomitizing brine would have flowed through the earlier precipitated dolomite causing overgrowths. Finally, fluids would have kept moving and precipitated a dolomite (type 4) cement, filling remaining pore spaces.

The main diagenetic process operating on uplift (telogenesis) of the Edwards Group in post-Oligocene–Miocene time, related to movement on the Balcones Fault Zone, is calcitization of dolomite (dedolomitization). This was caused by circulating fresh-water dissolving gypsum, which elevated the Ca/Mg ratio of the pore-water and resulted in the replacement of dolomite by calcite (cf. Evamy 1967; Abbott 1974; Longman and Mench, 1978; Ellis 1986; Barker and Ardis 1996). Leached dolomite cores (hollow) are observed (Fig. 5e), since the core would

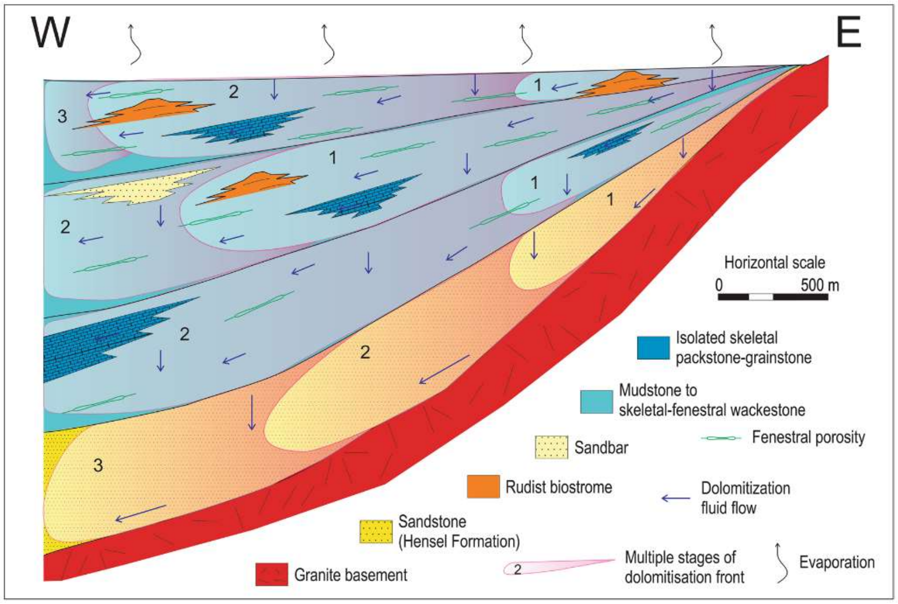

Fig. 13 The multiple stages of a downward fluid-flow model or density-head driving-mechanism through mainly fenestral porosity as the permeability pathway for dolomitization of the Edwards Group carbonates in Mason County. Note the decreasing frequency of fenestral porosity downwards and the large vertical exaggeration to show the interconnected fenestral porosity

originally have been less stable or poorly ordered and so susceptible to dissolution; the dolomite cortex on the other hand is preserved.

Fluid-flow mechanism

This Early Cretaceous succession was deposited above the Precambrian basement and it had a very simple burial history; the diagenetic processes are well constrained into a narrow range of environments, which make the interpretation of fluid-flow quite simple. There are probably three possible scenarios of fluid-flow directions in this succession: (1) dolomitizing fluids that flowed downwards (a density head mechanism), (2) fluids that flowed upwards due to evaporative pumping, and (3) fluids that flowed upwards from the basement or through the basal Edwards layers, which would suggest compaction-driven fluid-flow from the Maverick Basin or a thermal component due to the higher thermal conductivity of the granitic basement.

The most likely scenario for dolomitizing fluid flow in this succession is the downward model (Fig. 13). This model invokes a density-head driving-mechanism whereby evaporation generates denser fluids than normal seawater, which then sink within the formation through gravity, so facilitating the initiation of dolomitization (Budd 1997; Saller and Henderson 1998; Saller and Henderson 2001; Whitaker et al. 2004; Jones and Xiao 2005). Eventually, fluid density reaches equilibrium at a certain depth as the Mg-rich brines are mixed with relatively Mg-depleted pore water. This situation would have triggered lateral or outward flow of the mixed pore water. In this model, dolomite crystal size and maturity should decrease downwards. However, in the Fort Terrett Formation, the dolomite crystal sizes show a scattered distribution, perhaps due to a more complex flow system controlled by different stratigraphic horizons with different properties. Initially, fluid flow may have operated through interconnected fenestral porosity (Fig. 6) and isolated skeletal packstone–grainstone layers operating as permeable pathways.

The Fort Terrett Formation is not entirely dolomitized (Figs. 2, 8). Completely dolomitized beds dominate in the upper part (dolomite ranges from 12 to 100%), whereas partially dolomitized mudstone to skeletal packstone predominate in the lower part of the formation (8 to 24% dolomite). Although, in the upper part of the succession there is only an average of 15% initial fenestral porosity, the fabric appears more commonly, which could have resulted in a higher connectivity, allowing fluids to move farther than in the lower part where higher dolomite percentages only occur in isolated samples (Fig. 2). It is suggested here that initial fenestral porosity could have provided the permeability pathways for the dolomitizing brines, which moved downward from a surface source (such as an evaporating lagoon or evaporative tidal flat), developed especially during deposition of the upper part of the formation, into sediments below, previously deposited.

At the base of the succession, the Hensel Formation presents a much simpler porosity-permeability system and the decreasing crystal size from the top layers downwards toward the basement (Fig. 5a, b) supports the hypothesis of gravity-driven dolomitization. The downward flow then became lateral flow when the dolomitizing brines reached the granitic basement as this rock has extremely low permeability. This fluid-flow situation allows more extensive dolomite cortex overgrowths to be precipitated around dolomite cores in Upper Hensel Formation, resulting in coarser dolomite crystals in conjunction with decreasing porosity (Fig. 12). Mg-rich brines allowed the dolomitizing processes to act from the depositional surface downwards, and then for the depleted brines to move farther downward and laterally.

There are other mechanisms that could have driven dolomitizing fluids upward through the succession including geothermal heat (Simms 1985; Land 1985; Budd 1997; Machel 2004) and compaction-drive from the nearest basin (Machel 2004; Whitaker et al. 2004). Both mechanisms could produce a burial or hydrothermal dolomite such as saddle dolomite. However, there is no evidence that these textures occur in the Edwards Group in Mason County. Another mechanism, i.e., evaporative pumping, draws dolomitizing fluids upward but since a decreasing dolomite crystal size is observed in the Hensel Formation, it is inferred that this model was unlikely to have been operating in the study area.

Conclusions

1. Through detailed analysis including sedimentological, petrographical, and geochemical approaches, this study is contributing towards the understanding of porosity types as a control on dolomitization and diagenetic evolution of the Early Cretaceous Hensel and Fort Terrett Formations in the Edwards Group of Mason County, Texas.
2. The results of this study suggest that interconnected fenestral porosity could have played a major role in the flow of dolomitizing fluids through mud-dominated facies with limited permeability.
3. The Lower Cretaceous Edwards Group in Mason County was subjected to a simple burial history followed by uplift related to the Balcones Fault Zone in the Miocene. The diagenetic sequence consists of early marine cementation and micritization, meteoric dissolution and cementation, and near-surface to shallow-moderate burial dolomitization, followed by telogenesis, involving dedolomitization.
4. Four types of dolomite have been recognized and they reflect textural evolution and maturity through increasing crystal size from dolomite overgrowth and cementation. Type 1 dolomite was the result of direct pore-precipitation and sediment replacement and/or organogenic precipitation; type 2 dolomite has a slightly larger crystal size, is a replacement type, and is probably linked to a shallow-burial setting; type 3 dolomite has a larger crystal size still, and is likely precipitated at a deeper burial depth; type 4 dolomite is a late-stage cement precipitated in voids, bioclast molds, and fenestrae.
5. The interpreted fluid-flow model applicable for the Edwards Group of Mason County is a density-driven, downward-flux mechanism related to the sinking of dense dolomitizing brines derived by evaporation within the Kirschberg Lagoon. Interaction with lower Mg-saturated pore water to reach an equilibrium initiated outward flow through fenestral porosity. A more complex porosity–permeability system in the Fort Terrett Formation resulted in a more scattered distribution of dolomite crystal size, whereas a much simpler flow system in the Hensel Formation resulted in a decreasing dolomite crystal size towards the underlying Precambrian.

Acknowledgements The authors would like to thank Pertamina, Indonesia, and Berg Hughes Center for Petroleum and Sedimentary System of Texas A&M University for the funding. For the fieldwork, we also express gratitude for the help of Riza El Putranto, J Campbell Craig and MMWMA management, especially Mark Mitchell, for letting us undertake the research in the area. We are grateful to Mike Pope as a proofreader that substantially improved this paper. We thank Maurice Tucker for thoughtful reviews.

References

Abbott PL (1974) Calcitization of Edwards Group dolomites in the Balcones Fault Zone aquifer, south-central Texas. Geology 2:359–362

Abduslam A (2012) Reservoir characterization and enhanced oil recovery potential in Middle Devonian Dundee Limestone reservoirs, Michigan Basin. Western Michigan University, USA

Anaya R (2004) Conceptual model for the Edwards-Trinity (Plateau) aquifer system, Texas. Texas Water Development Board Report, Austin

Bain RJ, Kindler P (1994) Irregular fenestrae in Bahamian eolianites: a rainstorm-induced origin. J Sediment Res A64:140–146

Barker RA, Ardis AF (1996) Hydrogeologic framework of the Edwards-Trinity aquifer system, West-Central Texas. vol 1421-B. US Geological Survey, Washington, DC

Barker RA, Bush PW, Baker ET (1994) Geologic history and hydrogeologic setting of the Edwards-Trinity aquifer system, west-central Texas. US Geological Survey, Austin

Barnes VE, Bell WC, Clabaugh SE, Cloud PE Jr., McGehee RV, Rodda PU, Young K (1972) Geology of the Llano region and Austin area: field excursion. vol no. 13. University of Texas at Austin, Austin

Bathurst R (1966) Boring algae, micrite envelopes and lithification of molluscan biosparites. Geol J 5:15–32

Budd D (1997) Cenozoic dolomites of carbonate islands: their attributes and origin. Earth Sci Rev 42:1–47

Burdige DJ (1993) The biogeochemistry of manganese and iron reduction in marine sediments. Earth Sci Rev 35:249–284

Bureau of Economic Geology (1992) Geology of Texas. The University of Texas at Austin, Austin

Buxton TM, Sibley DF (1981) Pressure solution features in a shallow burled limestone. J Sediment Res 51:19–26

Choquette PW, Hiatt EE (2008) Shallow-burial dolomite cement: a major component of many ancient sucrosic dolomites. Sedimentology 55:423–460

Choquette PW, Pray LC (1970) Geologic nomenclature and classification of porosity in sedimentary carbonates. AAPG Bull 54:207–250

Collins EW (1987) Characterization of fractures in limestones, northern segment of the Edwards aquifer and Balcones fault zone, Central Texas. Gulf Coast Assoc Geol Soc Trans 37:43–54

Compton JS (1988) Degree of supersaturation and precipitation of organogenic dolomite. Geology 16:318–321

Deffeyes K, Lucia FJ, Weyl P (1964) Dolomitization of Recent and Plio-Pleistocene sediments by marine evaporite waters on Bonaire Netherlands Antilles. SEPM Spec Publ 13:71–88

Dodd JR (1966) Processes of conversion of aragonite to calcite with examples from the Cretaceous of Texas. J Sediment Res 36:733–741

Dunham RJ (1962) Classification of carbonate rocks according to depositional textures. In: Ham WE (ed) AAPG memoir 1: classification of carbonate rocks-a symposium. The American Association of Petroleum Geologists, Tulsa, pp 108–121

Elderfield H (1981) Metal-organic associations in interstitial waters of Narragansett Bay sediments. Am J Sci 281:1184–1196

Ellis PM (1986) Post-Miocene carbonate diagenesis of the Lower Cretaceous Edwards Group in the Balcones fault zone area, south-central Texas. In: Abbott PL, Woodruff CMJ (eds) The Balcones escarpment. Geological Society of America Annual Meeting, San Antonio, pp 101–114

Enos P, Sawatsky LH (1981) Pore networks in Holocene carbonate sediments. J Sediment Petrol 51:961–985

Evamy B (1967) Dedolomitisation and the development of rhombohedral pores in limestones. J Sediment Petrol 37:1204–1215

Ewing TE (2005) Phanerozoic development of the Llano uplift. Bull South Tex Geol Soc 45:15–25

Fisher WL, Rodda PU (1969) Edwards Formation (Lower Cretaceous), Texas: dolomitisation in a carbonate platform system. AAPG Bull 53:55–72

Flügel E (2004) Microfacies of carbonate rocks: analysis, interpretation and application. Springer, London

Folk RL (1974) Petrology of the sedimentary rocks. Hemphill Publishing Company, Austin

Garcia-Fresca B, Lucia FJ, Sharp JM Jr, Kerans C (2012) Outcrop-constrained hydrogeological simulations of brine reflux and early dolomitisation of the Permian San Andres Formation. AAPG Bull 96:1757–1781. doi:10.1306/02071210123

Gebelein C, Steinen R, Garrett P, Hoffman E, Queen J, Plummer L (1980) Subsurface dolomitization beneath the tidal flats of central west Andros Island, Bahamas. SEPM Special Publication 28:31–49

Gregg JM, Howard SA, Mazzullo S (1992) Early diagenetic recrystallization of Holocene (<3000 years old) peritidal dolomites, Ambergris Cay, Belize. Sedimentology 39:143–160

Grossman EL (2012) Applying oxygen isotope paleothermometry in deep time. In: Ivany LC, Huber BT (eds) Reconstructing earth's deep-time climate—the state of the art in 2012, vol Paleontological Society Short Course. The Paleontological Society Papers, pp 39–68

Grove C, Jerram DA (2011) jPOR: an ImageJ macro to quantify total optical porosity from blue-stained thin sections. Comput Geosci 37:1850–1859

Grover G Jr, Read J (1978) Fenestral and associated vadose diagenetic fabrics of tidal flat carbonates, Middle Ordovician New Market Limestone, southwestern Virginia. J Sediment Petrol 48:453–473

Halley RB, Rose PR (1977) Significance of fresh-water limestone in marine carbonate successions of Pleistocene and Cretaceous age. In: Bebout DG, Loucks RG (eds) Cretaceous Carbonates of Texas and Mexico, application to subsurface exploration. Bureau of Economic Geology The University of Texas at Austin, Austin, pp 206–215

Helper M (2006) Geologic map of north-central Mason County, Texas. The University of Texas at Austin, Austin

Hesse R (1988) Diagenesis#13 Origin of chert: diagenesis of biogenic siliceous sediments. Geosci Can 15:171–192

Hesse R (1989) Silica diagenesis: origin of inorganic and replacement cherts. Earth Sci Rev 26:253–284

Hudson J (1977) Stable isotopes and limestone lithification. J Geol Soc 133:637–660

Jacka AD (1977) Deposition and diagenesis of the Fort Terrett Formation (Edwards Group) in the vicinity of junction, Texas. In: Bebout DG, Loucks RG (eds) Cretaceous Carbonates of Texas and Mexico, application to subsurface exploration. Bureau of Economic Geology The University of Texas at Austin, Austin, pp 182–199

Jones GD, Xiao Y (2005) Dolomitization, anhydrite cementation, and porosity evolution in a reflux system: insights from reactive transport models. AAPG Bull 89:577–601. doi:10.1306/12010404078

Katz A (1971) Zoned dolomite crystals. J Geol 79:38–51

Knauth LP (1979) A model for the origin of chert in limestone. Geology 7:274–277

Land L (1973) Contemporaneous dolomitisation of Middle Pleistocene reefs by meteoric water, North Jamaica. Bull Mar Sci 23:64–92

Land LS (1985) The origin of massive dolomite. J Geol Educ 33:112–125

Lawton TS (2008) Laramide sedimentary basins. In: Miall AD (ed) Sedimentary basins of the world, vol 5. Elsevier, Amsterdam, pp 429–450

Longman MW, Mench PA (1978) Diagenesis of Cretaceous limestones in the Edwards aquifer system of south-central Texas: a scanning electron microscope study. Sed Geol 21:241–276

Machel HG (2000) Application of cathodoluminescence to carbonate diagenesis. In: Pagel M, Barbin V, Blanc P (eds)

Cathodoluminescence in geosciences, 1st edn. Springer, Berlin, pp 271–301

Machel HG (2004) Concepts and models of dolomitisation: a critical reappraisal. Geol Soc Lond Spec Publ 235:7–63

Maclay RW (1995) Geology and hydrology of the Edwards Aquifer in the San Antonio area, Texas. US Geological Survey, Austin

Maliva RG, Siever R (1989) Nodular chert formation in carbonate rocks. J Geol 97:421–433

Mazzullo S (2000) Organogenic dolomitisation in peritidal to deep-sea sediments. J Sediment Res 70:10–23

Mazzullo S (2004) Overview of porosity evolution in carbonate reservoirs. Kans Geol Soc Bull 79:20–28

Mazzullo S, Birdwell BA (1989) Syngenetic formation of grainstones and pisolites from fenestral carbonates in peritidal settings. J Sediment Petrol 59:605–611

Mench PA, Pearson FJ, Deike RG (1980) Stable isotope evidence for modern freshwater diagenesis of the Cretaceous Edwards Limestone, San Antonio area, Texas (abstract). AAPG Bull 64:749

Miall AD, Blakey RC (2008) The Phanerozoic tectonic and sedimentary evolution of North America. In: Miall AD (ed) Sedimentary basins of the world, vol 5. Elsevier, Amsterdam, pp 1–29

Moore DW (2010) Geologic map of the Edwards aquifer and related rocks in northeastern Kinney and southernmost Edwards counties, south-central Texas. US Geological Survey, Reston

Mosher S (1998) Tectonic evolution of the southern Laurentian Grenville orogenic belt. Geol Soc Am Bull 110:1357–1375

Murray R, Lucia F (1967) Cause and control of dolomite distribution by rock selectivity. Geol Soc Am Bull 78:21–36

Pascual-Cebrian E, Götz S, Bover-Arnal T, Skelton PW, Gili E, Salas R, Stinnesbeck W (2016) Calcite/aragonite ratio fluctuations in Aptian rudist bivalves: correlation with changing temperatures. Geology 44:135–138. doi:10.1130/G37389.1

Payne JH, Scott AJ (1982) Facies analysis of the Cretaceous Hensel formation, response of a fluvial system to a marine transgression. Gulf Coast Assoc Geol Soc Trans 32:92–100

Perkins RD, Dwyer GS, Rosoff DB, Fuller PA, Lloyd RM (1994) Salina sedimentation and diagenesis: West Caicos Island, British West Indies. In: Purser B, Tucker ME, Zenger D (eds) Dolomites: A, vol in. Honour of Dolomieu, vol Special Publication The International Association of Sedimentologists. The International Association of Sedimentologists, Oxford, pp 35–54

Phelps RM, Kerans C, Loucks RG, Da Gama RO, Jeremiah J, Hull D (2014) Oceanographic and eustatic control of carbonate platform evolution and sequence stratigraphy on the Cretaceous (Valanginian–Campanian) passive margin, northern Gulf of Mexico. Sedimentology 61:461–496

Pittman Jr J (1959) Silica in Edwards Limestone, Travis County, Texas. Society of Economic Paleontologists and Mineralogists Silica in Sediments SP7: 121–134

Railsback LB (1993) Lithologic controls on morphology of pressure-dissolution surfaces (stylolites and dissolution seams) in Paleozoic carbonate rocks from the mideastern United States. J Sediment Pet 63:513–522

Rose PR (1972) Edwards Group, surface and subsurface, central Texas. Bureau of Economic Geology. The University of Texas at Austin, Austin

Saller AH, Henderson N (1998) Distribution of porosity and permeability in platform dolomites: insight from the Permian of west Texas. AAPG Bull 82:1528–1550

Saller AH, Henderson N (2001) Distribution of porosity and permeability in platform dolomites: insight from the Permian of west Texas: reply. AAPG Bull 85:530–532

Scholle PA, Ulmer-Scholle DS (2003) A color guide to the petrography of carbonate rocks: grains, textures, porosity, diagenesis. AAPG Memoir 77. The American Association of Petroleum Geologists, Tulsa, Oklahoma

Scotese C, Boucot A, McKerrow W (1999) Gondwanan palaeogeography and paleoclimatology. J Afr Earth Sci 28:99–114

Sellards EH, Adkins WS, Plummer FB (1932) The geology of Texas: stratigraphy vol The University of Texas Bulletin. Bureau of Economic Geology, Austin

Shinn EA (1968) Practical significance of birdseye structures in carbonate rocks. J Sediment Pet 38:215–223

Shinn EA, Robbin DM (1983) Mechanical and chemical compaction in fine-grained shallow-water limestones. J Sediment Pet 53:595–618

Sibley DF, Gregg JM (1987) Classification of dolomite rock textures. J Sediment Pet 57:967–975

Simms MA (1985) Diagenesis by Kohout Convection in Carbonate Platform Margins. Gulf Coast Assoc Geol Soc Trans (abstract) 35:493

Steuber T, Löser H (2000) Species richness and abundance patterns of Tethyan Cretaceous rudist bivalves (Mollusca: Hippuritacea) in the central-eastern Mediterranean and Middle East, analysed from a palaeontological database. Palaeogeogr Palaeoclimatol Palaeoecol 162:75–104

Swart PK (2015) The geochemistry of carbonate diagenesis: the past, present and future. Sedimentology 62:1233–1304. doi:10.1111/sed.12205

Tucker ME (1986) Formerly aragonitic limestones associated with tillites in the late Proterozoic of Death Valley, California. J Sediment Petrol 56:818–830

Tucker ME, Wright VP (1990) Carbonate sedimentology. Blackwell Science Ltd., Malden

Vasconcelos C, McKenzie JA (1997) Microbial mediation of modern dolomite precipitation and diagenesis under anoxic conditions (Lagoa Vermelha, Rio de Janeiro, Brazil). J Sediment Res 67:378–390

Vasconcelos C, McKenzie JA, Warthmann R, Bernasconi SM (2005) Calibration of the δ^{18}O paleothermometer for dolomite precipitated in microbial cultures and natural environments. Geology 33:317–320. doi:10.1130/G20992.1

Veizer J (1983) Chemical diagenesis of carbonates: theory and application of trace element technique. SEPM Stable Isot Sediment Geol 10:1–100

Walker N (1992) Middle Proterozoic geologic evolution of Llano Uplift, Texas: evidence from U-Pb zircon geochronometry. Geol Soc Am Bull 104:494–504. doi:10.1130/0016-7606

Warren J (2000) Dolomite: occurrence, evolution and economically important associations. Earth Sci Rev 52:1–81

Whitaker Fiona F, Smart Peter L, Jones Gareth D (2004) Dolomitization: from conceptual to numerical models. Geol Soc 235(1):99–139